Title
Formulation and Development of Clinically Relevant Drugs

Author
Plamthottam, Sheba

Publication Date
2018

Peer reviewed|Thesis/dissertation

UNIVERSITY OF CALIFORNIA
Los Angeles

Formulation and Development of Clinically Relevant Drugs

A dissertation submitted in partial satisfaction of the requirements for the degree
Doctor of Philosophy in Chemistry

by

Sheba Plamthottam

2018

ABSTRACT OF THE DISSERTATION

Formulation and Development of Clinically Relevant Drugs

by

Sheba Plamthottam

Doctor of Philosophy in Chemistry

University of California, Los Angeles, 2018

Professor Jeffrey I. Zink, Chair

This dissertation makes contributions to the fields of anticancer drug formulation, synthesis and applications of nanoparticle adjuvants, and structure-activity relationships in drug discovery. Many drugs that are promising clinical candidates are potent *in vitro*, however their solubility and pharmacokinetic properties are suboptimal. Here we used various nano-formulations, primarily mesoporous silica nanoparticles, to improve the solubility and release properties of these drugs. *In vivo* results show that these nanoparticles are safe, multifunctional carriers that can be used for clinical imaging using positron emission tomography. In the second part of this work, porous aluminum oxide nanoparticles were synthesized for applications as immunological adjuvants, and polymer-coated mesoporous silica nanoparticles were used to deliver cyclic dinucleotides to stimulate the innate immune response. Lastly, UV-Vis spectroscopic assays were developed and used to understand how electronic properties of iron-binding heterocyclic thiosemicarbazone analogs are related to their inhibition of ribonucleotide reductase, an important target for cancer therapy. The structure-activity relationships that were discovered led to a promising drug scaffold for the treatment of cancers sensitive to nucleotide deprivation.

The dissertation of Sheba Plamthottam is approved.

Robert Thompson Clubb

Caius Gabriel Radu

Jeffrey I. Zink, Committee Chair

University of California, Los Angeles

2018

Acknowledgements

I would like to thank my PhD advisors Professor Jeffrey Zink and Professor Caius Radu for being wonderful mentors and giving me the unique opportunity to work across disciplines. I would also like to thank Professor Robert Clubb for serving on my doctoral committee. In the Radu Lab I learned cell culture techniques, had the opportunity to work directly with organic chemistry and pharmacology graduate students and postdocs on many collaborative projects, and I was able to use clinically-relevant therapeutics in my research. In addition to his guidance, I thank Caius for teaching me rare and valuable skills like how to create professional presentations from my research and communicate science across disciplines. In the Radu Lab, particularly, I would like to thank Evan Abt and Thuc Le for their patient guidance and teaching. I also worked on fascinating projects that would not have been possible without wonderful collaborators in the David Geffen School of Medicine—Professor Marcus Horwitz, Daniel Clemens, and Bai-Yu Lee.

I am so thankful for Dr. Zink's guidance with all my experiments, and especially for introducing me to the wonderful world of spectroscopy. Without his excitement for science, thoughtful insights, and fun discussions about my projects, none of my research would have been possible. I would like to thank Jeffrey Valuenzuela, my exceptional undergraduate student who did an extensive amount of work on the development of iron binding assays for 3-AP analogs. Without his help, the project would not have progressed as it did. In the Zink Lab, I am thankful to have worked with great colleagues, who taught me so much about nanomaterials and spectroscopy. I would especially like to acknowledge Philippe Saint-Cricq-Riviere, Daniel Pazo, Zilu Li, Ruining Wang, and Bastian Ruehle for all their guidance. Bastian you are an amazing mentor, the most patient teacher, and a wonderful friend. I wouldn't be the researcher I am today without all your guidance and advice during the program. Thank you so much for taking the time to teach me the fundamentals of so many different techniques.

I would like to thank my parents for their support through all my studies and for fostering my excitement about science and art from a young age and, my brother Roshan for his encouragement along the way. I would like to thank my oldest and dearest friends Alykhan, Ryan, Karlyn, Sanjana, Oh Sung, and Nicole. I could not have survived without them, as well as my sweet friends at UCLA—Daniel Sun, Sayoni Ray, Natcha Wattanatorn, and Dimitri Bikos, for all the fun conversations, advice about labwork, and endless support through graduate school. Finally, thank you to my sweetheart Maxim Marshalik for all his support, and for actually listening to me when I talk about my research.

Formulation and Development of Clinically Relevant Drugs

Table of Contents

List of Figures

List of Tables

Vita

2009-2013	B.S. Chemical Biology College of Chemistry University of California, Berkeley
2013	Dorothy Radcliffe Dee Fellowship Division of Physical Sciences University of California, Los Angeles
2013-2018	Teaching Assistant/Associate/Fellow Department of Chemistry and Biochemistry University of California, Los Angeles
2015-2018	Graduate Student Researcher Zink Lab University of California, Los Angeles

1 Introduction

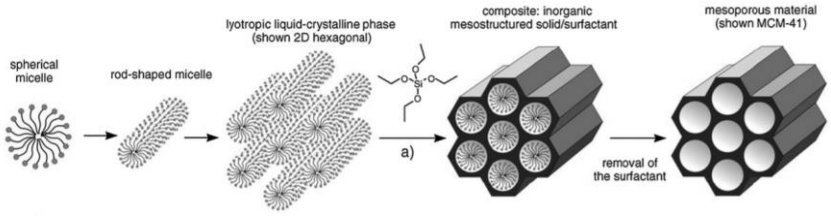

Figure 1.1 Synthesis overview of mesoporous silica nanoparticles. Image from Gibson et. al.[1]

Ordered mesoporous silica nanoparticles (MSN) are synthesized with structure-directing agents that include anionic and cationic surfactants or polymers in the presence of a silica precursor, whose hydrolysis and condensation is catalyzed by the addition of acid or base (Figure 1.1).[1] The type of surfactants, reaction time, reaction temperature, pH, and reagent concentrations can be used to control the size and morphology of the resulting nanoparticles. Of particular interest in this work are MCM-41-type nanoparticles. MCM-41 synthesis involves CTAB-surfactant directed hydrolysis of tertraethylorthosilicate (TEOS) in basic conditions. Surfactants are removed by acid extraction or ion exchange to produce nanoparticles with high surface areas (1000 m^2/g) and 2D-hexagonally-packed mesopores, generally 2.2 nm in diameter.[2,3] MCM-41-type MSN were first reported by Mobil Corporation in 1992 for use as catalysts due to their high surface areas.[4] However, further work on their physio-chemical properties and biocompatibility prompted them to be used as drug-carriers.[3,5] Large pore volumes in MCM-41 enable drug loading, while surface silanols allow for chemical modifications such as the addition of stimuli-responsive caps for triggered release in the body or the addition of targeting agents to promote uptake by cells of interest.[6] MSN have shown successes in loading anticancer drugs,[7,8] antibiotics,[9,10] and small molecule siRNA[11,12] and releasing them in the body. The pores of MSN can be modified with agents that have affinities for hydrophobic drugs, while keeping the surface of the nanoparticle hydrophilic.[3] This property is especially useful in the formulation of clinical agents that have solubility issues *in vivo*.

In this work, I discuss three major classes of anticancer drugs for formulation. The first are heterocyclic thiosemicarbazone (HCT) ribonucleotide reductase (RNR) inhibitors, an extensive class of metal-binding redox-active drugs whose

structure-activity relationships have been studied as far back as the mid-1900's.[13] In the past, structural modifications to pyridine HCT compounds were made to improve drug-like properties, eventually resulting in the phase II clinical agent, 3-aminopyridine-2-carboxaldehyde thiosemicarbazone (3-AP). 3-AP is a tridentate chelator that functions by the formation of the 3-AP iron(II) complex, which actively quenches the tyrosyl radical in the enzyme's active site, resulting in inhibition of RNR.[14] In the final chapter, I explore the structure-activity relationships of the biologically active Fe(II) complex of 3-AP and analog complexes. Using spectral commonalities of 3-AP analog iron complexes, we develop assays with UV-Vis spectroscopy that can be used to measure oxidation rates, pH effects, and iron binding affinities to these thiosemicarbazone ligands. Results from these studies have resulted in a better understanding of structural modifications that can be made to the 3-AP scaffold. In addition to designing analogs that have improved activity against RNR *in vitro*, in Chapter 3, we develop both MSN and emulsion alternatives to improve drug-like properties of 3-AP and analogs *in vivo*.

The second class of drugs discussed here are deoxycytididine kinase (dCK) inhibitors, which have been used in combination therapies to treat mice with acute lymphoblastic leukemia.[15] Its fluorinated analog, Clofarabine, is also currently being used as PET probe for detection of tumors with high dCK expression.[16] Lastly, I discuss formulation of a dihydroorotate dehydrogenase (DHODH) inhibitor and antiviral agent, in which poor water solubility results in lower bioavailability of the drug. In Chapters 2 and 3, I show that MSN are drug delivery vehicles that can solve some problems that prevent advancement of these drugs, as well as discuss the development of alternative emulsion-based oral formulations that went on to be used successfully *in vivo* to treat B-ALL leukemia in a mouse model.

In Chapter 4, we explore how an MSN carrier can bypass transferrin receptors on the surface of the cell and deliver lethal doses of free iron into the lysosome. We find that these nanoparticles induce cell death via an ROS-mediated Fenton pathway, giving them the potential to be used in combination therapies to sensitize cancer cells to the effects of anticancer drugs.

In Chapter 5, the physio-chemical properties of different types of silica nanoparticles and their toxicities are discussed. In Chapter 6, the pharmacokinetics and mechanism of action of a successful *in vivo* study of antibiotic-loaded snap-top

MSN against tularemia is presented, as well as a pilot study using PET imaging to better understand the biodistribution of these particles *in vivo*.

In addition to applications in cancer, in Chapters 7 and 8, I discuss nanoparticles that can be used as immunological adjuvants. In Chapter 7, we synthesize a nanoparticle carrier that effectively protects and delivers a cyclic dinucleotide to activate the STING pathway, an intrinsic pathway in the cell that is responsible for the innate immune response following tumorigenesis, viral infections, or radiation therapy. While a lot of work has been done in tuning and controlling the synthesis of silica nanoparticles, the synthesis of aluminum oxide nanoparticles is much more difficult to control due to the higher rate of hydrolysis of aluminum alkoxide precursors. In Chapter 8, I develop a novel method to synthesize porous alumina nanoparticles, which have potential as immunological adjuvants.

2 Nanoparticle formulation of hydrophobic dihydroorotate dehydrogenase inhibitors (DHODHi)

This chapter is based on work done with my colleagues Daniel Sun and Soumya Poddar.

2.1 Abstract

Recently-discovered inhibitor of dihydroorotate dehydrogenase and potent antiviral agent NITD-982 is a promising clinical candidate. However, poor water solubility and high lipophilicity has prevented further work on this drug. We use hydrophilic mesoporous silica nanoparticles with hydrophobic phenyl pore modifications as a drug carrier for NITD-982. Preliminary *in vitro* experiments in *Jurkat T-ALL* show that NITD-982-loaded nanoparticles are potent inhibitors of DHODH.

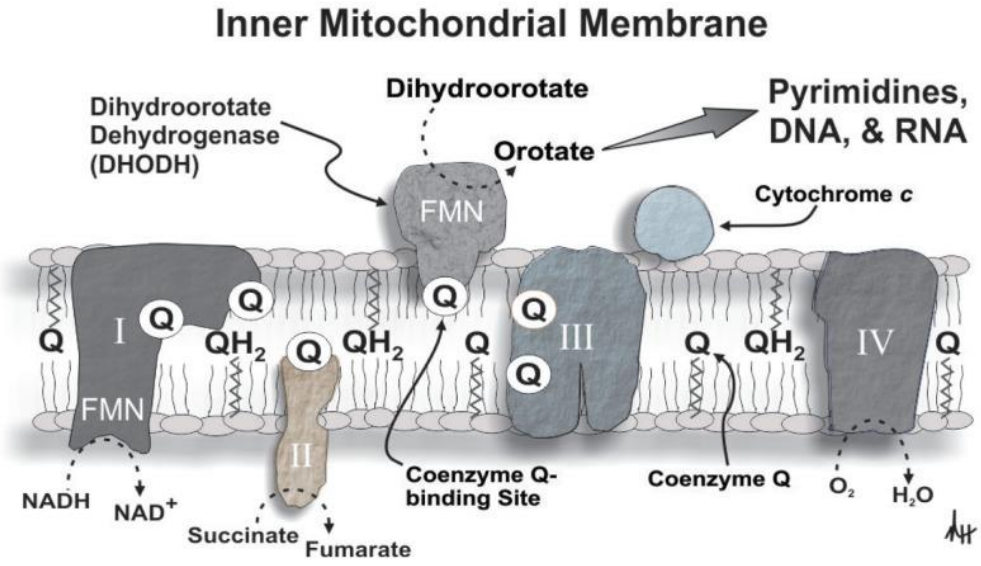

Figure 2.1 The role of dihydroorotate dehydrogenase in mitochondrial bioenergetics and the *de novo* pathway for nucleotide biosynthesis. Image from Velez. et. al.[17]

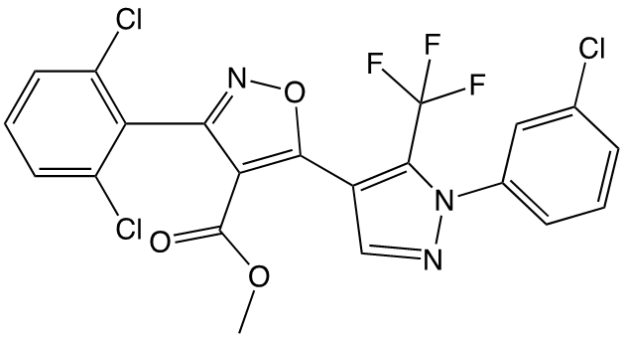

Figure 2.2 Structure of antiviral agent NITD-982, a potent inhibitor of DHODH.

2.2 Introduction

A high-throughput screen using cells infected with the antibiotic resistant "superbug" *Carbapenemase-producing enterobacteriaceae* (CPE) was used to identify a new class of antiviral agents with an isoxazole-pyrazole core. NITD-982 was in this class of compounds and was found to have nanomolar potency against four different RNA virus families: *Flaviviridae*, *Paramyxoviridae*, *Orthomyxoviridae*, and *Retroviridae*.[18] However, its effectiveness did not translate *in vivo* potentially due to its poor water solubility and high lipophilicity (cLogP=7.3), high plasma uridine which counteract its effects, and high plasma protein binding affinity. *In vivo* studies use corn oil to dissolve the compound before subcutaneous administration, where t_{max} was found to be 8 hours and C_{max} was 528 nM.[19] Addition of solubilizing groups to this compound failed to produce analogs as potent as the original molecule, so further experiments on this compound were limited to *in vitro* work where its specific target was discovered to be dihydroorotate dehydrogenase (DHODH), a mitochondrial protein in the *de novo* pathway that catalyzes the oxidation of dihydroorotate to orotate.[18] This highly specific compound has potential not only as an antiviral agent, but also as an inhibitor of *de novo* nucleotide synthesis in combination therapies to treat cancer.[20] To improve the drug delivery properties of this molecule, we package this highly lipophilic drug into mesoporous silica nanoparticles, study release properties from the nanoparticles, and compare activity *in vitro* compared to the drug dissolved in DMSO.

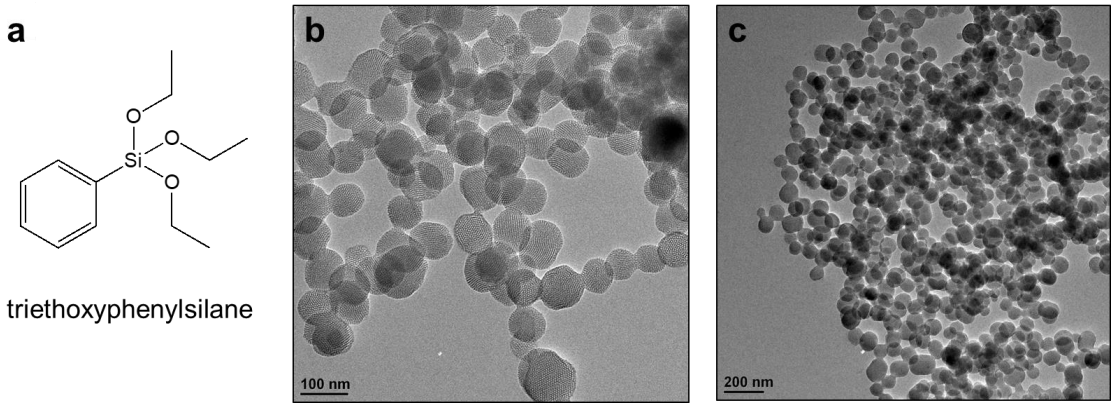

Figure 2.3 TEM images of (b) mesoporous silica nanoparticles and (c) triethoxyphenylsilane-modified mesoporous silica nanoparticles.

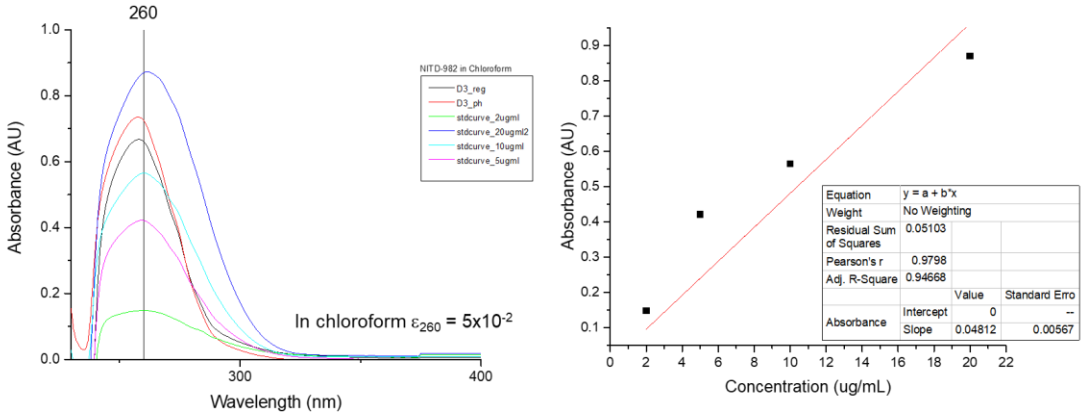

Figure 2.4 (a) Absorbance spectra of NITD-982 in chloroform and (b) standard curve used to calculate release efficiency and release capacity of the drug.

2.3 Results and Discussion

Regular mesoporous silica nanoparticles are synthesized and phenyl pore-modified MSN are synthesized by co-condensation of triethoxyphenylsilane to maintain hydrophilicity of the outer surface of the nanoparticle (Figure 2.3). Co-

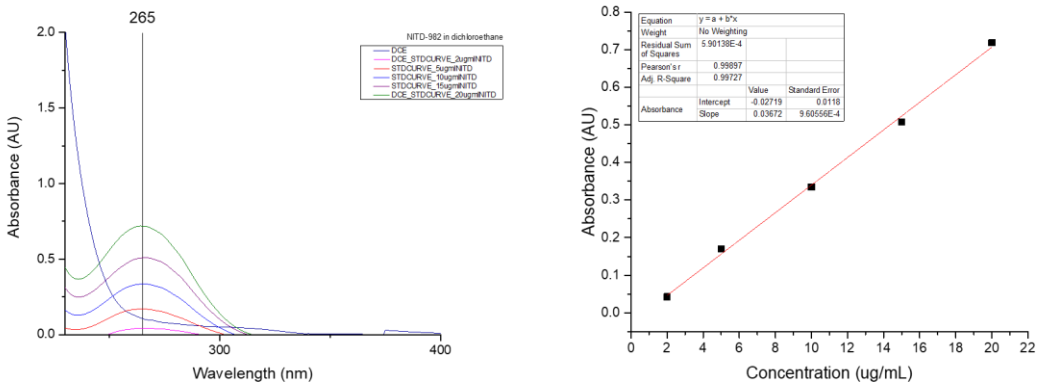

Figure 2.5 (a) Absorbance spectra of NITD-982 in dichloroethane and (b) standard curve used to calculate loading efficiency and loading capacity of the drug.

condensation of triethoxyphenylsilane did not significantly change the morphology of the nanoparticles (Figure 2.3c).

Since the drug is not soluble in water, chloroform (Figure 2.4) and dichloroethane (Figure 2.5) are used as loading solvents. Their low boiling point allowed for vacuum drying of the nanoparticles after loading to remove any residual solvent.

UV-Vis is used to quantify release efficiency, release capacity, loading efficiency, and loading capacity reported in Table 2.1. We find that unmodified nanoparticles have very high loading capacity (30%) for this lipophilic drug. Phenyl-modified nanoparticles (Ph-MSN) do not improve the loading capacity (20%) but slightly improve the ability of the drug to get released from the nanoparticle.

The cell proliferation assay in Figure 2.6 shows that the IC_{50} of the free drug in DMSO and nanoparticle drug are comparable after 72 hour treatment. *In vivo* pharmacokinetic experiments would be useful to explore the release properties of the nanoparticle carrier in the blood.

MSN	Release Efficiency (% drug uptake) In CHCl3	Release Capacity (% drug per particle released in chloroform, mg drug/mg MSN) In CHCl3	Loading Efficiency (% drug loaded) In DCE	Loading Capacity (% drug per particle mg drug/mg MSN) In DCE
Regular MSN	2.2	7.6	32	30
Ph-MSN	2.4	8.4	21	20

Table 2.1 Table summarizing uptake and release properties of NITD-982-loaded nanoparticles

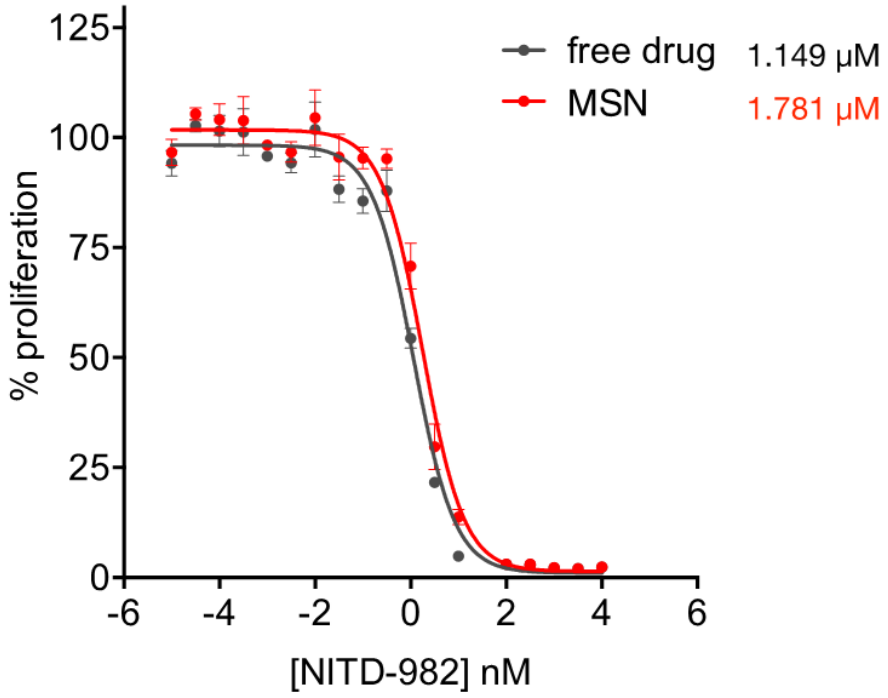

Figure 2.6 Cell-TiterGlo cell proliferation assay in *Jurkat T-ALL* after 72 hour treatment with NITD-982@MSN and free NITD-982 (in DMSO stock).

2.4 Conclusions

Loading capacity of NITD-982 in MSN can be as high as 30% in bare MSN. NITD-982@MSN is are comparably potent to the free drug *in vitro* with an IC_{50} of 1.781uM in *Jurkat T-ALL*. Encapsulation of NITD-982 into water-soluble mesoporous silica nanoparticles is a promising method to combat the poor water solubility of this potent clinical agent. *In vivo* experiments are needed to test the interactions of the drug released from these nanoparticles in the body.

2.5 Materials and Methods

Materials

Tetraethylorthosilicate 98% (Sigma Aldrich). Phenyltriethoxysilane 98% (Sigma Aldrich). Sodium hydroxide (Thermo Fisher). Hexadecyltrimethylammonium bromide (CTAB) ≥98% (Sigma Aldrich). NITD-982 is made in-house according to published procedures.[21]

Nanoparticle synthesis

200mg CTAB and 1.2mL of 1M NaOH is added to 100mL of Millipore water and heated to 80°C. For regular MSN, 1.2mL TEOS is added dropwise. For phenyl-modified MSN, 585uL of TEOS is added dropwise, and immediately following, a mix of 585uL TEOS and 30uL phenyltriethoxysilane is added dropwise. After silane precursors are added, the solution is stirred well for 2 hours at 80°C. Solution is cooled and nanoparticles are centrifuged and supernatant is discarded. MSN are washed twice with water and twice with ethanol. Surfactant is extracted by suspending nanoparticles in 20 mg/mL NH_4NO_3 in ethanol and refluxing for 1 hour. Particles are cooled and washed with ethanol three times. This extraction procedure is done twice to ensure complete surfactant removal.

Characterization

After CTAB extraction, clean nanoparticles suspended in ethanol are dropped on a carbon-coated copper grid for TEM imaging (T12 cryo-electron microscope, FEI Tecnai).

Drug loading and release

For a typical loading study, 5mg MSN are washed with the loading solvent of choice (chloroform or dichloroethane) three times and suspended in a solution of NITD-982 in chloroform or DCM. After 24 hours loading on a rotator, the drug solution before and after nanoparticle addition is quantified using UV-Vis to determine loading capacity (mg drug/mg MSN x 100%) and efficiency (% drug loaded into nanoparticles vs. total drug added). Loaded particles are washed with water until UV-Vis absorbance of supernatant is zero. Particles are then suspended in chloroform or DCM and stirred on the rotator for 24 hours. Release capacity (mg drug released/mg MSN x 100%) and efficiency (% drug released from nanoparticles) are then calculated from the absorbance of the supernatant.

Cell culture conditions

Jurkat acute T-cell leukemia cell line was purchased from ATCC and cultured in standard incubation conditions using ATCC-formulated RPMI-1640 Medium containing L-glutamine, supplemented with 10% FBS and 1% penicillin-streptomycin at a humidified 37°C with 5% CO_2. Subcultures were established by centrifugation with subsequent resuspension at 1 x 10^5 viable cells/mL. Cell density was maintained between 1 x 10^5 and 1 x 10^6 viable cells/mL.

Cell proliferation assay

Jurkat cells are plated at a density of 1500 cells/well in the center of a 96-well plate and left in the incubator for 24 hours. After 24 hours, treatments are administered. 72 hours after treatment, Promega CellTiter-Glo® Luminescent Cell Viability Assay is used to assess cell viability on a Tecan M1000 Plate Reader. Treatments are done in triplicates and consist of titrations of NITD-982 from 20mM DMSO stock and NITD-982@Ph-MSN equivalent to the free drug dose. Release capacity of NITD-982-loaded nanoparticles was used to calculate the concentration of NITD-982 in NITD-982@Ph-MSN treatment in the dose response curve in Figure 2.6.

3 Nanoformulations of ribonucleotide reductase inhibitors (RNRi)

This chapter is based on work done with my colleagues Evan Abt, Soumya Poddar, Andreaa Stuparu, and undergraduate students Chloe, Janet, Vincent, and Todd. Work done with nanoemulsion formulation was done with consultant Peter Rix and Soumya Poddar and is featured in the following publication.

Thuc M. Le et. al. ATR inhibition facilitates targeting of leukemia dependence on convergent nucleotide biosynthetic pathways, Nature Communications, volume 8, 241 (2017).

3.1 Abstract

3-AP has had some clinical success, but its pharmacokinetic properties are suboptimal. A variety of different nanoparticles were screened for their compatibility to load and release 3-AP and the more potent isoquinoline analogs of 3-AP: MAIQ and IQ-2, which have even greater solubility issues. 3-AP was successfully loaded into pH-valve nanoparticles, however release of the drug *in vitro* was slow due to strong interactions of the pore wall with the positively charged, highly polar drug. MAIQ and IQ-2, which are less polar due to their lipophilic isoquinoline rings, were loaded into bare nanoparticles without caps with promising release profiles *in vitro*. These drugs are potent inhibitors of RNR and may have improved pharmacokinetic (PK) profiles with the addition of a nanoparticle carrier, but their release profiles have yet to be tested *in vivo*. In addition to nanoparticle formulations, self-microemulsifying drug delivery systems (SMEDDS) were formulated for oral administration of 3-AP in combination with the dCK inhibitor, DI-82, and the ATR inhibitor, VE-822. This formulation has shown promising *in vivo* efficacy as a triple combination therapy.

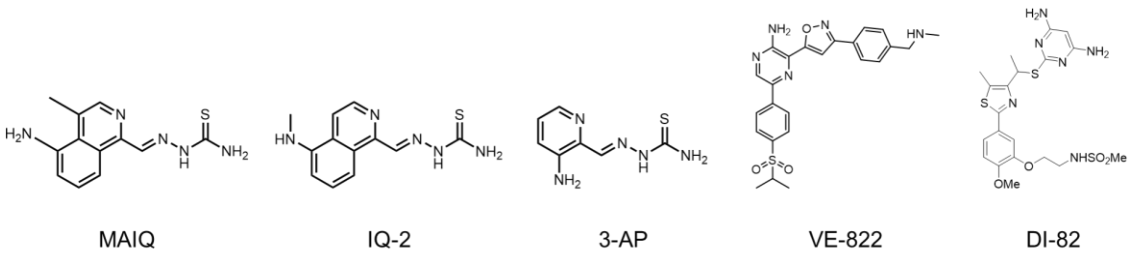

Figure 3.1 Structures of RNR inhibitors (MAIQ, IQ-1, and 3-AP), ATR inhibitor (VE-822), and dCK inhibitor (DI-82).

3.2 Introduction

3-AP and DI-82 are inhibitors of enzymes involved in nucleotide metabolism. 3-AP is an inhibitor of the enzyme ribonucleotide reductase (RNR), involved in *de-novo* synthesis of dNTPs, and DI-82 is an inhibitor of deoxycytidine kinase (dCK), involved in the nucleotide salvage pathway. These two drugs in combination with VE-822, an inhibitor of ATR involved in the replication stress response, causes depletion of dNTP pools leading to DNA replication stress and cell death, particularly in tumor cells, which have an increased demand for nucleotides. This triple combination therapy has shown therapeutic efficacy in leukemia models, but treatment of solid tumors remains a challenge.[15]

Quickly-cleared drugs require continuous large doses in the plasma before therapeutic effects are seen.[22] However, cytotoxicity to healthy cells increases if the concentration in the blood spikes too quickly. Our *in-vivo* dosing studies have determined the importance of both C_{max}, the maximum drug concentration in the plasma, and clearance time of the drug. In this chapter, we explore MSN and emulsion formulation alternatives to improve *in vivo* dosing of these drugs. Controlled delivery of these therapeutic agents would be a feasible way to control the PK properties of these quickly-cleared drugs, maintain them at therapeutic concentrations for longer, and, in the case of using a nanoparticle carrier, direct them to sites of solid tumors.[23,24] Here, we screen different types of nanoparticles with various modifications to find the best carrier for these drugs. Specifically, we compare pH-responsive MSN and uncapped nanoparticles to deliver RNR inhibitors 3-AP, MAIQ, and IQ-2 or the dCK inhibitor DI-82. We also formulate these drugs into emulsions for oral administration with success in an *in vivo* B-ALL leukemia model.

3.3 Results and discussion

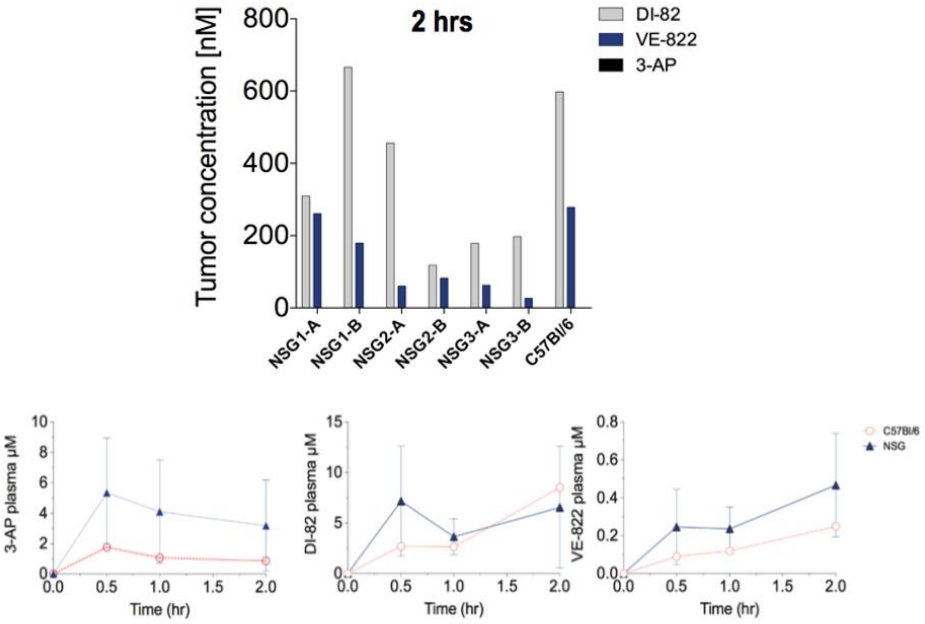

Figure 3.2 (a) Tumor and (b) plasma concentrations of 3-AP, DI-82, VE-822 in mice with various xenograft tumors. Determined using LC-MS.

Pharmacokinetic analyses of mice treated with the triple combination therapy were done to quantify drug concentration in plasma over time and in solid tumors after 2 hours of i.p. drug administration (Figure 3.2). The percent of drug delivered to plasma vs. solid tumors was determined by LC-MS to be 12-35%, 2-9%, and 0% for VE-822, DI-82, and 3-AP respectively. Although therapeutic doses of 3-AP were detected in the plasma, 3-AP was undetectable in the solid tumors. 3-AP has been shown to be effective in *in-vitro* studies of solid liver and pancreatic cancer tumors (SNU449 and MiaPaCa-2). This finding suggests that the lack of efficacy in *in vivo* tumor models is due to inefficient drug delivery, not drug potency. Methods to improve delivery to solid tumors is needed to improve efficacy of the three drugs, particularly 3-AP and analogs.

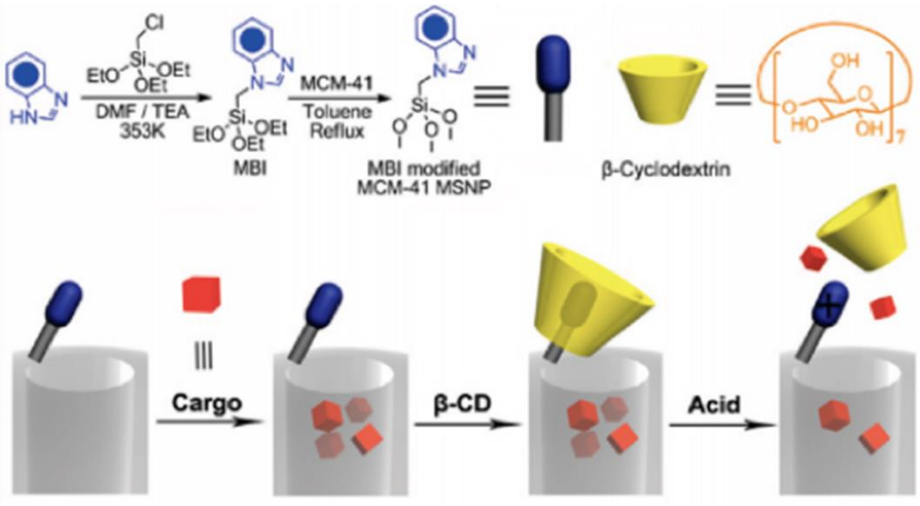

Figure 3.3 Benzmidazole-modified nanoparticles with acid-responsive beta-cyclodextrin caps are used to cap cargo in the pores of the nanoparticles and uncap and release cargo upon a pH decrease (such as in the lysosome). Figure from Meng et. al.[25]

MSN have been shown to accumulate in the leaky vasculature of certain tumors which is postulated to be due to the enhanced permeability and retention effect (EPR) of small macromolecules.[23,26] Furthermore, properties of MSN can be easily tuned or functionalized with targeting agents due to the presence of –OH groups on the surface. Here, we synthesize pH-responsive capped nanoparticles that have shown efficacy against human differentiated myeloid (THP-1) and squamous carcinoma (KB-31) and use them to load 3-AP and DI-82.[25] The above scheme summarizes the synthesis of benzimidazole-modified MSN (Bz-MSN), and their drug release mechanism. After drug loading, interactions between the deprotonated benzimidazole moiety and the beta-cyclodextrin sugar are used to cap the particles with drug. When the benzimidazole stalk gets protonated (such as after endocytosis, when the nanoparticle is in the lysosome), the cap loses affinity for the stalk and the cap comes off and the drug gets released.[25]

After attachment of benzimidazole on the surface of the nanoparticles, to ensure that surface area and pore size of the nanoparticles are high enough for drug loading, Bz-MSN are characterized by nitrogen sorption measurements and BET analysis. Modification of benzimidazole on the surface did not reduce the pore size

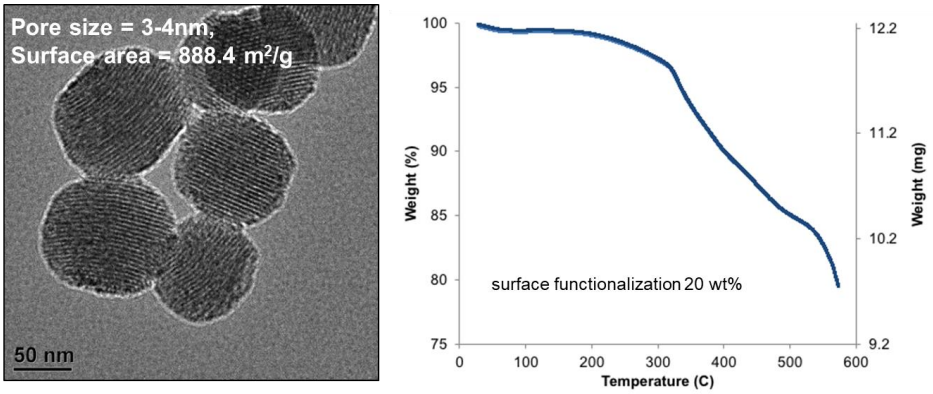

Figure 3.4 (a) TEM of pH-valve nanoparticles. Reported pore size and surface area are from BET analysis of nitrogen sorption curves

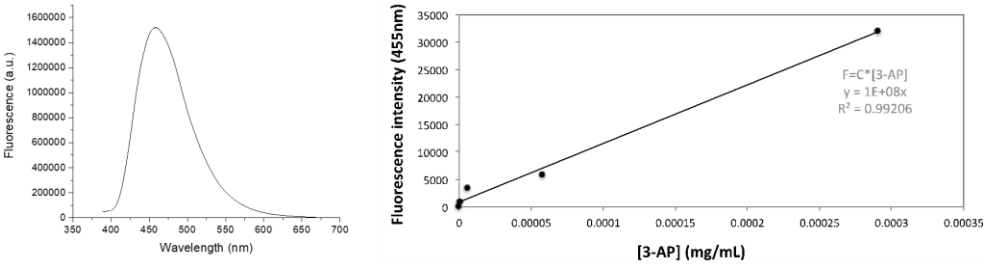

Figure 3.5 (a) Fluorescence spectrum of 3-AP in water and (b) fluorescence calibration curve of 3-AP in water (367 nm excitation wavelength).

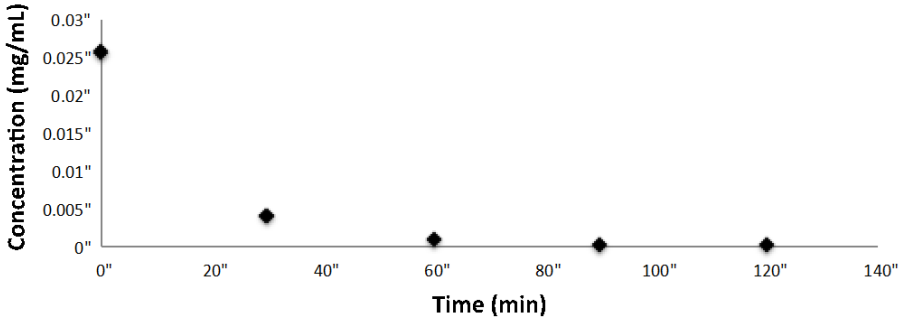

Figure 3.6 (a) Fluorescence is used to determine loading capacity of 3-AP into nanoparticles. 3-AP release in PBS from bare MSN shows the need for a capping agent.

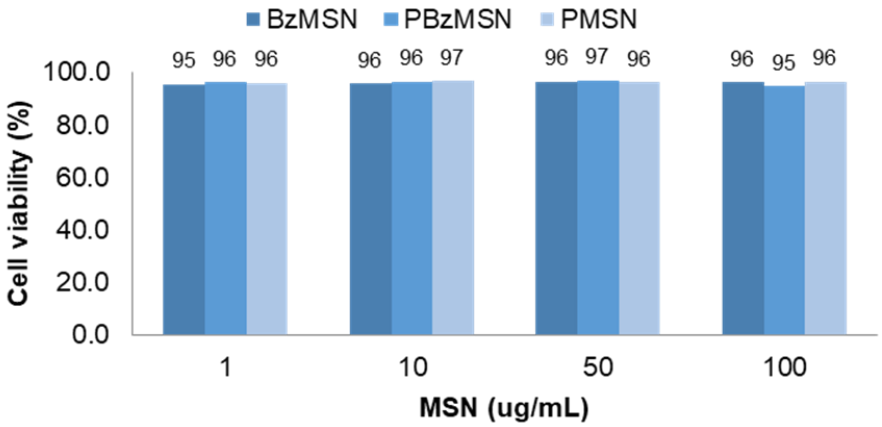

Figure 3.7 Trypan blue cell toxicity assay for benzimidazole-modified MSN (BzMSN), benzimidazole and phosphate-modified MSN (PBzMSN), and phosphate-modified MSN (PMSN) in *p185* cells (24h treatment).

or drastically change the surface area, which, after the modification, are 3-4 nm and 888 m^2/g, respectively, typical of MCM-41 (Figure 3.4).

3-AP has a bright fluorescence emission peak at 450 nm (Figure 3.5), which is used to determine release profile of the drug over time from the nanoparticle (Figure 3.6). Loading capacity of 3-AP in THF was determined to be 30% (mg drug/mg MSN). In Figure 3.6, the release profile of uncapped nanoparticles loaded with 3-AP without the beta-cyclodextrin cap show the need for a capping agent, as most of the loaded drug gets released by 1 hour.

Cell toxicity assay of MSN and Bz-MSN with and without phosphonate pore modification are used to determine the tolerated dose of these nanoparticles in this cell line (Figure 3.7).

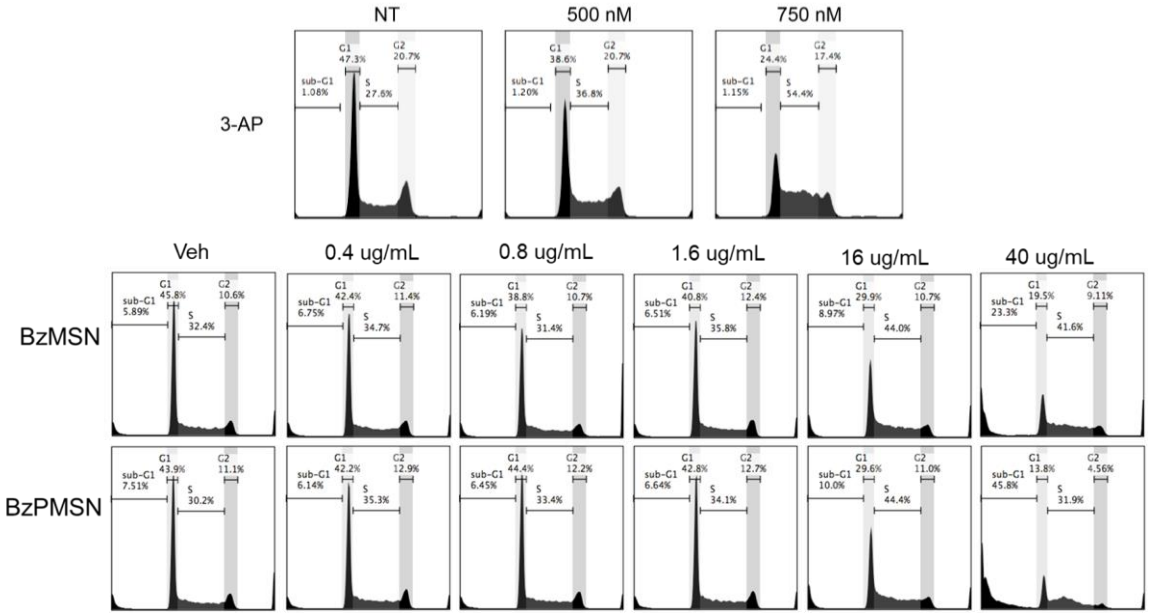

Figure 3.8 Cell cycle profiles of 3-AP, 3-AP-loaded Bz-MSN, and 3-AP-loaded BzP-MSN treatment after 24 hours. Concentration values of ug/mL are weight of MSN per mL.

After ensuring that the nanoparticles are non-toxic, 3-AP or DI-82 is loaded into Bz-MSN and capped with beta-cyclodextrin. Due to limited water solubility of the drugs, release capacity is more accurately determined *in vitro*. 3-AP release capacity from Bz-MSN in water is 3% (mg drug/mg MSN) and is limited by the solubility of the drug in water. Treatment of free 3-AP results in S-phase arrest after 24 hours (Figure 3.8, upper panel). For 3-AP@Bz-MSN and 3-AP@BzPMSN, cell cycle profiles in *p185 ALL leukemia cells* are determined using flow cytometry after 24 hour treatment (Figure 3.8, lower panels). 3-AP-induced S-phase arrest occurs with 500 nM of drug. 3-AP loaded into pH-valve MSN with and without phosphate groups have similar effects on cell cycle profiles, with both showing significant S-phase arrest with the 16 ug/mL (ug MSN/mL) treatment. Although it is clear that there is not complete release of the loaded drug, with the highest nanoparticle treatment condition 40 ug/mL, there is substantial sub-G1 arrest (23-45%), highest in the phosphonate-modified particles. This may be indicative of DNA-damage resulting from substantial depletion of *de novo* nucleotide pools. In this way, the phosphonated MSN may be a promising candidate for 3-AP

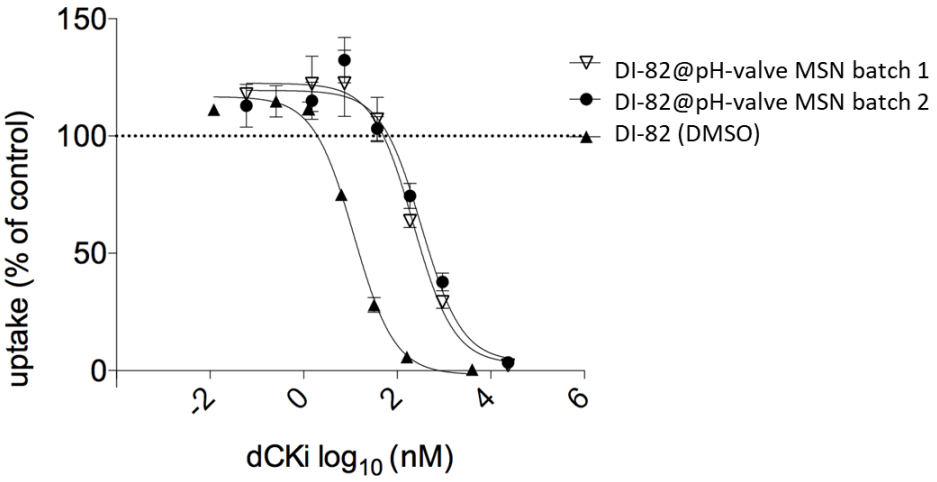

Figure 3.9 H^3dC uptake is a direct measure dCK inhibition after treatment of DI-82 nanoparticle and free drug (2 hours treatment)

formulation *in vivo*. They are slightly more potent than the non-phosphonated particles due to the higher loading capacity from electrostatic interactions between the negatively-charged phosphonated pores and positively-charged 3-AP molecules. Future *in vivo* pharmacokinetics experiments will give us a better understanding of the drug release profiles over time.

Similarly, DI-82 is loaded into pH-valve BzMSN (release capacity in water: 16%) and tritiated deoxycytidine (^{3}HdC) uptake is measured in *p185 ALL* cells with a beta-counter after 2-hour treatment. DI-82 is an inhibitor of dCK, which catalyzes one of the initial steps in the DNA salvage pathway—the phosphorylation of dC. Figure 3.9 shows that DI-82-loaded Bz-MSN inhibit dCK, but are not as potent as the free drug after 2 hours treatment. Complete release of the drug from the nanoparticle may take as long as 24 hours, so a longer incubation time with DI-82@Bz-MSN may be useful to try.

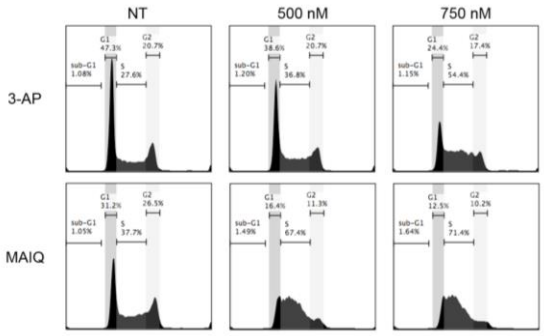

Figure 3.10 Cell cycle profiles of 3-AP and MAIQ after 24 hours treatment in *MIA PaCa cells*.

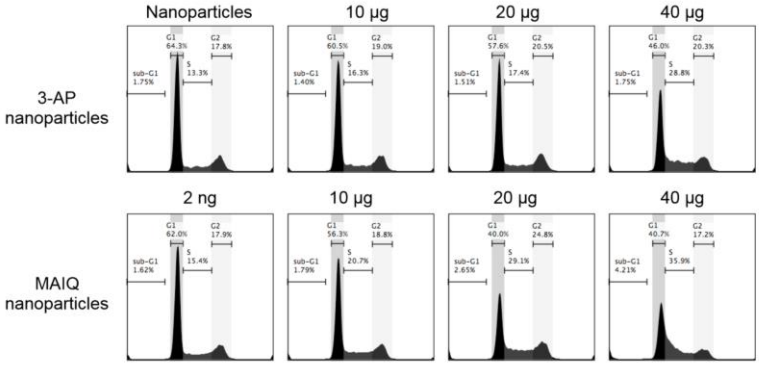

Figure 3.11 Cell cycle profiles of 3-AP@MSN and MAIQ@MSN after 48 hours treatment in *MIA PaCa cells*. Concentration values of ug/mL are weight of MSN per mL.

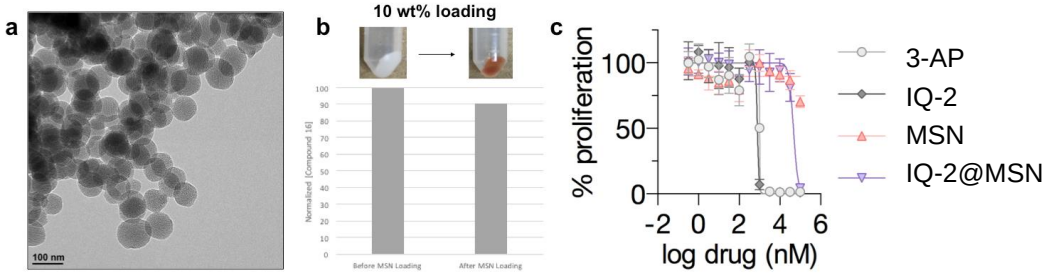

Figure 3.12 (a) TEM image of PEG-modified MSN for IQ-2 loading. (b) Loading capacity of nanoparticle in DMSO are determined using UV-Vis absorbance of drug at 340 nm. (c) CTG viability assay of bare PEG-modified MSN (MSN), drug-loaded MSN (IQ-2@MSN), and free drug (IQ-2, 3-AP).

In addition to loading 3-AP, we loaded MAIQ and IQ-2, the less polar isoquinoline analogs of 3-AP into uncapped MSN. With the MSN formulation of MAIQ, more potent S-phase arrest of *MIA PaCa-2 cells* are observed *in vitro* compared to 3-AP@MSN. MAIQ in bare MSN have a much better cell-killing profile than 3-AP in bare MSN, most likely due to the higher release capacity of the more lipophilic drug (Figure 3.11). Loading capacity of the other isoquinoline-modified analog, IQ-2, in PEG-modified MSN was determined by UV-Vis. CellTiter-Glo assay was used to measure cell proliferation, and the IC_{50} of the free drug in DMSO vs. the drug in the MSN carrier (Figure 3.12). Although IQ-2@PEG-MSN outperformed 3-AP@MSN, IQ-2 was less potent than the free drug *in vitro* and pharmacokinetics experiments would be useful in determining their applicability *in vivo*.

Lastly, in order to design an oral formulation for the clinical candidates 3-AP, DI-82, and VE-822, we screened a variety of excipients to find ones that solubilized these three drugs. A variety of 30 different lipids, surfactants, co-surfactants, and solvents were initially tested with these three drugs. Single candidates from each class of the initial screen were then combined to form SMEDDS emulsions 10 nm or smaller in size. These microemulsions are used in the research and development stages of drug formulation with success in increasing bioavailability of lipophilic drugs. They form spontaneously with little mixing and handling and are thus highly thermodynamically stable.[27–29] The resulting formulation was evaluated for toxicity and showed promising results *in vivo*.[15] IQ-2 was also screened for solubility in these excipients. However, its solubility was less than 2 mg/mL in the emulsion formulations. Concentrations as high as 5 mg/mL were achieved for IQ-2 in Captisol formulations. Data from these screens can be found in Figure S3.13-Figure S3.16.

3.4 Conclusions

3-AP and DI-82 were successfully loaded into pH-responsive MSN. Due to their limited water solubility, the release capacity is difficult to determine. However, *in vitro* cell cycle analysis and cell proliferation assays show the drugs remain functional after loading into the nanoparticle carriers. Further *in vivo* work must be done to access the effect on their pharmacokinetics profile. In addition,

SMEDDS emulsion formulations and Captisol formulations successfully solubilized 3-AP, DI-82, VE-822, and IQ-2 for further *in vivo* studies.

3.5 Supplemental information

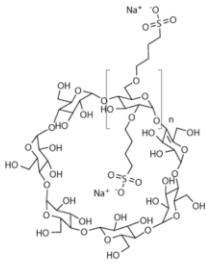

Captisol

Formulation	Solubility (heat and sonication, 2 days)
mol Captisol: mol drug = 1:1, 10% DMSO	< 2 mg/mL
mol Captisol: mol drug = 1:1, no DMSO	< 2 mg/mL
Solid phase to solution complexation method, gradual wetting 10% DMSO	< 2 mg/mL
Acetate buffer, solution pH=5.6 (concentration of neutral IQ-2 microspecies higher), no DMSO	< 2 mg/mL
HEPES buffer, solution pH=3.8 (concentration of positively charged IQ-2 microspecies higher), no DMSO	< 2 mg/mL
40% Captisol, 10% DMSO	5 mg/mL (as high as 10 mg/mL after heating to 50°C, crashes slowly after cooled)

Figure S3.13 Solubility of IQ-2 in various Captisol formulations.

Solubility of DI-82 in Individual Excipients

Excipient Class		Excipient	80 mg/mL	40 mg/mL	20 mg/mL	10 mg/mL	Overnight @ RT
Lipids	1	Labrafac Lipo WL 1349	insol	insol	insol	insol	
	2	Labrafac PG	insol	insol	insol	insol	
	3	Peceol	insol	insol	insol	insol	
	4	Maisine 35-1	insol	insol	insol	insol	
	5	Capmul MCM	insol	insol	insol	insol	
	6	Coconut oil	insol	insol	insol	insol	
	7	Sesame seed oil					
	8	Safflower seed oil	insol	insol	insol	insol	
Surfactants	1	**Labrasol**	**insol**	**insol**	**insol**	**H&S 20 min**	**clear**
	2	Gelucire 44/14	insol	insol	insol	insol	
	3	Labrafil M 2130 CS	insol	insol	insol	insol	
	4	Labrafil M 1944 CS	insol	insol	insol	insol	
	5	Labrafil M 2125 CS	insol	insol	insol	insol	
	6	Gelucire 50/13	insol	insol	insol	insol	
	7	Cremophor EL	insol	insol	insol	insol	
	8	Cremophor RH-40	insol	insol	insol	insol	
	9	**Tween-20**	**insol**	**insol**	**insol**	**H&S 25min**	**clear**
	10	Tween-80	insol	insol	insol	insol	
Cosurfactants	1	Capryol 90	insol	insol	insol	insol	
	2	Capryol PGMC	insol	insol	insol	insol	
	3	Lauroglycol 90	insol	insol	insol	insol	
	4	Lauroglycol FCC	insol	insol	insol	insol	
	5	Plurol Oleique CC 497	insol	insol	insol	insol	
	6	VitE-TPGS					
Solvents	1	Ethanol	insol	insol	insol	insol	
	2	Propylene Glycol					
	3	**PEG-200**	**insol**	**clear**	**/**	**/**	**clear**
	4	**PEG-300**	**insol**	**H&S 10 min**	**/**	**/**	**clear**
	5	**PEG-400**	**insol**	**H&S 20 min**	**/**	**/**	**clear**
Misc.	1	Phosal 50 PG					
	2	Phosal 53 MCT					
	3	**Transcutol**	**insol**	**insol**	**H&S 15 min**	**/**	**clear**
	4	**Solutol HS-15**	**insol**	**insol**	**insol**	**insol**	

Figure S3.14 Solubility of DI-82 in individual excipients.

Solubility of 3-AP in Individual Excipients							
Excipient Class		Excipient	80 mg/mL	40 mg/mL	20 mg/mL	10 mg/mL	Overnight @ RT
Lipids	1	Labrafac Lipo WL 1349	insol	insol	insol	insol	
	2	Labrafac PG	insol	insol	insol	insol	
	3	Peceol	insol	insol	insol	insol	
	4	Maisine 35-1	insol	insol	insol	insol	
	5	Capmul MCM	insol	insol	insol	insol	
	6	Coconut oil	insol	insol	insol	insol	
	7	Sesame seed oil	insol	insol	insol	insol	
	8	Safflower seed oil					
Surfactants	1	Labrasol	insol	insol	insol	insol	
	2	Gelucire 44/14	insol	insol	insol	insol	
	3	Labrafil M 2130 CS	insol	insol	insol	insol	
	4	Labrafil M 1944 CS	insol	insol	insol	insol	
	5	Labrafil M 2125 CS	insol	insol	insol	insol	
	6	Gelucire 50/13	insol	insol	insol	insol	
	7	Cremophor EL	insol	insol	insol	insol	
	8	Cremophor RH-40	insol	insol	insol	insol	
	9	Tween-20	insol	insol	insol	H&S 10 min	Clear
	10	Tween-80	insol	insol	insol	insol	
Cosurfactants	1	Capryol 90	insol	insol	insol	insol	
	2	Capryol PGMC	insol	insol	insol	insol	
	3	Lauroglycol 90	insol	insol	insol	insol	
	4	Lauroglycol FCC	insol	insol	insol	insol	
	5	Plurol Oleique CC 497	insol	insol	insol	insol	
	6	VitE-TPGS	insol	insol	insol	insol	
Solvents	1	Ethanol	insol	insol	insol	insol	
	2	Propylene Glycol					
	3	PEG-200	insol	insol	H&S 10 min	insol	Clear
	4	PEG-300	insol	insol	insol	H&S 10 min	Clear
	5	PEG-400	insol	insol	insol	H&S 30 min	Clear
Misc.	1	Phosal 50 PG					
	2	Phosal 53 MCT					
	3	Transcutol	insol	insol	insol	H&S-30 min	Almost clear
	4	Solutol HS-15	insol	insol	insol	insol	

Figure S3.15 Solubility of 3-AP in individual excipients.

Solubility of VE-822 in Individual Excipients

Excipient Class		Excipient	80 mg/mL	40 mg/mL	20 mg/mL	10 mg/mL	Overnight @ RT
Lipids	1	Labrafac Lipo WL 1349	insol	insol	insol	insol	
	2	Labrafac PG	insol	insol	insol	insol	
	3	Peceol	insol	insol	insol	insol	
	4	Maisine 35-1	insol	insol	insol	insol	
	5	Capmul MCM	insol	insol	insol	insol	
	6	Coconut oil	insol	insol	insol	insol	
	7	Sesame seed oil	insol	insol	insol	insol	
	8	Safflower seed oil					
Surfactants	1	Labrasol	insol	insol	insol	H&S - 20min	
	2	Gelucire 44/14	insol	insol	insol	insol	
	3	Labrafil M 2130 CS	insol	insol	insol	insol	
	4	Labrafil M 1944 CS	insol	insol	insol	insol	
	5	Labrafil M 2125 CS	insol	insol	insol	insol	
	6	Gelucire 50/13	insol	insol	insol	insol	
	7	Cremophor EL	insol	insol	insol	insol	
	8	Cremophor RH-40	insol	insol	insol	insol	
	9	Tween-20	insol	insol	insol	insol	
	10	Tween-80	insol	insol	insol	insol	
Cosurfactants	1	Capryol 90	insol	insol	insol	insol	
	2	Capryol PGMC	insol	insol	insol	insol	
	3	Lauroglycol 90	insol	insol	insol	insol	
	4	Lauroglycol FCC	insol	insol	insol	insol	
	5	Plurol Oleique CC 497	insol	insol	insol	insol	
	6	VitE-TPGS					
Solvents	1	Ethanol	insol	insol	insol	insol	
	2	Propylene Glycol	insol	insol	insol	insol	
	3	PEG-200	insol	insol	insol	H&S - 20min	
	4	PEG-300	insol	insol	insol	H&S - 30min	
	5	PEG-400	insol	insol	insol	H&S - 30min	
Misc.	1	Phosal 50 PG					
	2	Phosal 53 MCT					
	3	Transcutol	insol	insol	insol	H&S - 20min	
	4	Solutol HS-15	insol	insol	insol	insol	

Figure S3.16 Solubility of VE-822 in individual excipients.

3.6 Materials and Methods

Materials

Tetraethylorthosilicate 98% (Sigma Aldrich). Hydroxy(polyethyleneoxy)-propyl triethyoxysilane (PEG-silane), 8-12 EO, 50% in ethanol (Sigma Aldrich). Diethylphosphatoethyltriethoxysilane (P-silane) 95% (Gelest). Sodium hydroxide (Thermo Fisher). Hexadecyltrimethylammonium bromide (CTAB) ≥98% (Sigma Aldrich).

Nanoparticle synthesis

pH valve nanoparticles are synthesized according to published procedures in Meng. et. al.[30] For pore-modified nanoparticles, 200mg CTAB and 1.2mL of 1M NaOH is added to 100mL of Millipore water and heated to 80°C. For regular MSN, 1.2mL TEOS is added dropwise. For P-modified MSN or PEG-modified MSN, 5% of TEOS is substituted with P-silane or PEG-silane. While stirring, the silane mixture is added dropwise. After silane precursors are added, the solution is stirred well for 2 hours at 80°C. Solution is cooled and nanoparticles are centrifuged and supernatant is discarded. MSN are washed twice with water and twice with ethanol. Subsequent attachment of benzimidazole on the particle surface, surfactant extraction, and beta-cyclodextrin capping is carried out per published procedures with slight modifications as described here.[30] Before capping, 3-AP-loaded nanoparticles are placed overnight in a vacuum oven to remove all excess THF or for 3 days to remove residual DMSO.

Drug loading and release

For a typical loading study, 5 mg MSN are washed with the loading solvent of choice (THF or DMSO for 3-AP) three times and suspended in a solution of drug in the same loading solvent. After 24 hours loading on a rotator, the drug solution before and after nanoparticle addition is quantified using UV-Vis or fluorescence to determine loading capacity (mg drug/mg MSN x 100%) and efficiency (% drug loaded into nanoparticles vs. total drug added). Since drugs are insoluble in water, the release capacity (mg drug released/mg MSN x 100%) and efficiency (% drug released from nanoparticles) are more accurately calculated from the *in vitro* data compared to free drug.

Fluorescence/UV-Vis Spectroscopy

Fluorescence measurements are taken with an Acton Spectra Pro 2300i CCD and excited by a CUBE 376 nm (Coherent Inc., Santa Clara, CA, USA) laser. All UV-Vis measurements are done on a Varian Cary 5000 UV-Vis-NIR Spectrophotometer.

TEM

After CTAB extraction, clean nanoparticles suspended in ethanol are dropped on a carbon-coated copper grid for TEM imaging (T12 cryo-electron microscope, FEI Tecnai).

TGA

Thermogravimetric analysis was performed on a Perkin Elmer Diamond Thermogravimetric/Differential Thermal Analyzer. Samples were loaded in platinum pans, and TG curves were recorded from 0 to 550 °C at a scan rate of 10 °C/min.

Nitrogen sorption measurements

Samples were outgassed at 220°C for 12 hours, and then nitrogen adsorption and desorption isotherms were taken at 77 K using an Autosorb-iQ (Quantachrome Instruments). An NLDFT equilibrium model of N_2 on silica was used to calculate pore size distribution and pore volume. Brunauer–Emmett–Teller model was used to calculate surface areas between partial pressures of 0.08-0.2 p/p0.

SMEDDS formulation

Procedure for SMEDDS formulation was provided by Peter Rix. The solubility screening for all drugs are as described, with procedure for DI-82 as an example. Add 10 mg DI-82 (neutral form) to clear conical polypropylene centrifuge tubes. If a salt form of DI-82 is used, increase mass as appropriate to give 10 mg neutral form/tube. Add ~120 µL of each excipient (80 mg/mL) and disperse with a micro weighing spatula, dulled hypodermic needle or even a toothpick. Be sure the volume of excipients is transferred to the bottom of the tubes (not up the sides). Tubes may be briefly centrifuged to bring all components together in the bottom. Vortex for up to 1 minute and note if clear solution achieved - if so record "clear" in first column. Otherwise use gentle warming (45 - 50°C) in a sonication bath, with

occasional vortexing as needed. If heat and sonication ("H&S") required, note approximate time to clear solution (e.g. "10 min w/ H&S"). If no clear solution is achieved within 30 min w/ H&S, write "Insol" and add additional excipient to the same tube as needed to generate the next dilution level (next column). Repeat the same steps for the next dilution level. Once a clear solution is obtained for a given excipient, no further experiments are required for that row (i.e. excipient). Once a solution is obtained, leave overnight at RT and check next day for drug precipitation (may need to warm first for semi-solids).

4 Intracellular iron delivery by an MSN carrier potentiates Fenton reactions *in vitro*

Synthesis and characterization of IDA-MSN was done by Chia-jung Yu and is published in the following:

Tarn et. al. In vitro delivery of calcium ions by nanogated mesoporous silica nanoparticles to induce cancer cellular apoptosis, Mol. Syst. Des. Eng., *2*, 384-392 (2017).

Tarn et. al. pH-Responsive Dual Cargo Delivery from Mesoporous Silica Nanoparticles with a Metal-Latched Nanogate, Inorg. Chem., *52* (4), 2044–2049 (2013).

4.1 Abstract

Cytotoxicity of unregulated metals in cells have been studied extensively with ion transport inhibitors and ionophore drugs, which shuttle ions like calcium, iron, and copper into the cell. Here, iminodiacetic acid-modified mesoporous silica nanoparticles (IDA-MSN) are used to bind iron ions and deliver them directly into the cell via endocytosis pathway. We find that increasing the amount of free iron in the cell using the nanoparticle iron carrier causes the generation of radical species through iron-catalyzed Fenton reactions. This subsequently causes generation of reactive oxygen species, resulting in potent cell killing. Results from these experiments have implications in the development of treatments for infections by iron-sensitive bacteria or for combination treatments, which rely on ROS induction to potentiate the effects of cancer therapeutics.

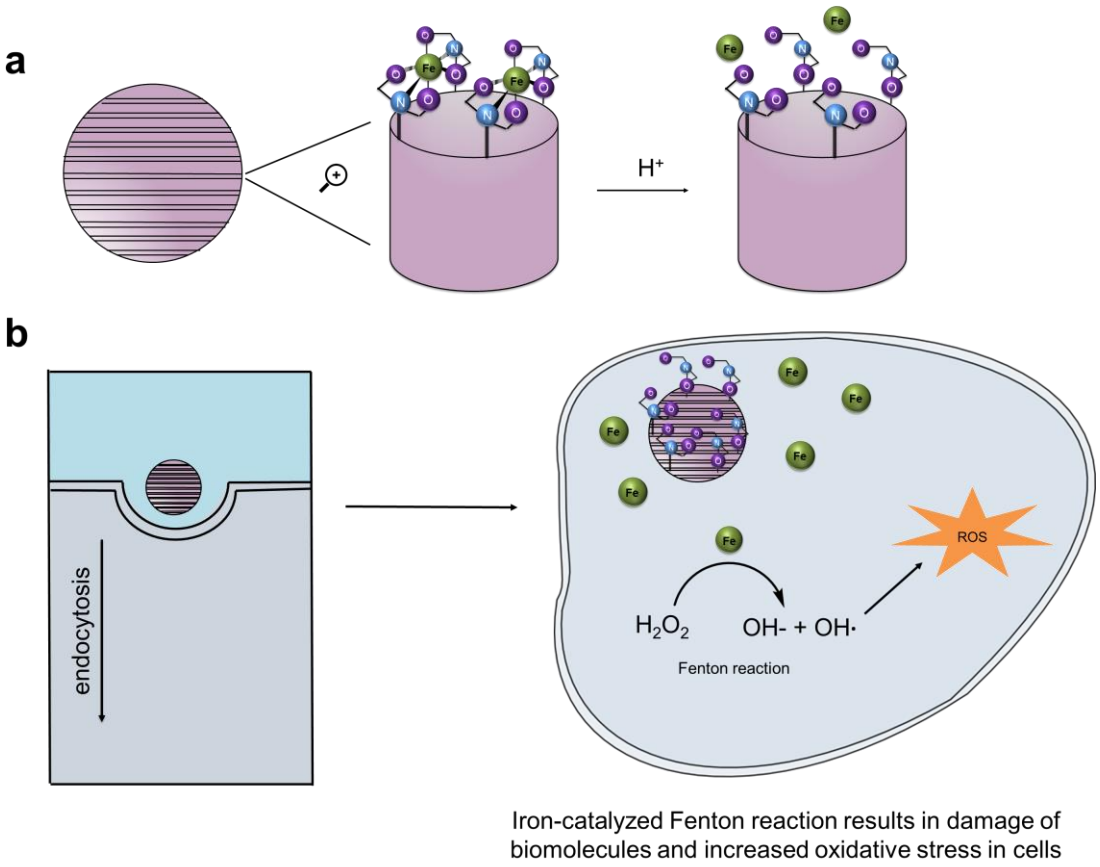

Figure 4.1 (a) IDA-modified MSN are used to chelate metal ions such as iron and release them upon protonation (b) MSN are endocytosed by cells and iron is released upon protonation of IDA groups in the lysosome. Free iron catalyzes Fenton reactions in the cell, resulting in ROS production and, ultimately, cell death.

4.2 Introduction

All cells require iron to maintain normal function. In most cells, circulating iron binds to the transferrin protein and enters the cells via receptor-mediated endocytosis after binding to the transferrin receptor on the surface of the cell. Iron is released from transferrin in acidic pH due to conformational changes in the protein.[31] In this way, the amount of labile iron in the cell is regulated. Regulation of iron in the cell is essential due to Fenton chemistry that results from excess iron in the cell. This reaction between hydrogen peroxide and ferrous salts can produce reactive species capable of oxidizing a wide variety of organic substrates. The iron-

catalyzed ROS produced by the Fenton reaction can cause cell death though a variety of downstream pathways, including iron accumulation, direct targets of ROS production, and mitochondrial ROS production.[32]

Small molecules called ionophores have been used to induce iron shuttling into the cell to provoke an iron imbalance, causing cells to undergo apoptosis and cell death.[33] Recently, a class of heterocyclic thiosemicarbazones were found to act as a copper ionophores, partaking in similar Fenton chemistry, and making cancer cells more sensitized by the induction of ROS.[33,34] While, metal ionophores are an emerging class of anticancer drugs, these small molecules are unspecific to cell type and lack targeting properties for directed treatment.

We design a nanoparticle carrier that can address these problems. We use IDA-chelator-functionalized mesoporous silica nanoparticles to carry iron into the cell and inhibit cell proliferation through the induction of ROS. Previously, confocal microscopy of fluorescently-labeled MSN show that after cell treatment, MSN can be seen inside cells as early as two hours after administration.[35] The route of entry of these particles is known to be endocytosis, and many studies have shown localization of nanoparticles in endosomes and lysosomes.[7,35] We take advantage of this unique point of entry to deliver excess Fe^{2+} directly into the cell using an MSN carrier, which can be easily functionalized with targeting agents of interest. We measure cell proliferation as a function of ATP content after treatment with free Fe, bare IDA-MSN, and Fe@IDA-MSN, and find that after 72 hours there is only cell killing with Fe@IDA-MSN, while bare IDA-MSNs without iron show no toxicity within the tested dose range. We find that cell killing resulting from the controlled delivery and release of iron into the cell is ROS-mediated and is followed by a necrosis phenotype, with their cell cycle profiles exhibiting sub-G1 arrest, indicative of DNA damage.

4.3 Results and Discussion

IDA-MSN have been shown to be biocompatible.[35] However, we test IDA-MSN without iron in cells to determine the maximum tolerated dose and ensure no off-target toxicity associated with these particles *in vitro* (Figure 4.2a). *HEK-293 human embryonic kidney* cells are used as a model cell line for these studies.

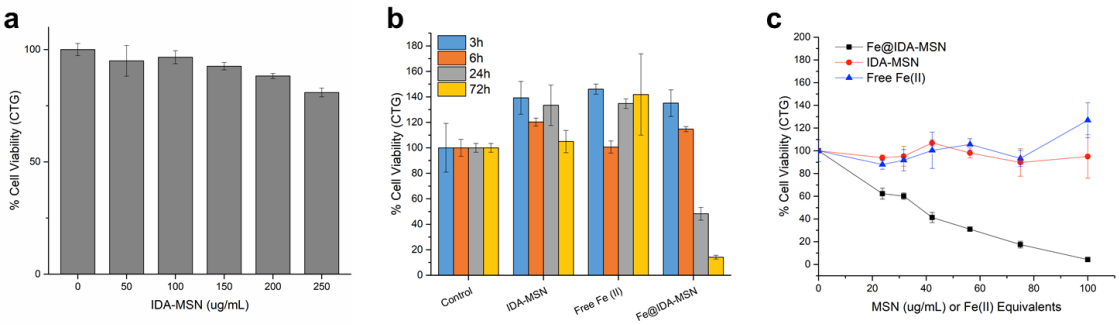

Figure 4.2 (a) Toxicity of bare IDA-MSN determined after 24-hour treatment. (b) Inhibition of cell proliferation over time is measured by ATP content after 3-, 6-, 24-, and 72-hour treatment with Fe@IDA-MSN. (c) 72-hour treatment of Fe@IDA-MSN and controls. In every case, the amount of Fe in Fe@IDA-MSN is equivalent to the free iron control.

Inhibition of cell proliferation is measured with the iron-loaded IDA-MSN (Fe@IDA-MSN) treatment and shows that there is no cell death within the first 6 hours of treatment. However, after 24 hours we see cell viability drop down to 50%, after 48 hours to 30%, and after 72 hours to 10% with the 100ug/mL Fe@IDA-MSN treatment (Figure 4.2). This is suggestive of ROS-induced cell death,[36] which at the initial 6 hours of induction does not show inhibition of cell proliferation, but after 24 hours a more obvious phenotype is seen.[37] Results from the Cell Titer-Glo viability assay over a larger concentration range of Fe@IDA-MSN suggest that Fe-mediated cell death has a threshold effect (Figure 4.2c). After 72 hours, viability drops to 60% with the lowest dose of Fe@IDA-MSN treatment (20 mg/mL), equivalent to only 7.2 µM Fe(II), showing that not much iron is needed for cell death.

Excess iron accumulation in mammalian cells can take part in Fenton chemistry, triggering cell death via ROS production. To test whether iron-induced cell death with these nanoparticles are ROS-mediated, we measure ROS using DCFH-DA assay (Figure 4.3). Relative to the control, we find that free Fe(II) causes some ROS at the 72 hour timepoint. However, Fe@IDA-MSN treatment causes ten times more ROS than free iron(II), suggesting that by delivering iron directly

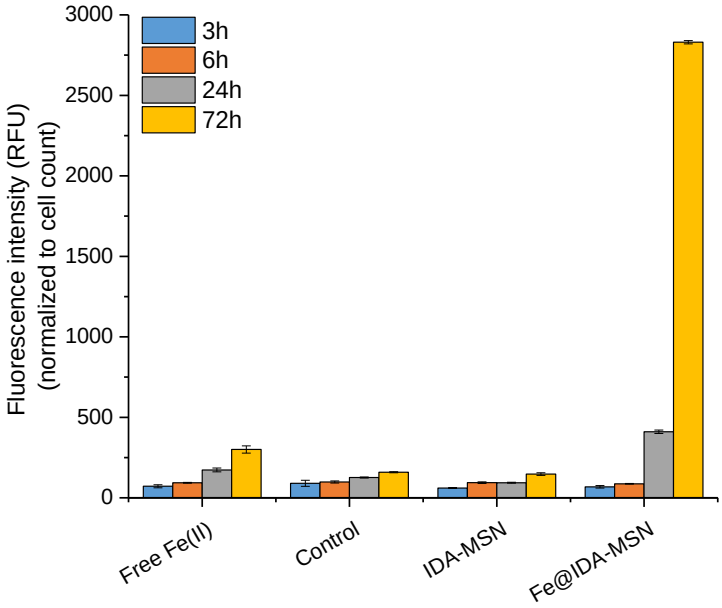

Figure 4.3 ROS is measured by DCFH-DA assay after 72-hour treatment and is normalized to the number of live cells. Cell line: *HEK-293*

into the cell with the nanoparticle carrier, bypasses the transferrin receptor and causes an imbalance of iron in the cell. High ROS production with the Fe@IDA-MSN treatment show that ROS is a mediator in the cell death process.

ROS produced by Fenton may cause cell death by a variety of mechanisms—through mitochondrial ROS production with an apoptosis phenotype, via mitochondrial ROS with a necroptosis phenotype, or a non-apoptotic cell death primarily by production of lipid ROS.[32,38] To further understand how intracellular delivered iron with IDA-MSN cause cell death, we use flow cytometry to stain for apoptotic and necrotic cells (Figure 4.4). Fe@IDA-MSN shows much higher population of necrotic cells (24%) compared to free Fe (9%) and controls (9%). Fe@IDA-MSN treatment shows a disrupted cell cycle profile, with a population of cells arresting in sub-G1 (Figure S4.6), indicative of a mechanism typical for DNA damaging agents.[39–41]

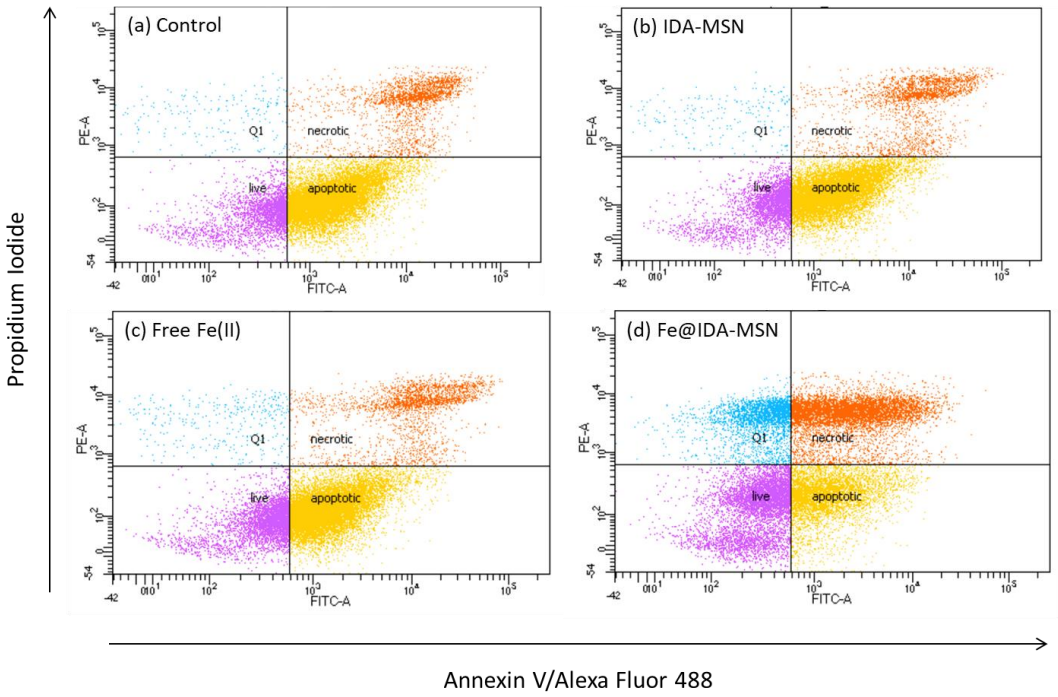

Figure 4.4 Cells treated with 250 ug/mL Fe@IDA-MSN, equivalents of free iron, or bare IDA-MSN for 24-hours are stained with propidium iodide dead cell nuclear stain and Annexin V-Alexa Fluor 488 conjugate, a marker of apoptosis. Dual staining for dead cells and apoptotic cells allows us to quantify the percent cell population undergoing apoptosis or necrosis using flow cytometry. Cell line: *HEK-293*

4.4 Conclusions

Intracellular iron delivery via Fe@IDA-MSN cause significant cell death after 72 hours, while free iron is non-toxic to cells. Bare IDA-MSN at the concentrations administered have no apparent toxicity. FACS measurements confirm cell death by intracellular iron delivery, which have a much higher population of necrotic cells. Intracellular ROS production measured by DCFH-DA conversion shows that Fe@IDA-MSN cause ten times more ROS per cell than free iron treatment. As metal ionophore drugs are becoming increasingly clinically-relevant, ROS-mediated cell death by Fe@IDA-MSN may have implications as a therapeutic to treat iron-

sensitive bacteria such as mycobacterium tuberculosis or as a sensitizer for cancer therapies.

4.5 Materials and Methods

IDA-MSN synthesis and characterization

MSN were prepared as previously described.[35,42]

Cell culture and culture conditions

HEK-293 human embryonic kidney cell line is purchased from ATCC and cultured in standard incubation conditions using Corning Dulbecco's Modified Eagle Medium supplemented with 10% Fetal Bovine Serum and 1% penicillin-streptomycin at a humidified 37°C with 5% CO_2. Subcultures were established by trypsinization (0.25% w/v Trypsin) and centrifugation with subsequent resuspension at 2 to 3 x 10^5 viable cells/mL. Cell density is maintained between 2 to 3 X 10^5 and 1 to 2 X 10^6 viable cells/mL.

Proliferation assays

HEK-293 cells are seeded at a density of 1500 cells/well in a 96-well plate and incubated in fresh culture medium at 37°C in a 5% CO_2 atmosphere for 24 hours. After 24 hours, cells are changed into fresh media and treatments are administered. Treatments are Fe@IDA-MSN, IDA-MSN, and free Fe(II) in the form of the ammonium iron(II) sulfate hexahydrate salt. 72 hours after treatment, ATP content is measured using Promega CellTiter-Glo Luminescent Cell Viability Assay (CTG) according to manufacturer's instructions, and analyzed by Tecan Infinite M1000 Plate Reader. For all viability data, treatments are done in triplicates. Release capacity of Fe@IDA-MSN (0.60 µmol Fe/mg MSN) from ICP-OES is used to calculate the concentration of free Fe(II) to add in the free iron treatment control condition.

Apoptosis assay

Cell death is also examined by using a dual staining method for apoptosis and necrosis. Cells are seeded 24 hours prior to treatments are administered. After 24 hours, cells are changed into fresh media and treatments are administered. Apoptosis and cell death are assayed after 24 hours using Annexin V-Alexa Fluor 488 and PI dual stain according to manufacturer's instructions (Alexa Fluor 488

Annexin V/Dead Cell Apoptosis Kit, Thermo Fisher Scientific). Single stain, dual stain, and no stain samples are also prepared as the compensation controls for FACS analysis. All flow cytometry data are acquired on a five-laser LSRII cytometer (BD Biosciences) and analyzed using FlowJo software.

Detection of reactive oxygen species

ROS production in live cells are measured after incubation with the dichloro-dihydro-fluorescein diacetate (DCFH-DA) probe that reacts with ROS in the cell and produces the highly fluorescent 2',7'-dichlorofluorescein (DCF) dye that is proportional to ROS species present. After incubation with the ROS probe, free Fe(II), bare IDA-MSN, and Fe@IDA-MSN are added to cells and ROS is measured over time by fluorescence of the DCF dye. Concurrently, cell viability is measured using Cell Titer-Glo at corresponding timepoints in order to normalize ROS production by the number of live cells. Detection of ROS is assayed according to manufacturer's instructions (OxiSelect Intracellular ROS Assay Kit, Cell BioLabs Inc.). *HEK-293* cells are stained with DCFH-DA reagent one hour prior to treatment. Cells are washed and resuspended in fresh media containing treatments. Fluorescence is measured for 10,000 cells in each treatment group in a 96-well plate 3 to 72 hours after treatment. Fluorescence is measured using a Tecan Infinite M1000 Plate Reader at an excitation wavelength of 480 nm and emission at 530 nm. Resulting fluorescence is proportional to ROS produced. Fe@IDA-MSN cause cell death after 24 hours, so final RFU data is normalized to the cell count corresponding to each treatment condition and timepoint.

4.6 Supplemental Information

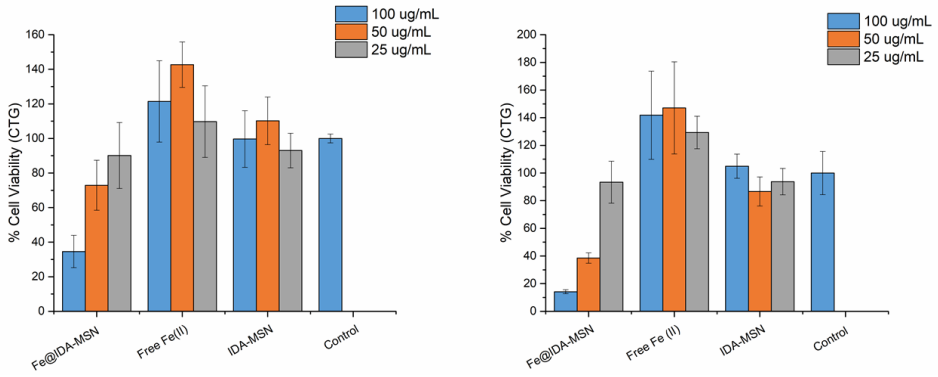

Figure S4.5 Inhibition of cell proliferation by three concentrations of Fe@IDA-MSN in *HEK-293* cells after (a) 48-hour treatment and (b) 72-hour treatment.

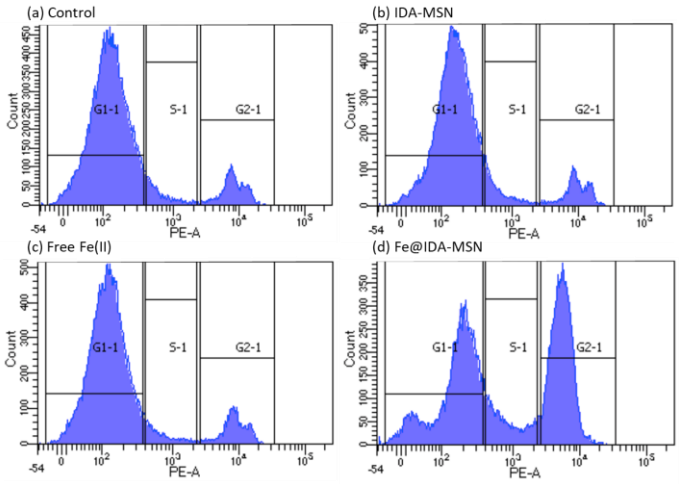

Figure S4.6 Cell cycle profiles of *HEK-293* cells after 24h treatment with Fe@IDA-MSN and controls.

5 Synthesis, modification, and biocompatibility of mesoporous silica nanoparticles

This brief work was based on a silica wormhole particle synthesis procedure provided by my colleague Philippe Saint-Cricq-Riviere.

5.1 Abstract

Physical properties and biological compatibility of MCM-41-type silica nanoparticles have been extensively studied.[2,4,5,26] Here we try a variety of synthesis to improve particle homogeneity and study how the addition NH_4Cl during the synthesis affects necking, pore structure, and biocompatibility of these nanoparticles.

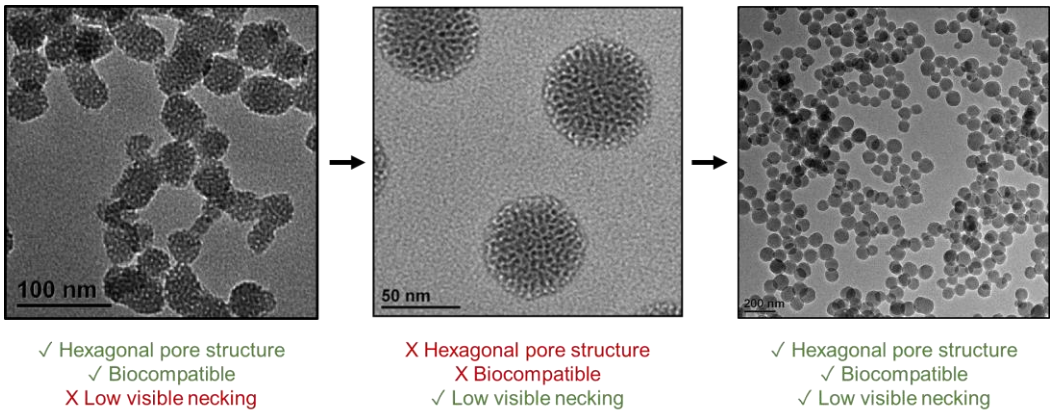

Figure 5.1 Structural properties and biocompatibility of three types of silica nanoparticles.

5.2 Results and Discussion

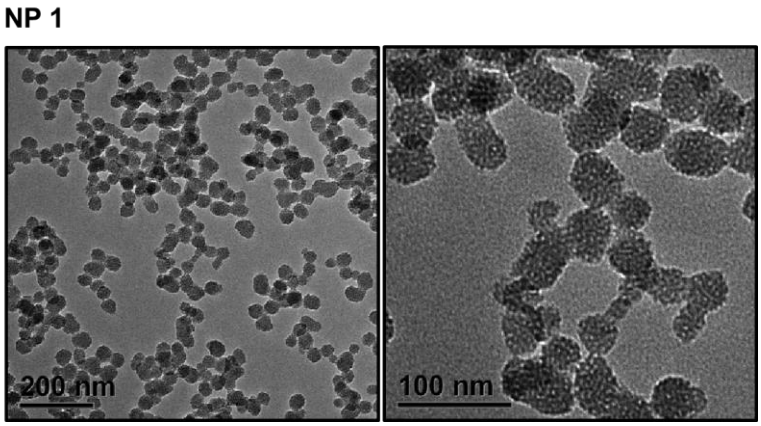

Figure 5.2 TEM images of MCM-41-type mesoporous silica nanoparticles modified with phosponates. Average diameter determined by DLS is 50 nm.

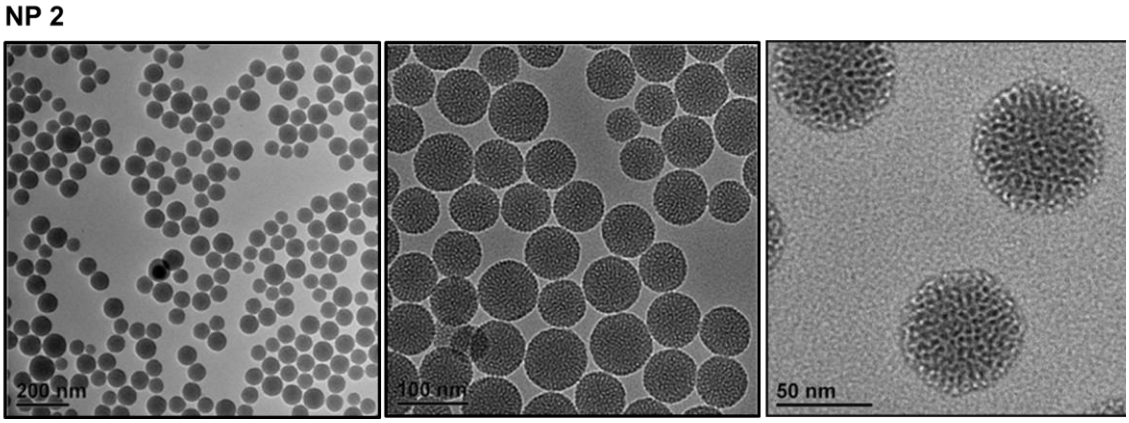

Figure 5.3 TEM images of wormhole pore silica nanoparticles. Average diameter determined by DLS is 50 nm. Addition of NH_4Cl in synthesis improves monodispersity and necking of particles but also changes self-assembly of CTAB or hydrolysis rates preventing formation of hexagonal mesopore structure.

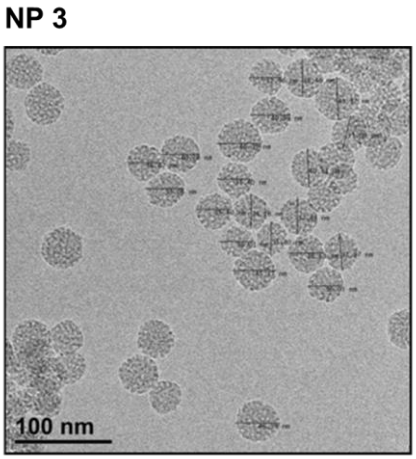

Figure 5.4 (a) TEM image of FITC-modified silica nanoparticles with wormhole pore structure

MCM-41 nanoparticles (NP-1) are synthesized as previously described.[8] A phosphonate silane is co-condensed 20 minutes after addition of the TEOS silane precursor to produce well-dispersed particles, with some necking between adjacent particles. With this synthesis, it is typical for smaller MCM-41 particles (<80 nm) to exhibit more necking. To reduce necking, addition of NH_4Cl acts as a buffer, and prevents drastic increases in pH, as in the case of MCM-41 synthesis. The resulting particles (NP-2) are highly symmetrical and monodisperse. They have little visible necking and are 50 nm in size. However, pore structure is no longer hexagonal and appears random and "wormhole"-like by TEM. NP-2 were synthesized by cocondensation of PEG to improve dispersity for in vitro experiments as well as APTES and coupled with FITC to make them fluorescent for confocal imaging in cells. When cell are treated with these wormhole-type nanoparticles (NP-2), they show loss of membrane integrity from CTAB which gets lodged in the matrix and is unable to be removed using typical extraction methods for MCM-41-type nanoparticles (Figure 5.5).

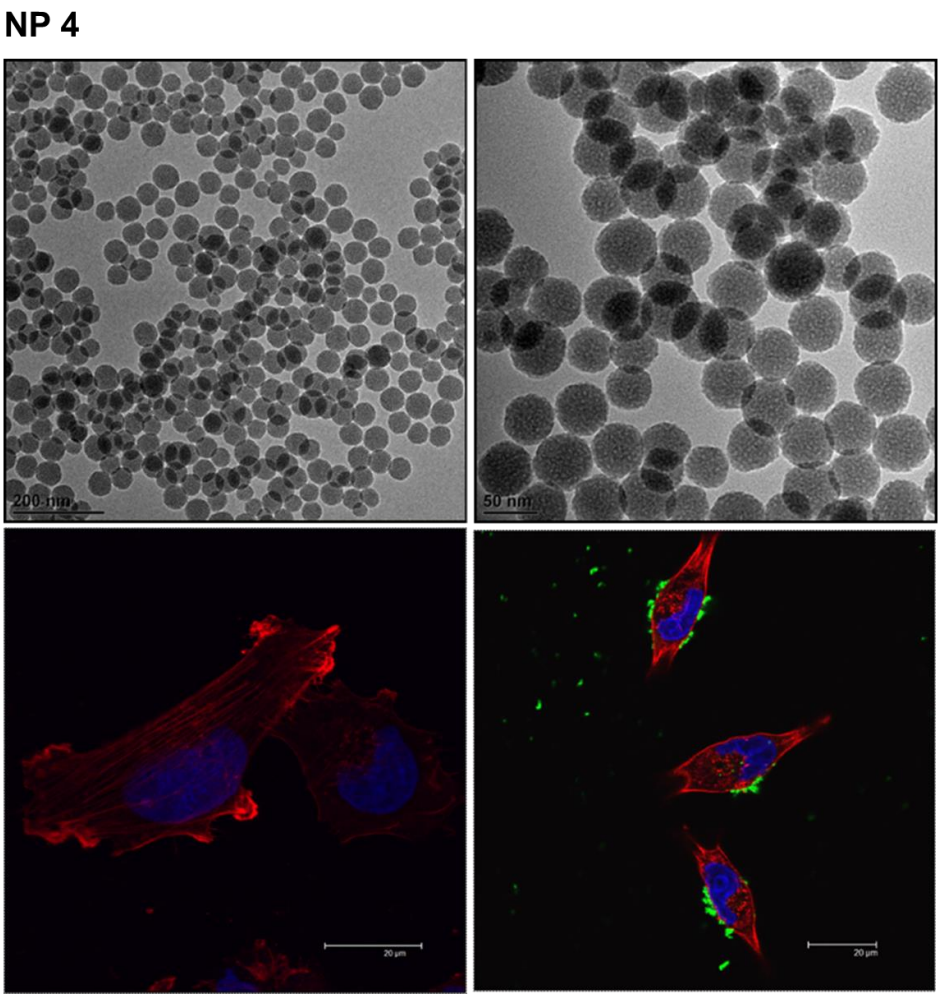

Figure 5.5 (a-b) TEM image of PEG-FITC-modified silica nanoparticles. PEG is added to lower macrophage uptake and clearance. Average diameter determined by DLS is 48 ± 4 nm. (c) *MIAPaCa-2 PDAC* cells are stained with actin and DAPI. (d) Cells treated with wormhole-type nanoparticles cause rupturing of the cell membrane. Nanoparticles are surface-modified with FITC for imaging (green).

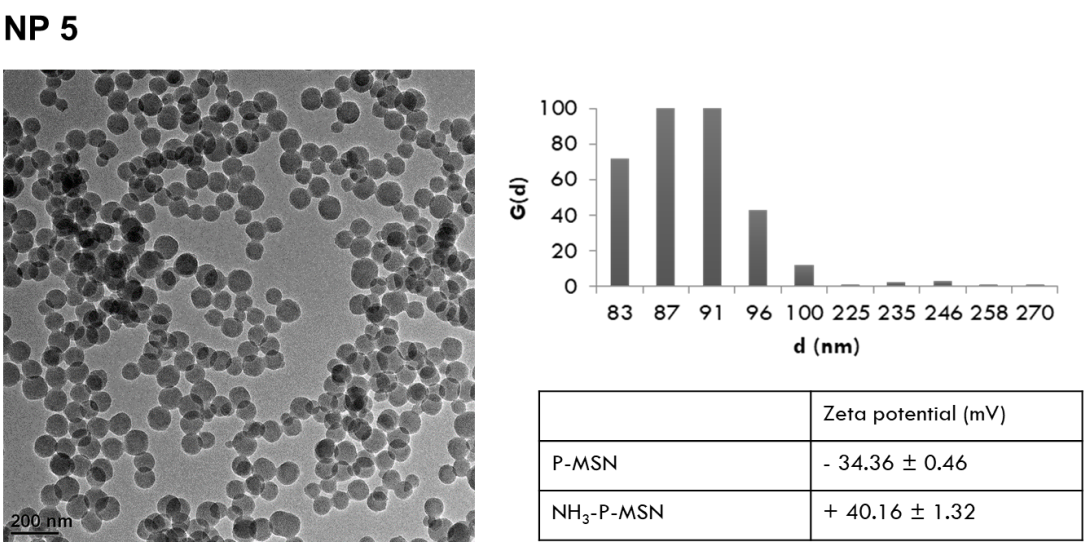

	Zeta potential (mV)
P-MSN	- 34.36 ± 0.46
NH_3-P-MSN	+ 40.16 ± 1.32

Figure 5.6 (a) TEM, DLS, and Zeta potential measurements for diethylphosphatoethyltriethoxysilane and APTES modified MCM-41 nanoparticles.

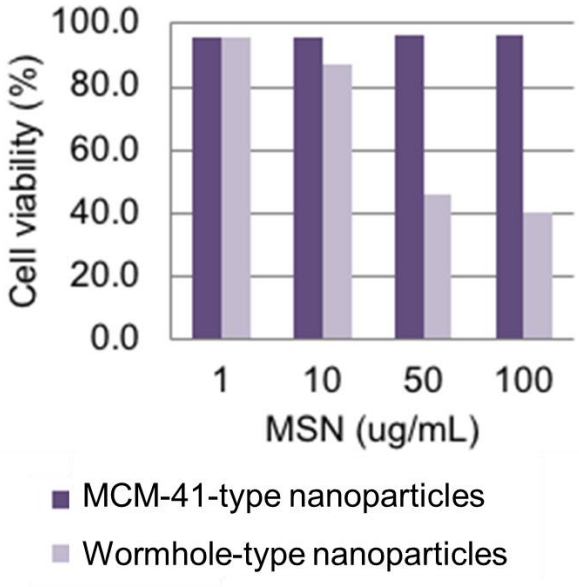

Figure 5.7 Trypan blue cell death assay in *p185* cells show that these wormhole-pore particles have a lower toxicity range (<10 ug/mL) than MCM-41-type silica nanoparticles (>100 ug/mL).

Synthesis of diethylphosphatoethyltriethoxysilane and APTES modified MCM-41 nanoparticles (NP-5) were synthesized to compare toxicity profiles to NP-2. The ethoxysilane hydrolyses slower, similar to TEOS, and produced more monodisperse particles compared to the hydroxide 3-(Trihydroxysilyl)propyl methylphosphonate used to synthesize NP-1. NP-5 are larger (90 nm average diameter) by DLS (Figure 5.6). However, there is visibly reduced necking with NP-5 vs. NP-1. We compare these two types of particles with a Trypan Blue cell death assay. Toxicity of lodged CTAB in NP-2 is further evidenced by the cell proliferation assay where we compare the biocompatibility of MCM-41 type MSN (NP-1), which do not effect cell proliferation, to wormhole silica nanoparticles (NP-2), which kill 50% of cells after 24 hour treatment (Figure 5.7)

5.3 Conclusions

Here, we synthesize different types of silica nanoparticles and compare their toxicity *in vitro*. We improve dispersity of typical phosphonated MCM-41 MSN by replacing the fast hydrolyzing 3-(Trihydroxysilyl)propyl methylphosphonate silane with the slower hydrolyzing diethylphosphatoethyltriethoxysilane and a PEG silane during the co-condensation step. We find that addition of NH_4Cl in MSN synthesis results in improved monodispersity and less necking, but compromises the biocompatibility of silica nanoparticles due to residual CTAB lodged in the framework.

5.4 Materials and Methods

NP-1 (50 nm P-MSN) is synthesized according to published procedures with NaOH as the base.[8] For NP-2 (50 nm wormhole NP), 25mL of water, 0.1g CTAB, 50uL NaOH, and 112 µL of 100mg/mL NH_4Cl_2 solution is combined and heated to 85°C with stirring at 1400 rpm. 375 µL TEOS is added dropwise and the solution is stirred for 3 hours at 85°C. For NP-3 (FITC-wormhole NP), NP are prepared as described with NP-2, except that 1 mg fluorescein isothiocyanate (FITC), 2 µL (3-Aminopropyl)triethoxysilane, and 450 µL anhydrous ethanol is mixed for 2 hours and then combined with the TEOS precursor. For NP-4 (PEG-FITC-wormhole NP), NP are prepared as described with NP-3 except after 3 hours, 20 µL hydroxy(polyethyleneoxy)-propyl triethyoxysilane is added and stirred for an additional 2 hours. For NP-5 (P-NH_3-MSN), hydroxy(polyethyleneoxy)-propyl

triethyoxysilane and (3-Aminopropyl)triethoxysilane are combined with 1.2 mL TEOS, added dropwise to a mixture of 200mg CTAB, 1.2mL (1M) NaOH, and 100mL mH2O, and stirred for 2 hours at 80^{o}C. For all nanoparticles, surfactant is extracted by stirring nanoparticles in 20 mg/mL NH_4NO_3 in ethanol and refluxing for 1 hour. Particles are cooled and washed with ethanol three times. This extraction procedure is done twice.

6 Mesoporous silica nanoparticle drug carriers *in vivo*

This chapter describes treatment and imaging applications of mesoporous silica nanoparticles that have been successfully tested *in vivo*, as well as some future applications of these systems.

6.1 Nanoparticles Improve Moxifloxacin Pharmacokinetics

This section is based on the article "Daniel L. Clemens, Bai-Yu Lee, Sheba Plamthottam. Michael V. Tullius, Ruining Wang, Chia-Jung Yu, Zilu Li, Barbara Jane Dillon, Jeffrey I. Zink, and Marcus A. Horwitz, Nanoparticle Formulation of Moxifloxacin and Intramuscular Route of Delivery Improve Antibiotic Pharmacokinetics and Treatment of Pneumonic Tularemia in a Mouse Model" submitted for review in 2018.

6.1.1 Abstract

Francisella tularensis causes a serious and often fatal infection, tularemia. We compared the efficacy of moxifloxacin delivered as free drug or by disulfide snap-top mesoporous silica nanoparticles (MSNs) in reducing bacterial burden in a mouse model of pneumonic tularemia and found that nanoparticle-delivered moxifloxacin was more effective than free drug and that the intramuscular and subcutaneous routes were markedly more effective than the intravenous route. Assay of tissue silica by inductively coupled plasma optical emission spectrometry showed that the enhanced efficacy of the MSNs and the intramuscular route of delivery was not due to better delivery of the MSNs to affected organs as intramuscular delivery led to much lower levels of silica in the lung, liver, and spleen than intravenous delivery. Moreover, in mice infected by respiratory challenge with GFP-expressing *F. tularensis* and then administered DyLight 650-labeled nanoparticles, the nanoparticles co-localized with GFP-expressing *F. tularensis* in mouse lung cells after intravenous, but not after intramuscular injection, on flow cytometry analysis. Assay of blood moxifloxacin levels over time in mice injected with free versus nanoparticle-delivered moxifloxacin demonstrated that the nanoparticle formulation provided a longer drug half-life and a longer time above the minimal inhibitory concentration, and that these advantages were greatest for the intramuscular route. We conclude that the superior efficacy of nanoparticle-delivered moxifloxacin over free drug and of the intramuscular route

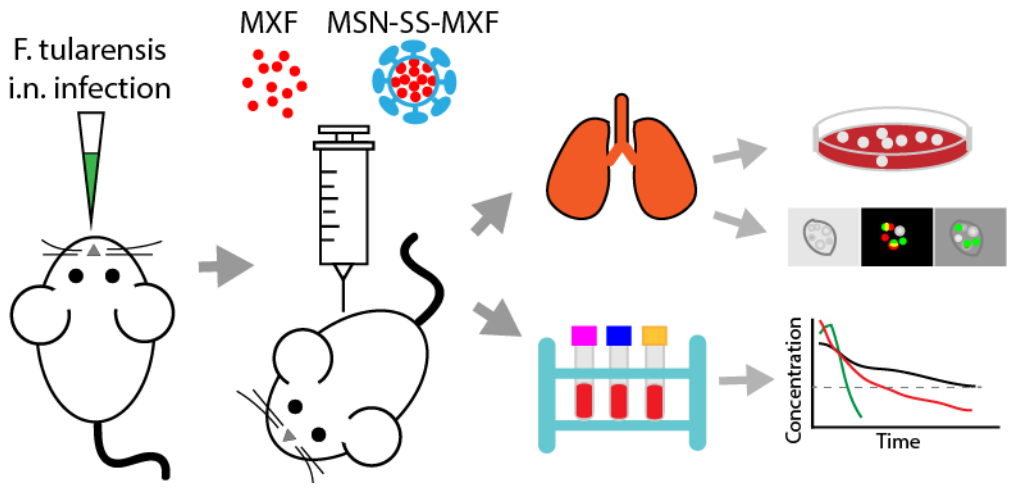

Figure 6.1 Summary of mice treatment and methods used to analyze pharmacokinetics of MXF treatment.

of nanoparticle delivery over the intravenous route is attributable to improved pharmacokinetics.

6.1.2 Introduction

Mesoporous silica nanoparticles (MSNs) are an attractive drug delivery platform for several reasons, including an extremely large internal surface area that allows high drug loading and a surface that is readily modified for targeting of specific cells and for controlled drug release in response to environmental cues.[23,43] For example, we have devised MSNs functionalized with disulfide snap-tops that release their drug cargo intracellularly in response to the intracellular redox potential.[9] We have previously shown that intravenous (i.v.) administration of moxifloxacin (MXF) via disulfide snap-top redox-operated mesoporous silica nanoparticles (MSN-SS-MXF) is much more effective for treatment of pneumonic tularemia in mice than an equivalent amount of free drug.[9] However, the basis for the enhanced efficacy is unclear. Nanoparticle (NP)-delivered antibiotics have been proposed to have numerous advantages over free drugs, including shielding the drug from excretion and metabolism, improved pharmacokinetics,[44] and specific targeting of macrophages in the lung and reticuloendothelial system, which are important host

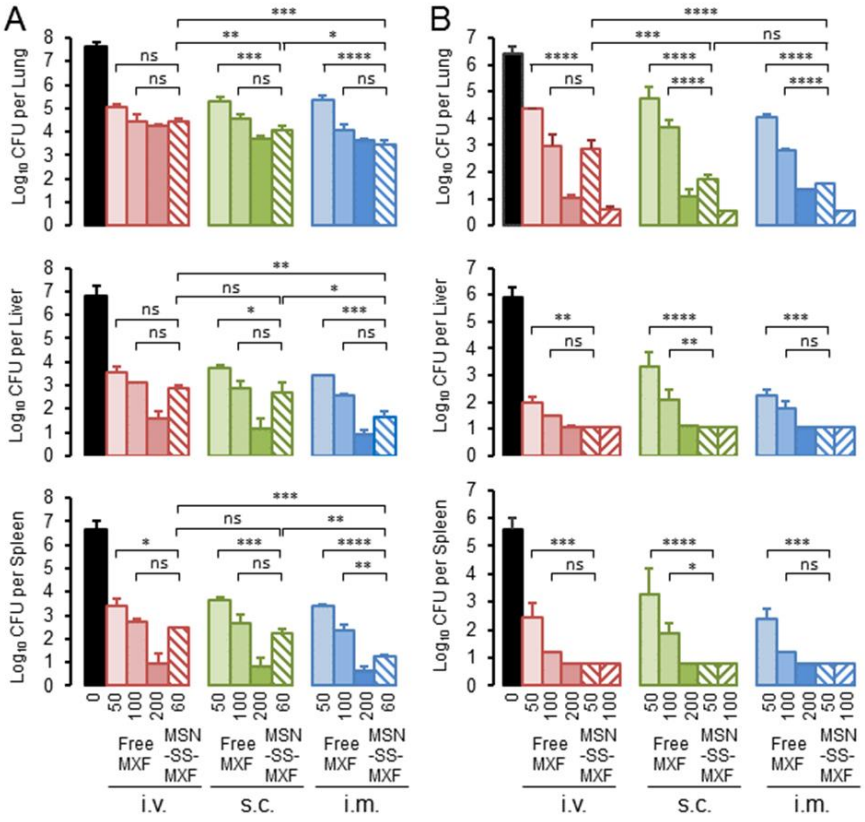

Figure 6.2 Efficacy of MSN-SS-MXF and free MXF administered by the i.v., s.c., or i.m. route in two independent experiments. BALB/c mice were infected with *F. tularensis* LVS i.n. at day 0. Mice were treated on day 1, 3, and 5 with free MXF (n = 3 mice per group) or MSN-SS-MXF (n = 4 mice per group) at the dose and route of administration indicated. Control mice were sham treated with PBS by the i.v. route. Doses of MSN-SS-MXF indicated in the first (A) and second (B) experiments were the amount of free MXF equivalent delivered. Bacterial burdens in the lung (top panel), liver (middle panel), and spleen (bottom panel) were determined one day after the last treatment on day 6. Data are shown as mean ± SEM. Treatment efficacy between groups was analyzed using two-way ANOVA with Tukey's correction. ****, $p < 0.0001$; ***, $p < 0.001$; **, $p < 0.01$; *, $p < 0.05$; ns, not significant

cells for replication of intracellular pathogens, such as *Francisella tularensis*[9,45] and *Mycobacterium tuberculosis*.[46] The relative contribution of various factors to the enhanced efficacy of mesoporous silica nanoparticle (MSN)-delivered drug treatment vs. free drug is often unclear.

A study in *Mycobacterium marinum* infected zebrafish embryos demonstrated that poly(lactic-co-glycolic acid) (PLGA) NPs administered i.v. are taken up by macrophages that traffic into *M. marinum* containing granulomas,[47] consistent with the concept that a NP platform can enhance drug delivery to infected cells and tissues.

However, the study did not examine whether the PLGA-delivered drug was more effective than free drug, or whether the i.v. route was more effective than other routes, e.g. the subcutaneous (s.c.) or intramuscular (i.m.) route, where trafficking of NP-containing drug to the site of infection might be less effective. Here we determined the efficacy of MSN-SS-MXF delivered by i.v., s.c., or i.m. routes against lethal respiratory infection with *F. tularensis* Live Vaccine Strain (LVS) in mice. We show that equivalent amounts of MXF exhibit the following order of efficacy for treatment of pneumonic tularemia in a mouse model: i.m. MSN-SS-MXF > i.v. MSN-SS-MXF > i.m. free MXF > i.v. free MXF. While i.m. administered MSN-SS-MXF was the most effective, we found few or no MSNs in the lungs of mice following i.m. administration, indicating that, for this NP platform, enhanced trafficking of MSN-SS-MXF to the site of infection is not responsible for the markedly enhanced efficacy of the i.m. route. On the other hand, the nanoparticle formulation yields a longer half-life than free drug and i.m. administration yields an even further prolongation of the half-life. In our model of pneumonic tularemia, time above the minimal inhibitory concentration (t>MIC) is the best predictor of MXF efficacy, and accordingly, i.m. administration of the nanoparticle formulation of MXF was superior to all other routes and to free MXF.

6.1.3 Results

Efficacy of MSN-SS-MXF and free MXF by 3 different routes of administration

We conducted two independent experiments to compare the treatment efficacy of MSN-SS-MXF delivered via three different routes in a mouse model of pneumonic tularemia. We infected BALB/c mice intranasally (i.n.) with 6 times

Experiment	Organ	MSN-SS-MXF Dose (μg)	Route of administration		
			i.v.	s.c.	i.m.
Experiment 1					
	Lung	60	2.10	2.40	3.36
	Liver	60	1.43	1.46	2.09
	Spleen	60	1.45	1.59	2.25
Experiment 2					
	Lung	50	1.84	3.28	3.58
		100	2.95	3.42	4.58
	Liver	50	4.19	4.19	4.11
		100	2.11	2.07	2.04
	Spleen	50	3.65	4.07	3.71
		100	1.84	2.02	1.88

Table 6.1 Efficacy Ratios of MSN-SS-MXF to Free MXF

the LD_{50} dose of *F. tularensis* Live Vaccine Strain (LVS) and one day later began treatment with MSN-SS-MXF or free MXF by the i.v., i.m., or s.c. route, administering the drug every 48 hours for a total of 3 doses.

In the first experiment, the number of live LVS [colony-forming units (CFU)] in the lung at 5 hours post-infection was determined to be 2.7 x 10^2 per lung. One day later, the bacterial burden increased to 1.4 x 10^5 CFU per lung. Without treatment, the bacteria continued to multiply in the lung and disseminate to other organs. At the end of the 6-day infection period, the bacterial number had multiplied to more than 10^7 CFU in the lung and $10^6 - 10^7$ CFU in the liver and spleen (Figure 6.1).

MSN-SS-MXF (60 μg) given by the i.m. route showed an efficacy in reducing the bacterial burden in the lungs that was comparable to that achieved by a 3.3-fold larger dose (200 μg) of free drug given by the same i.m. route. MSN-SS-MXF delivered by the i.m. route was also more effective than equal amounts of MSN-SS-MXF given by the s.c. or i.v. route. MSN-SS-MXF (60 μg) given by the s.c.

Treatment	Organ	MXF dose (μg)	Route of administration		
			i.v.	s.c.	i.m.
Free MXF	Lung	50	1.00	0.87	1.21
		100	1.00	0.69	0.94
		200	1.00	1.00	0.86
	Liver	50	1.00	0.19	0.69
		100	1.00	0.46	0.70
		200	1.00	0.95	1.09
	Spleen	50	1.00	0.49	0.98
		100	1.00	0.69	1.16
		200	1.00	0.90	0.89
MSN-SS-MXF	Lung	50	1.85	2.87	3.07
		100	2.86	3.09	3.17
	Liver	50	4.20	4.23	4.15
		100	2.11	2.06	2.06
	Spleen	50	3.57	3.61	3.57
		100	1.80	1.78	2.26

Table 6.2 Efficacy ratios relative to i.v. free MXF in experiment 2

route was more effective than 100 μg of free MXF given by the s.c. route, and MSN-SS-MXF (60 μg) given by the i.v. route showed an efficacy comparable to that of 100 μg of free MXF. In the liver, i.m. MSN-SS-MXF (60 μg) was more effective than 100 μg of free MXF given by the i.m. route and was more effective than MSN-SS-MXF (60 μg) given by the i.v. or s.c. route. MSN-SS-MXF (60 μg) given by the i.m. route reduced bacterial burden in the spleen to a greater extent than did 100 μg of free MXF given by the same route. MSN-SS-MXF (60 μg) given by the i.v. or s.c. route also decreased bacterial burden to a greater extent than did 100 μg of free MXF given by the same routes.

In the second experiment, the number of bacteria in the lung at 5-hours and 1-day post infection was 1.5 x 10^2 CFU and 8 x 10^4 CFU, respectively. At day 6, the organ burden of bacteria was approximately 10^7 CFU in the lung and 10^5 – 10^6

CFU in the liver and spleen (Figure 6.1). Similar to the first experiment, MSN-SS-MXF (50 μg) given i.m. was as effective as a 4-fold higher dose (200 μg) of free MXF delivered by the same route in reducing bacterial burden in the lung. Also as observed in the first experiment, MSN-SS-MXF administered by the i.m. route was more effective in reducing the bacterial load in the lung than equal amounts of MSN-SS-MXF given by the s.c. or i.v. route. In the liver and spleen, the effect of MSN-SS-MXF given by these three different routes could not be compared because bacterial number in these organs was reduced to a level below the experimental detection limit after treatment with three 50 μg doses, the lower of the two doses tested.

We used the median-effect equation[48,49] to model the dose – response relationship between free MXF administered by each of the routes and reduction in bacterial burden in each of the organs. This allowed us to calculate – for each route and for each organ – the dose of free drug that would yield a comparable reduction of bacterial burden. We define the efficacy ratio as the ratio of the free drug to MSN-delivered drug that yields the same reduction in bacterial burden.

Table **6.1** indicates the ratio of bio-equivalent amounts of MSN-SS-MXF to free MXF when both are given by the same route. The efficacy ratios in the lung for MSN-SS-MXF vs. free MXF administered i.m., s.c., or i.v. were 2-3:1 in the first experiment and 3-4:1 in the second experiment (

Table **6.1**). The i.m. route had higher MSN-SS-MXF to free MXF efficacy ratios than s.c. and i.v. routes in liver and spleen in the first experiment and about the same efficacy ratios as s.c. and i.v. routes in the liver and spleen in the second experiment (

Table **6.1**); in the latter experiment, any potential improvements in the efficacy ratio by the i.m. route could not be ascertained because the efficacy of MSN-SS-MXF was already at a

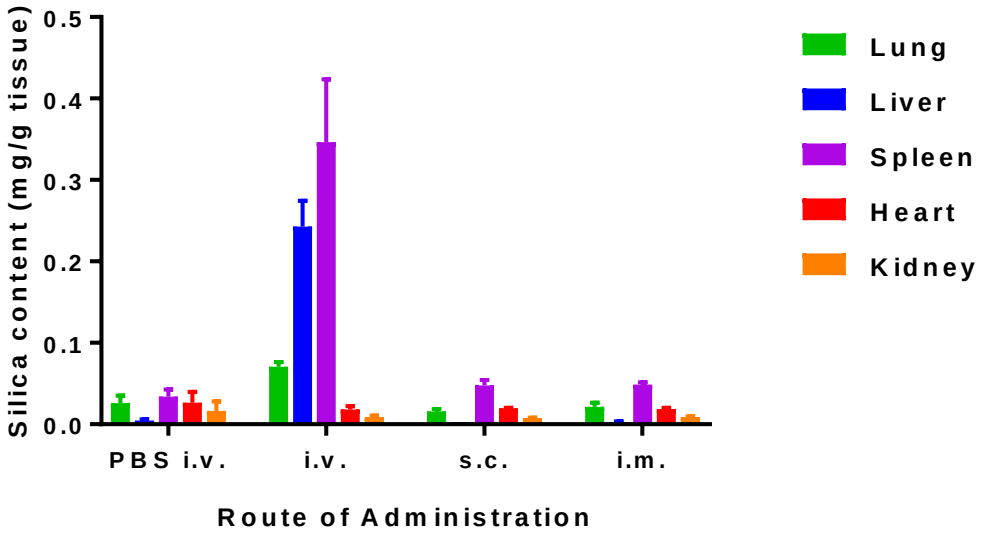

Figure 6.3 Organ biodistribution of silica. The amount of silica in organs from *F. tularensis* LVS infected mice was determined after administration of MSN-SS-MXF via the route indicated. Data are presented as mean ± SD of 3 mice in the PBS i.v. group and 4 mice each in the MSN-SS-MXF i.v., s.c., and i.m.groups.

maximum, i.e., the bacterial burden in the liver and spleen - even with MSN-SS-MXF administered i.v. - was already reduced to the limit of detection (Table 6.2).

Table 6.2 shows the ratio of the bio-equivalent amounts of MSN-SS-MXF and free MXF administered i.v., s.c., and i.m. relative to free MXF administered i.v. It is clear from Table 6.2 that MSN-SS-MXF are more efficacious than free drug by all routes of administration. Moreover, in the lung after administration of the 50 µg dose of MSN-SS-MXF, the only site and dose level where CFU were above the limit of detection, the i.m. and s.c. routes were more efficacious than the i.v. route. Analysis of MSN silica in mouse organs by ICP-OES following i.m., s.c., and i.v. administration of MSN-SS-MXF

To determine whether greater delivery of MSNs to infected tissues could account for the greater efficacy of the i.m. route of administration of MSN-SS-MXF, we measured MSN uptake into organs using inductively coupled plasma optical emission spectrometry (ICP-OES). Mice were given 3 doses (one dose every 48 hours) of MSN-SS-MXF by the i.v., s.c., or i.m. route or 3 doses of PBS by the i.v. route. The mice were killed 24 hours after the last injection, their organs

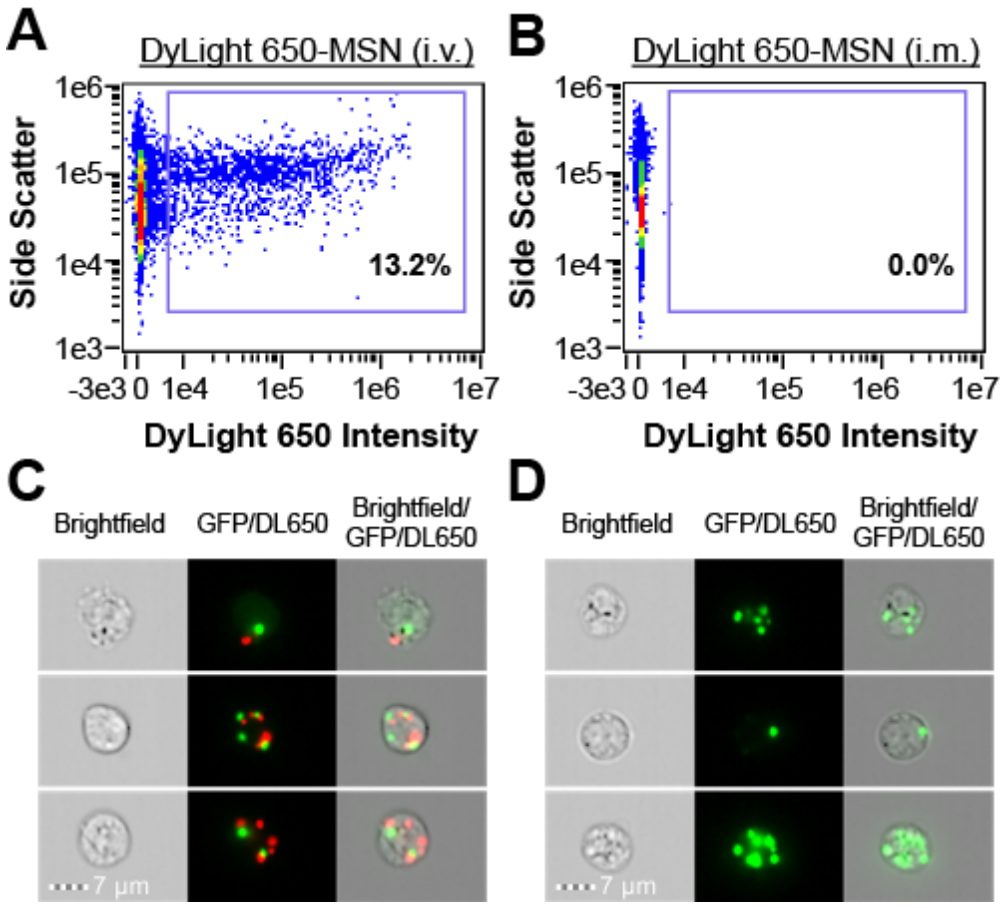

Figure 6.4 DyLight 650-labeled MSNs are detected in lung cells after i.v. but not after i.m. administration. (A, B) Imaging flow cytometry density plots of lung cells from mice infected with LVS-GFP one day after i.v. (A) or i.m. (B) administration of DyLight 650-labeled MSN. (C) Images from (A) showing DyLight 650 positive lung cells that are also GFP positive (i.e. infected with LVS-GFP). (D) Images from (B) showing DyLight 650 negative lung cells that are infected with LVS-GFP.

digested with acid, and the amount of silica assayed by ICP-OES. We found that the level of silica in the lung, liver, and spleen of mice treated with MSN-SS-MXF by the i.m. or s.c. routes was comparable to the background level of silica in mice receiving sham (PBS) injections (Figure 6.3). Only in mice treated with MSN-SS-

MXF by the i.v. route were levels of silica in the organs greater than that in sham-treated mice (Figure 6.3).

Fluorescent MSNs are detected in the cells of infected organs after i.v. but not after i.m. administration

To assess the trafficking of MSNs to infected cells and tissues, we infected mice i.n. with *F. tularensis* LVS that express GFP (LVS-GFP) and two days later injected DyLight 650-labeled MSNs into the mice by the i.v. and i.m. routes. One day after injection, the organs were digested enzymatically and by physical methods, immunostained with a fluorescent antibody to F4/80 (a mouse macrophage marker), and the cells examined with an ImageStream Mark II flow cytometer to assess co-localization of the MSNs and the LVS-GFP. Whereas MSNs were present in infected F4/80+ macrophages of the lung and spleen (as well as F4/80- cells) following i.v. administration, they were not present in any cells (infected or uninfected) of these mouse organs after i.m. administration (Figure 6.4).

Pharmacokinetics of MXF in the blood following administration of free or MSN-SS-MXF by i.v. and i.m. routes

Mice were given equivalent amounts of free MXF or MSN-SS-MXF by i.v. or i.m. routes and blood was obtained at sequential times thereafter for determination of MXF concentration by LC-MS (Figure 6.5). The area under the curve (AUC) calculated by the linear trapezoidal method was lowest for the i.v. free MXF and similar for the i.v. MSN-SS-MXF, i.m. free MXF, and i.m. MSN-SS-MXF (Table 6.3). When calculated by the linear up, log-down trapezoidal method, i.m. MSN showed the greatest AUC, but the difference does not appear to be great enough to account for its markedly greater efficacy (Table 6.3). On the other hand, the i.m. MSN-SS-MXF yielded a much longer half-life for MXF (6.9 hours), which was longer than i.v. MSN-SS-MXF (4.8 hours) and considerably longer than i.v. and i.m. free MXF (0.9 and 0.7 hours, respectively). Because of its much longer half-life, the time above the MIC is longer following i.m. MSN-SS-MXF (24 hours) than for i.v. MSN-SS-MXF (14 hours) and dramatically longer than for free MXF administered either i.v. or i.m. (5.1 and 5.5 hours, respectively).

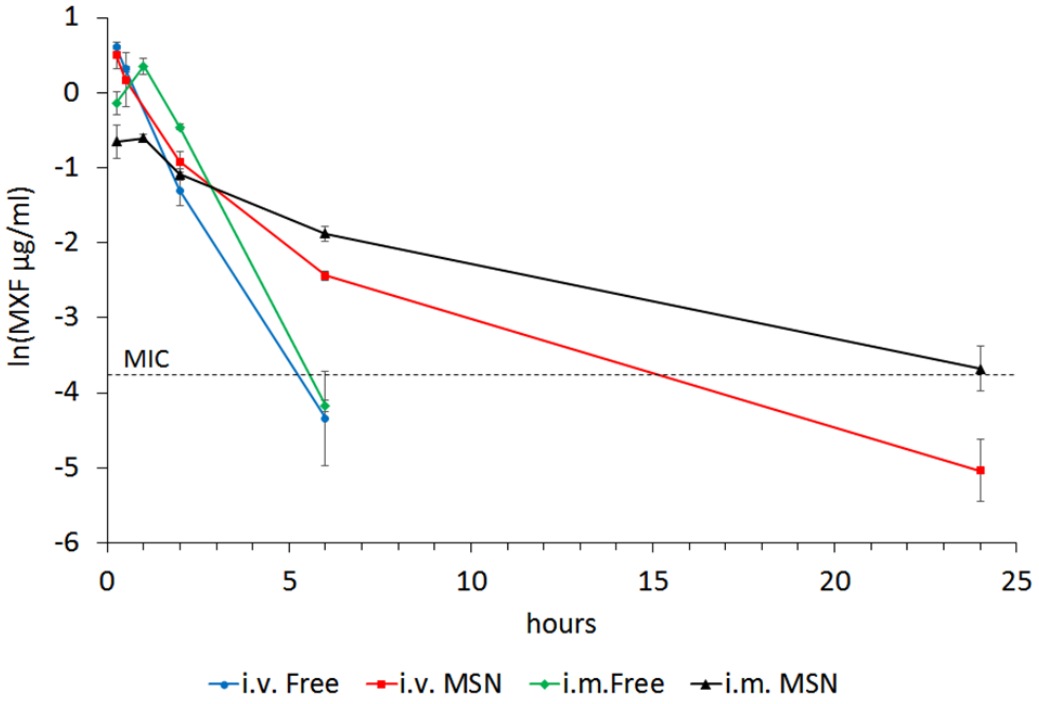

Figure 6.5 Blood levels of MXF (plotted as natural log of µg/ml concentrations) after i.v. or i.m. administration of 0.28 mg of MXF either as free drug or as MSN-SS-MXF. The MXF MIC for LVS (0.025 µg/ml) is indicated with a dotted horizontal line. Blood MXF levels were below the limit of detection at time points greater than 6 hours after i.v. and i.m. administration of free MXF. Data shown are means ± SEM of determinations from 3 mice for each data point.

Parameter	Free MXF		MSN-SS-MXF	
	i.v.	i.m.	i.v.	i.m.
K_{el} (hours^{-1})	0.76	0.93	0.14	0.10
$t_{1/2}$ (hours)	0.90	0.70	4.80	6.90
Linear trapezoidal $AUC_{0\text{-}48h}$ (µg·hours)	2.54	3.42	3.56	3.49
Linear-up Log-down trapezoidal $AUC_{0\text{-}48h}$ (µg·hours)	1.66	2.62	2.70	3.33
t>MIC (hours)	5.14	5.50	14.65	24.06

Table 6.3 Pharmacokinetic Parameters of MSN-SS-MXF and Free MXF after i.v. and i.m. administration.

6.1.4 Discussion

We have demonstrated in a mouse model of pneumonic tularemia that MXF formulated in redox-operated MSNs is markedly more efficacious than an equivalent amount of free drug and that this greater efficacy is further enhanced by administration of the MSNs by the i.m. as opposed to the i.v. route. We have shown here that the greater efficacy is not attributable to enhanced delivery of the MSNs to infected cells or tissues, but is instead attributable to the markedly prolonged half-life of the MXF and the markedly longer duration that blood levels of MXF are above the MIC.

Three different pharmacokinetic parameters have been correlated with antibiotic treatment efficacy in various antibiotic-infection models: the ratio between peak blood level and MIC (Cmax/MIC); the AUC/MIC ratio; and time above MIC (t>MIC).[50–52] While administration of free MXF or MSN-SS-MXF by the i.v. route leads to much higher Cmax than does administration of MSN-SS-MXF by the i.m. route (Table 6.3), the higher Cmax does not result in greater efficacy, suggesting that t>MIC or AUC/MIC is a more important factor in treatment efficacy. The linear-up/log-down trapezoidal AUC is likely a more accurate estimation of AUC than the linear trapezoidal AUC as it corrects for the

logarithmic as opposed to linear decline in MXF blood levels during the elimination phase. Calculated by this method, the AUC/MIC ratio predicts the following efficacy ranking: i.m. MSN-SS-MXF > i.v. MSN-SS-MXF = i.m. free MXF > i.v. free MXF. On the other hand, t>MIC predicts an efficacy ranking of i.m. MSN-SS-MXF > i.v. MSN-SS-MXF > i.m. free MXF = i.v. free MXF. Table 6.2 data (excluding data for sites and doses at the limit of detection) show that the observed efficacy ranking is i.m. MSN-SS-MXF > i.v. MSN-SS-MXF > i.v. free MXF = i.m. free MXF, thus matching the t>MIC prediction rather than the AUC/MIC prediction. This suggests that for our mouse model of tularemia, MXF efficacy is more time-dependent than concentration-dependent, i.e. concentrations substantially higher than the MIC do not provide more rapid killing but concentrations above the MIC for a longer time do.

In our system, i.m. administration of MXF in redox-operated snap top nanoparticles led to a dramatically prolonged half-life and prolonged t>MIC. While t>MIC was the best predictor of efficacy in our model of MXF treatment of pneumonic tularemia, in other infection-antibiotic models, such as the clinical response to aminoglycoside therapy, the higher Cmax/MIC ratio provided by i.v. free drug may be more important to therapeutic efficacy. On the other hand, many infectious disease treatments are now shifting to drugs and formulations with longer half-lives as a means to improve treatment efficacy and to decrease the need for frequent dosing.

While we did not observe trafficking of our i.m. and s.c. delivered MSNs to lung, liver, or spleen, it is possible that different formulations of NPs or that an intradermal (i.d.) route of administration would have yielded more delivery of the MSNs to lung, liver, and spleen. In this regard, it is noteworthy that i.d. delivered pluronic-stabilized poly(propylene sulfide) NPs (<100 nm) have been shown to traffic through lymphatics to reach the blood and then be taken up by mononuclear phagocytes in the spleen.[53] Indeed, the i.d. delivered NPs provided a 50% greater bioavailability in the blood than NPs delivered i.m.[53]

In these studies, our MSN-SS-MXF have not been modified to include any specific targeting features, but instead rely on passive uptake. When given by the i.v. route, uptake is primarily into cells of the mononuclear phagocytic system in liver, spleen, and lung, which correlates well with the cells that are infected by *F. tularensis*. Indeed, our fluorescence flow cytometry analysis confirmed successful targeting of the nanoparticles administered by the i.v. route to infected cells in the lung. Nevertheless, we observed higher efficacy when the MSN-SS-MXF was given

by i.m. and s.c. routes that did not lead to uptake of the nanoparticles by infected cells in these organs. While pharmacokinetic parameters proved more important than nanoparticle targeting in these studies, it is possible that incorporation of additional design features that further enhance nanoparticle targeting and delivery to infected cells[54] would enhance the efficacy of the i.v. route of NP administration.

6.1.5 Materials and Methods

Bacteria

Francisella tularensis subsp. holarctica Live Vaccine Strain (LVS) was acquired from the Centers for Disease Control and Prevention (Atlanta, GA). Frozen stocks of LVS and LVS expressing green fluorescent protein (LVS-GFP) were prepared from cultures on GC II agar with hemoglobin and IsoVitaleX enrichment (BD BBL) and pre-titered for use directly in animal experiments. F. tularensis subsp. novicida (F. novicida) was cultivated at 37°C with aeration in trypticase soy broth (BD BBL) supplemented with 0.2% cysteine (TSBC) for use in the bioassay for MXF.

MSN-SS-MXF and DyLight 650-labeled MSN

MSN-SS-MXF were prepared as previously described.[9] Briefly, cetyltrimethylammonium bromide (CTAB, 0.7 mmol) was mixed with NaOH (2 M, 1.7 mmol) in deionized water (120 ml). The solution was maintained at 80°C during dropwise addition of tetraethylorthosilicate (TEOS, 5.4 mmol). After 15 minutes, 3-(trihydroxysilyl) propyl methylphosphonate (HTMP, 0.5 mmol) was added to the mixture. The reaction temperature was maintained at 80°C for an additional 2 hours after which the MSNs were collected by centrifugation and washed three times with water and ethanol. The MSNs were modified with thiol groups by dispersing the MSNs and (3-mercaptopropyl) trimethoxysilane in dry toluene and refluxing under nitrogen atmosphere. CTAB was removed by suspending the MSNs (200 mg) in ethanol (80 ml) with the addition of concentrated HCl (10 ml) and refluxing for 1 hour, twice. The adamantane moiety was conjugated to the MSNs through the formation of a disulfide bond. Typically, 1-adamantanethiol (17 mg, 0.1 mmole) and thiol group modified MSNs (100 mg) were mixed and suspended in anhydrous toluene (10 ml). The oxidizing reagent thiolcyanogen was prepared separately by dispersing lead thiocyanate (800 mg) in

10 ml chloroform and titrating with bromine (200 µl) dissolved in chloroform (10 ml). The resultant mixture was filtered to obtain thiolcyanogen, which was slowly added to the MSNs mixture at 4°C under nitrogen atmosphere. The adamantane-modified MSNs (MSN-SS-Ada) were washed thoroughly with toluene, ethanol and deionized water. The loading procedure of MXF was performed by suspending MSN-SS-Ada (10 mg) in 1 ml of 40 × 10−3 M MXF in 1X PBS solution and rotating overnight. β-cyclodextrin (40 mg) was then added to the solution as capping agent and the solution was rotated for an additional 6 hours. The loaded MSNs (MSN-SS-MXF) were washed thoroughly prior to further use.

Dylight 650 labeled MSNs were prepared by first mixing (3-aminopropyl) triethoxysilane (APTES, 0.2 mmol) with TEOS (4.5 mmol) and then adding the solution dropwise to the basic CTAB solution. After the removal of CTAB, MSNs were suspended in DMF, and DyLight 650 NHS-Ester (500 µl) was added to allow covalent coupling to the amine groups grafted within the MSNs. After dye labeling, the particles were washed and processed as described above for disulfide snap-top modification.

Measurement of MSN-SS-MXF Release Capacity

We used a modification of our previously described F. novicida bioassay[9] to determine the maximum amount of MXF released from particles. With this assay we measured the amount of drug released from MSN-SS-MXF in PBS or DMSO or acidified DMSO with and without 2-mercaptoethanol by determining the inhibition of F. novicida growth in broth cultures.

Mouse Model of Pneumonic Tularemia

BALB/c mice of age 8-9 weeks (Envigo) were acclimated for one week prior to infection with 4000 CFU (~6 x LD50) of F. tularensis LVS by the i.n. route. Two mice were euthanized after infection (day 0) for determination of initial organ burden of F. tularensis. One day later (day 1), 3 additional mice were euthanized to determine the level of F. tularensis at the time point immediately before the start of treatment. Mice were treated with one of three doses of free MXF (3 mice per group for each dose) or one of two doses of MSN-SS-MXF (4 mice per group for each dose) i.v., s.c., or i.m. every other day (day 1, 3, and 5 for a total of three treatments). Sham-treated mice (3 mice per group) received an equal volume of PBS i.v. every other day on the same schedule. The mice were euthanized one day

(day 6) after their third treatment, the organs harvested, and the number of CFU determined by plating serial dilutions of the organ homogenates on GCII chocolate agar plates containing sulfamethoxazole (40 μg/ml), trimethoprim (8 μg/ml), and erythromycin (50 μg/ml) to prevent growth of contaminants. Bacterial colonies on each plate were counted after incubation at 37 °C for 4 days.

Biodistribution of MSN-SS-MXF

BALB/c mice were provided with a low silica diet and water throughout the experiment to improve measurement of silica in the organs. The mice were infected with F. tularensis LVS i.n. and were administered either PBS i.v. or 0.28 mg MSN-SS-MXF i.v., s.c., or i.m. (4 mice for each route) every other day for a total of 3 treatments, and euthanized 24 h later, as described above. Their organs were harvested, homogenized in PBS, digested with 0.1% HNO3, and analyzed by ICP-OES (ICPE-9000, SHIMADZU, Japan).

Flow Cytometry

BALB/c mice of age 8-9 weeks (Envigo) were acclimated for one week and then infected with 4000 CFU LVS-GFP by the i.n. route or left uninfected as a negative control. Two days later, the infected mice were injected i.v. or i.m. with 1 mg of DyLight 650-labeled MSN or left untreated. Three days after infection with LVS-GFP, approximately 24 h after injection with DyLight 650-labeled MSNs, the mice were euthanized and their spleens and lungs harvested for analysis.

Single-cell suspensions of splenocytes were prepared by gently pressing the cells out of the spleen sac, lysing red blood cells with PharmLyse (BD Pharmingen), washing the cells, and filtering the cells through a 70-μm nylon cell strainer (Falcon). To prepare single-cell suspensions of total lung cells, the lungs were quickly chopped into small pieces with a scalpel and digested for 1 h in 10 ml lung digestion solution [PBS containing 300 U/ml Collagenase type II (Worthington) and 0.15 mg/ml DNase I (Worthington)] at 37°C with shaking (300 rpm). The lung cells were filtered through a 40-μm nylon cell strainer (Falcon), red blood cells were lysed with PharmLyse, and the lung cells washed. Advanced RPMI 1640 (Invitrogen), supplemented with 2% heat-inactivated fetal bovine serum, 2 mM l-alanyl-l-glutamine (Glutamax; Invitrogen), 10 mM HEPES buffer, 50 μM β-mercaptoethanol, and penicillin (100 IU/ml)-streptomycin (100 μg/ml), was used as the medium. Surface staining was performed in a 96-well V-bottom plate kept

on ice. Lung and spleen cells (2 to 4 x 106 cells per well) were blocked with 4 µg anti-mouse CD16/32 (TruStain fcX, BioLegend), stained with 0.2 µg PE labeled anti-mouse F4/80 (1:100 dilution) (BioLegend), washed, and fixed in 1% formaldehyde in PBS. Fixed cells were analyzed on an ImageStream Mark II Imaging Flow Cytometer and 30,000 events at 60x magnification were recorded for each sample gated by focus and aspect ratio vs. area parameters to obtain predominantly single cells. To obtain high quality single cell images, events were gated post acquisition with IDEAS® software version 4.0 (Amnis) using focus, aspect ratio vs. area, circularity, perimeter, diameter, and contrast parameters. This further refinement resulted in ~10,000 to 14,000 images for samples of lung cells and ~19,000 to 21,000 images for samples of spleen cells. Images with internalized LVS-GFP or internalized DyLight 650-labeled MSN were identified using intensity, max pixel, and internalization parameters. Samples from uninfected and/or untreated (i.e. not injected with MSN) mice were used as negative controls to determine where to draw the selection gates. Cells positive for F4/80 surface staining were gated using a side scatter vs. intensity plot with an unstained control used to determine the location of the selection gate.

Median-effect Plots

The fraction of inhibition for samples treated with different doses of MXF was calculated using bacterial CFU in base-10 logarithm (log CFU) with the equation: Fraction of inhibition = 1 – (log CFU from sample treated with a known concentration of MXF or releasable MXF from MSN-SS-MXF / log CFU from untreated sample). A median-effect plot[49] for MXF or MSN-SS-MXF was generated using MXF or MXF equivalent (MSN) dose in base-10 logarithm as the X-axis and the fraction of surviving bacteria divided by the fraction of killed bacteria in base-10 logarithm as the Y-axis.

Determination of MXF blood levels by LC-MS

MXF concentrations in blood were determined by a modification of published methods (16, 17). Heparinized blood (0.1 ml) was collected by retro-orbital bleed at sequential times after administration of free MXF or MSN-SS-MXF by i.v. or i.m. routes. Ciprofloxacin (75 ng) was added to each sample as an internal standard and 9 volumes (0.9 ml) of acetonitrile were added and mixed thoroughly. The sample was stored overnight at 4°C, mixed again by vortex action, and

insoluble material pelleted by centrifugation at 10,000 X g for 10 minutes. The supernatant fluid was transferred to a new tube and dried under vacuum. The dried material was resolubilized in 50 µl water and MXF was quantified by reverse phase C18-LC-MS. LC analysis was performed on a Waters LCT Premier (TOF) Mass Spectrometer (positive electrospray ionization mode) with Acquity UPLC. Chromatographic separations were achieved by an Acquity UPLC BEH C18 column (1.7 µm, 2.1 x 50 mm). The mobile phase consisted of a water 0.3% formic acid / acetonitrile 0.3% formic acid mixture at a flow rate of 0.2 ml/min, with a sample injection volume of 5 µl. Linearity and recovery were assessed by spiking different MXF concentrations in mouse plasma with a ciprofloxacin internal standard. Calibration curves were fitted by a linear regression method through measurement of the ratios of peak areas corresponding to MXF and ciprofloxacin internal standard.

Statistics

Statistical analyses were performed using GraphPad Prism software (version 7.04). Means were compared across groups by two-way analysis of variance (ANOVA) using the Tukey criteria to adjust p values for multiple comparisons. Comparisons of mean bacterial log CFU in the lung, liver, and spleen between mice treated with MSN-SS-MXF or an equivalent amount of free MXF were based on a logit transform linear dose response model for the log CFU results for free drug, not assuming parallel dose response relationships. The adjusted mean for treatment with free drug was computed under this model, adjusted to the equivalent dose of MSN-SS-MXF, along with the corresponding p value for comparing the adjusted free drug mean to the MSN-SS-MXF mean. A P value of 0.05 or less was considered statistically significant.

Study approval: All experiments with mice were conducted within the guidelines and according to the protocol approved by the UCLA Institutional Animal Care and Use Committee.

6.1.6 Acknowledgments

We thank Saša Masleša-Galić, Susana Nava and Greg Khitrov (UCLA MIC) for excellent technical assistance. Flow cytometry was performed in the UCLA Jonsson Comprehensive Cancer Center (JCCC) and Center for AIDS Research

Flow Cytometry Core Facility, which is supported by National Institutes of Health awards P30 CA016042 and 5P30 AI028697, and by the JCCC, the UCLA AIDS Institute, the David Geffen School of Medicine at UCLA, the UCLA Chancellor's Office, and the UCLA Vice Chancellor's Office of Research.

6.1.7 Funding Information

This work was supported by Defense Threat Reduction Agency Grant HDTRA1-13-1-0046.

6.2 Comparing routes of MSN administration by positron emission tomography

This section is based on work done with my colleagues Roger Slavik, Christine Mona, Andreea Stuparu, Larry Pang, and Liu Wei.

6.2.1 Abstract

Mesoporous silica nanoparticles have been used extensively as drug delivery vehicles with no toxicity in mice within tolerated doses. However, biodistribution and drug release characteristics have not been rigorously characterized due to limitations of current techniques. We take advantage of the facile surface functionalization properties of MSN to synthesize a NODAGA chelator-functionalized MSN that can bind radiolabeled ^{64}Cu for tracking using PET imaging. This simple technique can be used to functionalize a variety of MSN to track their biodistribution. We did a pilot study with the labeled MSN to understand the biodistribution in healthy BALB/C mice when administered via IV, SC, and IM routes, and found the biodistribution in healthy mice is strongly dependent on the route of administration and that the MSN concentration per organ varies over time. We also theorize an equation dependent on nanoparticle pore volume measurements that can be used to calculate the number of MSN per organ.

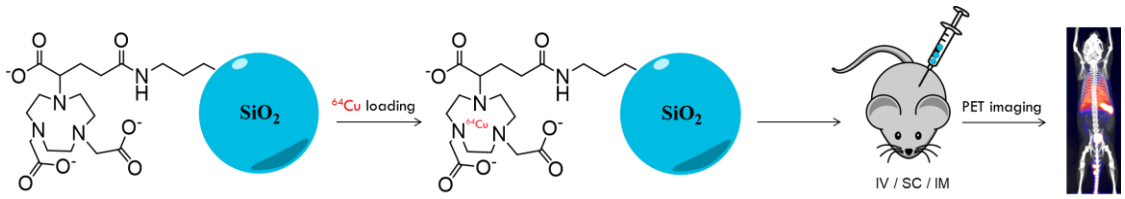

Figure 6.6 The biodistribution of mesoporous silica nanoparticles can be tracked using PET imaging of ^{64}Cu-labeled nanoparticles.

6.2.2 Introduction

As discussed in Chapter 6.1, mesoporous silica nanoparticles have shown promising results in a mouse model of pneumonic tularemia *in vivo*. ICP-OES is the primary method that is currently used to measure silica biodistribution in organs,[26,55] which although detects ppb quantities of Si, have a major disadvantage. Endogenous silica is found naturally in the body and often interferes with quantification. Mice need to be fed a Si-free diet in order to lower the baseline levels of Si. The other common method used to track nanoparticles is to fluorescently label them with a dye such as fluorescein isothiocyanate. However, problems with dye self-quenching can be a problem in organs with a high concentration of particles.[26,55] Here, we develop a facile method to track MSN that is highly specific: no detection of endogenous silica or problems with dye self-quenching. We develop a nanoparticle with a 1,4,7-triazacyclononane,1-glutaric acid-4,7-acetic acid (NODAGA) chelator commonly used in immunoconjugates[56] that has a high copper binding strength. Modification of this chelator on the surface of the nanoparticle allows us to radiolabel MSN with ^{64}Cu for *in vivo* tracking applications using non-invasive PET imaging.

6.2.3 Synthesis

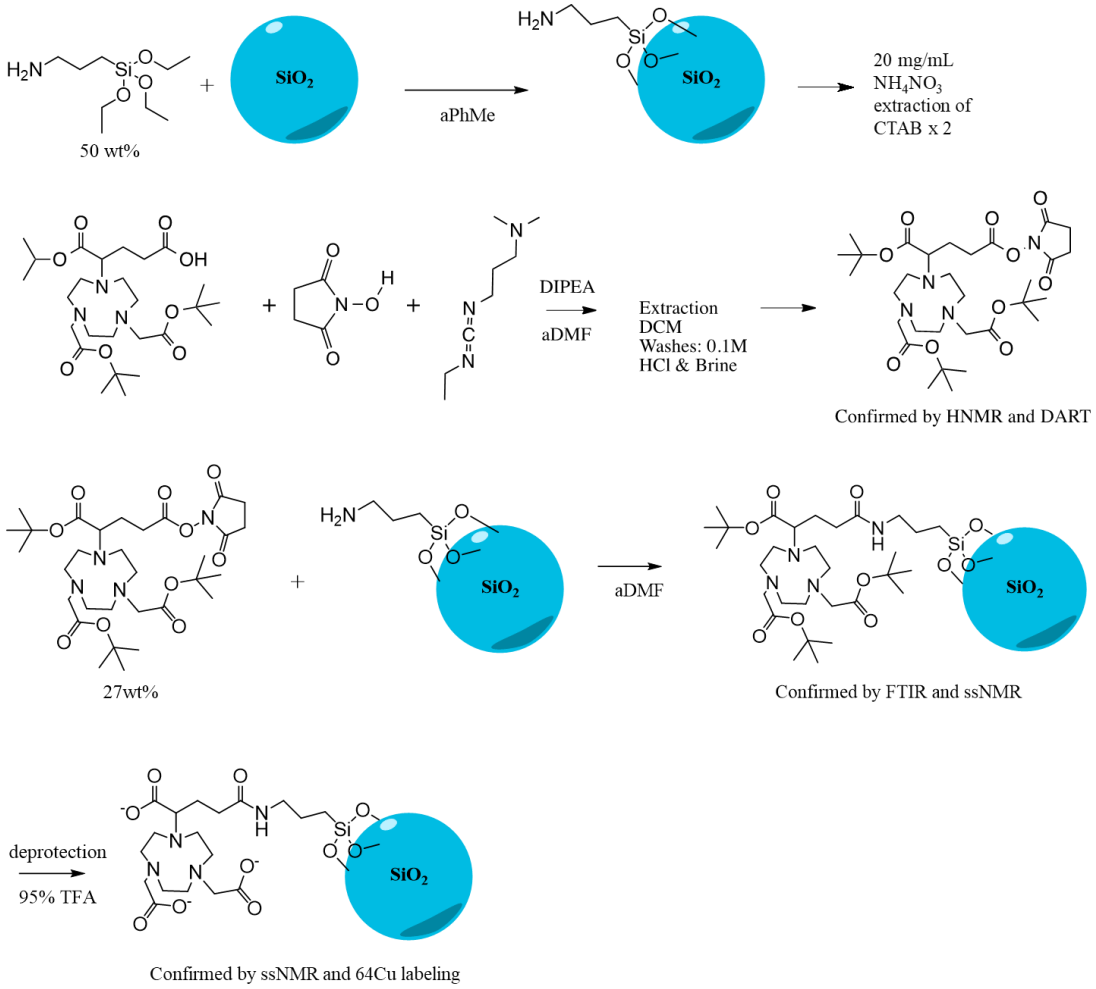

Figure 6.7 Overview of synthesis steps for the preparation of NODAGA-modified MSN

Mesoporous silica nanoparticle synthesis

MCM-41-type MSN were prepared as previously described in Chapter 2. As-synthesized MSN (~160 mg) were washed and dispersed in anhydrous toluene, mixed with aminopropyltrimethoxysilane (APTES, 50wt%), and refluxed at 120°C under N_2 for 24 hours. The APTES-modified nanoparticles were cooled and washed with toluene to remove unreacted material. The final clean product was centrifuged, washed, and stored in ethanol. After APTES modification, MSN were dispersed in 20 mg/mL NH_4NO_3 in EtOH and stirred for 1 hour at 60°C. Reaction was cooled and centrifuged, and then washed with EtOH multiple times. This process was done twice to remove all CTAB surfactant.

Note: Product was dried under vacuum before solid state NMR and FT-IR characterization. For characterization by CP/MAS, a high concentration of APTES (50wt%) was used for post-grafting, but lower concentrations can be used to tailor the number of NODAGA per particle as well as control the overall charge of the particle.

NHS ester formation of NODAGA(tBu)$_3$

To a solution of NODAGA(tBu)$_3$ (CheMatech #C083) (17.4 mg, 0.032 mmol) in 500 µL of dry DCM was added to 11.15 µL of DIPEA. Following dissolution, 2eq. of NHS (7.37 mg, 0.064 mmol) and 2eq. of EDC.HCl (12.27 mg, 0.064 mg) were added. The reaction was stirred at room temperature overnight and analyzed the following day by DART and M+1 was mostly observed in the sample. Following analysis, the reaction mixture was diluted with 5 mL of DCM and transferred to a separatory funnel containing 0.1M of HCl. Organic phase was washed 2 times with HCl 0.1M and once with brine. The organic phase was dried over $MgSO_4$, filtered, and concentrated under reduced pressure to a slightly yellowish oil. The product was brought onto the next step as is (Yield: 88%).

NHS ester coupling onto APTES-modified MSN

160 mg APTES-modified MSN was dispersed well with sonication in 20 mL dry DMF. To this mixture, 40 mg NODAGA NHS-Ester was added and stirred overnight under N2. The final product was centrifuged down, washed with DMF to remove unreacted material, and then washed and redispersed in EtOH.

Deprotection of NODAGA(tBu)$_3$

50 mg MSN was added to 975 µL TFA, 25 µL water, and 27 µg phenol at RT and placed on a rotator for 6 hours. The deprotected product was then washed with water and ethanol.

6.2.4 Results and Discussion

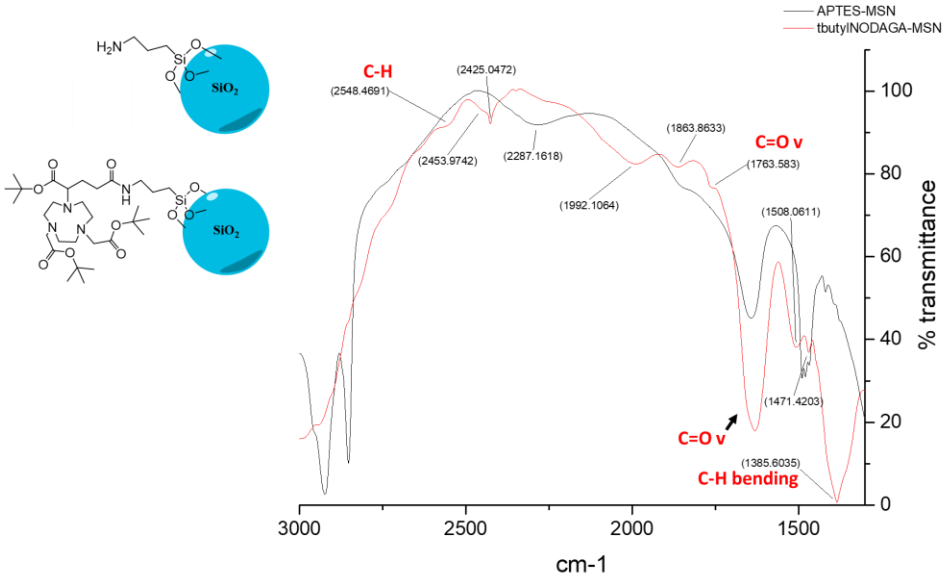

Figure 6.8 FT-IR of t-butyl NODAGA-modified MSN after t-butyl NODAGA NHS-ester coupling.

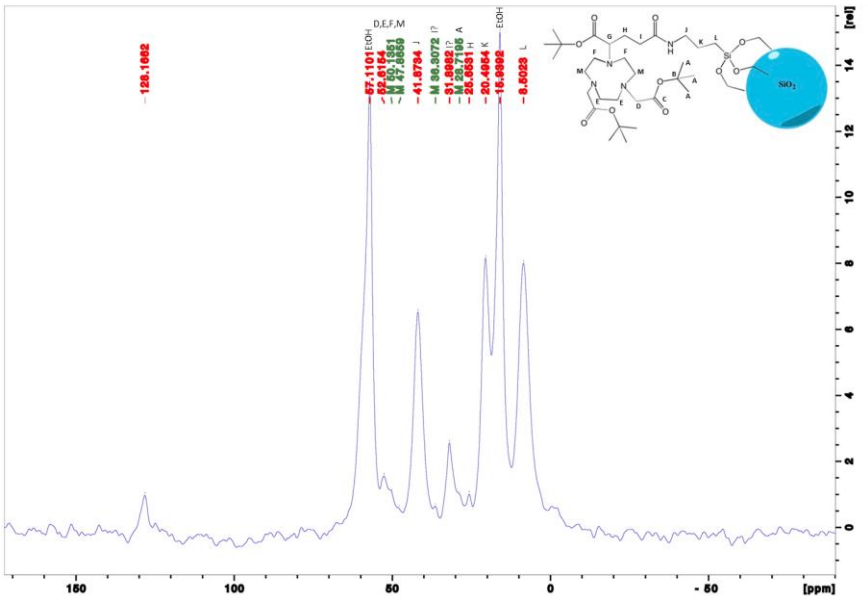

Figure 6.9 CP/MAS ^{13}C-NMR of t-butyl NODAGA-modified MSN (before deprotection).

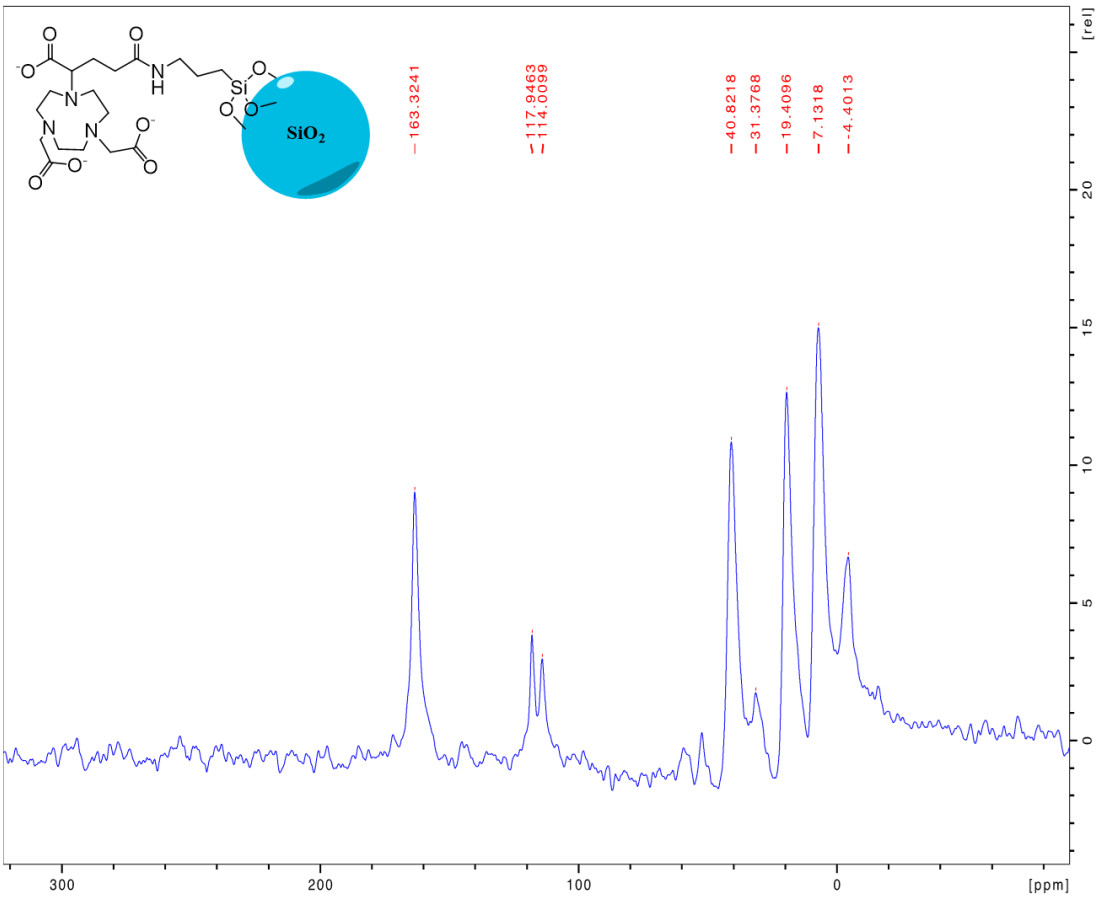

Figure 6.10 CP/MAS ^{13}C-NMR of NODAGA-modified MSN (after deprotection).

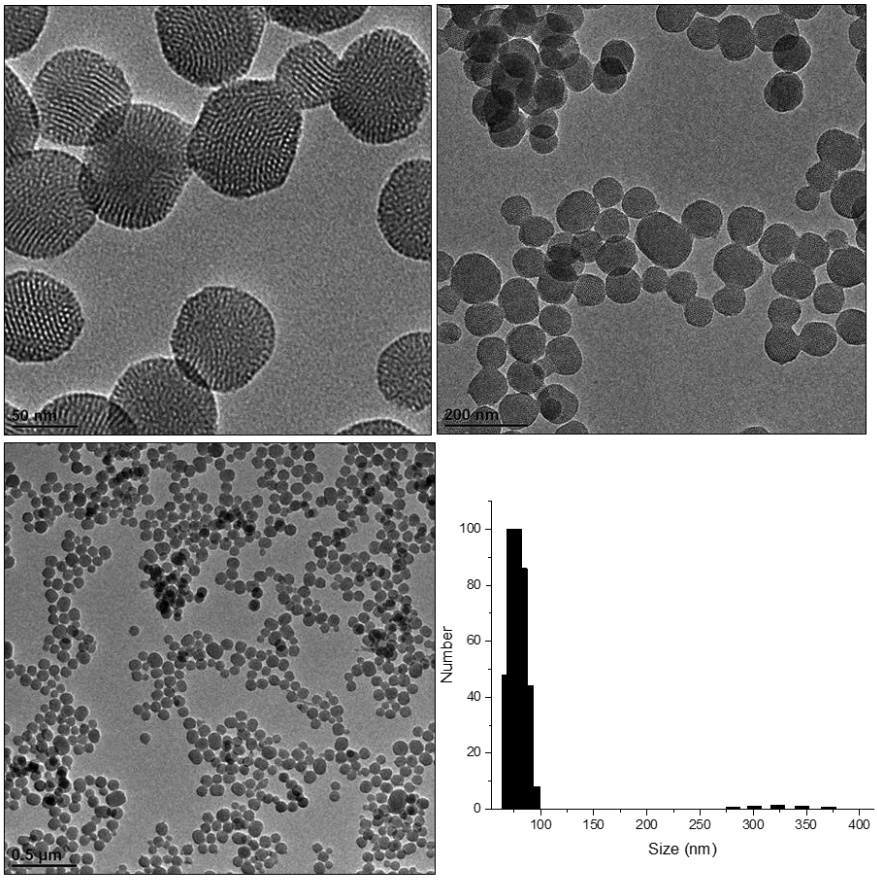

MSN	Zeta (mV)	DLS average size (nm)
APTES-MSN	+42.13 ± 3.29	n/a
tbutyl-NODAGA MSN	+33.82 ± 1.42	82

Figure 6.11 TEM and DLS data for particles after all synthesis steps.

Successful attachment of NODAGA is characterized by CP-MAS ^{13}C-NMR (Figure 6.10). Particles are positively charged due to initial grafting of APTES on the surface (Figure 6.11). After conjugation, MSN maintain dispersity and are have an average diameter of 82 nm by DLS.

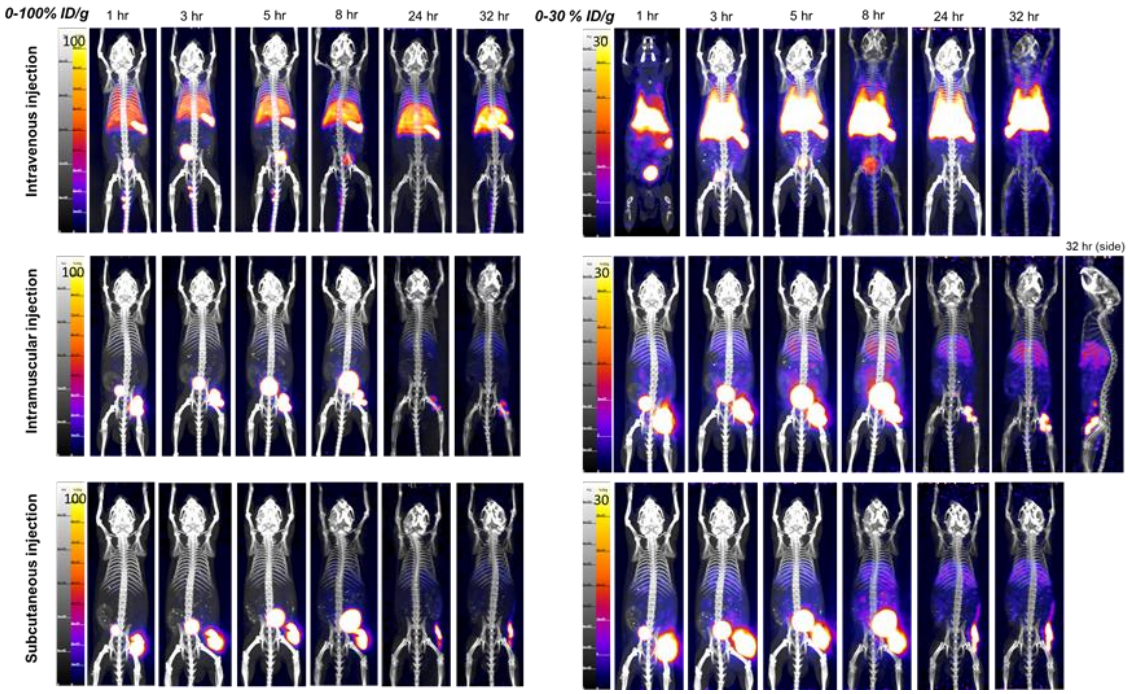

Figure 6.12 PET images of BALB/C mice after IV, IM, or SC administration from 1-32 hours. Images are overlaid with CT scans.

PET images of IV, IM, and SC injection of Cu^{64} NODAGA-MSN are taken from 1 hour to 32 hour after administration (Figure 6.12). Intravenous adminstration show uptake in the liver, lungs, and bladdar as early as 1 hour after treatment. After 24 hours, there are still some MSN in the lungs, but most of the nanoparticles reside in the liver. Intramuscular injection shows a high concentration of MSN at the site of injection up to 8 hours, in the lymph nodes, as well as in the bladdar and liver for clearance out of the body. Subcutanrous injection shows a high concentration of MSN at the site of injection up to 8 hours, some in the lung and bladdar, and some in lymph notes. At later timepoints in SC injection, particles are cleared through the liver. This pilot study is a proof of concept experiment for tracking radiolabeled nanoparticles in the body. Nanoparticles can be loaded with therapeutics and can be imaged in disease models such as solid tumors or metastatic cancers.

6.2.5 Future work

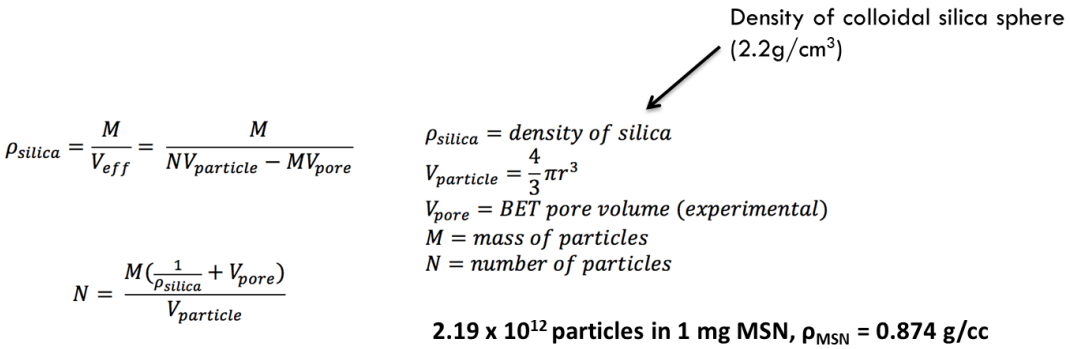

	Mathematical Modeling (Bastian et. al.)	Theoretical Equation (Sheba et. al.)
Number of MSN in 1 mg (100 nm MSN)	2.14E+12	2.19E+12
Density Estimate	0.894	0.874

Figure 6.13 Equation used to estimate the density of mesoporous silica nanoparticles. The density calculated from the equation is in agreement with density calculations using a mathematical modeling method.

Mesoporous silica nanoparticles are porous and less dense that typical colloidal silica spheres. The true density of MSN remains unknown, so we developed an equation to estimate their density based on pore volume determination from experimental nitrogen sorption data. This pore volume term takes into account density changes due to different pore modifications. From the calculated density, we can calculate the number of particles per gram MSN. From radiolabeling control experiments we know mCi per weight of MSN. For future work, the number of particles can be estimated just based on this equation and PET imaging analysis.

7 Nanoparticle formulation of cGAMP for tumor immunity: combating toxicities of lipofectamine carriers

This chapter is based on work done with my colleagues Evan Abt, Amanda Maas, and Thuc Le.

7.1 Abstract

Phosphonated mesoporous silica nanoparticles were synthesized and coated with a 1.8kD PEI polymer. Cyclic dinucleotide 2'-3'-cGAMP was then loaded electrostatically on the surface of the nanoparticles. Loading capacity was determined by LC-MS/MS. Western Blot confirmed cGAMP@PEI-MSN stimulates expression of pTBK1 and pIRF3 in Hs766t cells. To evaluate the downstream effects of STING pathway activation, we assessed for mRNA levels of INF-β, IFIT-1, and SAMHD-1 pathway activity following transfection with the STING ligand cGAMP. We compared Lipofectamine and nanoparticle as cGAMP transfection methods, and found that cGAMP@PEI-MSN treatment contributed to the highest gene expression with significantly less toxicity than the Lipofectamine carrier. cGAMP@PEI-MSN can have interesting applications in the production of interferon to treat viral infections or enhance the innate immune response in radiotherapy for the treatment of cancers.

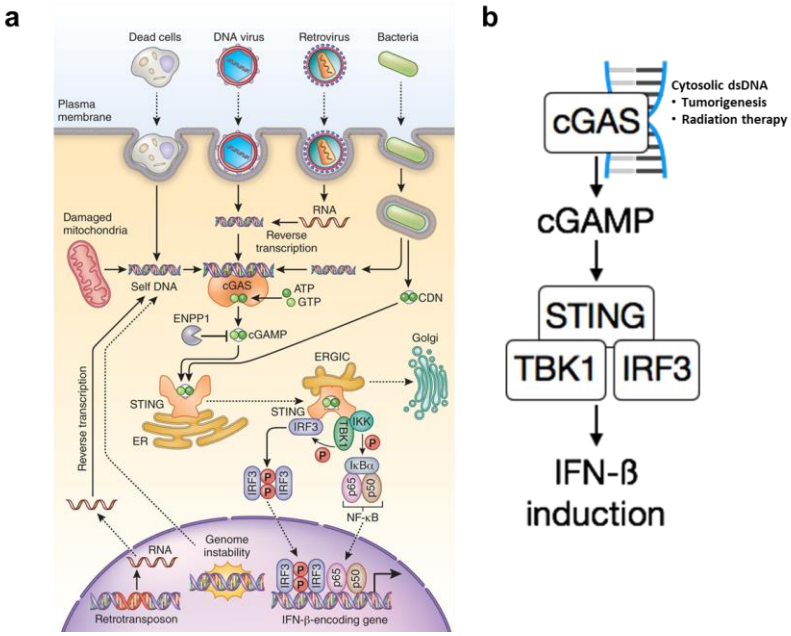

Figure 7.1 (a) cGAS sensing of cytosolic DNA stimulates the STING pathway, ultimately resulting the expression of INF-β encoding genes. (b) The role of secondary-messenger cGAMP in the production of INF-beta.

7.2 Introduction

DNA is normally found in the nucleus of the cell. Localization of DNA to the cytosol, resulting from viral infection, tumorigenesis, or radiation therapy is associated with translation of the Stimulator of Interferon Genes (STING). The STING pathway is a component of the innate immune system that functions to detect the presence of cytosolic DNA and, in response, trigger expression of inflammatory genes. Recently, the Chen lab identified cGAS, which directly binds to cytosolic DNA, forms a dimer and synthesizes cGAMP (cyclic GMP-AMP) from GTP and ATP. The cyclic dinucleotide cGAMP binds to STING with high-affinity and induces STING conformational change and interferon expression.[57–60] Radiation therapy has been shown to enhance cytosolic DNA sensing for type I IFN induction by endogenous production of the secondary messenger cGAMP. Furthermore, radiation therapy coupled with injection of cGAMP directly in solid tumors has shown to promote Type I Interferon-dependent antitumor immunity in

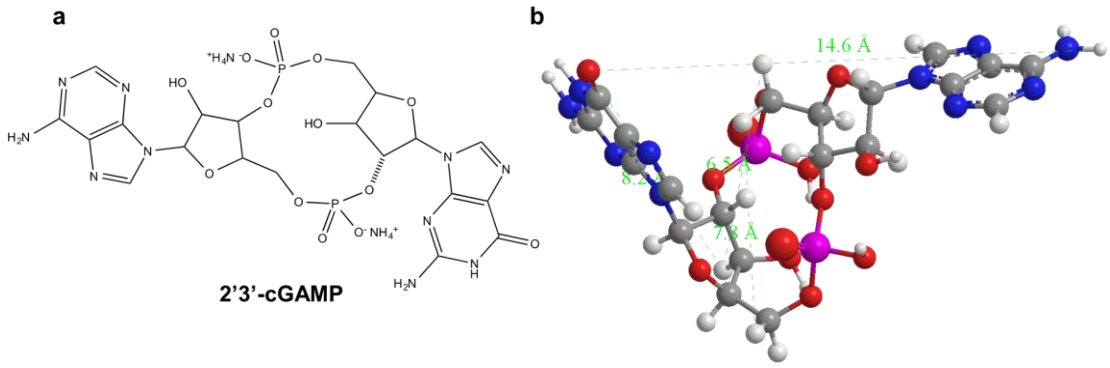

Figure 7.2 (a) Structure of the ammonium salt of 2'3'-cGAMP. (b) 3D structure of 2'3'-cGAMP and estimated dimensions of the lowest energy configuration determined using geometric modeling.

immunogenic MC-38 tumors.[61] Delivery of these agonists directly to tumor sites would greatly improve radiation therapy.[62] However, 2'3'-cGAMP contains phosphodiester linkages which are degraded by phosphodiesterases in the blood, preventing systemic administration.[60] Here, we develop a cGAMP nanoparticle carrier that can be administered via IV, SC, or IM routes. Treatment with cGAMP-loaded polyethyleneimine-coated mesoporous silica nanoparticles (cGAMP@PEI-MSN) show induction of Type I IFN, without the toxicities associated with a Lipofectamine carrier in vitro. cGAMP-loaded nanoparticles have the potential to promote protective immunity through the STING pathway.

7.3 Results and Discussion

2'3'-cGAMP is less than 2 nm and is negatively charged due to the two phosphodiester groups (Figure 7.2). These bonds are relatively unstable and have reported to be broken by phosphodiesterases in the blood.[60] To test the stability of the free compound, the degradation of cGAMP in RPMI media is measured by mass spectrometry after incubation for 24 hours under standard *in vitro* conditions. After 24 hours under these conditions, more than 90% of the cGAMP degrades.

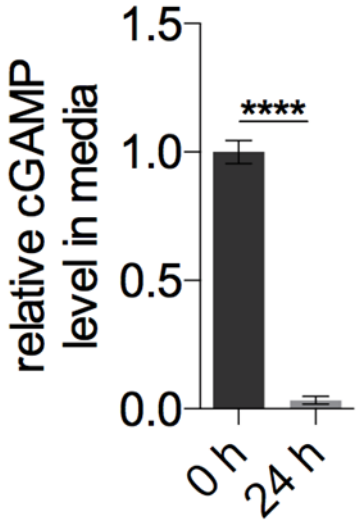

Figure 7.3 Degradation of cGAMP. Levels of 2'3'-cGAMP in RPMI media supplemented with 10% FBS are measured by mass spectrometry after 0h and 24h under typical cell culture conditions (37°C, 5% pCO_2).

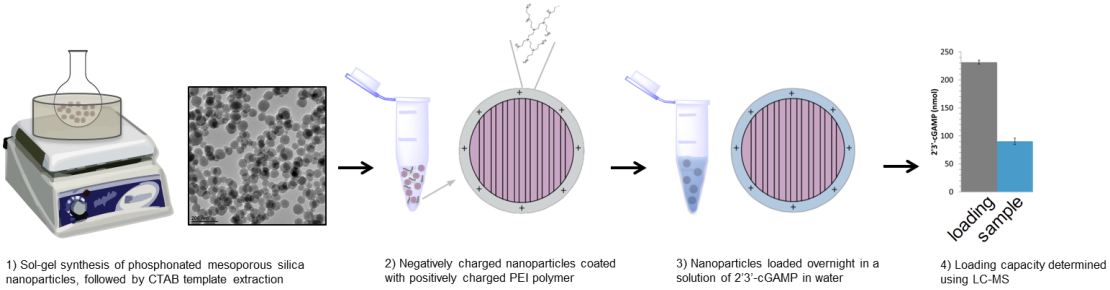

Figure 7.4 Synthesis and loading overview of cGAMP@PEI-MSN.

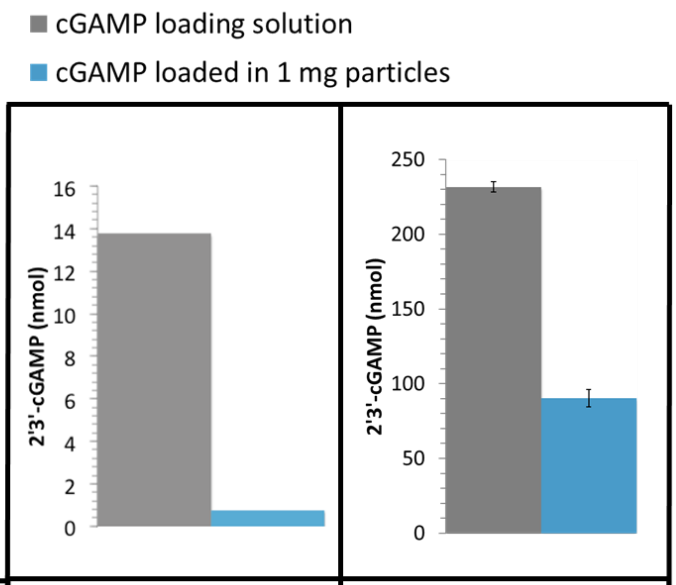

	Method 1	Method 2
Loading Solution (nmol)	13.75	231.66
After loading (nmol)	12.46	141.31
Difference (nmol/1 mg MSN)	0.78	90.35
Loading efficiency (nmol loaded /nmol loading solution)	5.6%	3.9%
Loading capacity (mg cGAMP/mg MSN)	0.05%	6.1%

Figure 7.5 Mass spectrometry determination of cGAMP loading into nanoparticles.

Polyethyleneimine-coated mesoporous silica nanoparticles have been used previously to protect and deliver siRNA *in vivo*.[63] A variety of polymer chain lengths were screened before the 1.8 kD PEI was found to be the least toxic and most effective carrier. Here MCM-41 type mesoporous silica nanoparticles are phosphonated and then electrostatically coated with 1.8kD branched PEI (PEI-MSN). cGAMP is then loaded into the polymer shell of the nanoparticles (cGAMP@PEI-MSN). The loading capacity of the nanoparticles is determined by LC-MS of the loading solution before and after addition of the nanoparticles. In Figure 7.5, high loading concentrations have 1.7% lower loading efficiency, but show much higher cGAMP loading per particle.

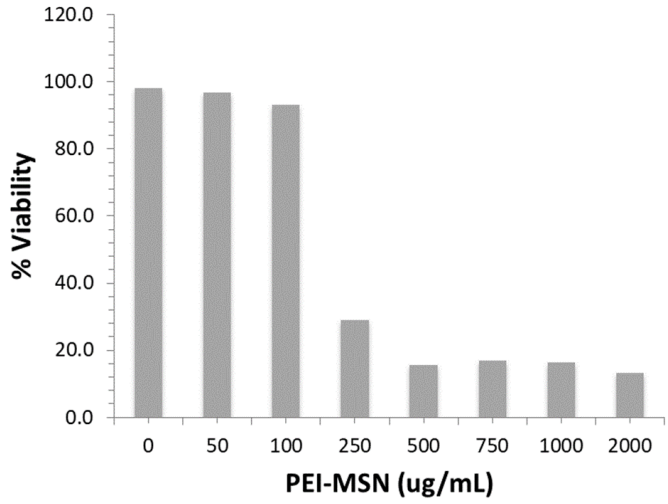

Figure 7.6 Toxicity of PEI-MSN. Trypan blue staining to determine viability of cells treated with bare PEI-MSN (without cGAMP).

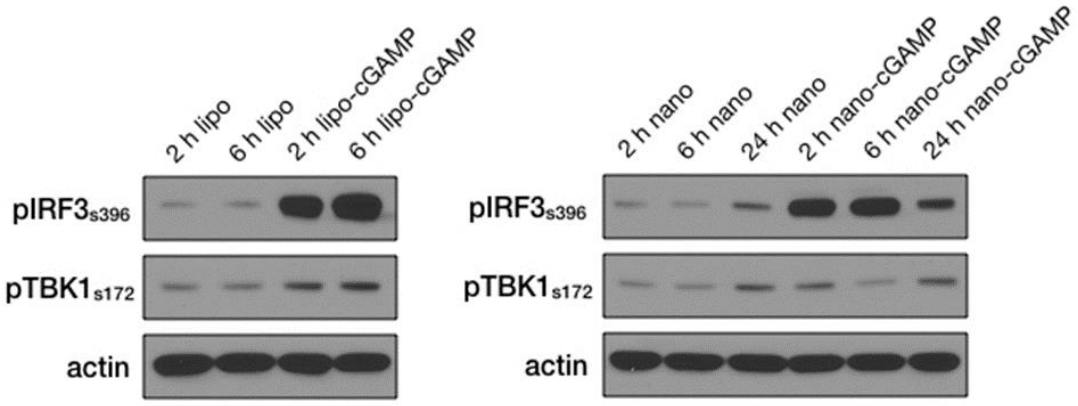

Figure 7.7 Western Blot markers of STING expression following treatment of Lipofectamine-loaded cGAMP (lipo-cGAMP) or cGAMP@PEI-MSN (nano-cGAMP) after 2, 6, and 24 hours treatment. Actin is used as a loading control. *Note: 4X lower concentration of cGAMP is used in the nanoparticle treatment condition.

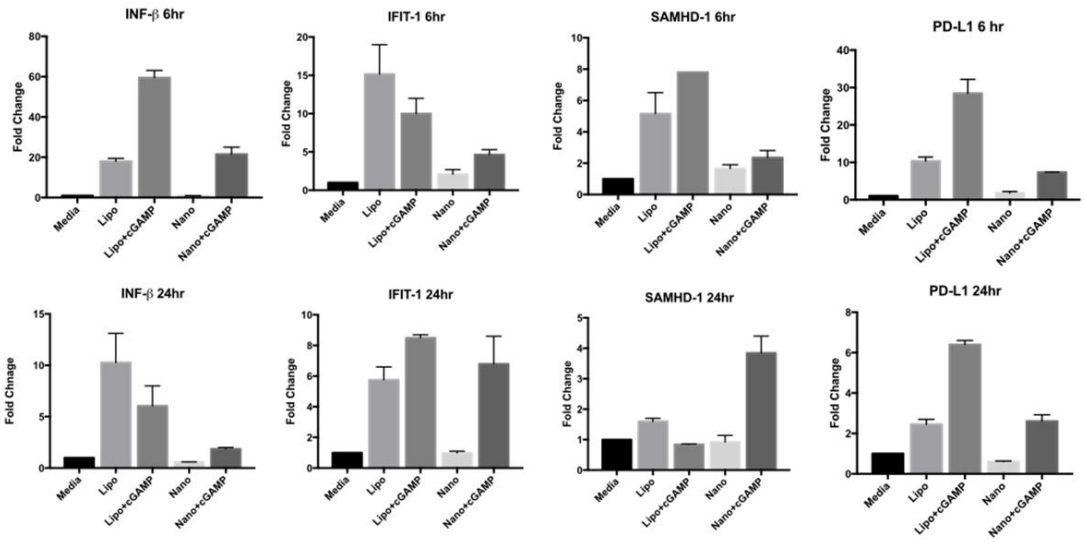

Figure 7.8 cGAMP stimulation of INF-β, IFIT-1, SAMHD-1, PD-L1 gene expression following Lipofectamine-loaded cGAMP ([cGAMP]=25 ug/mL) or cGAMP@PEI-MSN treatment ([cGAMP]=6.5 ug/mL).

*Note: 4X lower concentration of cGAMP is used in the nanoparticle treatment condition.

Hs766t PDAC cells, which have high STING expression, are used as a model cell line for these studies. The toxicity of bare PEI-MSN are tested to find the maximum concentration that can be used in cell culture (Figure 7.6). We find that particles are safe below 100 ug/mL. Cells are treated with cGAMP@PEI-MSN or 4X cGAMP prepared with Lipofectamine transfection reagent. Western Blot of cell lysates show pIRF3 and pTBK1, markers of STING expression, following treatment of Lipofectamine-loaded cGAMP (4X) or cGAMP@PEI-MSN (1X) by 2 hours after treatment (Figure 7.7). cGAMP stimulation of INF-b, IFIT-1, SAMHD-1, PD-L1 gene expression following Lipofectamine-loaded cGAMP (4X), cGAMP@PEI-MSN (1X), PEI-MSN, or Lipofectamine treatment controls show that the nanoparticle treatment has much less toxicity than the lipofectamine carrier and outperforms the lipo-cGAMP treatment even with four times less drug (Figure 7.8). The nanoparticle cGAMP treatment induces 20-fold increase in INF-

B production after 6 hours treatment and 3 fold more SAMHD1 induction than the lipo-cGAMP treatment at 24 hours (Figure 7.8), with less total cGAMP than the lipofectamine-cGAMP treatment.

7.4 Conclusions

We successfully synthesize PEI polymer-coated mesoporous silica nanoparticles loaded with 2'3'-cGAMP. *In vitro* experiments in *Hs766t* cells show that the nanoparticle carrier is much less toxic than the Lipofectamine carrier. Western blot of pTBK1 and pIRF3 and RT-PCR experiments show that nanoparticle-loaded cGAMP is more potent inducer of the STING pathway. Further studies are required to determine their efficacy *in vivo*. Immunohistology staining has shown that STING is expressed in cancer cells and stroma of patient-derived pancreatic tumors, however it is poorly expressed in normal pancreas cells.[59,62] Mesoporous silica nanoparticles have been shown to accumulate in tumors and can be chemically modified with ligands such as folate that can increase tumor uptake.[55] STING-dependent Type I INF induction with cGAMP@PEI-MSN has the potential to improve radiotherapy treatments of solid tumors or treat viral infections.

7.5 Materials and Methods

LC-MS/MS

20 µM 2'3'-cGAMP samples (triplicates) are made in RPMI media (10% FBS). Samples are incubated for 0 hours or 24 hours at 37°C, 5% CO_2.

PEI-MSN preparation and 2'3'-cGAMP loading

Phosphonated MSN (P-MSN) are prepared as previously described.[63] 2 mg P-MSN are washed in ethanol. 2.5 mg 1.8kD PEI (branched, Alfa Aesar) is dissolved in 1 mL of ethanol. 200 µL of this PEI stock solution is added to P-MSN and particles are placed on a rotator for 30 minutes. MSN are centrifuged down and washed with ethanol. 200 µL of the PEI stock is added for the second coat and particles are placed on rotator again. After 30 min, particles are washed with ethanol once and with water thrice. cGAMP loading solution is then added and particles are placed on rotator for loading for 2 days. After 2 days, particles are centrifuged down and washed with water to remove residual cGAMP.

Western blot and RT-PCR

Hs766t cells are plated in 24 well plates for 16 hours. Fresh media is added and wells are treated with one of the following: 4x Lipofectamine control (20 µL lipo2000 + 55 µL optimem), 4x Lipofectamine-cGAMP (25 µL cGAMP (1mg/mL) + 20uL lipo2000 + 55 µL optimem), [final cGAMP]= 25 ug/mL, 1x PEI-MSN (100 µg MSN/mL), 1x cGAMP@PEI-MSN (100 µg MSN/mL), [final cGAMP]= 6.5 ug/mL. After 2, 6, or 24 hours, cells are collected for RT-PCR and protein lysate is collected using RIPA buffer for Western Blot.

8 Synthesis and imaging of porous alumina nanoparticles—a new drug delivery vehicle

8.1 Abstract

Synthesis of porous alumina nanoparticles usually requires high temperature techniques such as spray pyrolysis. Here, we synthesize mesoporous alumina nanoparticles using a simple sol-gel method with excess surfactant to prevent densification during calcination. Particles characterized by transmission electron microscopy and dynamic light scattering reveal average sizes of 200 nm. X-ray photoelectron spectroscopy measurements are used to look at their surface properties, and zeta potential measurements reveal they are positively charged across a broad pH range due to surface waters and protonation of hydroxyls on the surface. X-ray diffraction measurements and FT-IR show the nanoparticles have amorphous boehmite-type structure, and nitrogen sorption measurements show nanoparticles have surface areas as high as 200 m^2/g with average pore sizes of 3 nm.

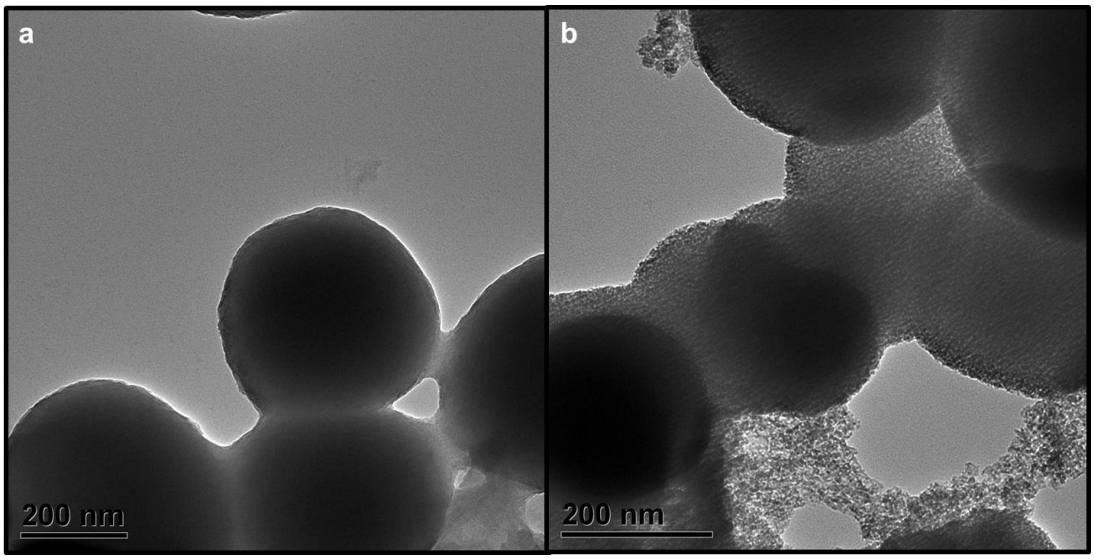

Figure 8.1 (a) TEM images of alumina nanoparticles after P123 extraction with multiple water and hot EtOH washes (before calcination). (b) Complete removal of P123 and CTAB surfactant after calcination at 550 ^{o}C for 5 hours maintains integrity of porous nanoparticles.

8.2 Introduction

Aluminum oxide nanoparticles are a potentially useful new drug delivery vehicle. Alum, a mostly amorphous heterogeneous collection of aluminum oxyhydroxide structures has been used since the 1920s, however the composition and fundamental mechanism of action is not completely understood. Nanoparticles have the potential to be used as adjuvants due to their high surface area, easily tunable surface properties, and well characterized structural properties. Alumina nanoparticles of various shapes have been successfully used as adjuvants in murine OVA immunization models. Surface properties of aluminum oxide nanoparticles that induce immune responses are not fully understood, however higher surface areas and the presence of more oxyhydroxide moieties on the surface correlate with better adjuvant properties. In particular, Sun et. al. show that shape, crystallinity, and hydroxyl content affect antigen-specific immune responses.[64] Here, we develop a facile sol-gel approach to make porous aluminum oxide that have the potential

as a new drug delivery vehicle. These porous nanoparticles have high surface areas and oxyhydroxide surface structures.

Due to the fast hydrolysis and uncontrolled polymerization of aluminum alkoxides, synthesizing discrete porous alumina nanoparticles using sol gel methods has been a challenge. However, mesoporous alumina nanoparticles have been synthesized using other techniques such as spray pyrolysis of an aluminum nitrate precursor with a block copolymer surfactant. However, spray pyrolysis techniques require complex procedures and equipment, and are difficult in scale up.

The fabrication of monodisperse, non-aggregated porous aluminum oxide spheres remains a challenge in sol gel. Templated approaches have used spherical templates such as polystyrene spheres to make metal oxide nanoparticles such at TiO_2, ZrO_2, SnO_2, and CeO_2 however these templated approaches did not work for Al_2O_3 due to what is thought to be densification of alumina particles during the calcination step.[65] Pluronic surfactant P123 has been used with aluminum isopropoxide by Somorjai et al. to synthesize mesoporous alumina films using a sol gel method. Here we use a facile sol-gel synthesis using two different types of surfactants, at concentrations above their CMC in ethanol. Excess surfactant was used to prevent the densification of spheres during the calcination process. Slow temperature ramp at 1^oC/min was used to prevent sudden structural changes.

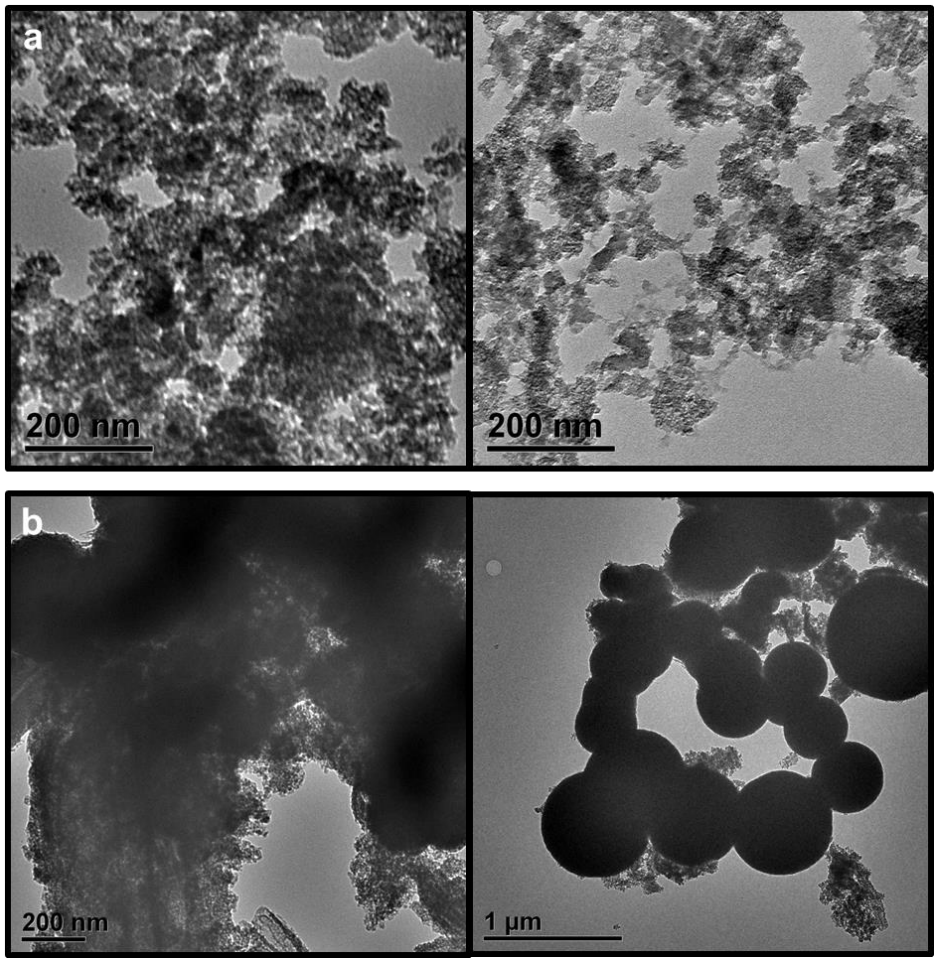

Figure 8.2 (a) TEM images of alumina nanoparticles synthesized with stirring during condensation step (b) increasing ramp rate to 5°C/min results in fusion of particles and asymmetric particle shapes

8.3 Results and Discussion

Formation of porous aluminum oxide nanoparticles

Formation of aluminum oxide from alkoxide precursors involves a two-step process: hydrolysis or alcoholysis of the alkoxide and condensation with neighboring molecules to form the metal oxide framework. Hydrolysis or alycoholysis occurs via

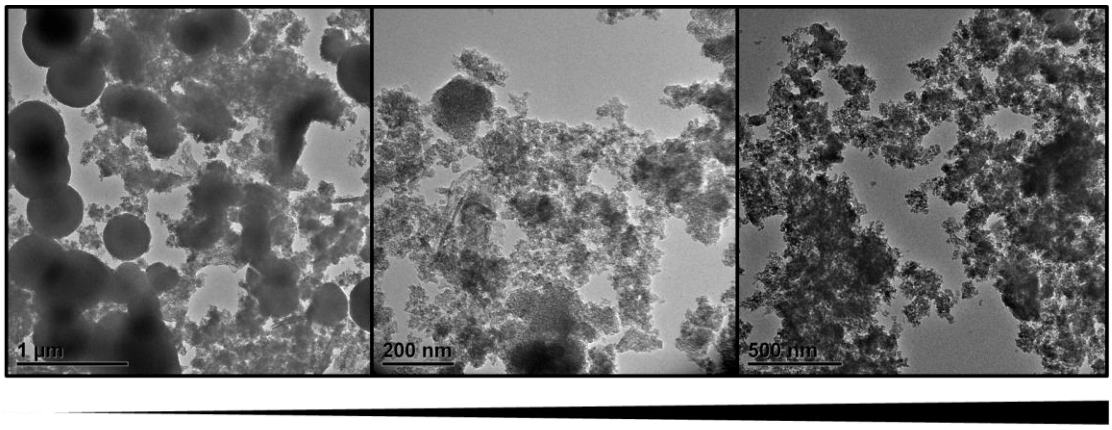

Figure 8.3 TEM images of alumina nanoparticles after addition of increasing amounts of HACAC

nucleophilic attack by either water or hydroxyl groups on the central metal, and the partial charge model suggests that electronegativity differences can be used to estimate stability and reactivity of alkoxides.[66] Silicon oxides can be made easily using sol-gel methods and silica nanoparticles of various sizes and porosity have been thoroughly studied. Since aluminum alkoxides have lower electronegativity than silicon alkoxides, where catalysts are used to enhance hydrolysis and condensation, aluminum alkoxides usually require additives to slow down sol-gel reactions. On the other hand, fast nucleation and slow growth is usually required in sol-gel preparation of monodisperse ordered porous nanoparticles. In order to understand how these properties affect formation of porous aluminum oxide nanoparticles, we did a series of syntheses with different alkoxide precursors and aluminum ligands that tune growth rate of the nanoparticles.

Formation of aluminum oxide from aluminum isopropoxide precursor involves hydrolysis of the alkoxide using a strong acid and condensation at higher temperatures to facilitate formation of the aluminum oxide network.[67] Using a combination of P123 and CTAB with aluminum isopropoxide we direct the formation of spherical particles, where we propose that CTAB stabilizes the nano-sized alumina particles and P123 prevents aggregation and densification of pores during calcination.

The effects of replacing ligands on alkoxide precursors is complicated and can affect a multitude of properties, not just the rate of the hydrolysis/condensation

a

Element	% composition
N	none
C	0.61± 0.01
H	0.88 ± 0.1
Br	1.27 ± 0.04
*O	11.6 ± 0.3
**Ash (Al_2O_3)	87.4

b

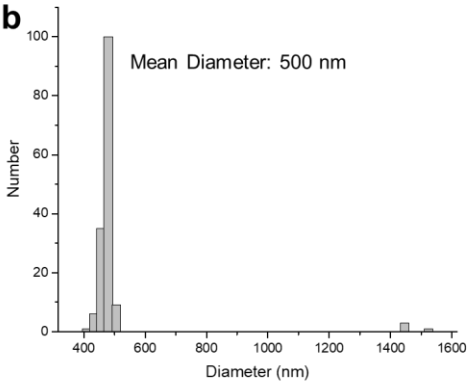

c

	Average zeta potential (mV)
H_2O	+24.0
pH=3	+41.3

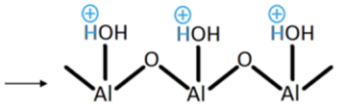

Figure 8.4 (a) Elemental analysis of aluminum oxide nanoparticles confirms >98% extraction efficiency of templating agents. Results are an average of two trials, *Oxygen bound to Al only partially shows up, **Ash is incombustible, inorganic material. This was a white sandy material left over after combustion at 1000°C under oxygen. (b) DLS data of particle size distributions of alumina nanoparticles. (c) Zeta potential measurements show particles are positively charged and can become even more charged at lower pHs as surface hydroxyl groups get protonated.

but could also affect the formation of clusters, the number of sites for hydrolysis, or have stereochemical effects by directing hydrolysis and condensation to particular sites. Aluminum isopropoxide in the synthesis produced discrete spherical nanoparticles. Acetylacetone is commonly used with high nucleophilic titanium alkoxides to substitute alkoxide ligands and slow down sol-gel reactions. While titanium is much more nucleophilic than aluminum, we added acetylacetone to the hydrolysis step and found that acetyl acetone slowed the reaction and formed small heterogeneous particles rather than spherical nanoparticles. We suspect slowing the reaction prevented quick nucleation required for spherical nanoparticles. Introducing acetylacetone during the hydrolysis or condensation

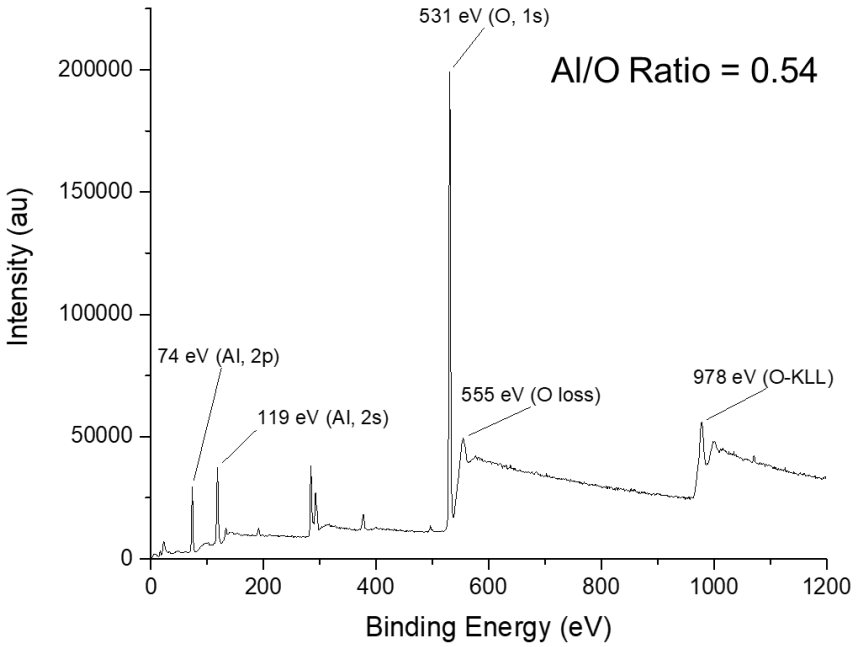

	Binding Energy	Atomic %
Al 2p	73.9	35.1
O 1s	531.1	64.9

Figure 8.5 XPS of alumina nanoparticles

steps did not produce spherical particles, but instead formed heterogeneous nanoparticulates.

Replacement of the aluminum isopropoxide with the faster-hydrolyzing aluminum chloride precursor resulted in the formation of sheets, indicating that structure directing properties of the aluminum precursor are important as well. We find that fast nucleation during the condensation step is required to form spherical particles. However, if is growth is too fast, as in the case of the chloride precursor, we get sheets or large non-spherical particulates. In order to maintain the porosity of the nanoparticles during removal of surfactant during calcination, low ramp rate of 1oC/min is used. High surfactant concentration and low ramp rate successfully prevented densification of the synthesized mesoporous aluminum oxide spheres. The BET surface area of our synthesized aluminum oxide particles is 193 m^2/g.

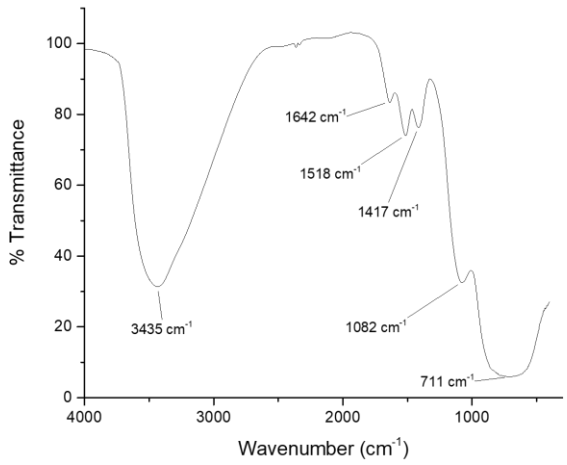

Figure 8.6 FTIR of aluminum oxide nanoparticles.

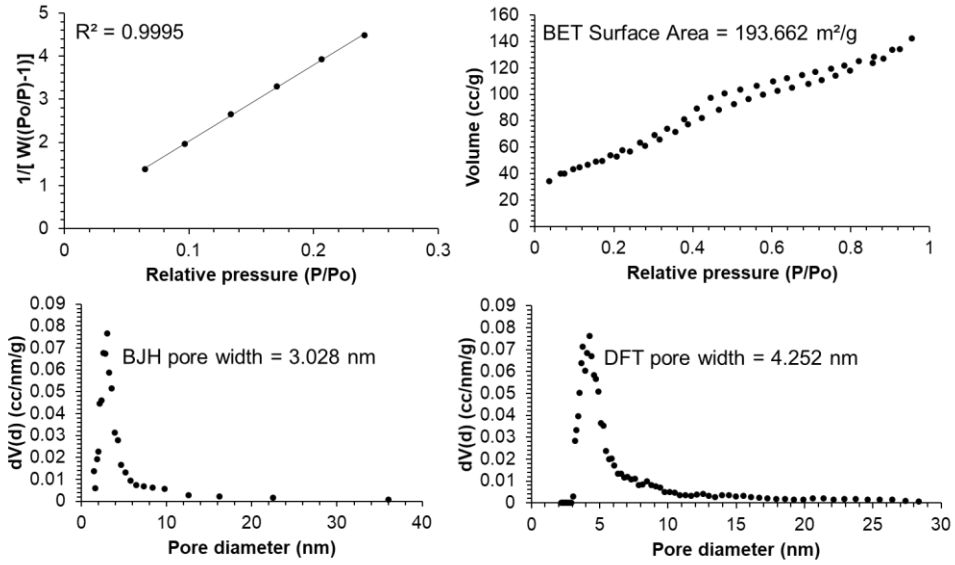

Figure 8.7 N_2 sorption measurements of porous alumina samples. (a) standard curve, (b) N_2 adsorption/desorption isotherm and surface area calculated using BET, (c) pore diameter calculations using BJH method, and (d) pore diameter calculations using DFT method

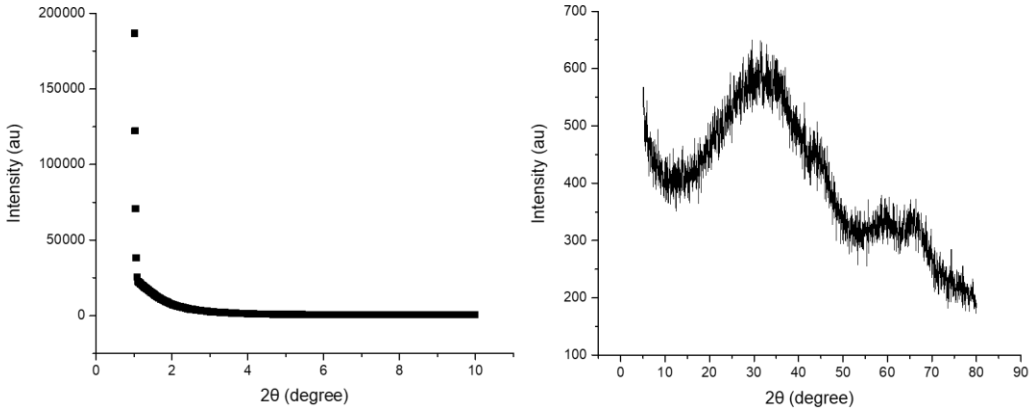

Figure 8.8 Low angle (a) and high angle (b) XRD of alumina nanoparticles

Somorjai et. al. have reported mesoporous aluminum oxide sheets with surface areas as high as 400 m^2/g.

Structural properties

Due to the high concentration of surfactants used, elemental analysis was used to confirm the complete removal of surfactant by calcination. X-ray patterns of the final calcined alumina nanoparticles show that the structure is amorphous and matches observed spectra for boehmite AlO(OH).[68] From low angle XRD measurements, there is no discernable ordered pore structure (Figure 8.8). Previous work has shown that addition of a bis-2-ethylhxyl sulfosuccinate surfactant before or during hydrolysis of the alkoxide precursor prevents grain growth of the boehmite by absorbing on the surface-forming clusters.[68] This results in an amorphous porous hydroxide structure by XRD. We suspect that in our synthesis, high concentration of surfactant added during the condensation step works with a similar mechanism i.e. grain growth of alumina is inhibited by the presence of so many surface active agents, resulting in disordered amorphous surface structure and small nano-particle size. TEM shows that particles range from 300-500 nm and the average hydrodynamic radius determined by DLS is 500 nm in water.

FT-IR of boehmite AlO(OH) usually show a broad band between 3300-3500 cm^{-1} characteristic of –OH stretching vibration from hydrogen bonding in the Al-OH matrix with water molecules. We observe this stretching mode, as well as a peak 1635 cm^{-1} is assigned to the bending mode of water molecules in the boehmite

structure based on previous work.[69–72] There is a broad stretch between 500-1000 cm^{-1} for the Al-O-Al stretch. At 1082 cm^{-1} there is a primary alcohol C-O stretch as well as -OH bending at 1417cm^{-1} from residual EtOH that the nanoparticles were stored in

8.4 Conclusions

Here, a facile sol-gel synthesis of high surface area mesoporous aluminum oxide nanoparticles with boehmite structure are reported. Usually, controlling the hydrolysis and condensation of aluminum alkoxide precursors is difficult. However, the addition of high concentrations of CTAB and P123 with the isopropoxide precursor produce discrete particles. To our knowledge, highly disperse uniform porous aluminum oxide has not been reported using simple sol gel procedures. Due to the simplicity of our method and high porosity of the nanoparticles, they have the potential to be used as adjuvants for immunotherapies or as catalysts.

8.5 Materials and Methods

Chemicals

Aluminum isopropoxide ($Al(OC_3H_7)_3$, Aldrich, >98%), Cetyl trimethylammonium bromide (CTAB, Sigma, >99%), Pluronic P123 (O-BASF), Nitric acid (Fisher, 67-70%), Ethanol (KOPTEC, anhydrous, 200 proof), Acetylacetone (Sigma, ≥99.3%), Aluminum (III) chloride (TCI, >98%).

Synthesis of aluminum oxide nanoparticles

10 mL ethanol is added to 4.075 g aluminum isopropoxide in a 20 mL glass vial. While stirring, 3.2 mL nitric acid is added dropwise, and the solution is capped and stirred for 24 hours. In another glass vial, 0.250 g CTAB, 2.0 g P123, and 5 mL ethanol are stirred well for 24 hours. After 24 hours, 300 µL of the aluminum precursor solution is added to the surfactant vial and stirred for 24 hours at room temperature. The sample is evaporated slowly at 45°C for 2 days, then at 65°C for 2 days to remove remaining ethanol before calcination. After drying, the sample (sticky solid) is transferred to a crucible and calcined at 550°C for 8 hours at 1°C/min ramp rate. Resulting particles can be dispersed in a solvent such as water or ethanol.

Elemental analysis

Elemental analysis was carried out by Midwest Microlab.

X-ray diffraction measurements

X-ray diffraction measurements are taken with calcined powdered sample using a Panalytical X'Pert Pro Powder X-ray Diffractometer.

Transmission electron microscopy

Samples were suspended in ethanol and dropped on a 200 mesh carbon coated copper grid. The ethanol is evaporated at room temperature. Images were recorded on a Tecnai T12 Quick CryoEM and CryoET (FEI) at an accelerating voltage of 120 kV.

Nitrogen sorption measurements

Samples were outgassed at 220^{o}C for 12 hours, and then nitrogen adsorption and desorption isotherms were taken at 77 K using an Autosorb-iQ (Quantachrome Instruments). An NLDFT equilibrium model of N_2 on silica was used to calculate pore size distribution and pore volume. Brunauer–Emmett–Teller model was used to calculate surface areas between partial pressures of 0.08-0.2 p/p0.

Zeta-potential analysis and dynamic light scattering

All DLS measurements were carried out on a ZetaSizer Nano (Malvern Instruments). Nanoparticles were suspended at concentrations of 0.4 mg NP/mL solvent.

8.6 Supplemental information

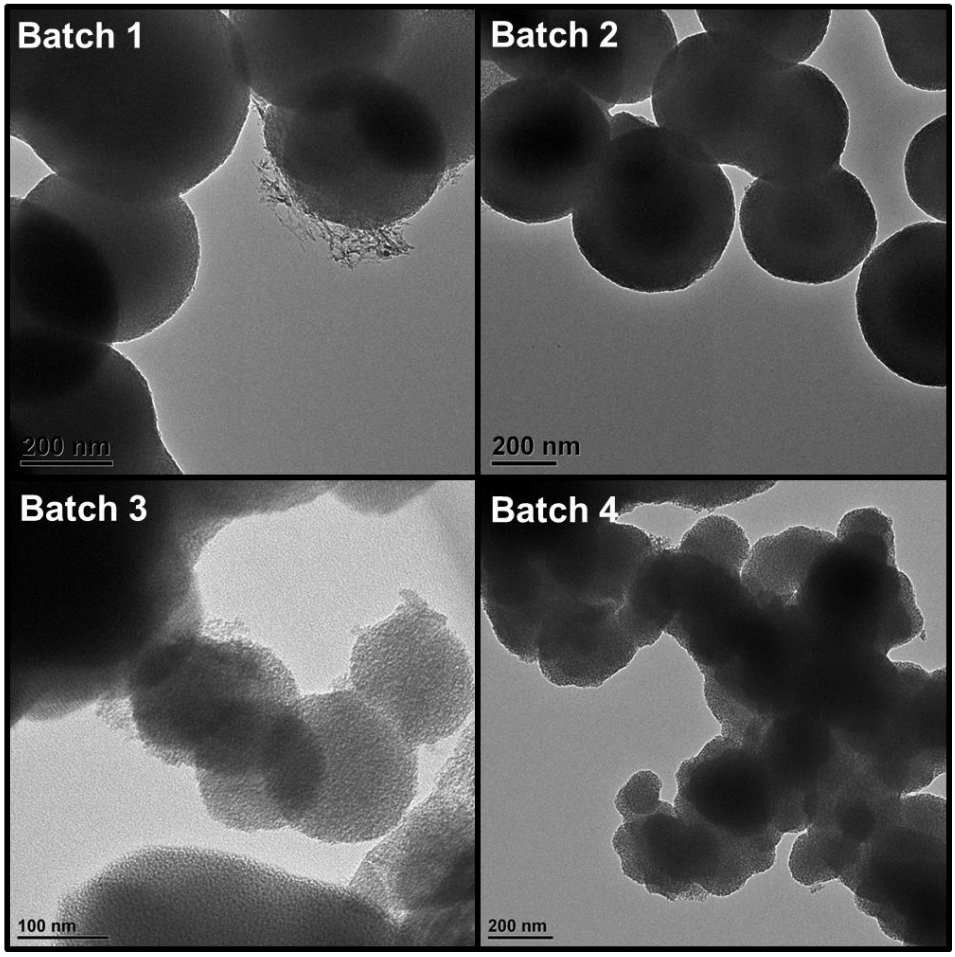

Figure S8.9 Mesoporous alumina nanoparticles synthesis and reproducibility. TEM images of alumina nanoparticles from four different batches show some batch to batch variation dependent on water content in the sample.

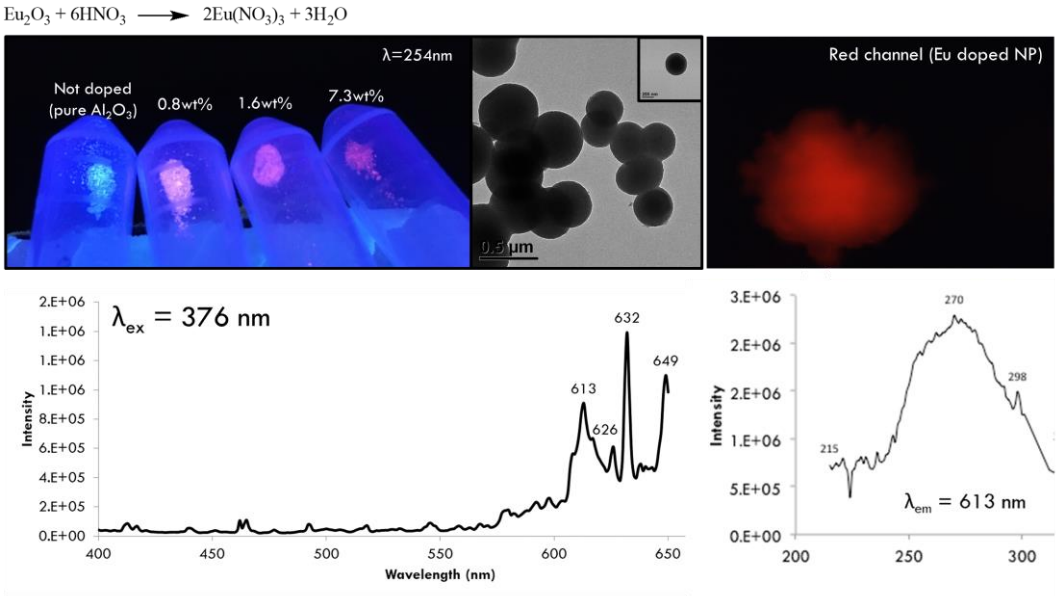

Figure S8.10 Aluminum oxide nanoparticles doped with europium. (a) Europium content in alumina nanoparticles measured by ICP-OES, where wt% Eu = mass Eu/total NP mass. (b) TEM of Eu-doped alumina. (c) DAPI channel (excitation = 340-380 nm) used to image Eu-doped alumina. (d) Excitation spectrum at 376 nm and (e) 270 nm emission peak at 613 nm excitation

8.7 Acknowledgements

Thank you to Kristopher Marsh for XPS measurements.

9 Spectrochemical assays to understand structure-activity relationships of anticancer drug Triapine and its analogs

This section is based on the article "Sheba Plamthottam, Daniel Sun, Juno Van Valkenburgh, Jeffrey Valenzuela, Bastian Ruehle, Dalton Steele, Soumya Poddar, Selena Hernandez, Caius Gabriel Radu, and Jeffrey I. Zink. Spectrochemical Assays to Understand Structure-Activity Relationships of Anticancer Drug Triapine and its Analogs" submitted for review in 2018.

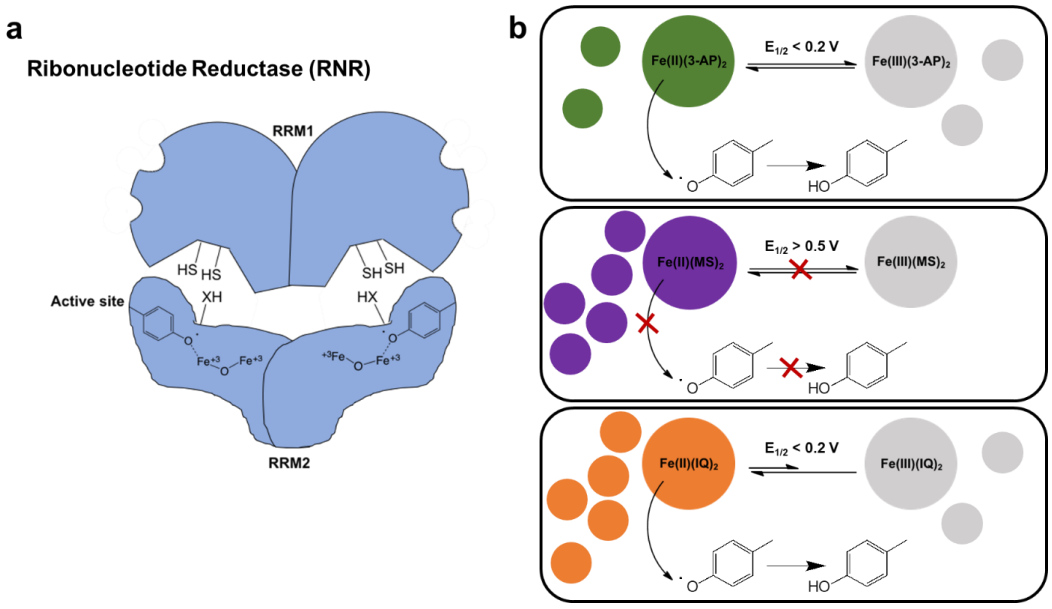

Figure 9.1 (a) The catalytic subunit, RRM2, of human Ribonucleotide Reductase (RNR), which contains a stabilized tyrosyl radical in the active site, and (b) the proposed mechanism of Group I, II, and III analog inhibition of RNR. The reduction potential, $E_{1/2}$, is expressed vs. NHE.

9.1 Abstract

Triapine (3-AP), a drug that is currently undergoing a Phase II clinical trial in the US, is an inhibitor of human ribonucleotide reductase (RNR), a rate-limiting enzyme in the *de novo* pathway of deoxyribonucleotide triphosphates (dNTPs) biosynthesis. Inhibition of RNR by 3-AP results in the depletion of dNTP precursors of DNA, thereby selectively starving fast-replicating cancer cells of nucleotides for survival. The active form of 3-AP directly responsible for inhibition of RNR is the Fe(II)(3-AP)$_2$ complex. In this work, we investigate the structure-activity relationship of 3-AP analogs based on the electronic properties of their iron complexes. Surprisingly, isoquinoline analogs of 3-AP favor the maintenance of the biologically active iron(II) complex, while still being able to redox cycle. UV-Vis analyses show that these analogs have strong pi-accepting character, change the ligand field strength, stabilize the low-spin iron(II) state, and in turn improve the potency of RNR inhibition *in vitro*. In contrast, methylation on the thiosemicarbazide secondary amine moiety of 3-AP produces analogs with much higher redox potentials that do not redox cycle and are found to be inactive against RNR *in vitro.*

9.2 Introduction

Ribonucleotide reductases are a unique class of interesting enzymes known for their unusual free radical mechanism of action. These enzymes reduce ribonucleotides to deoxyribonucleotides, a process essential for DNA replication and repair.[73–75] Inhibitors of RNR are potential drug targets through a mechanism by which they cause nearly complete depletion of dNTP pools, thereby selectively starving fast-replicating cancer cells of nucleotides required for DNA synthesis and replication.[76,77] Specifically, this has been shown with the Phase II clinical trial drug Triapine, also known as 3-AP (3-aminopyridine-2-carboxaldehyde thiosemicarbazone), a potent RNR inhibitor.[78–85] 3-AP used in combination therapies to treat acute lymphoblastic leukemia has been shown to trigger lethal replication stress *in vivo* and lead to long-term disease-free survival in mice with acute lymphoblastic leukemia (ALL) without detectable toxicity.[77]

Despite its great potential, the mechanism of 3-AP inhibition on RNR is still not completely known.[14,86] Human RNR is composed of two subunits, RRM1 (α_2), the site of nucleotide reduction, and RRM2 (β_2), where a diferric tyrosyl radical

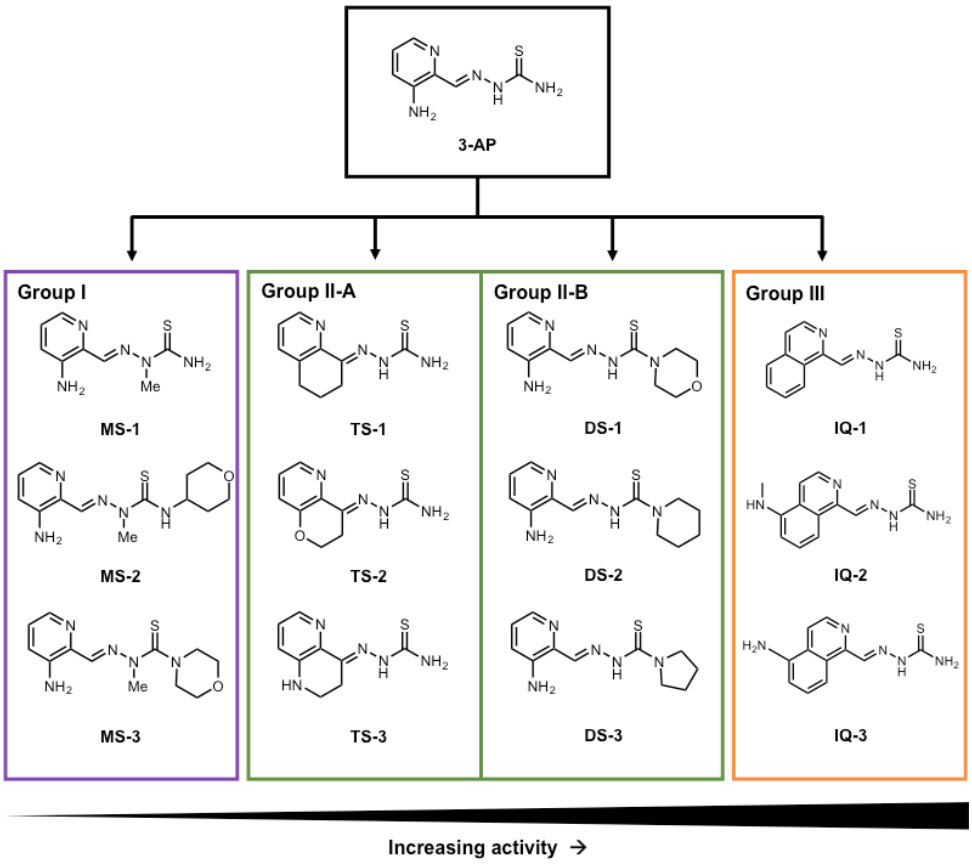

Figure 9.2 Structures of synthesized 3-AP analogs.

cofactor resides (Figure 9.1a).[14,74] In 2012, *Aye et. al.* used EPR to show that the primary mode of RNR inhibition is donation of an electron by the reduced iron complex of 3-AP, directly quenching the tyrosyl radical on the β_2 subunit. Formation of the Fe(II)(3-AP)$_2$ complex is essential for the inhibitory effect of the drug 3-AP, while the Fe(III) complex of 3-AP is inactive.[14] The inhibition of RNR by the reduced Fe(II) complex of 3-AP suggests a new avenue to improve current RNR inhibitors by stabilizing the Fe(II) form.

In this work, 3-AP drug analogs are made in-house, and using spectroscopic methods, we investigate the binding affinity of the synthesized analogs to iron(II), the effect of pH on the half-life of the active Fe(II) complexes, the oxidation rates of the analog complexes, as well as use electrochemical studies to determine their redox potentials. These findings help to design more potent 3-AP analogs based on an understanding of the electronic structure of their iron complexes.

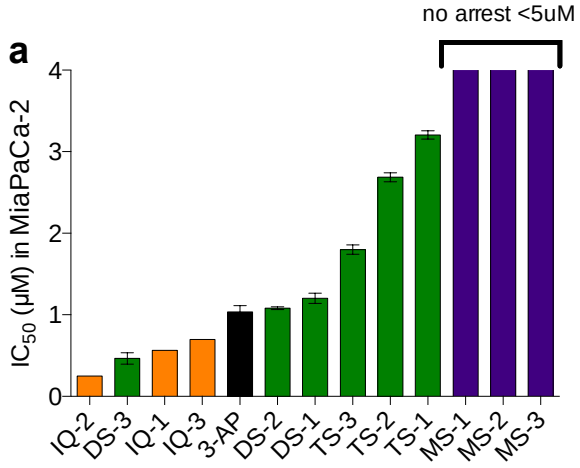

b

Drug	Minimum [drug] for S-phase arrest (uM)
IQ-1	0.25
DS-3	0.25
IQ-2	0.50
3-AP	0.50
DS-1	0.75
DS-2	0.75
IQ-3	1.50
TS-3	1.86
TS-2	3.75
TS-1	5.00
MS-1	No arrest (>5uM)
MS-2	No arrest (>5uM)
MS-3	No arrest (>5uM)

Figure 9.3 (a) IC_{50} of 3-AP analogs in *MIA PaCa-2* PDAC cells. (b) Concentration at which S-phase arrest is induced (increase in population of S-phase cells by 20%) in MIAPaCa-2 cells by 3-AP analogs, determined by flow cytometry.

9.3 Results and Discussion

Structure of ligands and biological activity. 3-AP is a potent and fast-acting RNR inhibitor *in vitro*.[87–89] Treatment of cells by 3-AP inhibits conversion of ribonucleotide diphosphates to deoxyribonucleotides diphosphates, thereby inhibiting DNA synthesis. S-phase arrest is a characteristic phenotype of cells treated with 3-AP.[77] The three classes of 3-AP analogs in Figure 9.2 are grouped by their structure and biological activity. IC_{50} values (Figure 9.3a) and S-phase arrest (Figure 9.3b) of the analogs in *MIA PaCa-2* PDAC cells are determined after 72h and 24h treatment, respectively. Group I compounds are all methylated on the secondary amine and show no RNR-specific activity. All the analogs except for the Group I compounds induce S-phase arrest in the concentration range of 250 nM to 5 μM. Group II compounds are the most structurally similar to 3-AP, and their iron complexes, as will be shown later, are the most spectroscopically similar to 3-AP with non-aromatic modifications made either on the left or the right side of the scaffold. Group II-A compounds have non-aromatic substituents on the pyridine

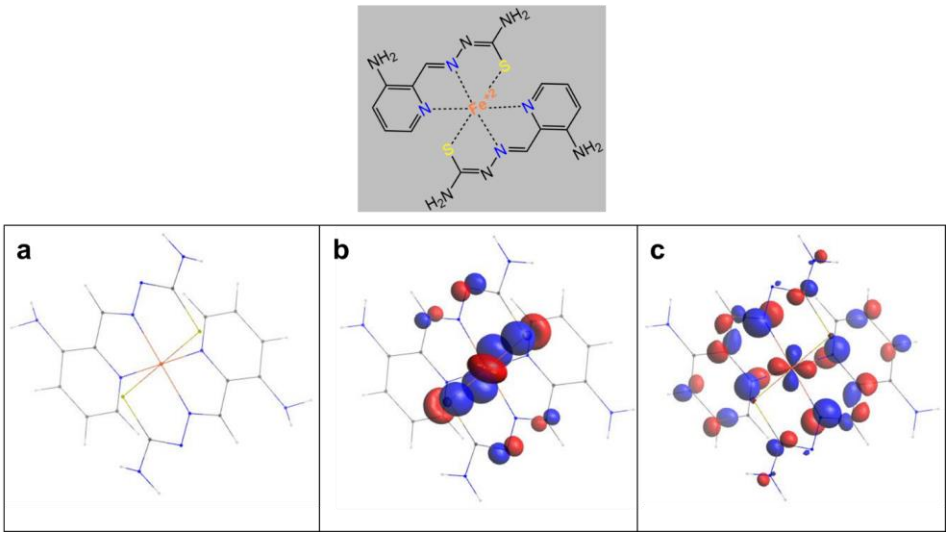

Figure 9.4 (a) Optimized geometry from DFT calculations of the Fe(II)(3-AP)$_2$ octahedral complex starting from a previously published crystal structure.[90] (b) Calculated HOMO and (c) LUMO orbitals of Fe(II)(3-AP)$_2$ complex.

ring (TS-1, TS-2, and TS-3), while Group II-B compounds have substituents to the primary amine part of the semicarbazone moiety (DS-1, DS-2, and DS-3). Group II-B compounds have similar IC_{50} values to 3-AP (1 μM), with DS-3 (470 nM) being slightly more potent than 3-AP, while Group II-A compounds are all less potent (IC_{50} values 1.7-3 μM). In Group III compounds, the pyridine ring of 3-AP was replaced with isoquinolines (IQ-1, IQ-2, and IQ-3). Group III compounds inhibit cell proliferation at similar or lower concentrations (250 nM-0.7 μM), with IQ-2 being four-fold more potent than 3-AP (250 nM). As will be discussed later, each class of compounds forms iron complexes with unique UV-Vis spectral and redox properties. In addition, their iron complexes share some spectral commonalities by UV-Vis that allow to develop spectroscopic assays to probe activity of the biologically active iron complex.

Iron binding affinities of 3-AP analogs. To test whether increased biological activity is attributed to an increased binding affinity of the ligand to the metal, relative binding constants of the synthesized analogs to Fe(II) were calculated. 3-AP is a strong iron chelator, binding to both Fe^{2+} and Fe^{3+}, and readily forms the

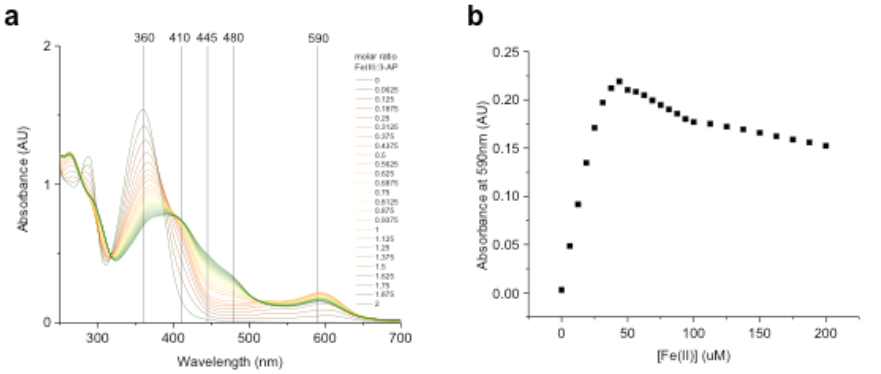

Fe(II) Complex	Relative K_a	R_2 Value
DS-1	1.8 x 10^4	0.9800
3-AP	2.6 x 10^4	0.9637
DS-2	2.8 x 10^4	0.9628
TS-2	2.9 x 10^4	0.9917
IQ-3	3.0 x 10^4	0.9345
IQ-1	3.1 x 10^4	0.9787
IQ-2	3.4 x 10^4	0.9587
TS-1	3.9 x 10^4	0.9894
DS-3	4.1 x 10^4	0.9682
MS-3	4.1 x 10^4	0.9477
MS-2	5.3 x 10^4	0.9713
MS-1	5.9 x 10^4	0.9726
TS-3	n/a	<0.5

Figure 9.5 Example calculation with the 3-AP ligand for determining the relative binding contants (K_a) of 3-AP analogs to Fe(II). (a) 3-AP is titrated under argon with Fe(II) to form the 2:1 (3-AP:Fe) species. (b) $\varepsilon_{complex}$ is determined from the maximum absorbance of the lowest energy charge transfer peak. (c) K_a is determined from the initial points of the titration. (d) Summary of the relative K_a values of the 3-AP analog iron(II) complexes.

octahedral bis-complex, $Fe(3\text{-}AP)_2$ (Figure 9.4a).[14,90] Formation of the redox-active bis-iron(II) complex is essential for the biological activity of the complex.[14] To determine relative K_a values for the 3-AP analogs, we developed a UV-Vis spectroscopic Fe(II) binding assay and found that maintaining the N-N-S thiosemicarbazone moiety allows sufficient binding of Fe(II) to all the drug analogs on the order of 10^4 (Figure 9.5). Relative K_a values for the compounds are close in value, and as such there are no obvious trends with iron binding strength and *in vitro* activity of Group I, II, and III analogs.

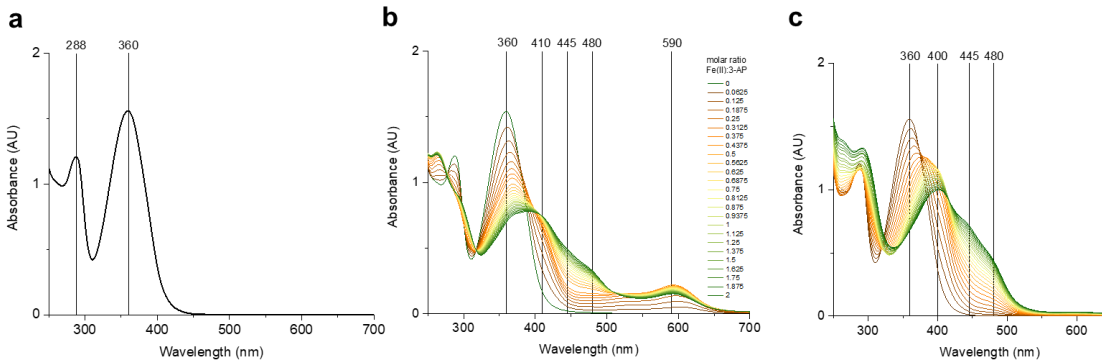

Figure 9.6 3-AP free ligand in water (a), 3-AP titrated with Fe(II) (b), and 3-AP titrated with Fe(III) (c) to form the bis-complex.

Absorption spectra. UV-Vis spectroscopic binding assays show that Fe(II) binding affinities on the order of 10^4 are sufficient for activity, and that small relative changes in Fe(II) binding affinity of the ligands did not explain the improved potency of the synthesized analogs. However, changes in the spectra of the iron complexes in the iron-binding assay revealed interesting properties based on the ligands that were used. 3-AP and analogs that contain the pyridine ring display two absorption bands in the in the UV between 260 and 450 nm corresponding to n→pi* and pi→pi*transitions (Figure 9.6 and Figure S9.11). Their iron(II) and iron(III) complexes have distinct absorbances. Upon complexation with Fe(II) and Fe(III), the 3-AP complexes display peaks in the 400-500 nm region characteristic of charge transfers, while only the Fe(II) complexes display metal-to-ligand charge transfer transitions (MLCT) in the visible region between 590-630 nm (Figure 9.6b). These lowest energy bands are very intense with molar absorptivities on the order of 3000-9000 M^{-1} (Figure 9.7b) and were thus assigned to be charge transfer transitions in the reduced complex. The wavelength of the lowest energy metal-to-ligand charge transfer transitions are characteristic to each class of compounds, where complexes of Group I compounds are blue-shifted while that of the Group III compounds are red-shifted relative to 3-AP (Figure 9.7a). DFT calculations support that the iron(II) complexes undergo MLCT. The HOMO of the 3-AP iron(II) complex shows strong pi antibonding interactions with d-orbitals of the iron center (Figure 9.4b). The LUMO has strong ligand character, with electron density distributed throughout the pi system and strongly localized on the secondary amine on the thiosemicabazone backbone (Figure 9.4c). The reduced

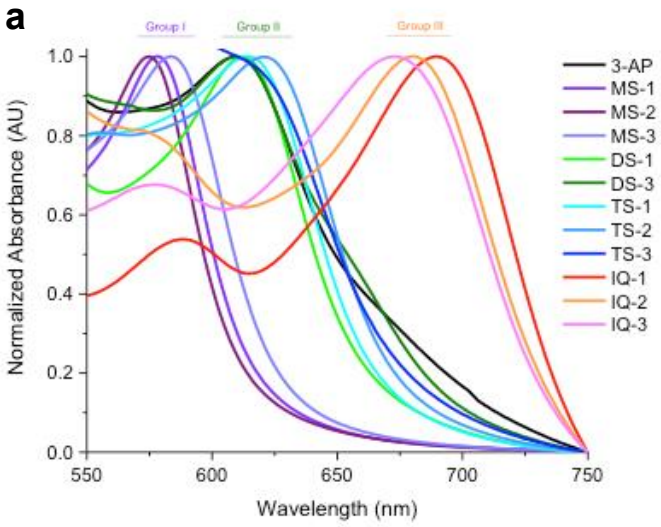

Iron(II) Complex	$\varepsilon_{complex}$
3-AP	4380
DS-1	7990
DS-2	6850
DS-3	6300
TS-1	3380
TS-2	4450
TS-3	8130
MS-1	5410
MS-2	5900
MS-3	7660
IQ-1	9360
IQ-2	8190
IQ-3	4700

Figure 9.7 (a) Bis-iron(II) complexes exhibit charge transfer peaks between 550 nm and 700 nm. Methylated Group I compounds are blue-shifted and isoquinoline Group III analogs are red-shifted, with respect to 3-AP. (b) Extinction coefficients of the Fe(II) complexes at the lowest energy charge transfer transition wavelength.

form of the 3-AP iron complex was determined to be the active species involved in β_2 inhibition,[14] and the lowest energy transitions of the reduced complexes tell us important features about their oxidation mechanism. This charge transfer peak, which is only present in the Fe(II) complex, can be used to track the stability of the Fe(II) 3-AP analog complexes.

Stability of the Fe(II) species. UV-Vis spectroscopic pH titrations were used to monitor the effect of pH on the stability of the iron(II) complexes in a reducing environment in order to understand the effect of ligand structure on metal complex formation. Cells are reducing environments which contain species such as glutathione and NADH that allow redox cycling of iron complexes.[91] Although pH stability is not necessarily an indicator of the most potent RNR inhibitor, there is a pH dependence on the stability of the active Fe(II) species with different ligands

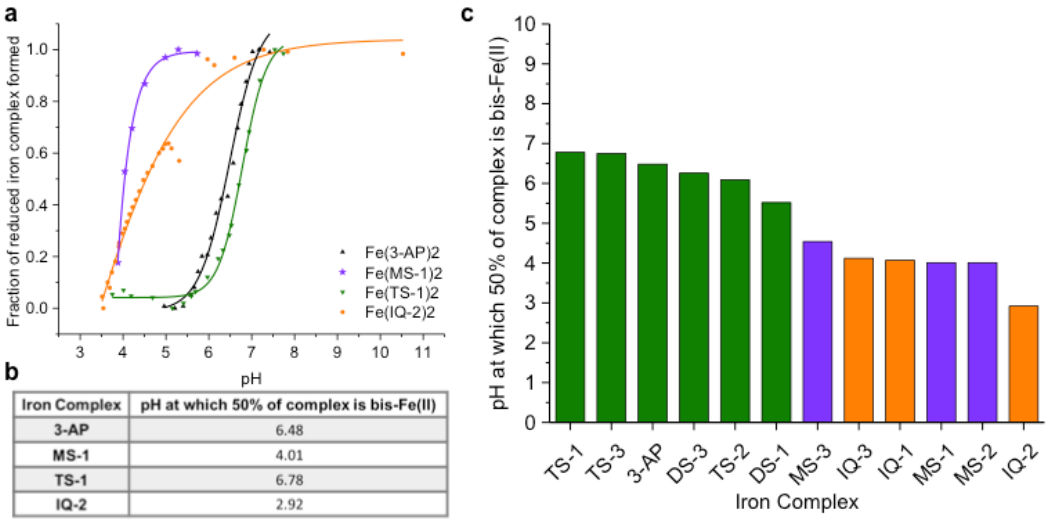

Iron Complex	pH at which 50% of complex is bis-Fe(II)
3-AP	6.48
MS-1	4.01
TS-1	6.78
IQ-2	2.92

Figure 9.8 (a) pH titrations of representative 3-AP iron (III) complexes in the presence of a reducing agent. The fraction of iron(II) complex formed is determined by UV-Vis from the absorbance of the lowest energy charge transfer peak. (b) Fraction of the active reduced species is plotted vs. pH and a sigmoidal curve fit is used to calculate the values in the table. (c) Summary of titration data for all the 3-AP analogs.

(Figure 9.8). The pH dependence may likely be due to protonation and ligand dissociation or oxidation. Most of the Fe(II) complexes stay in their active form at pH values 6.1-6.8. However, the most drastic differences are seen in the Group I methylated series (compounds MS-1, MS-2, MS-3), wherein the Fe(II) bis-complexes are in active form even at pH 4.0. In the Group III isoquinoline series (compounds IQ-1, IQ-2, and IQ-3), the active complexes are stable at pH 2.9-4.0. It is rather surprising to find increased stability of the Fe(II) complexes over a broad pH range with the isoquinoline ligands, which may be one reason why they are extremely potent RNR inhibitors.

To understand if the maintenance of the active iron(II) species is related to the activity of the compound, spectroscopic methods were used to calculate the half-life of the reduced complexes t_{50}, the time taken for 50% of the complex to get oxidized under the given experimental conditions (Figure 9.9). Compounds fall into three groups: non-oxidizers with no RNR-specific activity, fast oxidizers

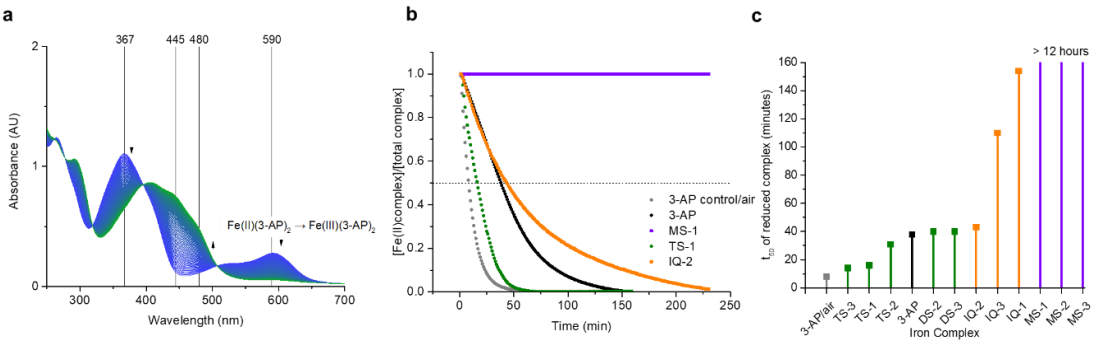

Figure 9.9 (a) UV-Vis spectra for the oxidation of Fe(II)$(3\text{-AP})_2$ over time, where absorption spectra are taken every 60 seconds. (b) Oxidation rate plotted as a function of absorbance of each 3-AP analog complex at the lowest energy charge transfer peak vs. time (c) Summary of t_{50} values for the 3-AP iron(II) complexes. T_{50} is defined at the time it takes for 50% of the complex to get oxidized under the given experimental conditions.

with low activity, and slow oxidizers with the greatest activity. Iron(II) complexes of the Group I ligands, MS-1, MS-2, and MS-3, which are inactive *in vitro*, do not get oxidized over the time frame of the experiment and stay in their reduced form for days. Group II-A compounds, with non-aromatic modifications on the left side (compounds TS-1, TS-2, and TS-3), form complexes that get oxidized faster than the 3-AP iron complex and are less potent RNR inhibitors (Figure 9.3). Addition of electron donating groups to the right side of the 3-AP scaffold (compounds DS-1, DS-2, and DS-3) results in similar maintenance of their reduced complex and are potent RNR inhibitors. The iron(II) complexes of the Group III ligands get oxidized slowly and are two to four times more potent than 3-AP *in vitro*. This increased activity may be due to slower oxidation, where there will be more species in the Fe(II)-complex form in the cell. Although the time it takes for the Fe(II) species to get oxidized is much longer than the redox cycling time, we would expect that there should be more of the complex in the Fe(II) form at any given time.

Reduction potentials and trends. It is quite likely that the increased stability of the reduced complex is related to the strength of the ligand. In the spectrochemical series, stronger ligands cause more d-orbital splitting. Isoquinolines

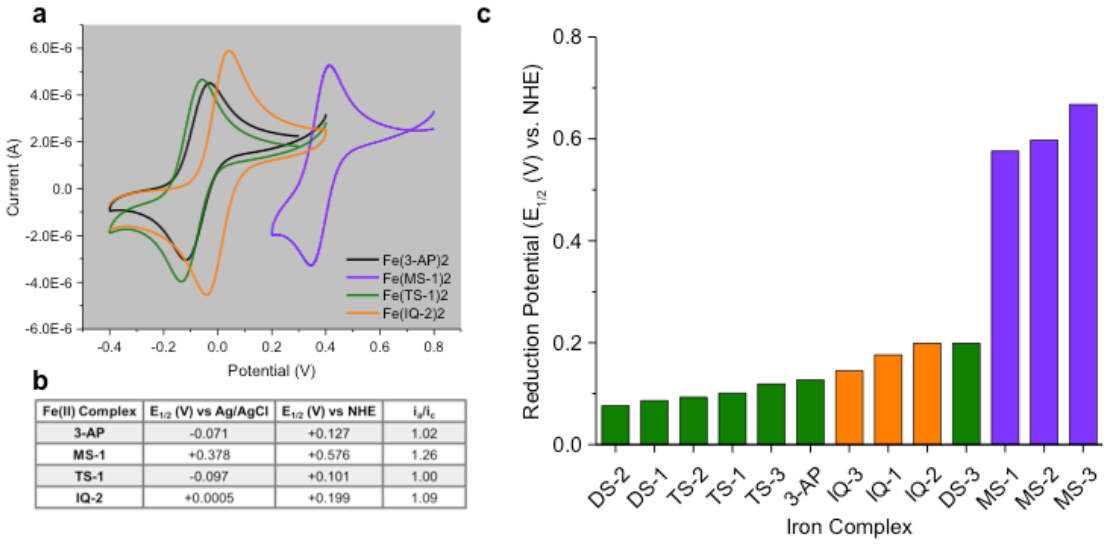

Fe(II) Complex	$E_{1/2}$ (V) vs Ag/AgCl	$E_{1/2}$ (V) vs NHE	i_a/i_c
3-AP	-0.071	+0.127	1.02
MS-1	+0.378	+0.576	1.26
TS-1	-0.097	+0.101	1.00
IQ-2	+0.0005	+0.199	1.09

Figure 9.10 (a) Cyclic voltammograms of representative 3-AP analog complexes, (b) Reduction potentials of complexes vs. Ag/AgCl and vs. NHE, and (c) Summary of reduction potentials for all the complexes.

act as strong Lewis bases and pi-acceptor ligands, which in the spectrochemical series tend to interact strongly with orbitals of transition metals to cause large splitting of d-orbital energies. In our case, the oxidation-reduction events change the complex from high spin to low spin, so the redox potential is proportional to the d-d splitting energy. Cyclic voltammetry was used to measure the reduction potential and found that the Group III isoquinolines complexes indeed had a higher reduction potential (Figure 9.10). Group III compounds are still able to get oxidized, but their potentials are still not out of the range of the cellular environment. The higher reduction potentials of the Group III complexes are consistent with the isoquinoline ligand's ability to stabilize the low-spin Fe(II) form. Adding conjugation on the pyridine ring of 3-AP, as in the case of the Group III series, increases sigma donation from the lone pair of the sp^2-hybridized pyridine nitrogen making isoquinoline ligands, IQ-1, IQ-2, and IQ-3, stronger Lewis bases than 3-AP. In turn, these modifications increase the pi-accepting character of the ligand and favor the biologically active low spin Fe(II) form of the complex. Furthermore, the long half-life required for oxidation of the Group III complexes is consistent with their ability to favor the Fe(II) form, as well as is their stability over a wider pH range.

An interesting case is that of complexes having redox potentials that are too high. It is evidenced in the case of the Group I compounds, MS-1, MS-2, and MS-3, which have high redox potentials outside the range of the cellular environment, are unable to redox cycle, and do not induce S-phase arrest of cells after 24-hour treatment *in vitro*. The mechanism of RNR inhibition requires donation of an electron from the reduced Fe(II) complex to a tyrosyl radical.[14] Redox potentials of the active 3-AP complexes need to be in the range of the cellular environment to inhibit RNR, because electron donation, i.e. oxidation of the iron complex, is ultimately required for inhibition. Furthermore, redox cycling is required for maintaining the function of the drug. All the other complexes have potentials in the range of the cellular environment.

9.4 Conclusions

There are other contributing factors that modulate activity of the 3-AP analogs against RNR such as cell uptake, solubility, and chemical stability of the ligand in a biological environment. However, the present studies give an understanding of the electronic components of what makes a potent 3-AP analog. In designing a potent RNR inhibitor, it is favorable but not required that their iron complexes form the active reduced species over a large pH range. Oxidation rates of the 3-AP analog Fe(II) complexes have shown to be a useful indicator of potency of the analogs *in vitro*. Oxidation rate can be determined from the decrease in the lowest energy charge transfer peak using UV-Vis spectroscopy. Due to its simplicity, this method has the potential to be used in a microplate assay with UV absorption-detection to quickly screen potential drug candidates.

Reduction potentials are also a good indicator of biological activity, where the most potent compounds have iron complexes with reduction potentials below 0.2 V, within the range of the cellular environment, so that the complex can undergo oxidation per its mechanism of action. Methylation on the secondary amine of the thiosemicarbazone drastically alters the reduction potential (>0.5 V), causing non-specific activity of the drug, in the case of the methylated Group I complexes. Group III-type isoquinoline modifications to the 3-AP scaffold have the potential to improve the potency of RNR inhibitors. They are an example of structural modifications of 3-AP that form iron complexes with adequate redox potentials, allow for redox cycling, favor the biologically active Fe(II) species, and thereby improve the potency of 3-AP *in vitro*.

9.5 Materials and Methods

Materials

Ammonium iron (II) sulfate hexahydrate (Sigma Aldrich), iron(III) nitrate nonahydrate (Alfa Aesar), Dimethyl sulfoxide (Sigma Aldrich), L-dithiothreitol (DTT) (Sigma Aldrich) were used as received. Potassium chloride (KCl) (Sigma) was recrystallized three times from water before use. Glassy Carbon and Ag/AgCl Reference Electrodes were obtained from CHI Instruments.

Synthesis of 3-AP analogs

Please see Supplemental Information File for synthesis and characterization data (^{1}H-NMR, ^{13}C-NMR, and HPLC).

Synthesis of Iron(II) and (III) complexes

100 mM stock solutions of Fe(II) and Fe(III) salts are made in degassed 18 megohm water. 10 mM 3-AP analog stocks are made in DMSO. Iron salt solution is added to the ligand solution at a molar ratio of 1:2 (Fe:3-AP). Upon addition of the iron salt, the bis-complex Fe(3-AP)$_2$ forms readily in solution and a color change follows.[14,92] The iron(III) complexes are quite stable, but the iron(II) compounds need to be degassed and stored under argon to prevent oxidation. For UV-Vis experiments, complexes are made and used at concentrations 100 µM-300µM. All UV-Vis measurements are done on a Varian Cary 5000 UV-Vis-NIR Spectrophotometer.

Cell culture conditions

Human cell line *MIA PaCa-2* was obtained from American Type Culture Collection and maintained in 10% FBS in DMEM, and were cultured at 37^{o}C, 20% O_2 and 5% CO_2. The cultures were regularly tested for mycoplasma contamination using MycoAlert kit (Lonza) following manufacturer's instructions.

Cell proliferation assay

Cells were plated in 384-well plates (500 cells/well in 30 µL volume). Drugs were serially diluted to desired concentrations and an equivalent volume of DMSO was added to vehicle control. 10 µL of the 4× diluted drugs were added to each well. Following 72 h incubation, ATP content was measured using CellTiter-Glo reagent according to manufacturer's instructions (Promega, CellTiter-Glo

Luminescent Cell Viability Assay), and analyzed by SpectraMax luminometer (Molecular Devices). IC_{50} values, concentrations required to inhibit proliferation by 50% compared to DMSO treated cells, were calculated using Prism 6.0 h (Graphpad Software).

FACS analysis of S-phase arrest

250,000 *MIA PaCa-2* cells were seeded per well in a 12-well plate. The cells were treated with indicated compounds for 24 hours. The cells were trypsinized and spun down at 450 x g for 5 min, washed with PBS twice, and resuspended in 300 µL Propidium iodide solution (containing Ribonuclease A and 0.3% Triton X-100). The samples were protected from light before acquisition by flow cytometry. All flow cytometry data were acquired on a five-laser LSR FORTESSA or LSRII (BD), and analyzed using the FlowJo software (Tree Star).

Energy transitions of 3-AP analog complexes

Extinction coefficients of the reduced complexes' lowest energy transition are calculated using the Beer-Lambert Law from the maximum absorbance of the 2:1 species.

Iron binding affinities of 3-AP analogs: calculating relative K_a's

To determine relative K_a values for the 3-AP analogs, we develop a spectroscopic Fe(II) binding assay, in which the drug is titrated with Fe(II) under argon such that the rate of oxidation is negligible. Iron and drug solutions are degassed for 10 min before the titration. The absorbance of the metal complex's charge transfer peak at ~600 nm is plotted against the equivalents of iron added, and the Beer-Lambert law is applied to determine the extinction coefficient of the complex at that wavelength. K_a is then determined from the slope of the line from the graph [Fe(II)] vs [complex]/[drug]. 10 mM stock solutions of drug are made in DMSO. All titrations are done with 3 mL of 100 µM drug in water (1% DMSO). To keep the volume change <10%, 7.5 µL of 2.5 mM ammonium iron (II) sulfate in water is added to get each spectrum (16 times). Then 15 µL is added (8 times). For iron(III) titrations, iron(III) nitrate nonahydrate is used as the iron source.

pH titrations

Spectroscopic pH titrations are used to monitor the effect of pH on the reduction of the iron(III) complexes in the presence of the reducing agent DTT. 3-AP analog Fe(III) complexes are synthesized as described previously. The appearance of the charge transfer peak at 600 nm, which is only present in the iron (II) complexes, is used to monitor the stability of the reduced Fe(II)(3-AP)$_2$ complexes after the addition of 500 nM-1 mM DTT. The pH at which 50% of the complex is in the bis-Fe(II) form is calculated using a sigmoidal dose-response fitting in Origin Pro 9.1. Changing the pH alone without the reducing agent does not affect the reduction of the complexes. Spectra are taken after solutions have reached equilibrium. Note that reduction of the Fe(III) complexes occur <1 min, whereas oxidation is slower.

Oxidation rate of Fe(II) complexes

Iron(II) complexes of 3-AP analogs are made at 2:1 ratio of ligand:Fe(II) salt under argon. The charge transfer peak that is only present in the reduced form of the complex is used to monitor the rate of oxidation of the iron (II) complex over time. The oxidation rate of Fe(II)(3-AP)$_2$ is plotted as a function of the absorbance at the ~600 nm peak vs time. T_{50}, the time it takes for 50% of the complex to get oxidized under the given experimental conditions, is calculated for all the 3-AP analog complexes.

Cyclic voltammetry (CV)

CV experiments are carried out under argon. 0.1 M KCl is used as the electrolyte solution. Due to solubility limitations, all compounds are dissolved in 30% DMSO/0.1 M KCl at 2 mM. The bis-complexes are made *in situ* by addition of ammonium iron (II) sulfate hexahydrate, where final [Fe] = 1 mM. The following parameters are used to acquire the voltammograms. Scan rate: 0.1 V/s, sensitivity 10^{-6}, reference electrode: Ag/AgCl, auxiliary and working electrode: glassy carbon.

Density Functional Theory calculations

DFT calculations are done using Gaussian09. Crystal structure for Fe(III)(3-AP)$_2$ from Kowol et al. is used as the starting point for geometry optimizations of the 3-AP complex.[90] DFT, B3LYP, 6-31+G* basis set is used for geometry optimization. The SDD basis set is used for Fe^{2+} and 6-31+G* is used for H, C, N, S, and O.

Single point energy calculations are done using a larger basis set (6-31+G**), with zero-point corrections from the converged frequency file.

9.6 Acknowledgements

Special thanks to Jon Brosmer and Maxim Marshalik for helpful discussions.

9.7 Supporting Information

Supporting information is available below and includes complete Fe(II) titrations, pH titrations, oxidation spectra, and cyclic voltammograms of all 3-AP analog complexes (Figures S1-S5); Synthesis procedures for compounds; HPLC traces of 3-AP analogs; ^{1}H-NMR and ^{13}C-NMR spectra (PDF).

Group I

MS-1

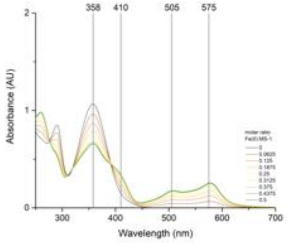

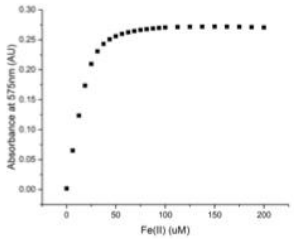

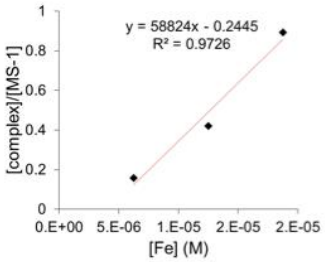

MS-2

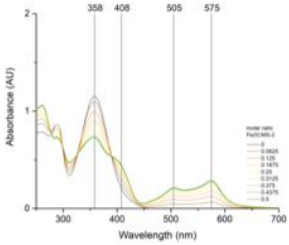

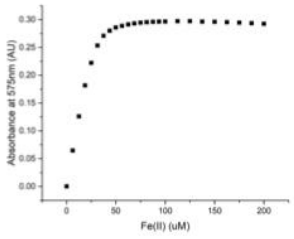

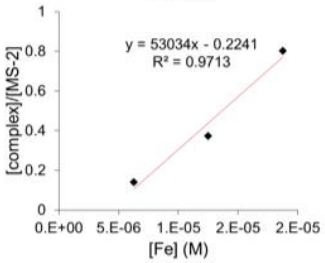

MS-3

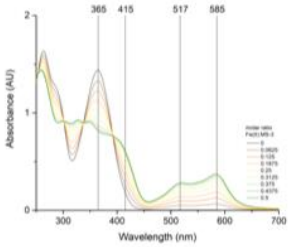

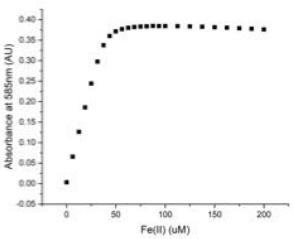

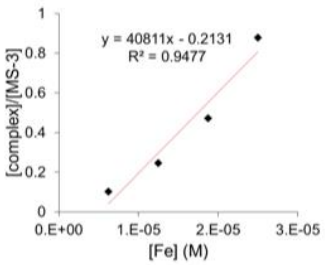

Group II-A

TS-1

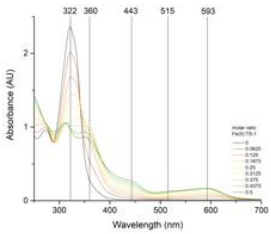

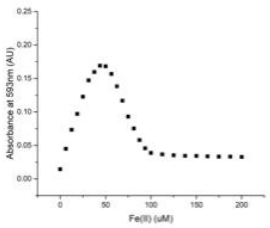

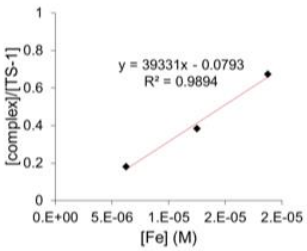

TS-2

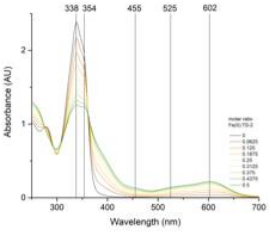

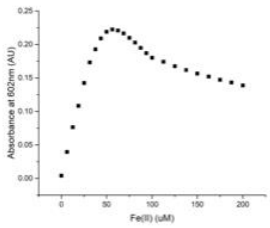

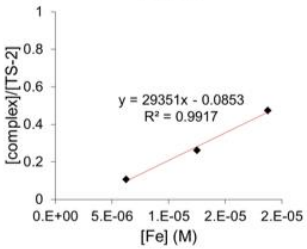

TS-3

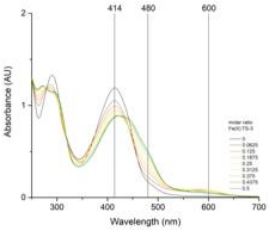

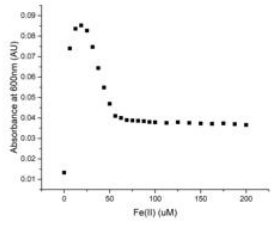

*Can not get accurate K_a. Oxidation of TS-3 not negligible.
$R^2 < 0.5$

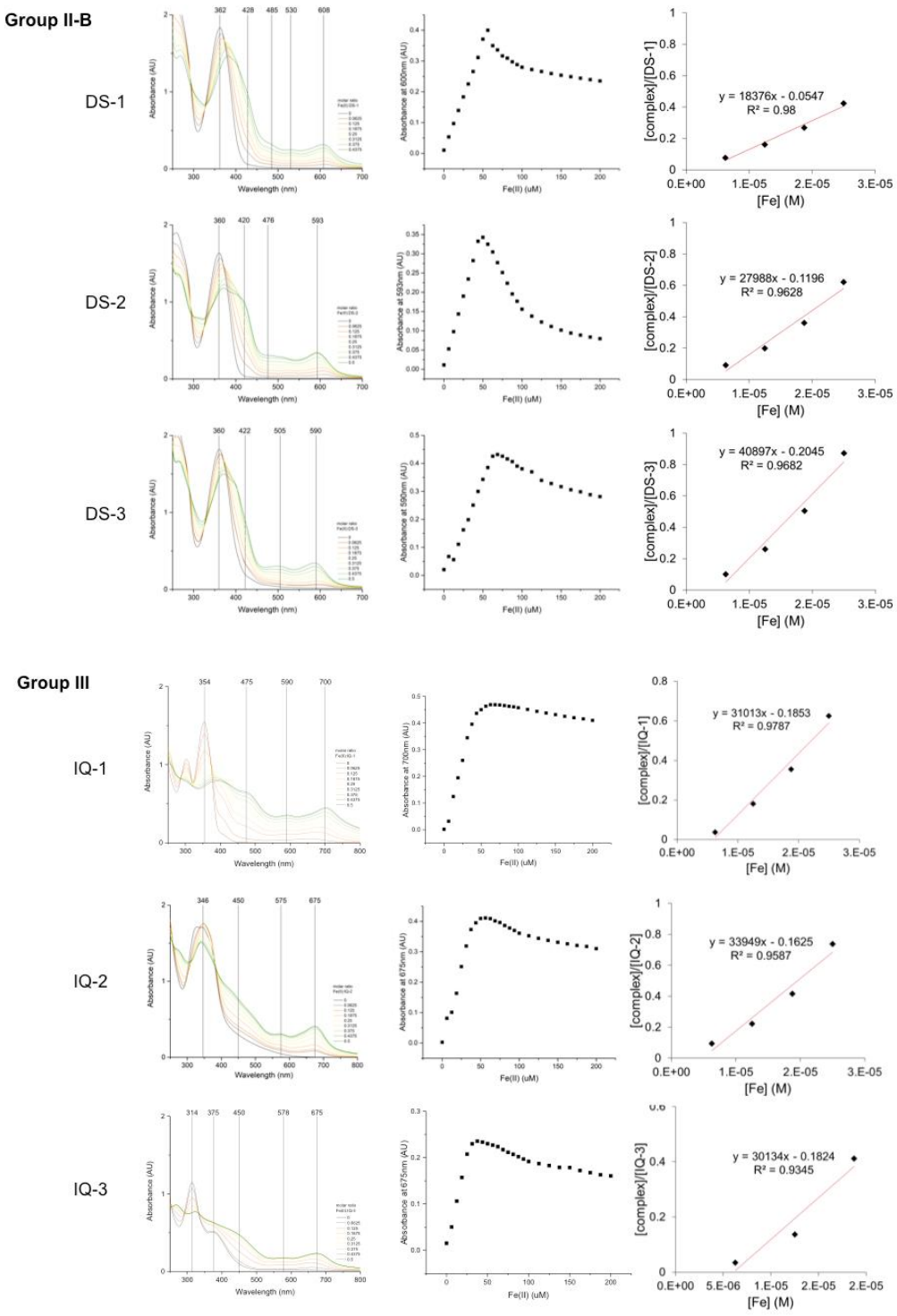

Figure S9.11 Spectroscopic Fe(II) titrations of 3-AP analogs (left), free iron concentration plotted vs. absorbance at the lowest energy charge transfer peak (middle), and line of best fit using the first few points of the titration (right).

a

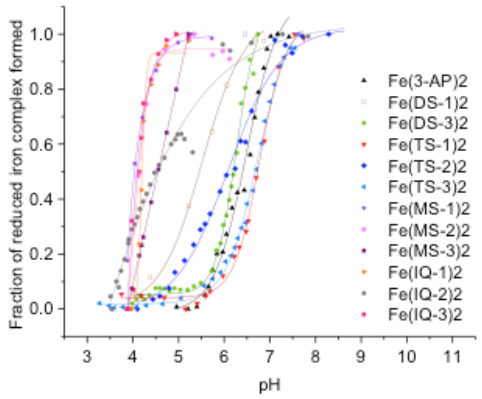

b

Iron Complex	pH at which 50% of complex is bis-Fe(II)	Standard error
IQ-2	2.92	1.3
MS-1	4.01	0.12
MS-2	4.01	0.00
IQ-1	4.07	0.11
IQ-3	4.12	0.20
MS-3	4.54	0.05
DS-1	5.52	0.07
TS-2	6.09	0.05
DS-3	6.26	0.03
3-AP	6.48	0.05
TS-3	6.75	0.02
TS-1	6.78	0.03

Figure S9.12 (a) pH titrations of all 3-AP analog Fe(III) complexes. (b) Table values are calculated from a sigmoidal dose response fit

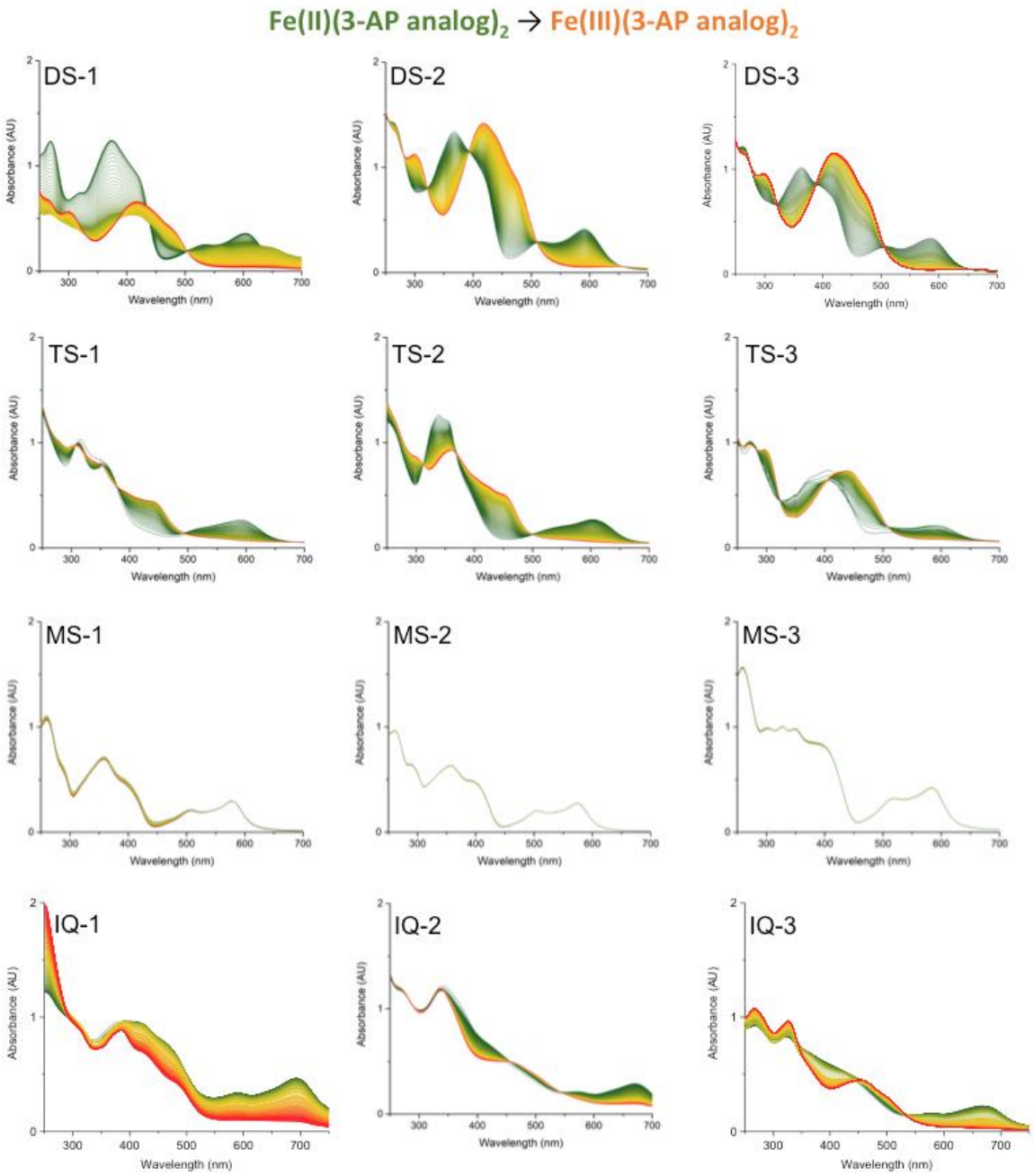

Figure S9.13 Oxidation of Fe(II) 3-AP analog complexes over time. Spectra are taken every 60 seconds.

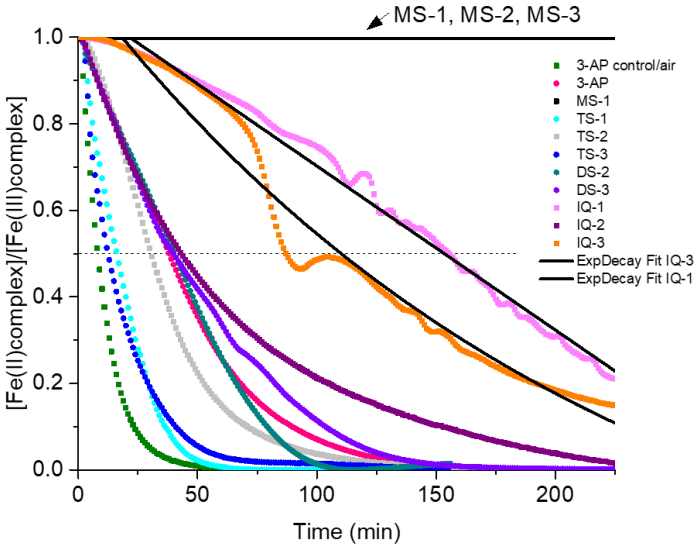

Figure S9.14 Oxidation rate curves for 3-AP analog complexes.

a

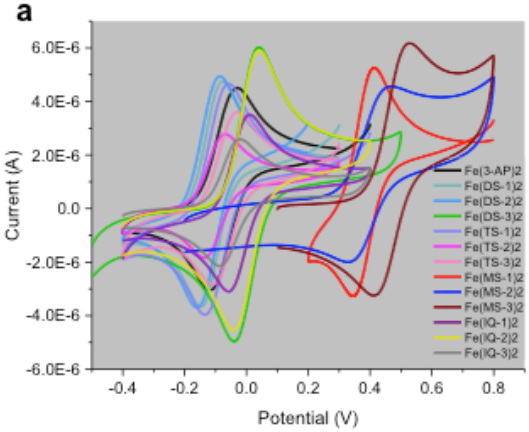

b

Fe(II) Complex	$E_{1/2}$ (V) vs Ag/AgCl	$E_{1/2}$ (V) vs NHE	i_a/i_c
3-AP	-0.071	+0.127	1.02
DS-1	-0.1115	+0.0865	1.03
DS-2	-0.1215	+0.0765	1.07
DS-3	+0.0005	+0.199	1.09
TS-1	-0.097	+0.101	1.00
TS-2	-0.105	+0.093	1.01
TS-3	-0.079	+0.119	0.973
MS-1	+0.378	+0.576	1.26
MS-2	+0.400	+0.5975	1.48
MS-3	+0.4695	+0.6675	1.47
IQ-1	-0.0225	+0.176	0.97
IQ-2	+0.0005	+0.199	1.09
IQ-3	-0.0530	+0.145	1.02

Figure S9.15 Cyclic voltammograms of 3-AP analog iron complexes

Chemistry materials and methods

All chemicals, reagents and solvents were obtained from commercial sources and were used without further purification unless otherwise specified. Compounds TS-1, TS-2, TS-3, MS-1, MS-2, and MS-3 were obtained from SYNthesis Med Chem (Shanghai, China). All reactions were performed under Ar atmoshphere. Analytical TLC was carried out on precoated silica plates (Merck silica gel 60, F254) and visualized with UV light. Column chromatography was performed with silica (Fisher, 230-400 mesh). ^{1}H NMR and ^{13}C NMR spectra were measured on Bruker AV 400 or AV 500 spectrometers. Chemical shifts were reported in parts per million (δ) relative to residual solvent signals. The signals observed were described as follows: s (singlet), d (doublet), t (triplet), q (quartet), dd (doublet of doublets), ddd (doublet of doublet of doublet), dt (doublet of triplets), m (multiplet). Mass spectra were performed on a Waters LCT Premier with ACQUITY UPLC mass spectrometer under electrospray ionization (ESI) or Thermo Fisher Scientific Exactive Plus with detection in real time (DART) ionization.

General procedures

General procedure A for synthesis of 2-(carbamothioylthio)acetic acids: To a solution of amine (1 eq) and NaOH (1.05 eq) in EtOH (1.0 M) was added CS_2 (1 eq). The mixture was stirred for 4 h then cooled to 0^{o} C. Sodium chloroacetate (1 eq) in water (0.5 M) was added. The mixture was allowed to warm to room temperature and stirred for 12 h. The solution was acidified to pH 2 with conc. HCl, and a white precipitate formed which was filtered and washed with 1.2 M HCl and water. The product was recrystallized from EtOH.

General procedure B for synthesis of thiosemicarbazides: The substituted 2-(carbamothioylthio)acetic acid (1 eq) was suspended in H_2O (1.0 M), and hydrazine hydrate (5 eq) was added. The solution was heated to 50 ^{o}C for 1 h, at which point a white precipitate formed and the reaction was cooled to room temperature. The precipitate was filtered, washed with water, and recrystallized from EtOH.

General procedure C for synthesis of thiosemicarbazones: S2 (1 eq) and the appropriate thiosemicarbazide (1 eq) were dissolved in EtOH (0.5 M) and the mixture was refluxed for 4 h. The precipitate was collected by filtration and washed with cold EtOH. The crude solid was dissolved in chloroform (1.0 M) and

trifluoroacetic acid (6 eq) was added dropwise. The mixture was stirred for 1 h and sat. $NaHCO_3$ was added to reach pH 9. A yellow precipitate formed immediately and the mixture was stirred for 1 h. The solid was collected by filtration, washed with water, and recrystallized from EtOH.

Synthesis of 3-AP

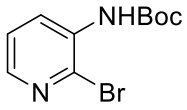

tert-Butyl-(2-bromopyridin-3-yl)carbamate (S1). To a solution of Boc_2O (30.26 g, 138.72 mmol) in THF (50 mL) was added DMAP (0.565g, 4.62 mmol). The mixture was stirred at 0 °C for 10 minutes, and 3-amino-2-bromopyridine (8.00 g, 46.2 mmol) was added. The mixture was refluxed for 6 h and cooled to room temperature. A solution of K_2CO_3 (19.17g, 138.72 mmol) in MeOH (50 mL) was added and the mixture was refluxed for 2 h, then cooled, filtered, and concentrated. The crude residue was purified by silica gel column (15-25% EtOAc/Hexanes) to afford S1 as a beige solid (10.86 g, 86%). ^{1}H NMR (400 MHz, DMSO-d_6) δ 8.74 (s, 1H), 8.16 (dd, J = 4.6, 1.8 Hz, 1H), 7.92 (dd, J = 7.9, 1.8 Hz, 1H), 7.42 (dd, J = 8.0, 4.6 Hz, 1H), 1.46 (s, 9H). ^{13}C NMR (100 MHz, DMSO-d_6) δ 152.92, 145.82, 137.83, 134.30, 134.11, 123.56, 79.97, 27.97. DART-MS: *m/z* calcd. for $C_{10}H_{13}BrN_2O_2$ $(M+H)^+$ 273.02332, found 273.02267.

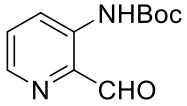

tert-Butyl-(2-formylpyridin-3-yl)carbamate (S2). To a solution of S1 (2.00 g, 7.32 mmol) in THF (20 mL) was added *n*-BuLi (1.6M, 9.15 mL, 14.65 mmol) and the mixture was stirred for 1 h at -78 °C. The mixture was warmed to 0 °C and *N*-formylpiperidine (0.89 mL, 8.05 mmol) was added and stirring commenced for 1 h. The solution was quenched with 1.0 M HCl (15 mL) then neutralized with solid K_2CO_3. The aqueous layer was extracted with ethyl acetate (3 x 10 mL) and the combined organic layers were washed with brine then dried over Na_2SO_4, filtered, and concentrated. The crude product was purified by column chromatography (0-15% EtOAc/Hexanes) to yield S2 as an off-white solid (1.18 g, 72%). ^{1}H NMR (400 MHz, Chloroform-*d*) δ 10.21 (s, 1H), 10.07 (d, J = 0.8 Hz, 1H), 8.83 (dt, J = 8.7, 1.1 Hz, 1H), 8.40 (dd, J = 4.4, 1.4 Hz, 1H), 7.44 (ddd, J = 8.7, 4.4, 0.6 Hz, 1H), 1.53 (s, 9H). ^{13}C NMR (100 MHz, Chloroform-*d*) δ 197.20, 152.76, 143.31, 139.28,

136.72, 128.67, 126.28, 81.69, 28.25. DART-MS: *m/z* calcd. for $C_{11}H_{14}N_2O_3$ $(M+H)^+$ 223.10772, found 223.10701.

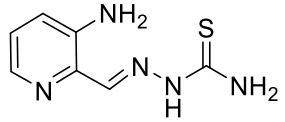

2-((3-aminopyridin-2-yl)methylene)hydrazine-1-carbothioamide (3-AP): To a solution of S2 (0.90 g, 4.05 mmol) and thiosemicarbazide (0.406 g, 4.45 mmol) in EtOH (10 mL) was added 6 M HCl (3.67 mL). The mixture was refluxed for 2 h then cooled to room temperature and the resulting precipitate was filtered off and suspended in 10 mL H_2O. 10 mL of 10% $NaHCO_3$ was added and the mixture was stirred for 1 hour then filtered, and the solid was washed successively with H_2O, EtOH, and Et_2O. 3-AP was obtained as a yellow solid (0.704 g, 89%). ^{1}H NMR (500 MHz, DMSO-d_6) δ 11.29 (s, 1H), 8.32 (s, 1H), 8.16 (s, 1H), 7.96 (s, 1H), 7.82 (dd, J = 4.3, 1.4 Hz, 1H), 7.14 (dd, J = 8.3, 1.5 Hz, 1H), 7.06 (dd, J = 8.3, 4.3 Hz, 1H), 6.44 (s, 2H). ^{13}C NMR (125 MHz, DMSO-d_6) δ 177.07, 149.20, 143.97, 137.11, 132.79, 124.43, 122.21 DART-MS: *m/z* calcd. for $C_7H_9N_5S$ $(M+H)^+$ 196.06514, found 196.06479.

Synthesis of MS and TS compounds

Compounds MS-1, MS-2, MS-3, TS-1, TS-2, and TS-3 were obtained from SYNthesis Med Chem (Shanghai, China).

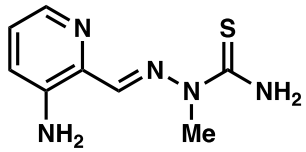

(*E*)-2-((3-aminopyridin-2-yl)methylene)-1-methylhydrazine-1-carbothioamide (MS-1): ^{1}H NMR (500 MHz, DMSO-d_6): δ 8.41 (s, 1H), 8.04 (s, 1H), 7.90 (dd, J = 4.3, 1.4 Hz, 1H), 7.79 (s, 1H), 7.19 (dd, J = 8.4, 1.5 Hz, 1H), 7.11 (dd, J = 8.3, 4.3 Hz, 1H), 6.38 (br s, 2H), 3.80 (s, 3H). ^{13}C NMR (125 MHz, DMSO-d_6): δ 180.84, 147.50, 144.23, 137.85, 134.01, 125.03, 123.17, 33.62.

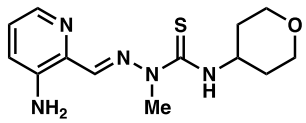

(*E*)-2-((3-aminopyridin-2-yl)methylene)-1-methyl-*N*-(tetrahydro-2*H*-pyran-4-yl)hydrazine-1-carbothioamide (MS-2): ^{1}H NMR (500 MHz, DMSO-d_6): δ 8.19 (d, J = 7.8 Hz, 1H), 8.06 (s, 1H), 7.92 (dd, J = 4.3, 1.5 Hz, 1H), 7.18 (dd, J = 8.3, 1.5

Hz, 1H), 7.12 (dd, J = 8.3, 4.3 Hz, 1H), 6.41 (br s, 2H), 4.36 (dddd, J = 14.9, 10.9, 8.4, 4.3 Hz, 1H), 3.85 (dt, J = 11.5, 3.5 Hz, 2H), 3.80 (s, 3H), 3.40 (dt, J = 11.5, 2.1 Hz, 2H), 1.91 (dd, J = 12.4, 2.4 Hz, 2H), 1.62 (qd, J = 11.4, 4.3 Hz, 2H). ^{13}C NMR (125 MHz, DMSO-d_6): δ 178.91, 145.85, 144.15, 138.11, 134.85, 124.89, 123.32, 66.38(2C), 51.77(2C), 33.87, 32.11.

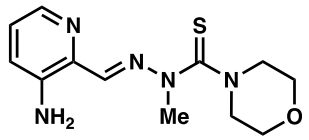

(*E*)-*N*'-((3-aminopyridin-2-yl)methylene)-*N*-methylmorpholine-4-carbothiohydrazide (MS-3): ^{1}H NMR (500 MHz, DMSO-d_6): δ 8.02 (s, 1H), 7.88 (dd, J = 4.3, 1.6 Hz, 1H), 7.13 (dd, J = 8.4, 1.6 Hz, 1H), 7.08 (dd, J = 8.3, 4.2 Hz, 1H), 6.76 (br s, 2H), 3.65-3.73 (m, 8H), 3.59 (s, 3H). ^{13}C NMR (125 MHz, DMSO-d_6): δ 189.39, 145.15, 143.90, 137.55, 134.46, 124.46, 122.66, 66.30(2C), 52.48(2C), 37.44.

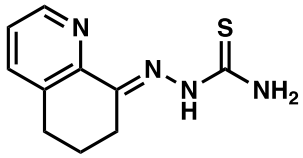

(*E*)-2-(6,7-dihydroquinolin-8(5*H*)-ylidene)hydrazine-1-carbothioamide (TS-1): ^{1}H NMR (500 MHz, DMSO-d_6): δ 11.08 (s, 1H), 9.17 (d, J = 4.6 Hz, 1H), 9.09 (s, 1H), 8.34 (s, 1H), 8.30 (d, J = 7.7 Hz, 1H), 7.97 (dd, J = 7.7, 4.6 Hz, 1H), 4.08 (s, 2H), 3.44-3.47 (m, 4H). ^{13}C NMR (125 MHz, DMSO-d_6): δ 179.93, 149.59, 148.37, 146.90, 137.17, 136.64, 124.25, 28.63, 26.86, 21.27.

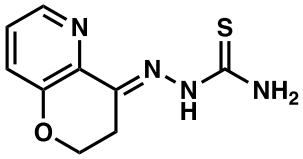

(*E*)-2-(2,3-dihydro-4*H*-pyrano[3,2-*b*]pyridin-4-ylidene)hydrazine-1-carbothioamide (TS-2): ^{1}H NMR (500 MHz, DMSO-d_6): δ 10.60 (s, 1H), 8.44 (s, 1H), 8.28 (dd, J = 4.1, 1.8 Hz, 1H), 7.58 (s, 1H), 7.32-7.37 (m, 2H), 4.29 (t, J = 6.2 Hz, 2H), 3.03 (t, J = 6.2 Hz, 2H). ^{13}C NMR (125 MHz, DMSO-d_6): δ 179.87, 154.68, 143.51, 141.95, 138.39, 126.10, 125.66, 65.26, 26.59.

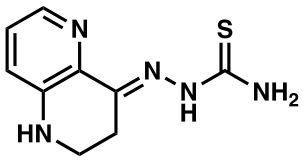

(*E*)-2-(2,3-dihydro-1,5-naphthyridin-4(1*H*)-ylidene)hydrazine-1-carbothioamide (TS-3): ^{1}H NMR (500 MHz, DMSO-d_6): δ 15.99 (br s, 1H), 10.89 (s, 1H), 9.06 (s, 1H), 8.62 (s, 1H), 8.02 (d, J = 5.3 Hz, 1H), 7.76-7.81 (m, 2H), 7.64 (dd, J = 8.7, 5.3 Hz, 1H), 3.36 (t, J = 6.6 Hz, 2H), 2.89 (t, J = 6.6 Hz, 2H). ^{13}C NMR (125 MHz, DMSO-d_6): δ 179.59, 146.88, 135.92, 130.64, 130.48, 127.11, 126.87, 38.07, 23.82.

Synthesis of DS compounds

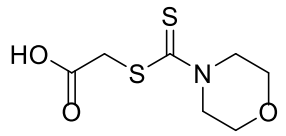

2-((morpholine-4-carbonothioyl)thio)acetic acid (S3). Synthesized according to general procedure A on 22.96 mmol scale. S3 was isolated as a white crystalline solid (0.401 g, 79%). ^{1}H NMR (500 MHz, DMSO-d_6) δ 12.75 (s, 1H), 4.20 (s, 2H), 4.14 (s, 2H), 3.94 (s, 2H), 3.68 (t, J = 4.9 Hz, 4H). ^{13}C NMR (125 MHz, DMSO-d_6) δ 195.39, 169.66, 66.04, 51.83, 50.70, 38.87. DART-MS: *m/z* calcd. for $C_7H_{11}NO_3S_2$ $(M+H)^+$ 222.02531, found 222.02470.

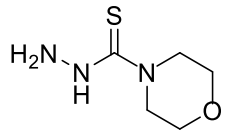

Morpholine-4-carbothiohydrazide (S4). Synthesized from S3 according to general procedure B on 13.56 mmol scale. S4 was isolated as a white crystalline solid (0.113 g, 72%). ^{1}H NMR (500 MHz, DMSO-d_6) δ 9.13 (s, 1H), 4.34 (s, 2H), 3.68 (dd, J = 5.7, 4.0 Hz, 4H), 3.56 (dd, J = 5.7, 4.0 Hz, 4H). ^{13}C NMR (125 MHz, DMSO-d_6) δ 182.93, 65.69, 47.75. DART-MS: *m/z* calcd. for C_5 H_{11} N_3 O S $(M+H)^+$ 162.06956, found 162.06923.

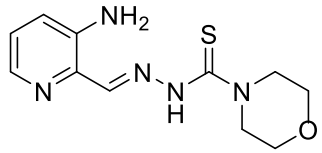

N'-((3-aminopyridin-2-yl)methylene)morpholine-4-carbothiohydrazide (DS-1). Synthesized according to general procedure C on 0.434 mmol scale. DS-1 was obtained as a yellow solid (0.069 g, 60%). ^{1}H NMR (500 MHz, DMSO-d_6) δ 11.37 (s, 1H), 8.49 (s, 1H), 7.83 (dd, J = 4.2, 1.6 Hz, 1H), 7.16 (s, 2H), 7.11 – 7.04 (m, 2H), 3.94 – 3.89 (m, 4H), 3.69 – 3.63 (m, 4H). ^{13}C NMR (125 MHz, DMSO-d_6) δ

179.90, 149.10, 143.77, 136.70, 133.74, 124.02, 121.99, 65.78, 48.84. DART-MS: *m/z* calcd. for $C_{11}H_{15}N_5OS$ $(M+H)^+$ 266.10701, found 266.10706.

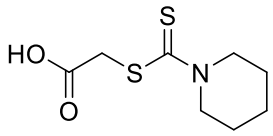

2-((piperidine-1-carbonothioyl)thio)acetic acid (S5). Synthesized according to general procedure A on 1.65 mmol. S5 was obtained as a white crystalline solid (0.277g, 77%). ^{1}H NMR (400 MHz, DMSO-d_6) δ 12.70 (s, 1H), 4.20 (s, 2H), 4.11 (s, 2H), 3.91 (s, 2H), 1.72 – 1.62 (m, 2H), 1.59 (s, 4H). ^{13}C NMR (125 MHz, DMSO-d_6) δ 193.01, 169.42, 52.70, 51.07, 38.69, 25.87, 25.22, 23.53. DART-MS: *m/z* calcd. for C_8 H_{13} N O_2 S_2 $(M+H)^+$ 220.04605, found 220.04581.

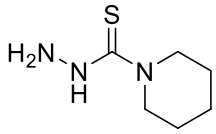

Pipiridine-1-carbothiohydrazide (S6). Synthesized from S5 on 1.23 mmol scale. S6 was obtained as a white solid (0.122 g, 62%). ^{1}H NMR (400 MHz, DMSO-d_6) δ 8.91 (s, 1H), 4.72 (s, 2H), 3.73 – 3.65 (m, 4H), 1.63 – 1.52 (m, 2H), 1.49 – 1.39 (m, 4H). ^{13}C NMR (125 MHz, DMSO-d_6) δ 181.99, 48.46, 25.25, 24.03. DART-MS: *m/z* calcd. for C_6 H_{13} N_3 S $(M+H)^+$ 160.09029, found 160.09035.

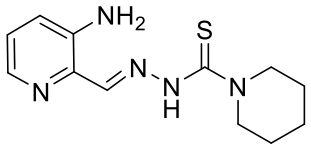

N'-((3-aminopyridin-2-yl)methylene)piperidine-1-carbothiohydrazide (DS-2). Synthesized from S2 and S6 according to general procedure C on 0.57 mmol scale. DS-2 was isolated as a yellow solid (0.098g, 66%). ^{1}H NMR (500 MHz, Acetonitrile-d_3) δ 9.65 (s, 1H), 8.33 (s, 1H), 7.90 (dd, J = 4.3, 1.5 Hz, 1H), 7.09 (ddd, J = 8.3, 1.5, 0.5 Hz, 1H), 7.04 (dd, J = 8.3, 4.3 Hz, 1H), 6.50 (s, 2H), 3.92 – 3.88 (m, 4H), 1.72 – 1.67 (m, 2H), 1.66 – 1.60 (m, 4H). ^{13}C NMR (125 MHz, Acetonitrile-d_3) δ 180.76, 149.70, 144.95, 138.92, 135.74, 125.40, 123.62, 51.34, 26.89, 25.42. DART-MS: *m/z* calcd. for $C_{12}H_{17}N_5S$ $(M+H)^+$ 264.12774, found 264.12488.

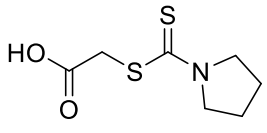

2-((pyrrolidine-1-carbonothioyl)thio)acetic acid (S7). Synthesized according to general procedure A on 2.81 mmol scale. S7 was obtained as a white crystalline solid (0.456 g, 79%). ^{1}H NMR (500 MHz, DMSO-d_6) δ 12.72 (s, 1H), 4.11 (s, 2H), 3.75 (t, J = 7.0 Hz, 2H), 3.64 (t, J = 6.9 Hz, 2H), 2.04 (p, J = 6.8 Hz, 2H), 1.92 (p, J = 6.6 Hz, 2H). ^{13}C NMR (125 MHz, DMSO-d_6) δ 190.06, 169.38, 55.22, 50.54, 38.12, 25.66, 23.80. DART-MS: *m/z* calcd. for C_7 H_{11} N O_2 S_2 $(M+H)^+$ 206.03040, found 206.02979.

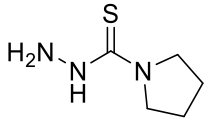

Pyrrolidine-1-carbothiohydrazide (S8). Synthesized from S7 according to general procedure B on 1.12 mmol scale. S8 was obtained as a white crystalline solid (0.112 g, 69%). ^{1}H NMR (500 MHz, DMSO-d_6) δ 8.57 (s, 1H), 4.59 (s, 2H), 3.45 – 3.40 (m, 4H), 1.88 – 1.80 (m, 4H). ^{13}C NMR (125 MHz, DMSO-d_6) δ 179.68, 49.28, 24.69. DART-MS: *m/z* calcd. for C_5 H_{11} N_3 S $(M+H)^+$ 146.07464, found 146.07411.

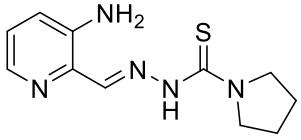

N′-((3-aminopyridin-2-yl)methylene)pyrrolidine-1-carbothiohydrazide (DS-3). Synthesized from S1 and S8 according to general procedure C on 0.40 mmol scale. DS-3 was obtained as a yellow solid (0.063 g, 63%). ^{1}H NMR (500 MHz, DMSO-d_6) δ 11.00 (s, 1H), 8.53 (s, 1H), 7.82 (dd, J = 4.2, 1.5 Hz, 1H), 7.18 (s, 2H), 7.06 (qd, J = 8.4, 2.9 Hz, 2H), 3.64 (s, 4H), 1.93 (s, 4H). ^{13}C NMR (125 MHz, DMSO-d_6) δ 176.04, 148.21, 143.63, 136.52, 134.01, 123.79, 121.85, 32.22. DART-MS: *m/z* calcd. for C_5 H_{11} N_3 S $(M+H)^+$ 250.11209, found 250.11212.

Synthesis of IQ compounds

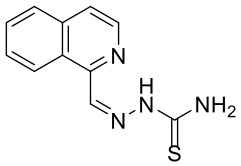

(isoquinolin-1-ylmethylene)hydrazine-1-carbothioamide (IQ-1): Synthesized as previously reported.[1] ^{1}H NMR (500 MHz, DMSO-d_6) δ 11.74 (s, 1H), 9.19 (d, J = 8.5 Hz, 1H), 8.60 – 8.54 (m, 2H), 8.49 (s, 1H), 8.02 (d, J = 8.1 Hz, 1H), 7.86 (d, J = 5.6 Hz, 1H), 7.84 – 7.78 (m, 2H), 7.75 (ddd, J = 8.3, 6.8, 1.4 Hz, 1H). ^{13}C NMR

(125 MHz, DMSO-d_6) δ 178.41, 150.78, 145.99, 142.13, 136.24, 130.47, 129.08, 127.22, 126.94, 125.58, 121.77. DART-MS: *m/z* calcd. for $C_{11}H_{10}N_4S$ $(M+H)^+$ 231.06989, found 231.06938

[1]Agrawal, et al., *J. Med. Chem.* 1968, *11*(4), 700-703.

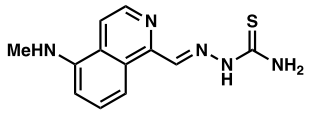

(*E*)-2-((5-(methylamino)isoquinolin-1-yl)methylene)hydrazine-1-carbothioamide (IQ-2): Synthesized as previously reported.[2] ^{1}H NMR (500 MHz, DMSO-d_6): δ 12.32 (br s, 1H), 9.07 (br s, 1H), 8.92 (s, 1H), 8.90 (s, 1H), 8.57 (d, J = 6.6 Hz, 1H), 8.52 (d, J = 6.7 Hz, 1H), 7.85 (t, J = 8.2 Hz, 1H), 7.56 (d, J = 8.3 Hz, 1H), 7.30 (br s, 1H), 7.01 (d, J = 8.0 Hz, 1H), 2.91 (s, 3H). ^{13}C NMR (125 MHz, DMSO-d_6): δ 179.40, 146.27, 146.00(2C), 133.09, 128.72, 126.76(2C), 119.39, 111.17, 110.68, 30.39.

[2]Sartorelli., et al., *J. Med. Chem.* 1974, *17*, 1145.

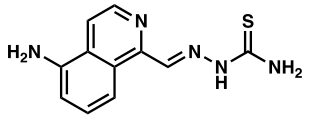

(*E*)-2-((5-aminoisoquinolin-1-yl)methylene)hydrazine-1-carbothioamide (IQ-3): Synthesized as previously reported.[3] ^{1}H NMR (500 MHz, DMSO-d_6): δ 11.66 (br s, 1H), 8.57 (s, 1H), 8.42 (d, *J* = 5.8 Hz, 1H), 8.31 (br s, 1H), 8.25 (d, *J* = 8.5 Hz, 1H), 7.98 (d, *J* = 5.8 Hz, 1H), 7.60 (br s, 1H), 7.42 (t, *J* = 5.8 Hz, 1H), 6.89 (d, *J* = 7.1 Hz, 1H), 6.02 (s, 2H). ^{13}C NMR (125 MHz, DMSO-d_6): δ 178.46, 150.36, 145.86, 144.62, 140.01, 129.74, 126.78, 125.83, 116.50, 113.12, 110.74.

[3]Sartorelli., et al., *J. Med. Chem.* 1968, *11*, 700.

^{1}H and ^{13}C NMR spectra

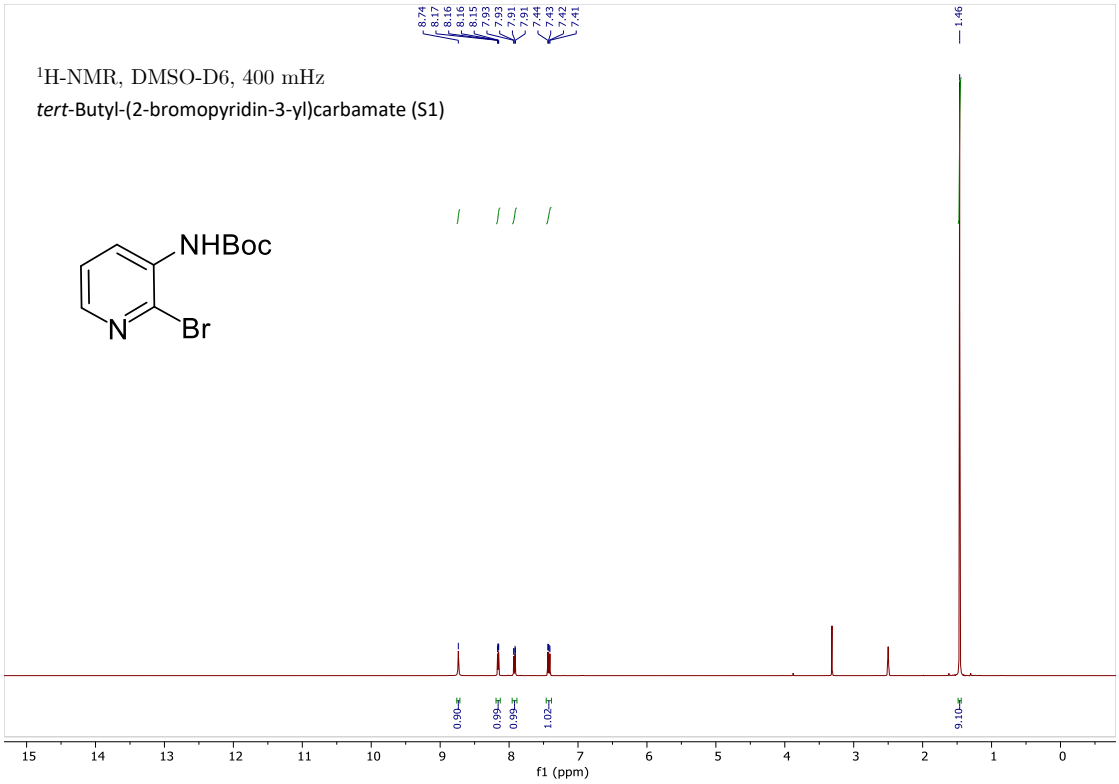

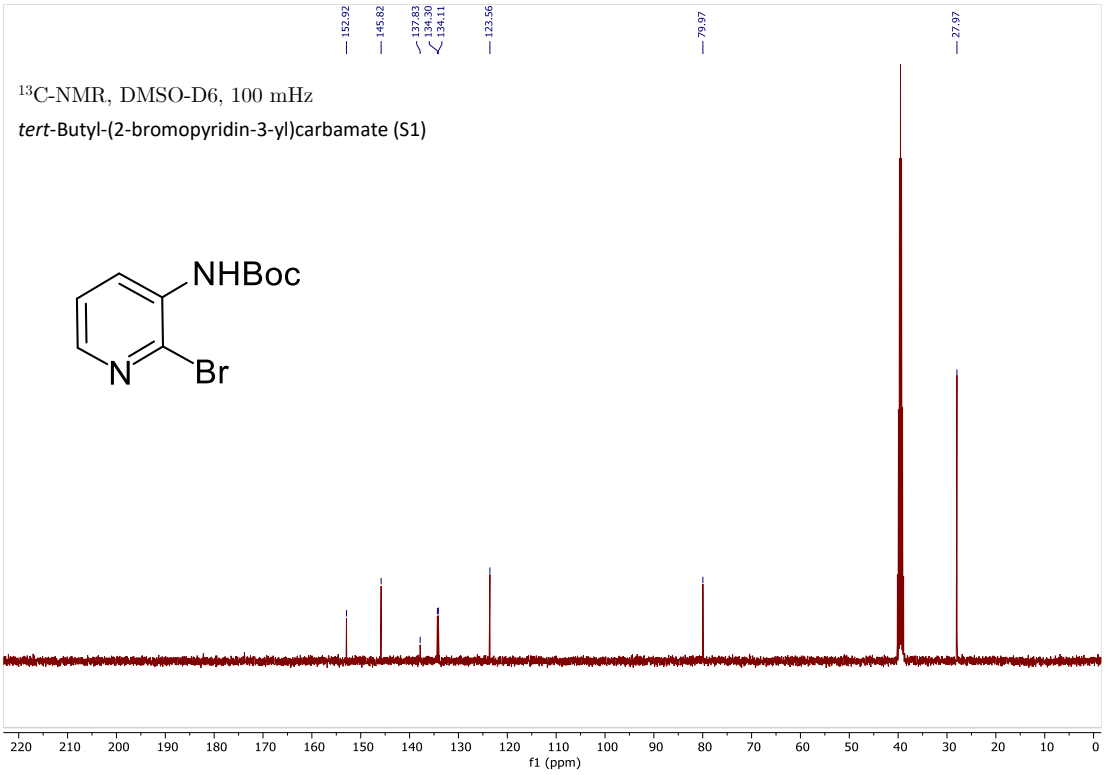
152.92
145.82
137.83
134.30
134.11
123.56
79.97
27.97
^{13}C-NMR, DMSO-D6, 100 mHz
tert-Butyl-(2-bromopyridin-3-yl)carbamate (S1)
NHBoc
N
Br
220 210 200 190 180 170 160 150 140 130 120 110 100 90 80 70 60 50 40 30 20 10 0
f1 (ppm)

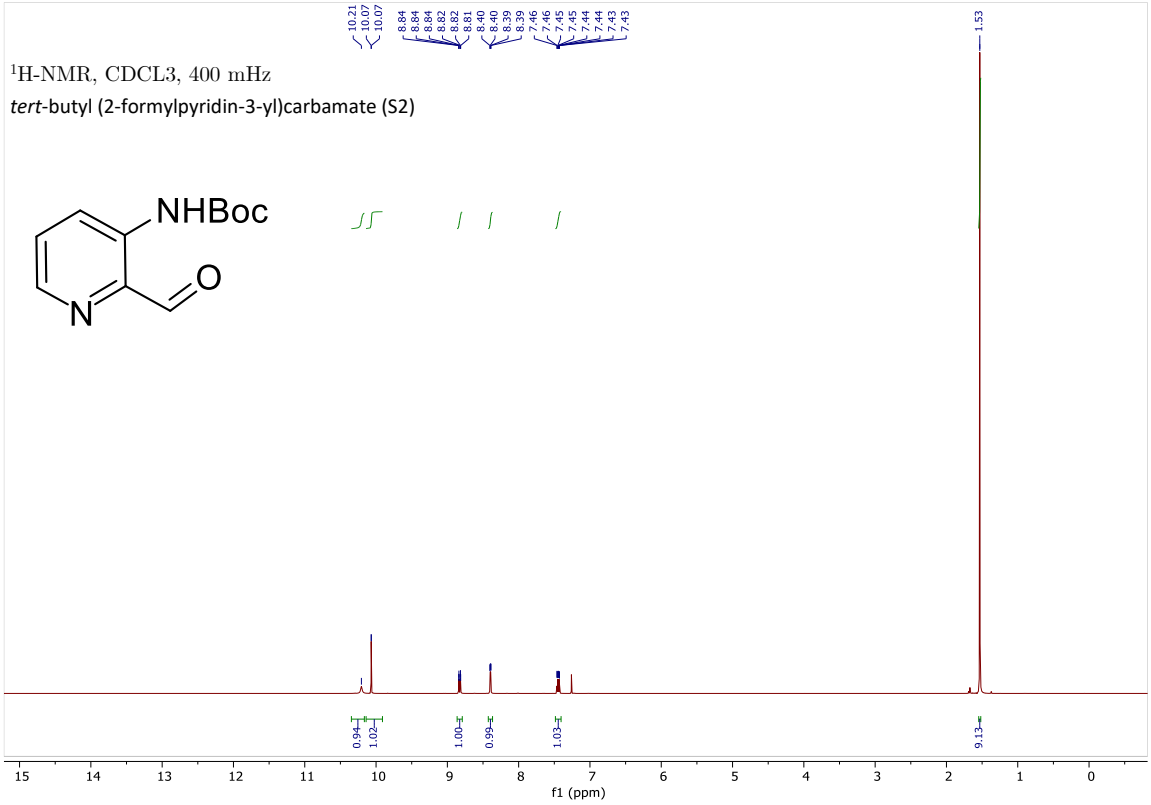
10.21
10.07
10.07
8.84
8.84
8.84
8.82
8.82
8.81
8.40
8.40
8.39
8.39
7.46
7.46
7.45
7.45
7.44
7.44
7.43
7.43
1.53
^{1}H-NMR, CDCL3, 400 mHz
tert-butyl (2-formylpyridin-3-yl)carbamate (S2)
NHBoc
O
N
0.94
1.02
1.00
0.99
1.03
9.13
15
14
13
12
11
10
9
8
7
6
5
4
3
2
1
0
f1 (ppm)

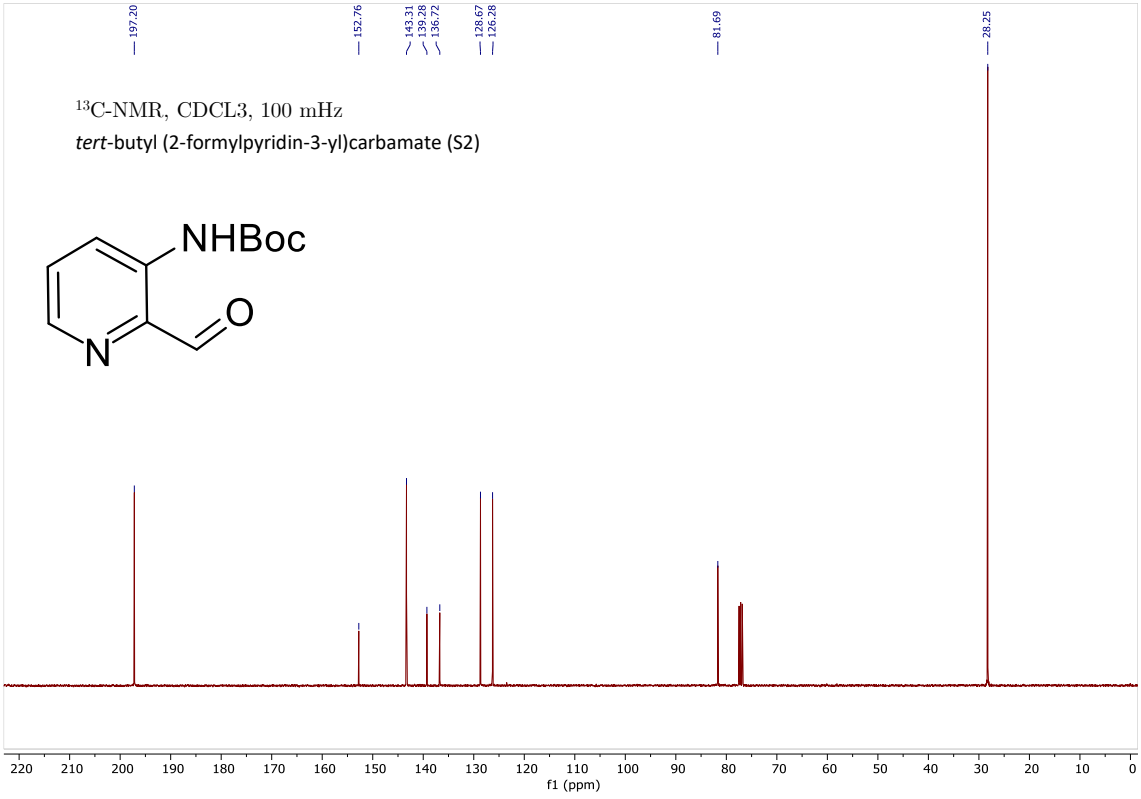
197.20
152.76
143.31
139.28
136.72
128.67
126.28
81.69
28.25
^{13}C-NMR, CDCL3, 100 mHz
tert-butyl (2-formylpyridin-3-yl)carbamate (S2)
NHBoc
O
N
220 210 200 190 180 170 160 150 140 130 120 110 100 90 80 70 60 50 40 30 20 10 0
f1 (ppm)

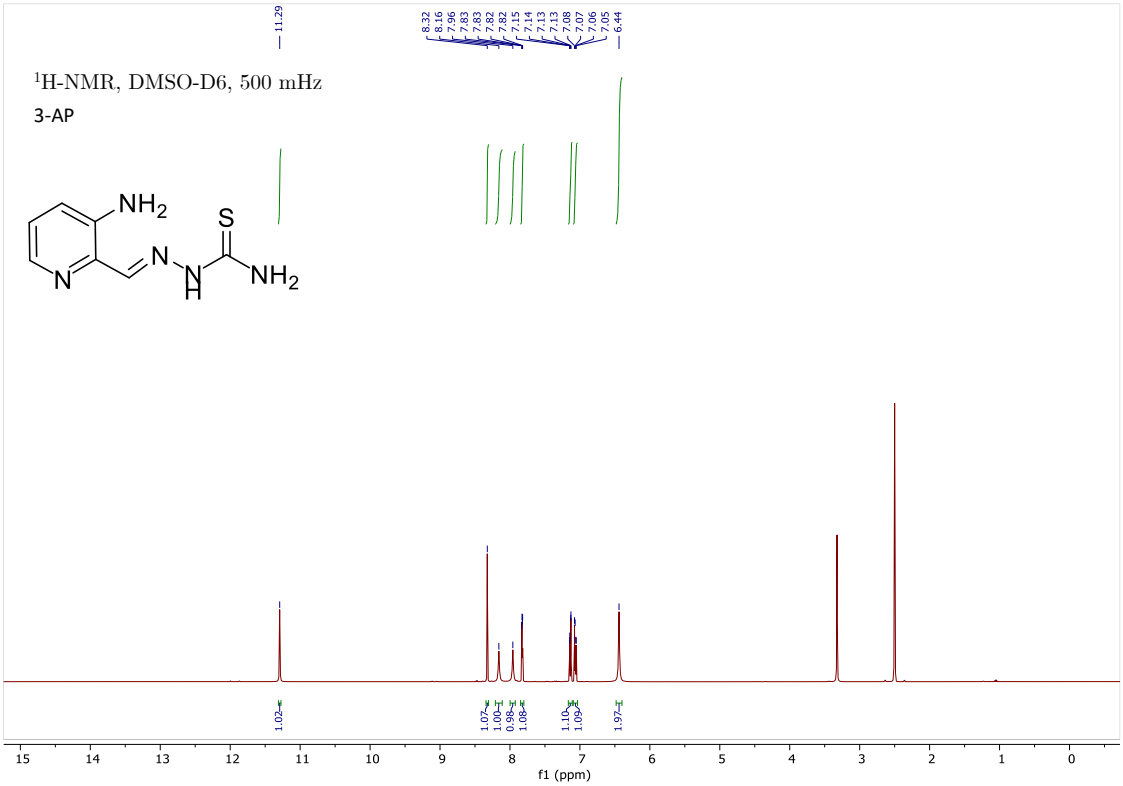
11.29
8.32
8.16
7.96
7.83
7.83
7.82
7.82
7.15
7.14
7.13
7.13
7.08
7.07
7.06
7.05
6.44
1H-NMR, DMSO-D6, 500 mHz
3-AP
NH2
S
N
N
N
H
NH2
1.02
1.07
1.00
0.98
1.08
1.10
1.09
1.97
15
14
13
12
11
10
9
8
7
6
5
4
3
2
1
0
f1 (ppm)

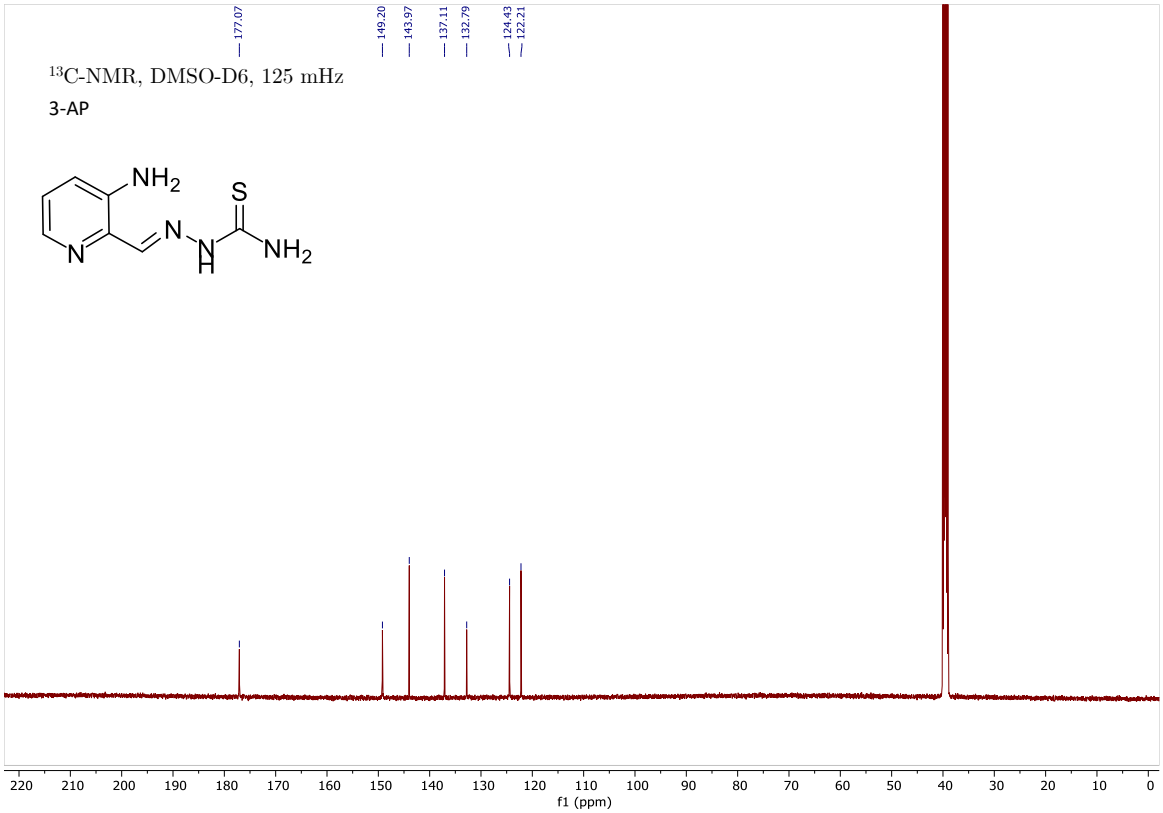
177.07
149.20
143.97
137.11
132.79
124.43
122.21
13C-NMR, DMSO-D6, 125 mHz
3-AP
NH2
S
N
N
N
H
NH2
220 210 200 190 180 170 160 150 140 130 120 110 100 90 80 70 60 50 40 30 20 10 0
f1 (ppm)

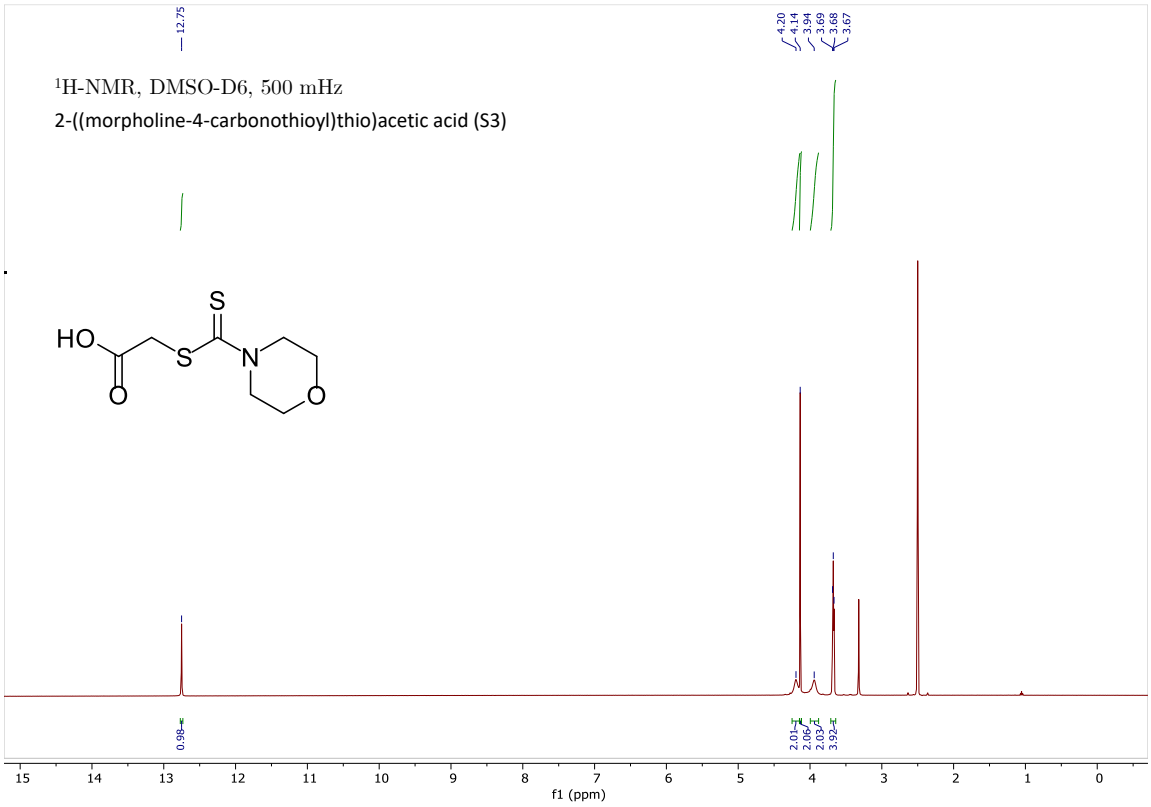
12.75
4.20
4.14
3.94
3.69
3.68
3.67
1H-NMR, DMSO-D6, 500 mHz
2-((morpholine-4-carbonothioyl)thio)acetic acid (S3)
HO
O
S
S
N
O
0.98
2.01
2.06
2.03
3.92
15
14
13
12
11
10
9
8
7
6
5
4
3
2
1
0
f1 (ppm)

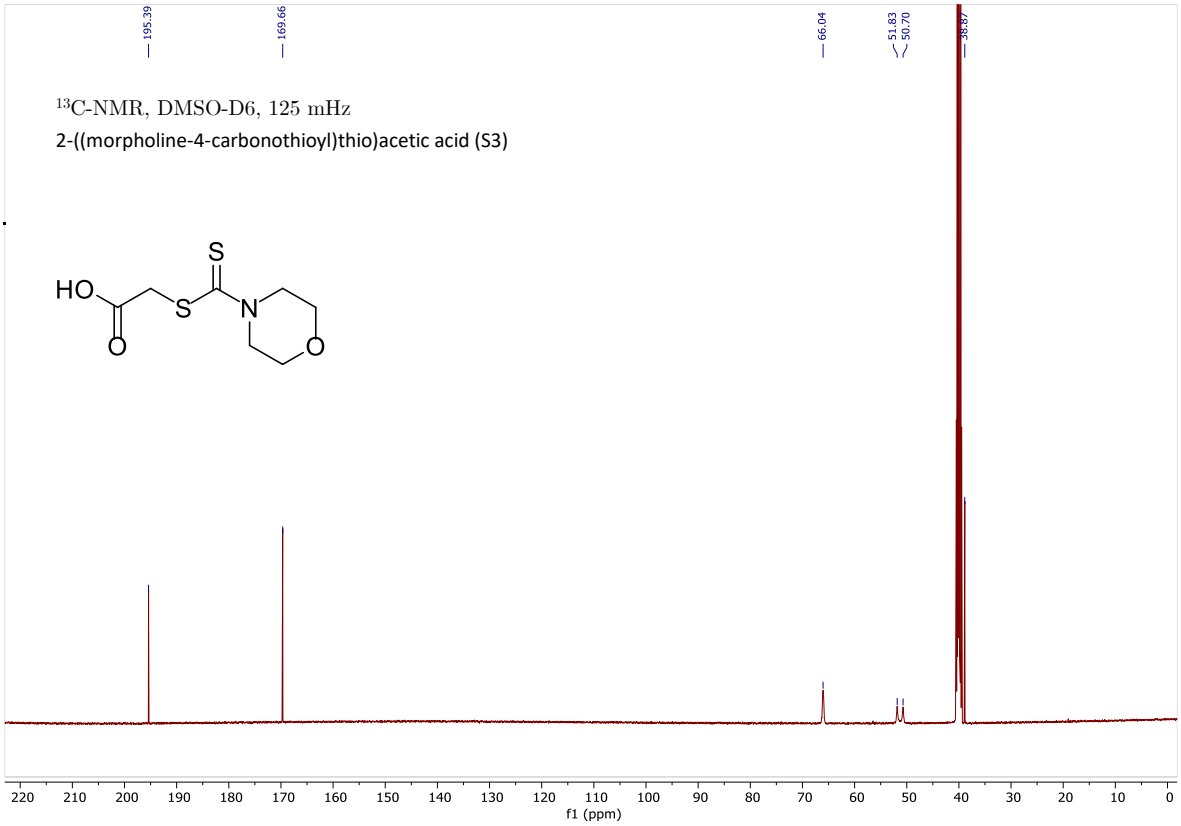
195.39
169.66
66.04
51.83
50.70
38.87
^{13}C-NMR, DMSO-D6, 125 mHz
2-((morpholine-4-carbonothioyl)thio)acetic acid (S3)
HO
O
S
S
N
O
220 210 200 190 180 170 160 150 140 130 120 110 100 90 80 70 60 50 40 30 20 10 0
f1 (ppm)

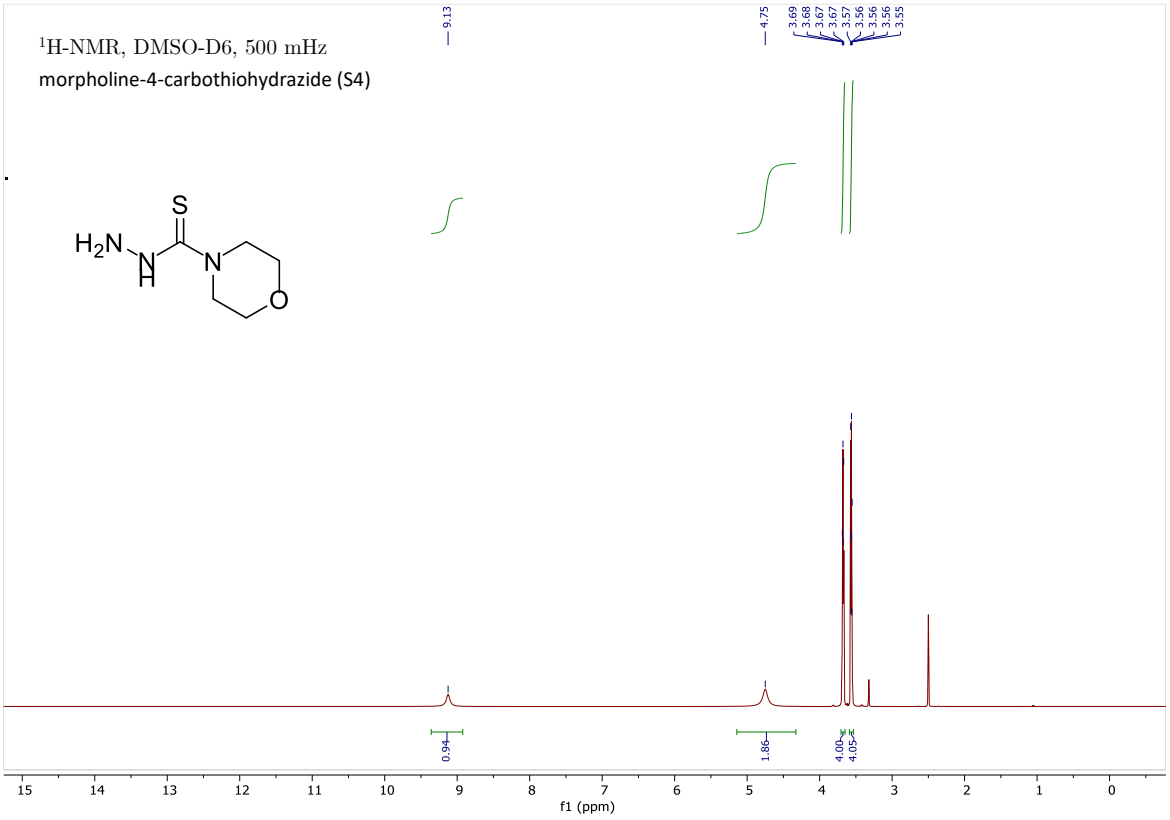
^{1}H-NMR, DMSO-D6, 500 mHz
morpholine-4-carbothiohydrazide (S4)
9.13
4.75
3.69
3.68
3.67
3.67
3.57
3.56
3.56
3.56
3.55
0.94
1.86
4.00
4.05
15
14
13
12
11
10
9
8
7
6
5
4
3
2
1
0
f1 (ppm)

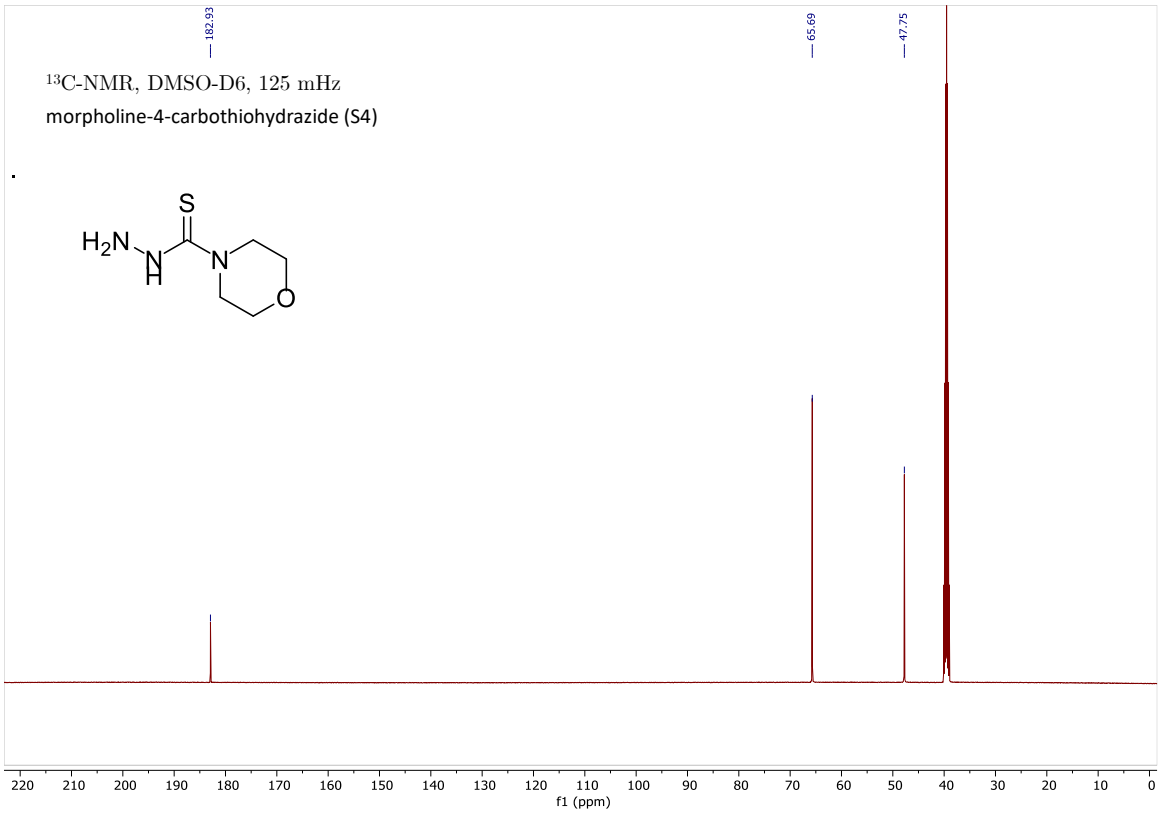
182.93
65.69
47.75
13C-NMR, DMSO-D6, 125 mHz
morpholine-4-carbothiohydrazide (S4)
S
H2N
N
H
N
O
220 210 200 190 180 170 160 150 140 130 120 110 100 90 80 70 60 50 40 30 20 10 0
f1 (ppm)

^{1}H-NMR, DMSO-D6, 500 mHz

Compound: MS-1

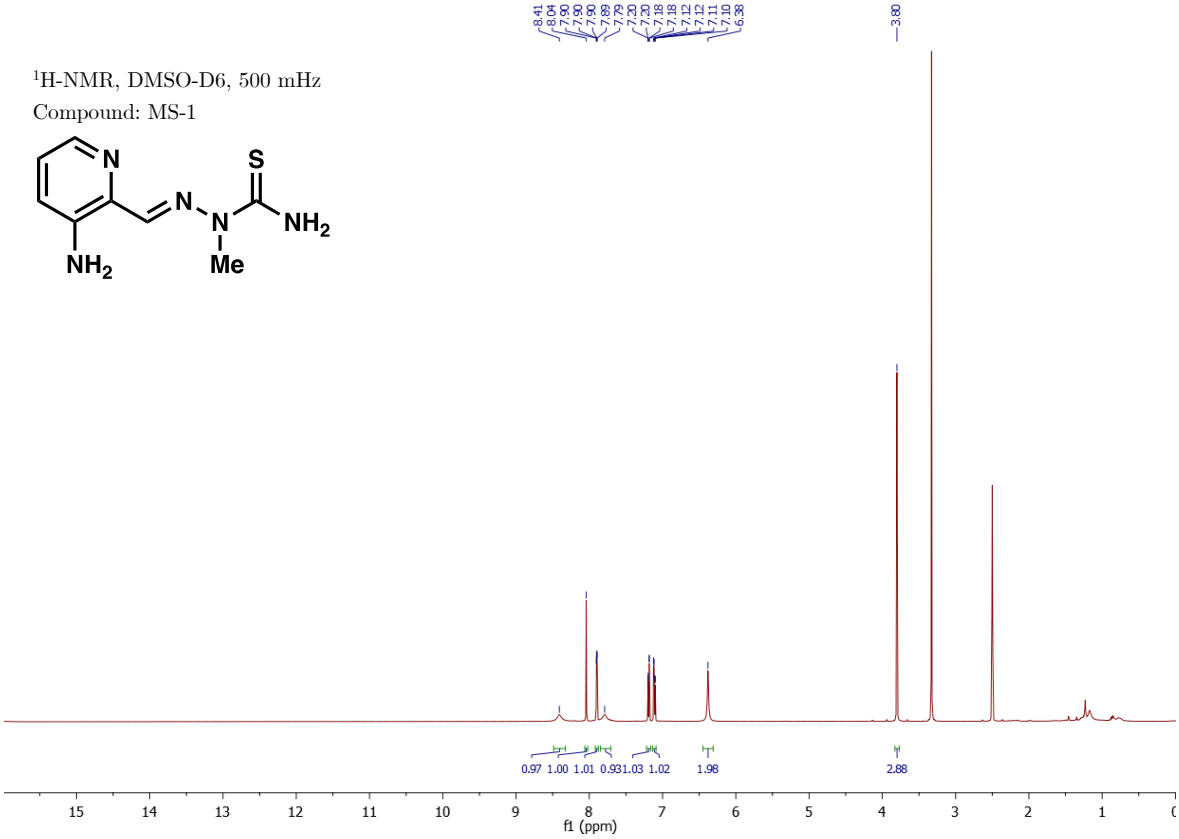

^{13}C-NMR, DMSO-D6, 125 mHz

Compound: MS-1

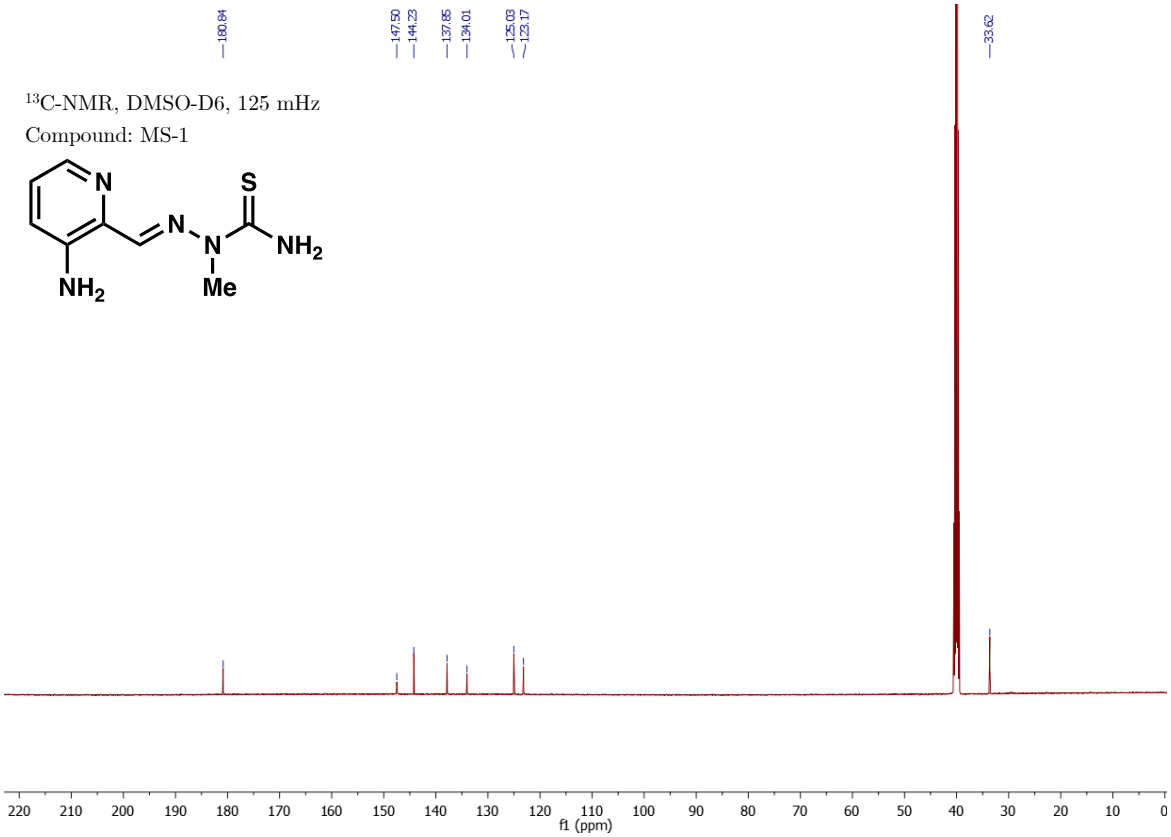

[1]H-NMR, DMSO-D6, 500 mHz

Compound: MS-2

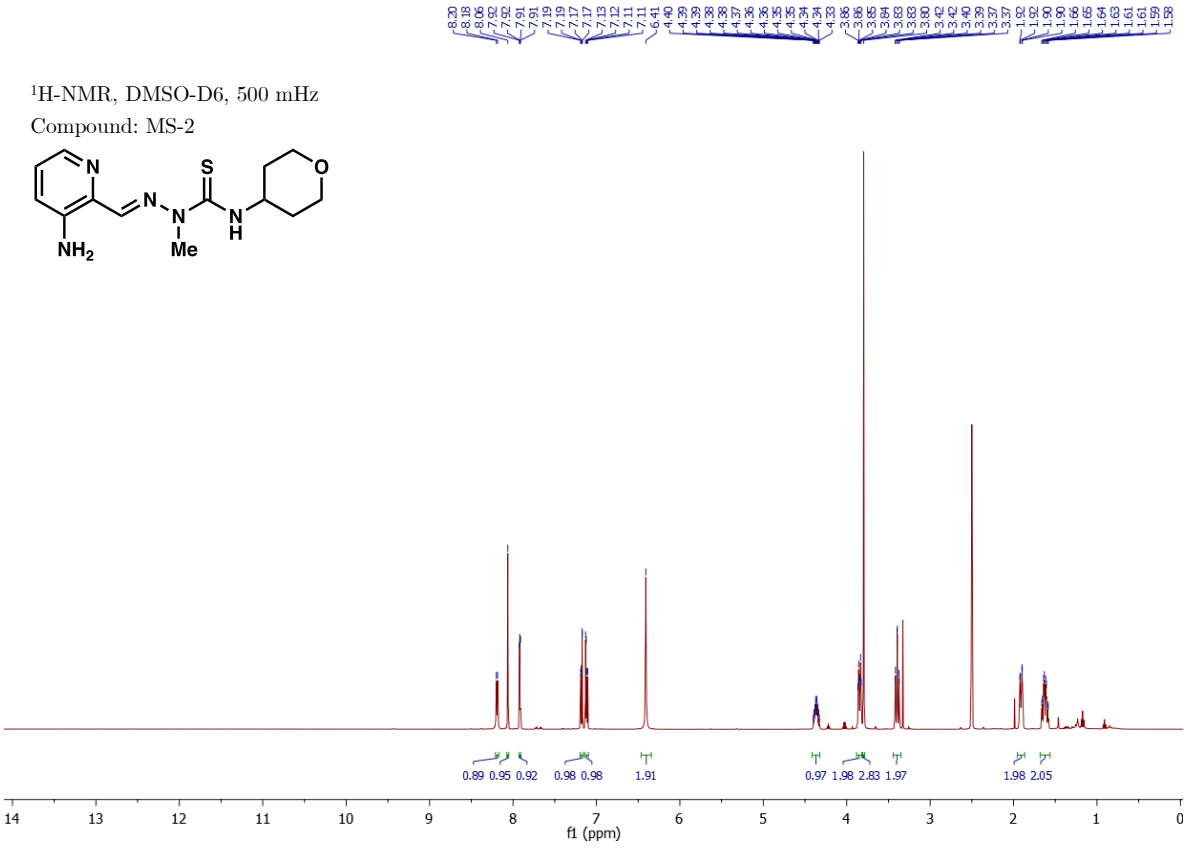

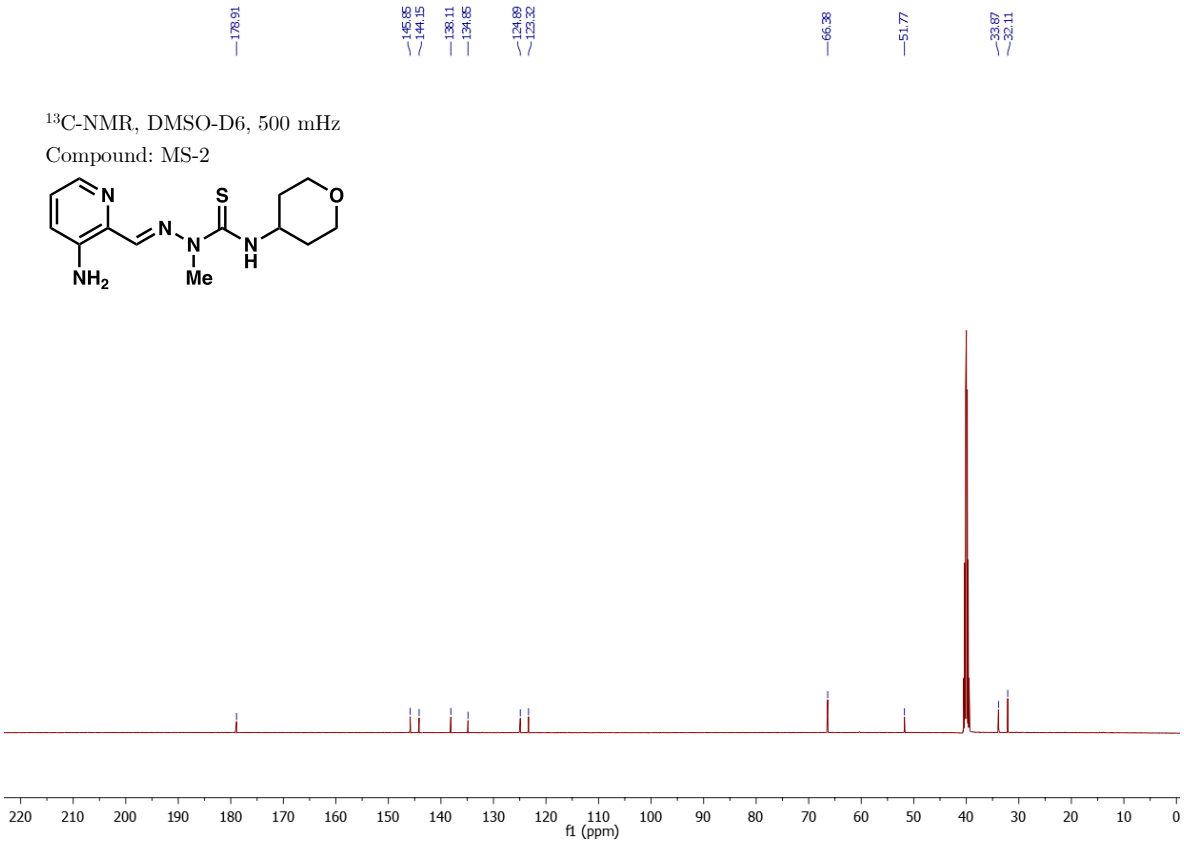

^{13}C-NMR, DMSO-D6, 500 mHz

Compound: MS-2

^{1}H-NMR, DMSO-D6, 500 mHz

Compound: MS-3

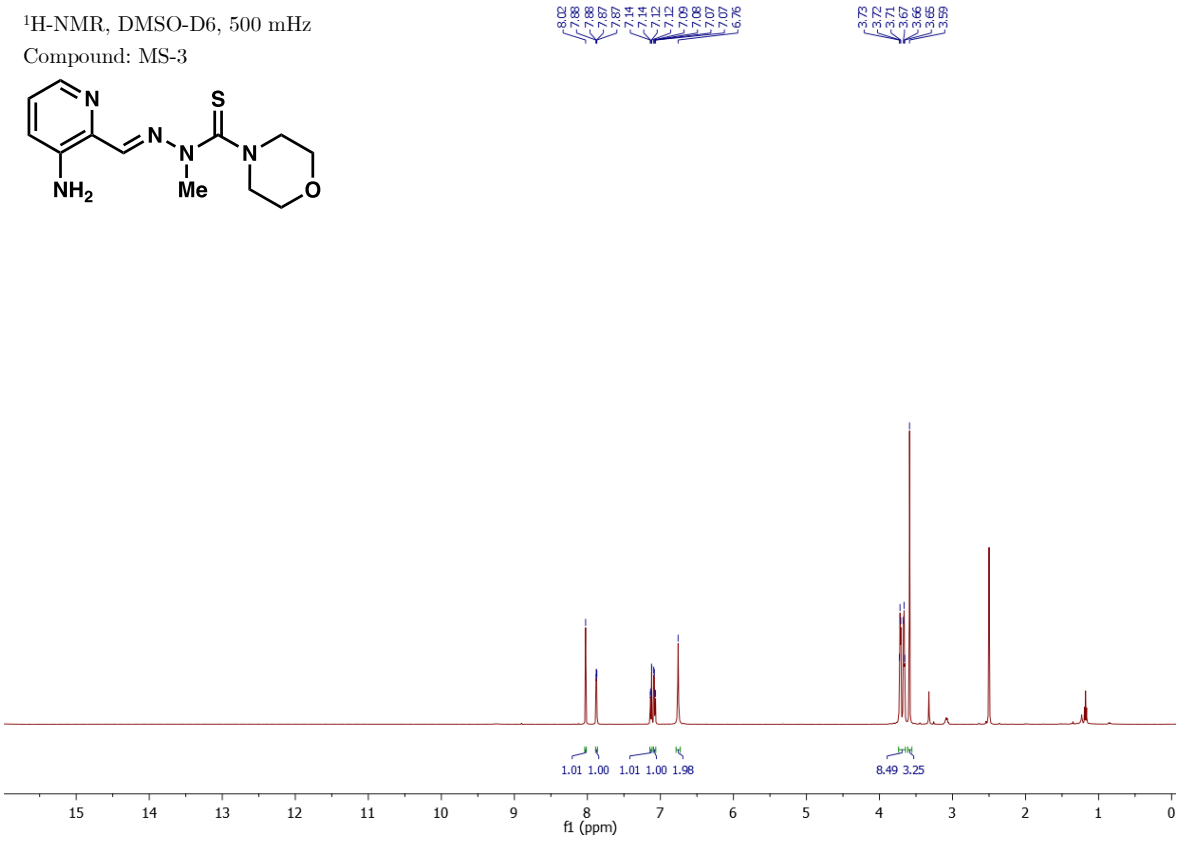

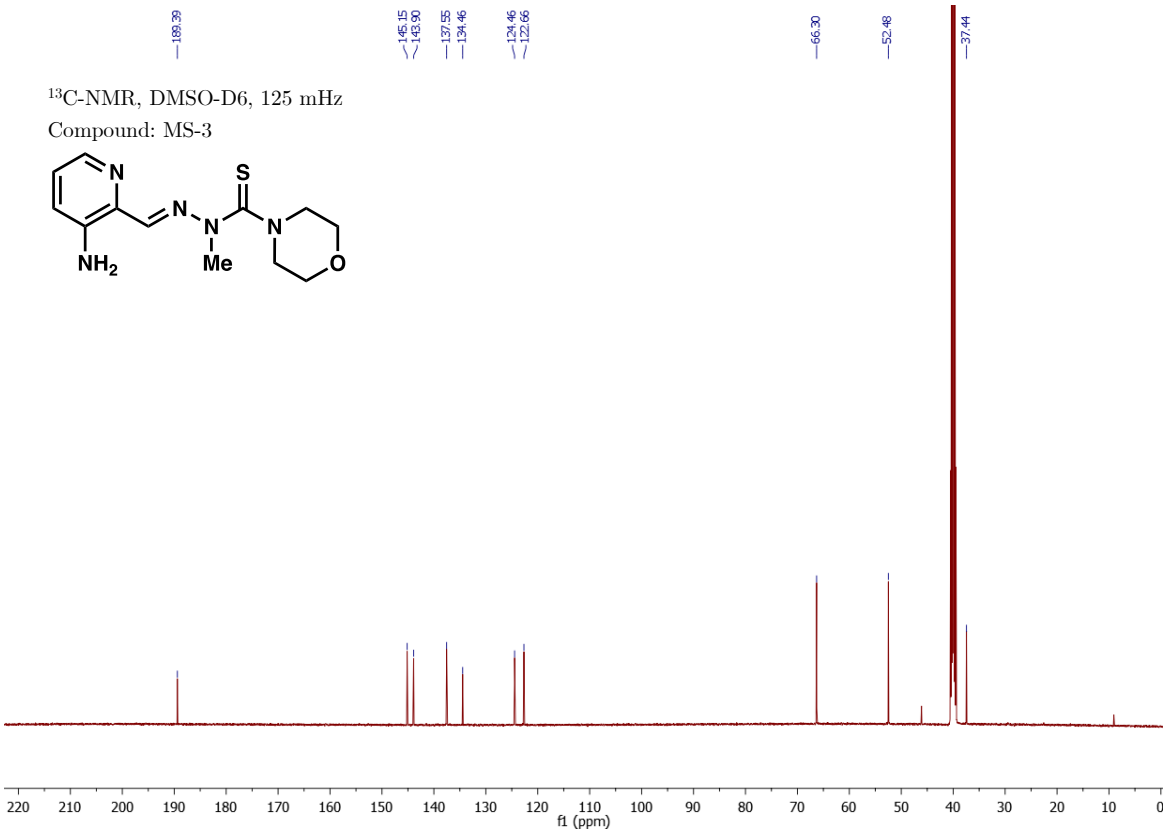

^{13}C-NMR, DMSO-D6, 125 mHz

Compound: MS-3

[1]H-NMR, DMSO-d_6, 500 mHz

Compound: TS-1

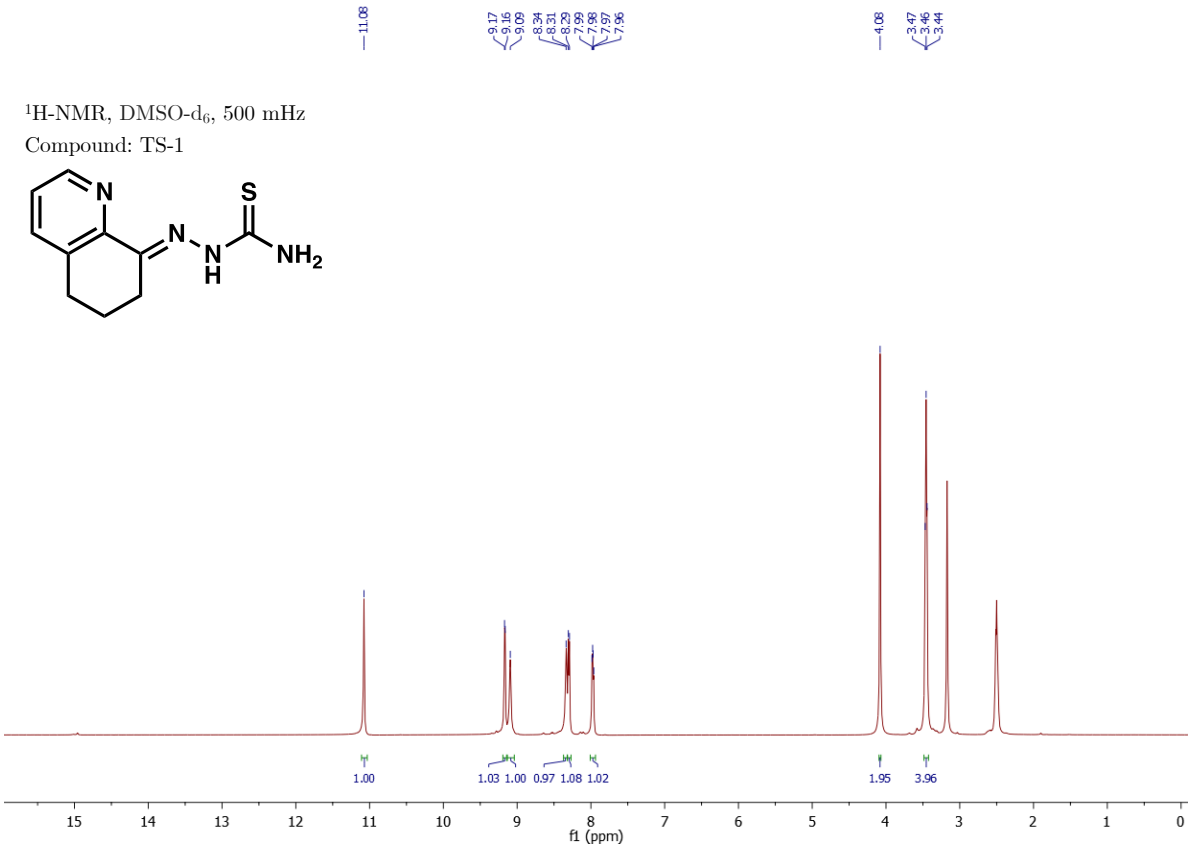

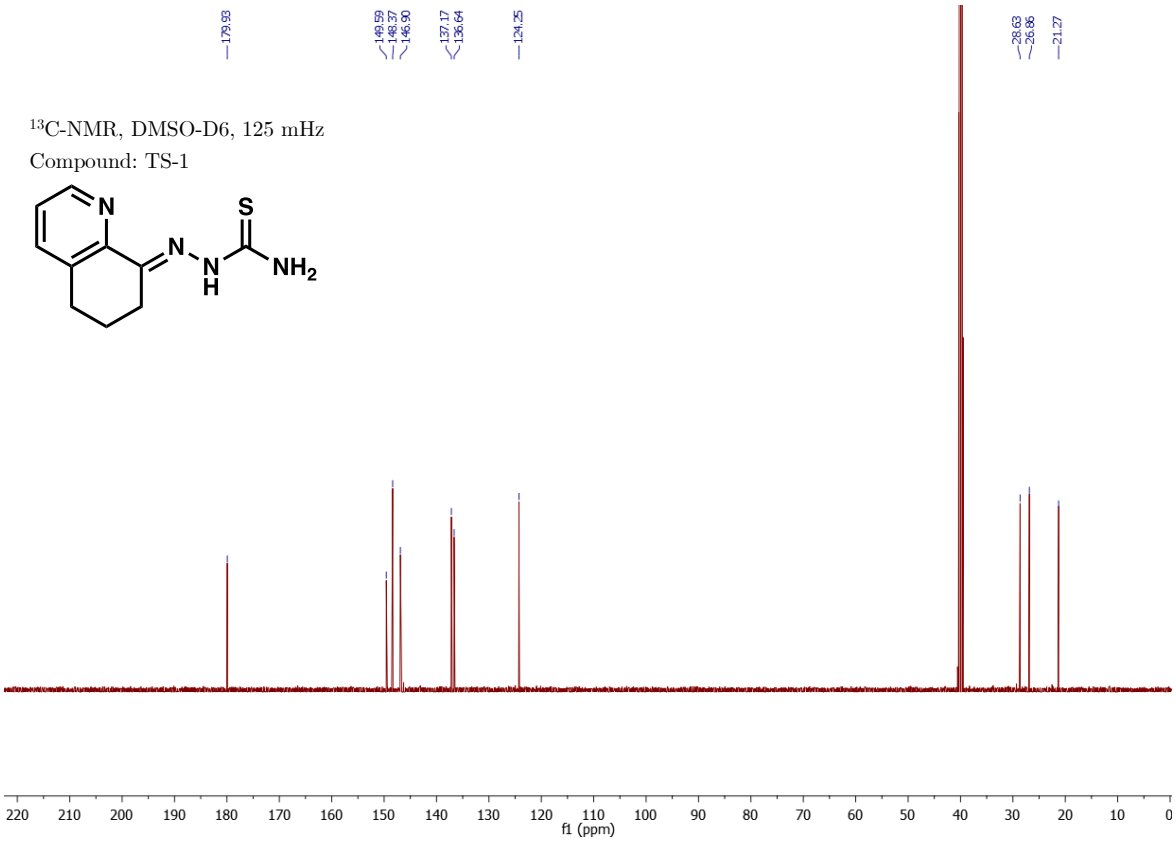
179.93
149.59
148.37
146.90
137.17
136.64
124.25
28.63
26.86
21.27
13C-NMR, DMSO-D6, 125 mHz
Compound: TS-1
N
S
N
N
H
NH2
220 210 200 190 180 170 160 150 140 130 120 110 100 90 80 70 60 50 40 30 20 10 0
f1 (ppm)

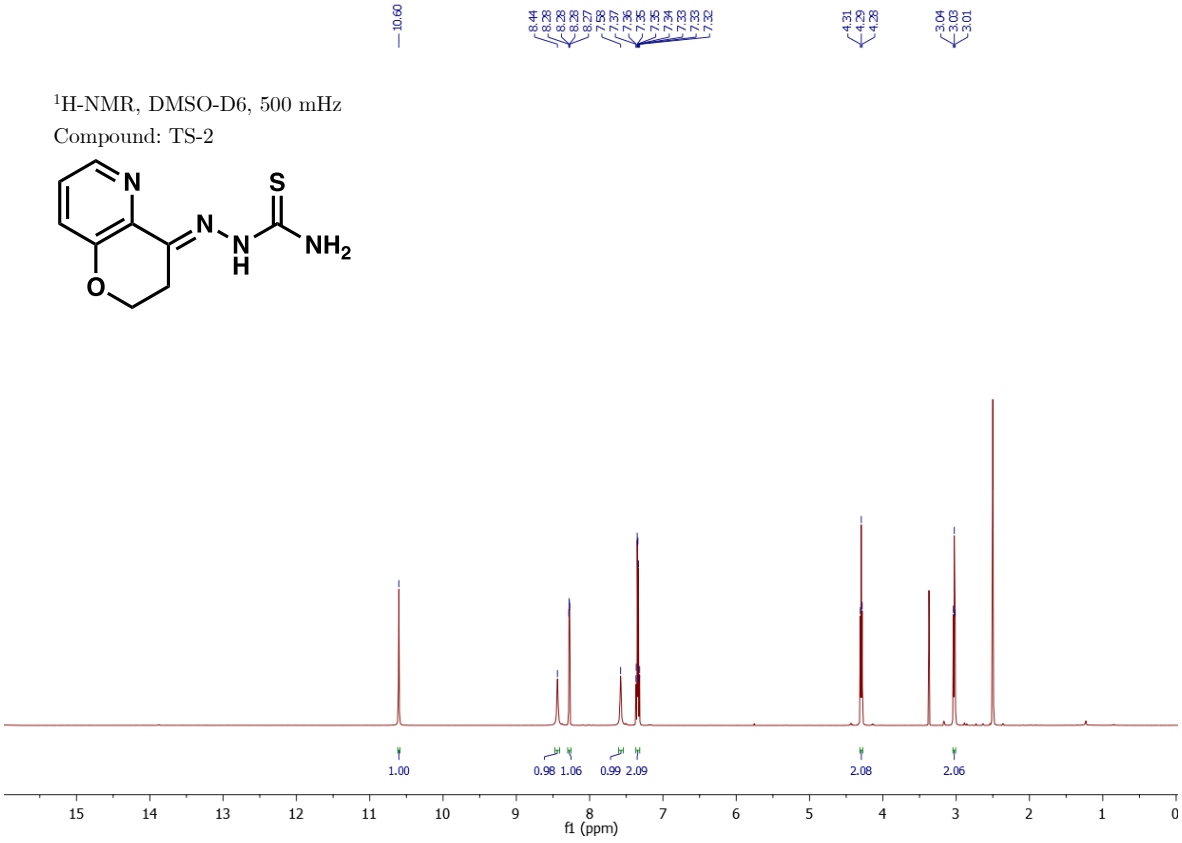

^{1}H-NMR, DMSO-D6, 500 mHz

Compound: TS-2

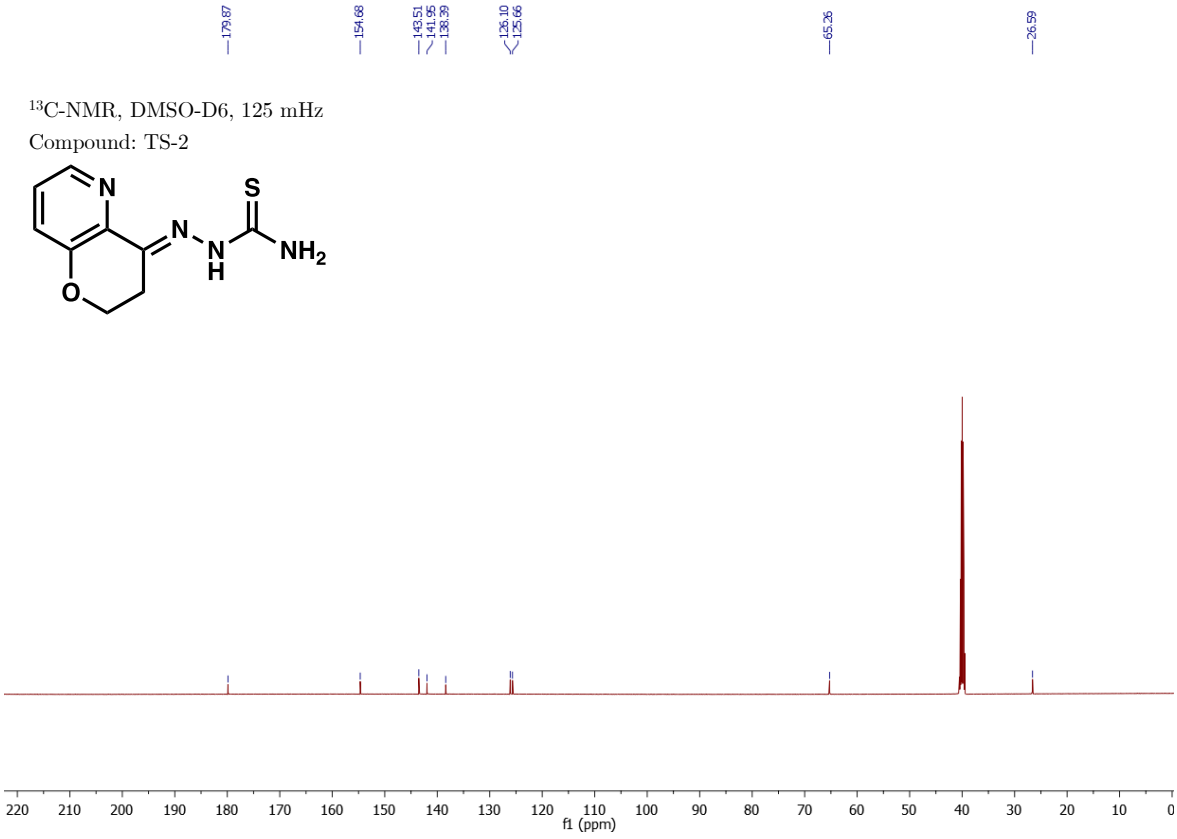

^{13}C-NMR, DMSO-D6, 125 mHz

Compound: TS-2

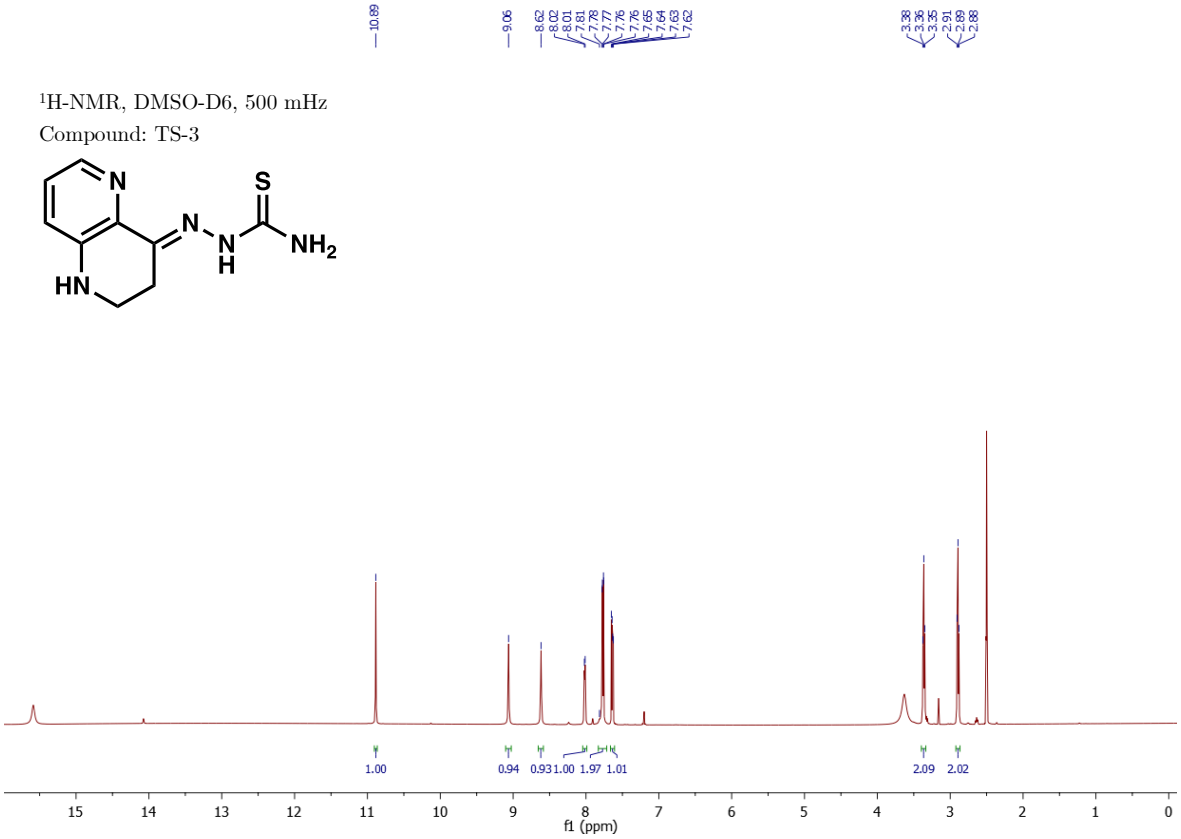

^{1}H-NMR, DMSO-D6, 500 mHz

Compound: TS-3

^{13}C-NMR, DMSO-D6, 125 mHz

Compound: TS-3

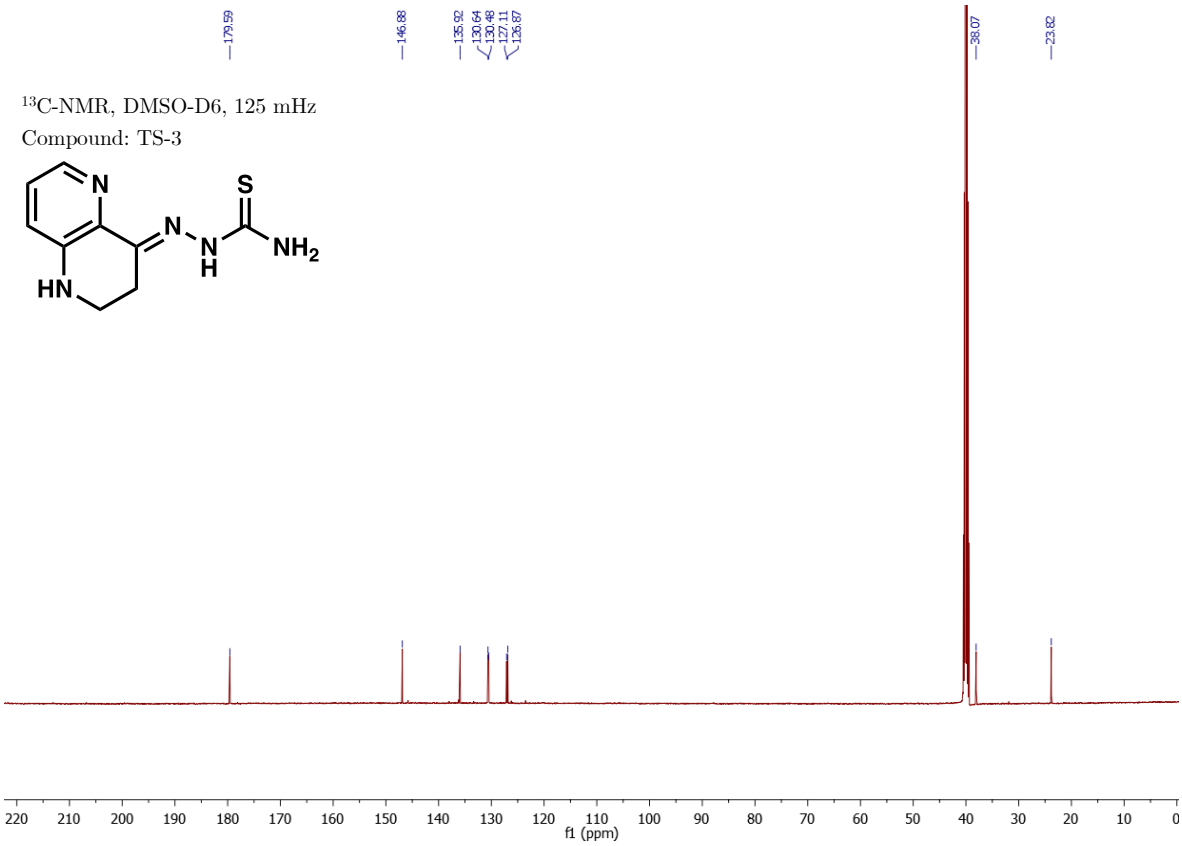

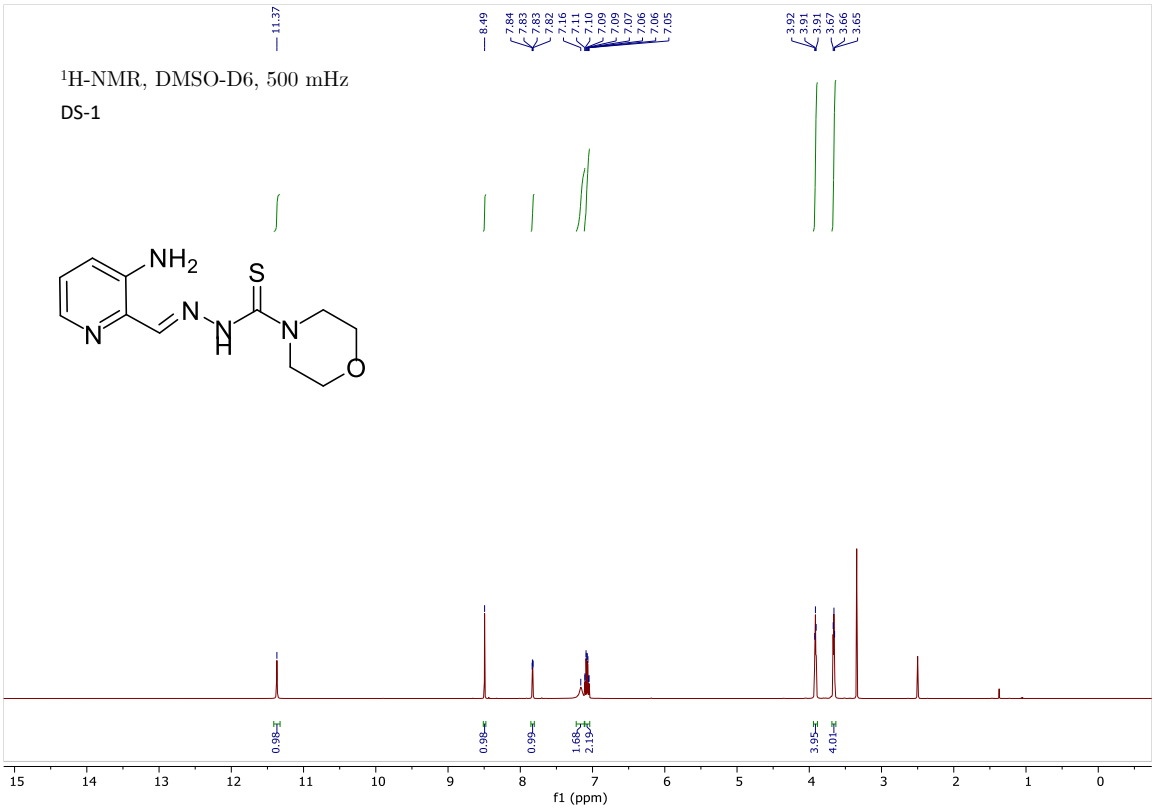
11.37
8.49
7.84
7.83
7.83
7.82
7.16
7.11
7.10
7.09
7.09
7.07
7.06
7.06
7.05
3.92
3.91
3.91
3.67
3.66
3.65
1H-NMR, DMSO-D6, 500 mHz
DS-1
NH2
S
N
N
H
N
O
0.98
0.98
0.99
1.68
2.19
3.95
4.01
15
14
13
12
11
10
9
8
7
6
5
4
3
2
1
0
f1 (ppm)

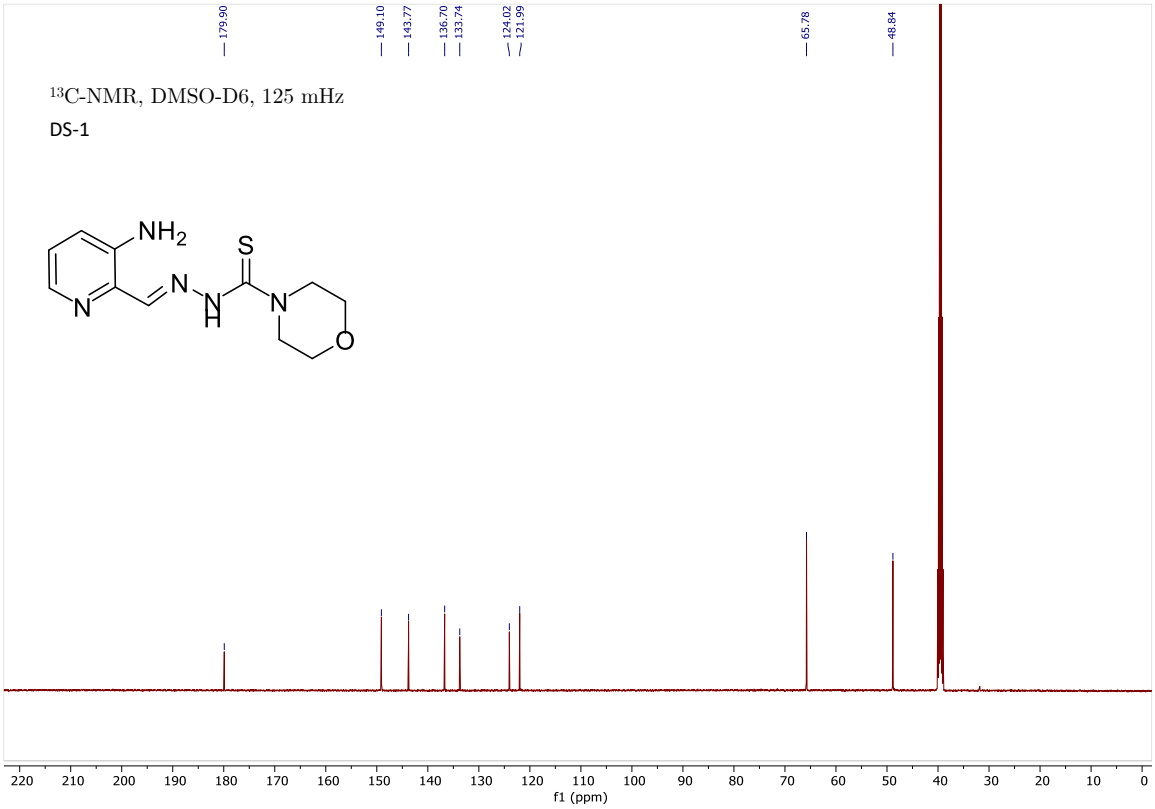
179.90
149.10
143.77
136.70
133.74
124.02
121.99
65.78
48.84
13C-NMR, DMSO-D6, 125 mHz
DS-1
NH2
S
N
N
H
N
O
220 210 200 190 180 170 160 150 140 130 120 110 100 90 80 70 60 50 40 30 20 10 0
f1 (ppm)

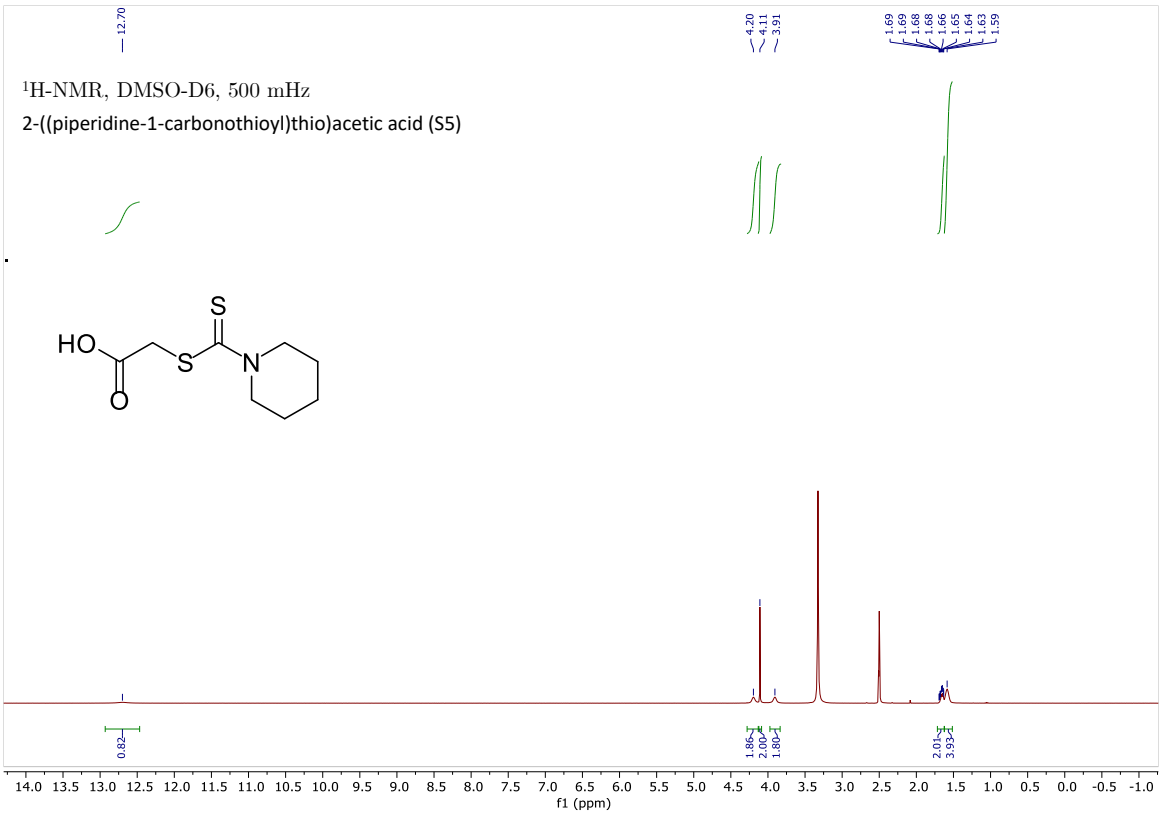
12.70
4.20
4.11
3.91
1.69
1.69
1.68
1.68
1.66
1.65
1.64
1.63
1.59
1H-NMR, DMSO-D6, 500 mHz
2-((piperidine-1-carbonothioyl)thio)acetic acid (S5)
HO
O
S
S
N
0.82
1.86
2.00
1.80
2.01
3.93
14.0 13.5 13.0 12.5 12.0 11.5 11.0 10.5 10.0 9.5 9.0 8.5 8.0 7.5 7.0 6.5 6.0 5.5 5.0 4.5 4.0 3.5 3.0 2.5 2.0 1.5 1.0 0.5 0.0 -0.5 -1.0
f1 (ppm)

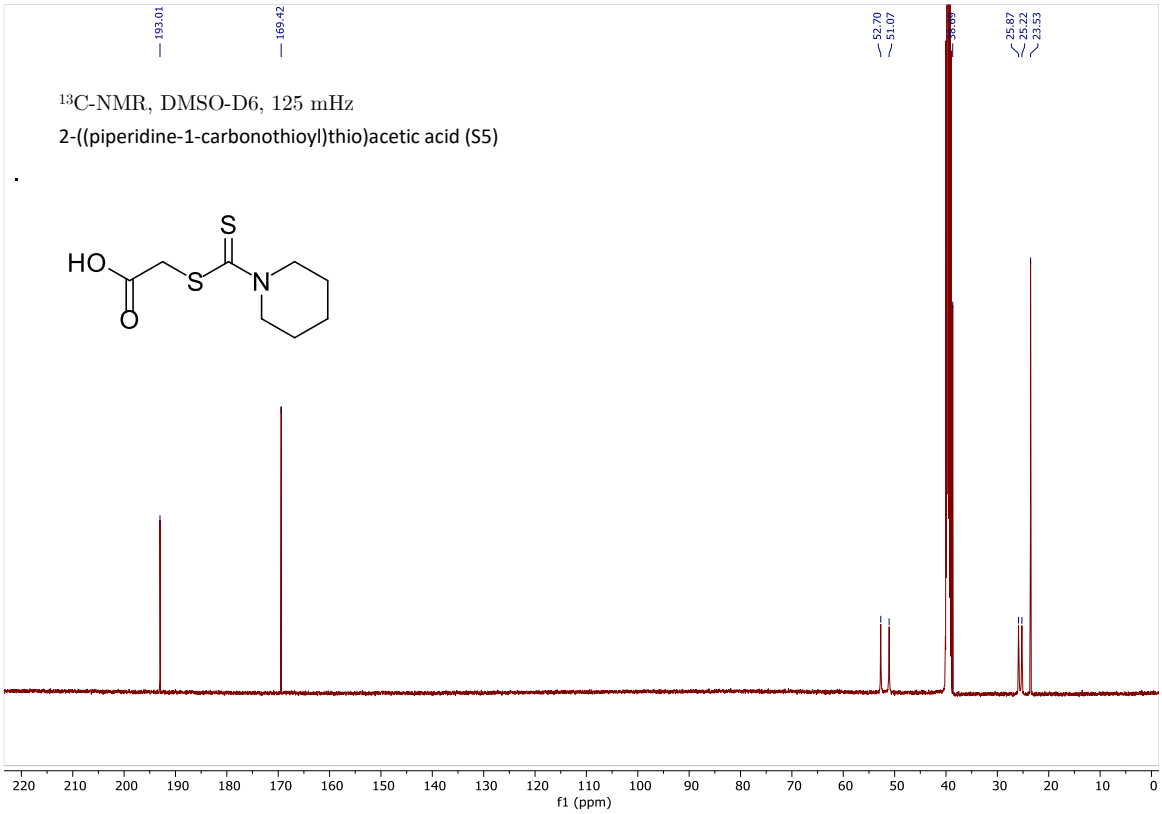
193.01
169.42
52.70
51.07
39.03
25.87
25.22
23.53
^{13}C-NMR, DMSO-D6, 125 mHz
2-((piperidine-1-carbonothioyl)thio)acetic acid (S5)
HO
O
S
S
N
220 210 200 190 180 170 160 150 140 130 120 110 100 90 80 70 60 50 40 30 20 10 0
f1 (ppm)

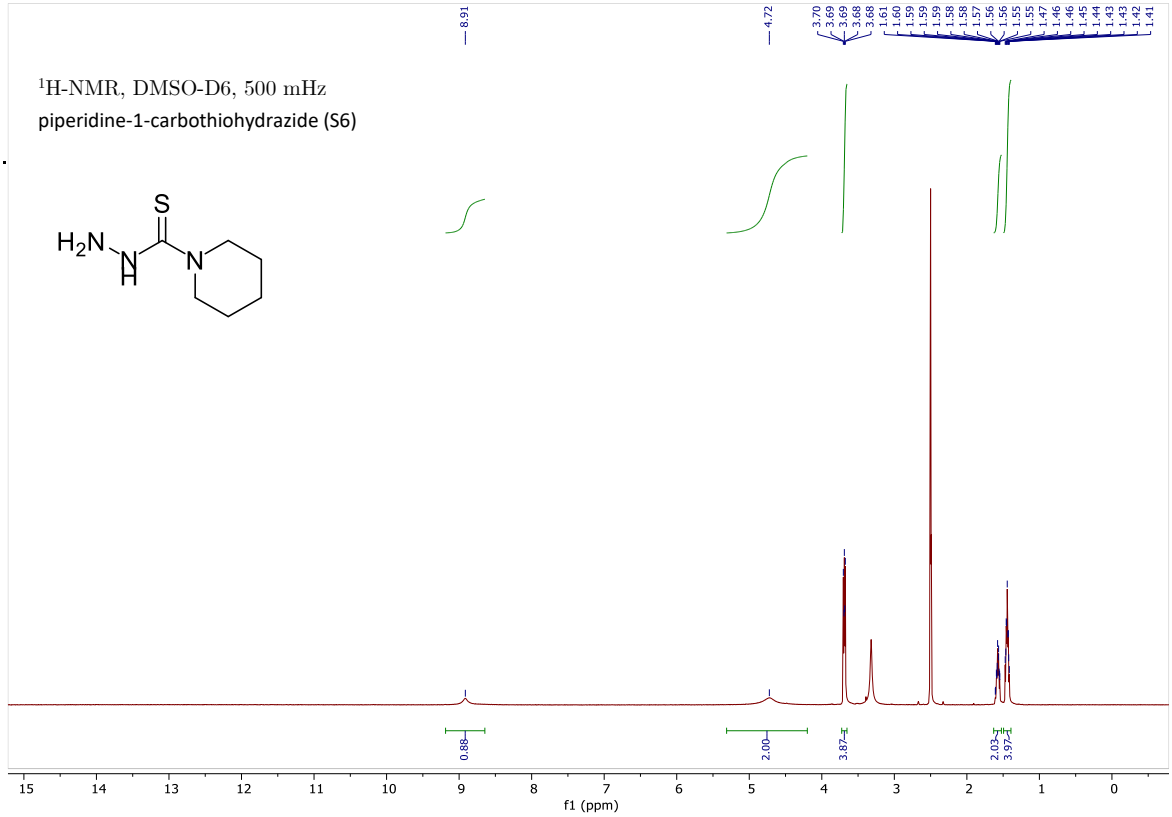
^{1}H-NMR, DMSO-D6, 500 mHz
piperidine-1-carbothiohydrazide (S6)
S
H_2N
N
H
N
8.91
4.72
3.70
3.69
3.69
3.68
3.68
1.61
1.60
1.59
1.59
1.59
1.58
1.58
1.57
1.56
1.56
1.55
1.55
1.47
1.46
1.46
1.45
1.44
1.43
1.43
1.42
1.41
0.88
2.00
3.87
2.03
3.97
15
14
13
12
11
10
9
8
7
6
5
4
3
2
1
0
f1 (ppm)

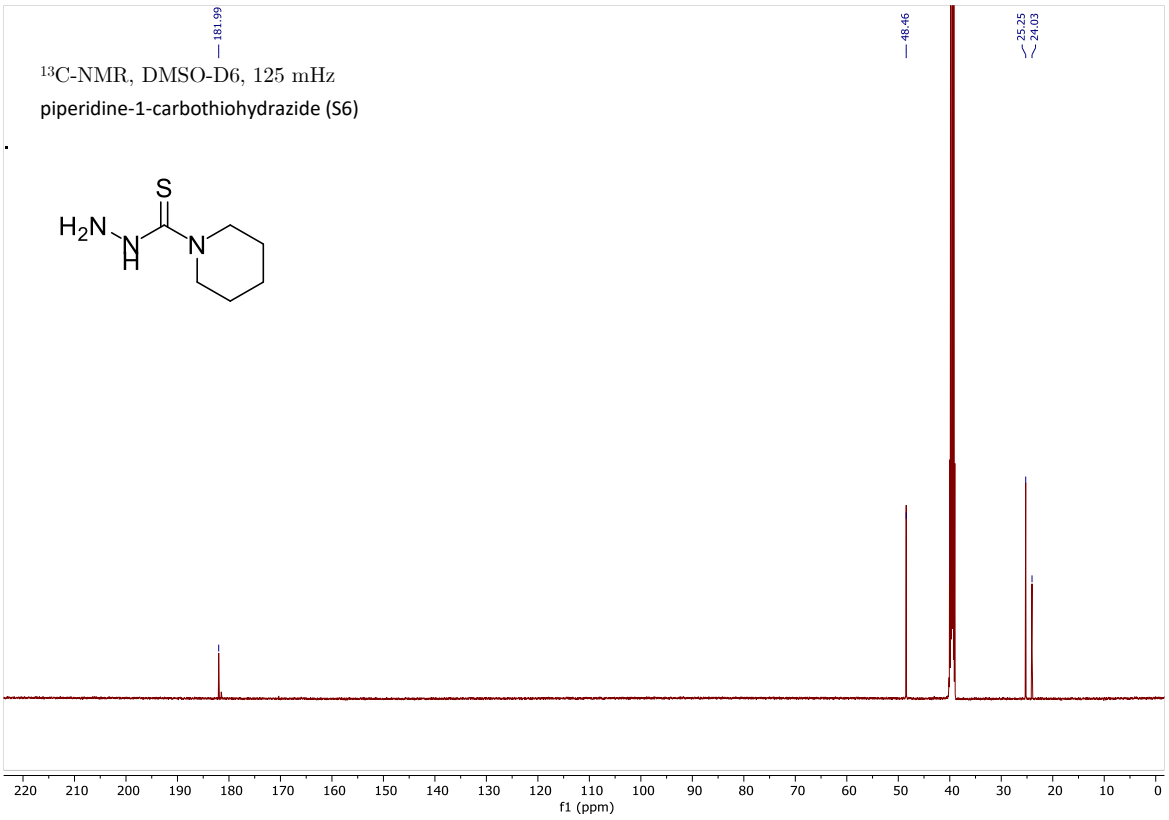
181.99
48.46
25.25
24.03
13C-NMR, DMSO-D6, 125 mHz
piperidine-1-carbothiohydrazide (S6)
S
H2N
N
H
N
220 210 200 190 180 170 160 150 140 130 120 110 100 90 80 70 60 50 40 30 20 10 0
f1 (ppm)

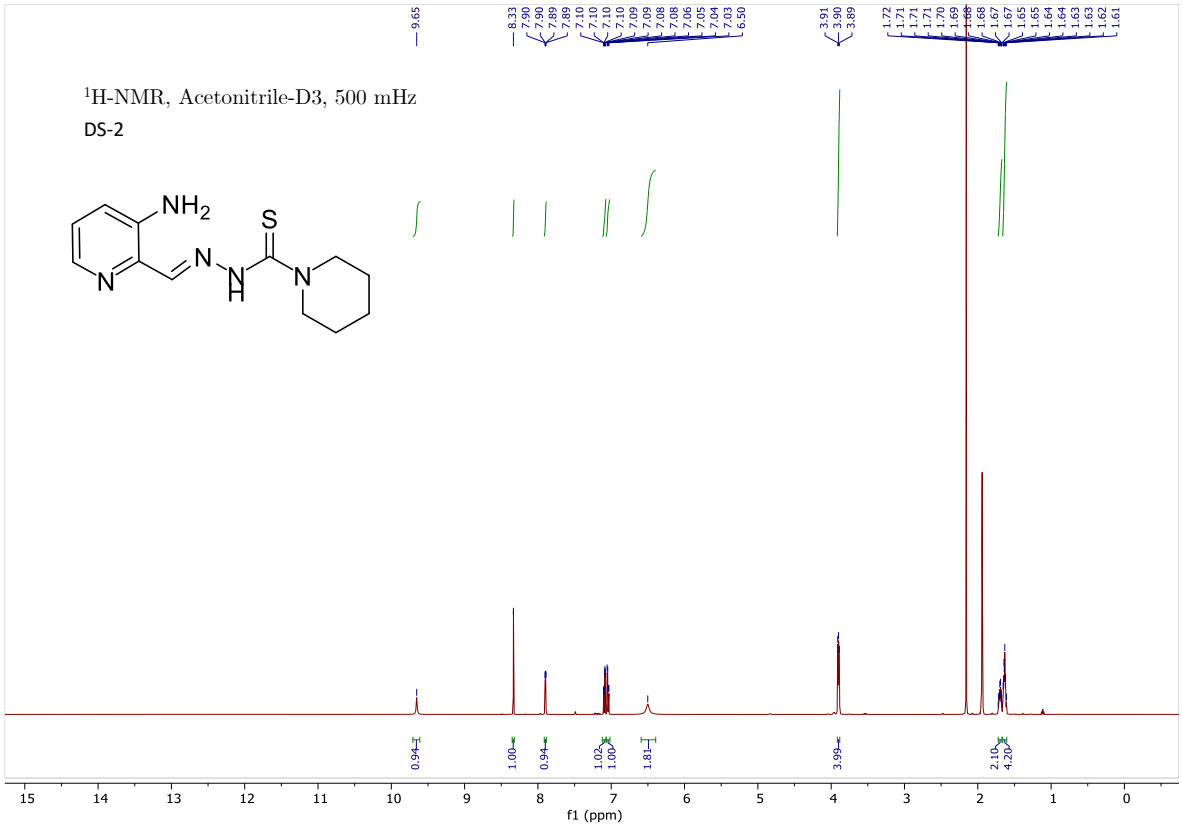
^{1}H-NMR, Acetonitrile-D3, 500 mHz
DS-2
NH2
N
N
H
S
N
f1 (ppm)

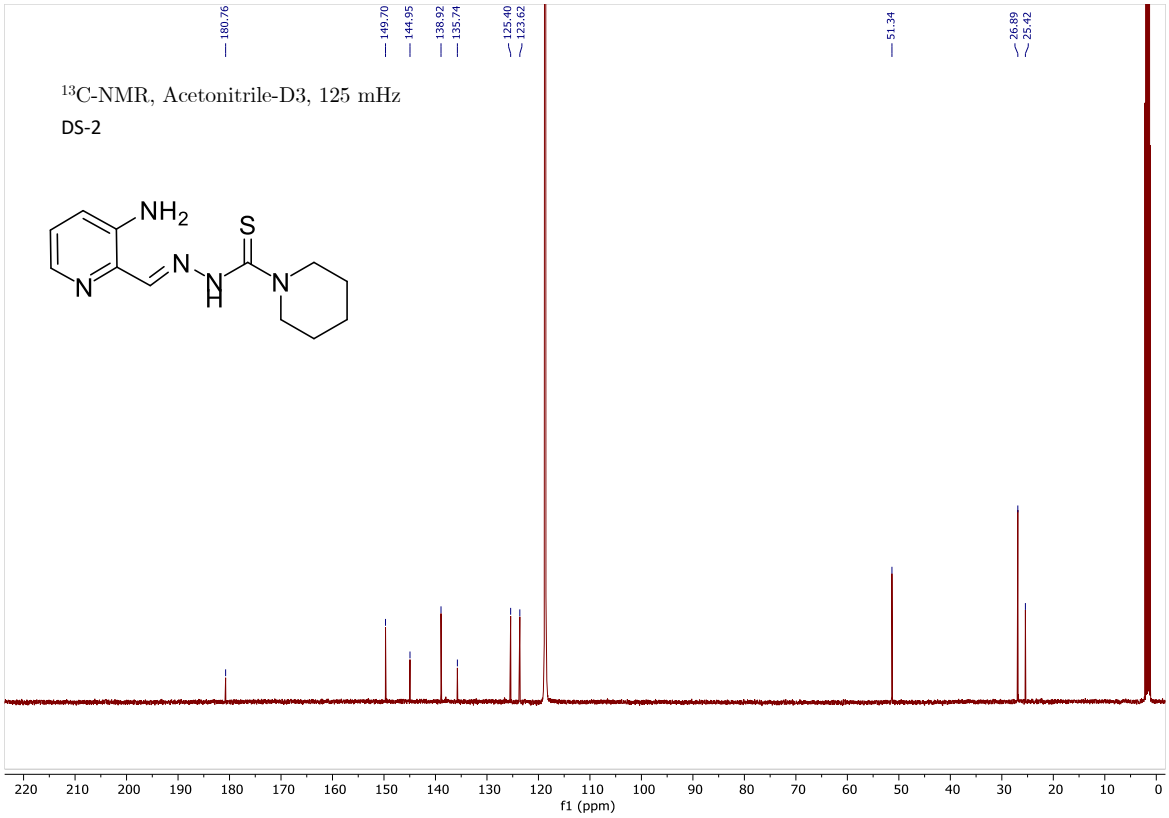
180.76
149.70
144.95
138.92
135.74
125.40
123.62
51.34
26.89
25.42
13C-NMR, Acetonitrile-D3, 125 mHz
DS-2
NH2
S
N
N
N
N
H
220 210 200 190 180 170 160 150 140 130 120 110 100 90 80 70 60 50 40 30 20 10 0
f1 (ppm)

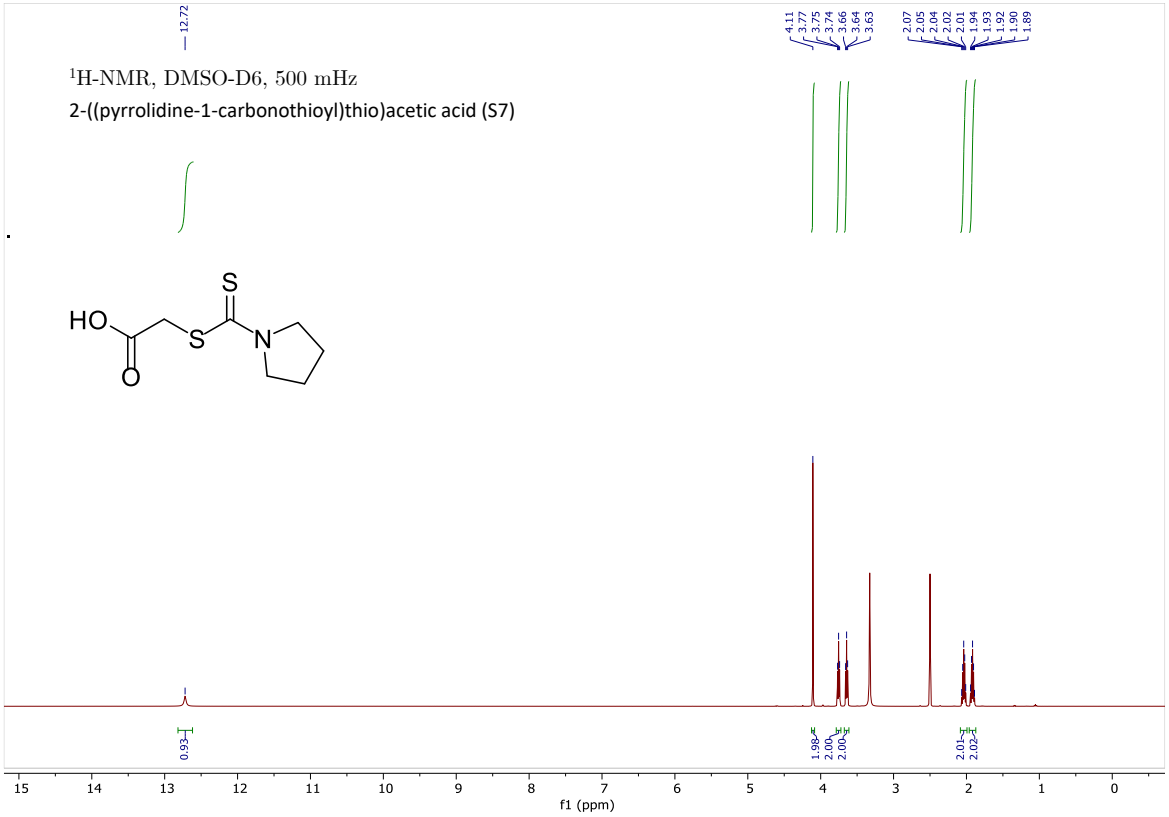
12.72
4.11
3.77
3.75
3.74
3.66
3.64
3.63
2.07
2.05
2.04
2.02
2.01
1.94
1.93
1.92
1.90
1.89
^{1}H-NMR, DMSO-D6, 500 mHz
2-((pyrrolidine-1-carbonothioyl)thio)acetic acid (S7)
HO
O
S
S
N
0.93
1.98
2.00
2.00
2.01
2.02
15
14
13
12
11
10
9
8
7
6
5
4
3
2
1
0
f1 (ppm)

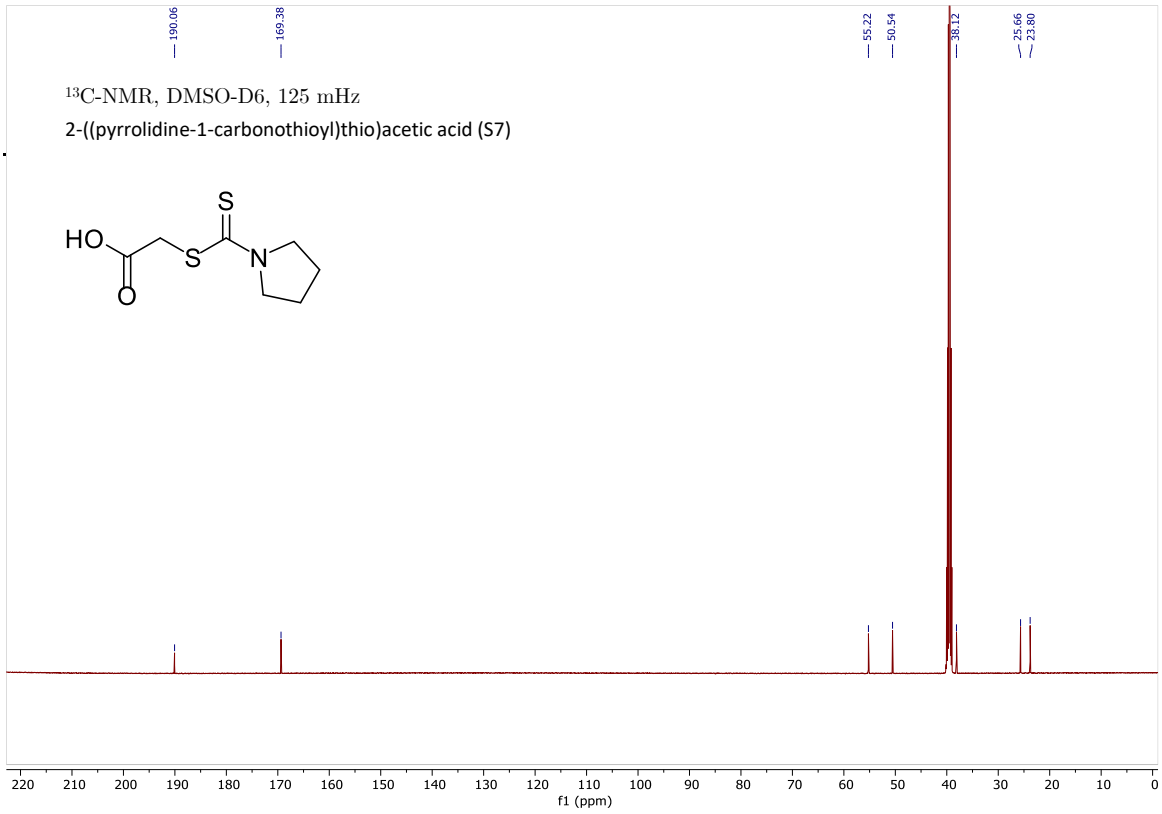
190.06
169.38
55.22
50.54
38.12
25.66
23.80
13C-NMR, DMSO-D6, 125 mHz
2-((pyrrolidine-1-carbonothioyl)thio)acetic acid (S7)
HO
O
S
S
N
220 210 200 190 180 170 160 150 140 130 120 110 100 90 80 70 60 50 40 30 20 10 0
f1 (ppm)

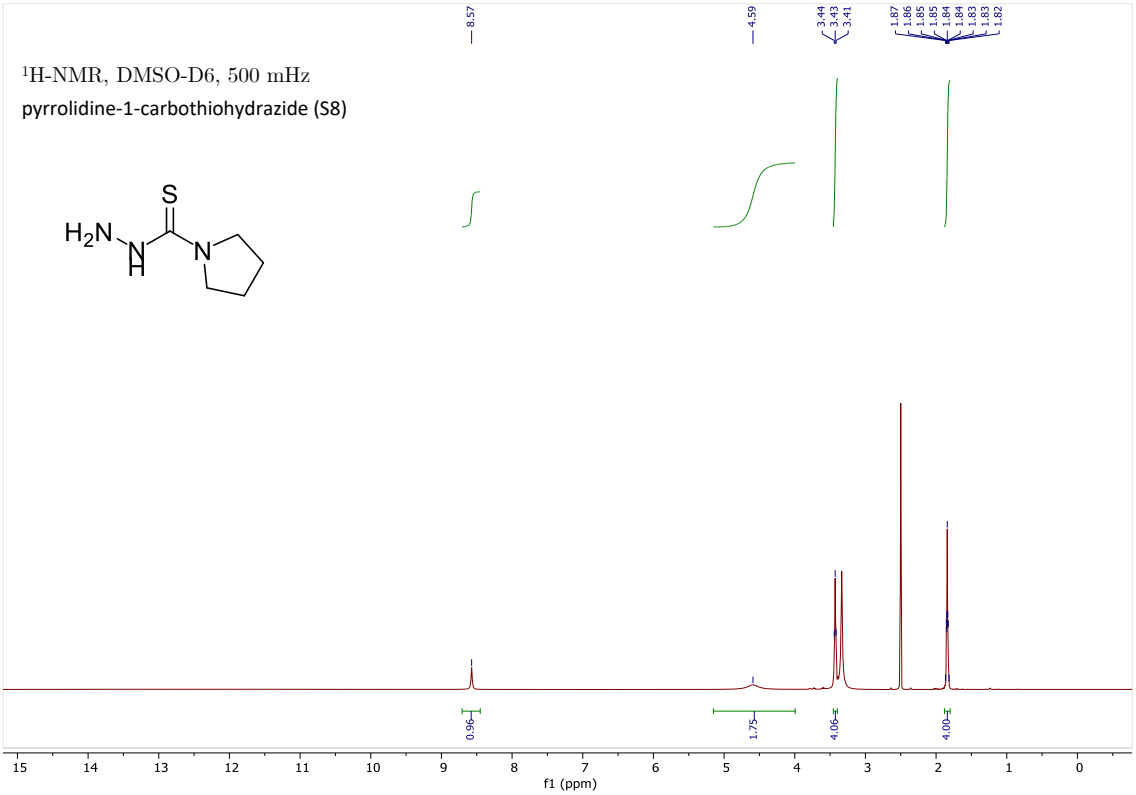
1H-NMR, DMSO-D6, 500 mHz
pyrrolidine-1-carbothiohydrazide (S8)
H2N
N
H
S
N
8.57
4.59
3.44
3.43
3.41
1.87
1.86
1.85
1.85
1.85
1.84
1.84
1.83
1.83
1.82
0.96
1.75
4.06
4.00
15
14
13
12
11
10
9
8
7
6
5
4
3
2
1
0
f1 (ppm)

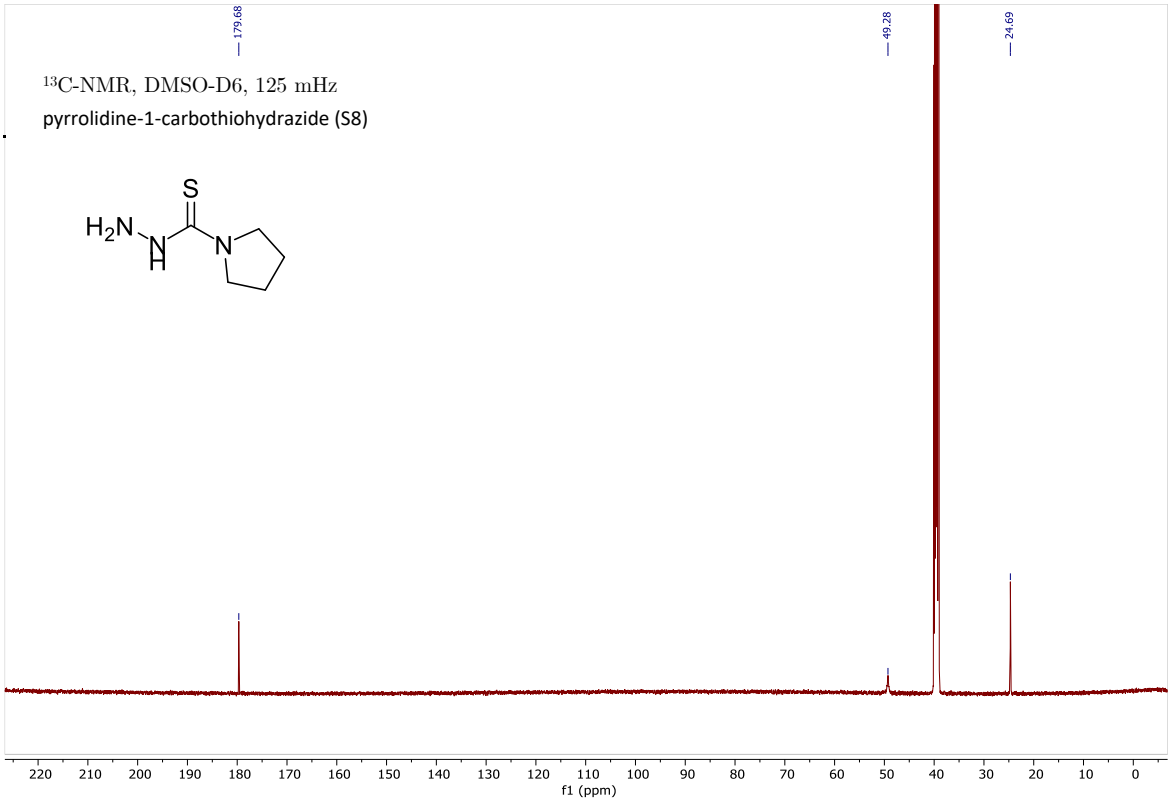
179.68
49.28
24.69
13C-NMR, DMSO-D6, 125 mHz
pyrrolidine-1-carbothiohydrazide (S8)
S
H2N
N
H
N
220 210 200 190 180 170 160 150 140 130 120 110 100 90 80 70 60 50 40 30 20 10 0
f1 (ppm)

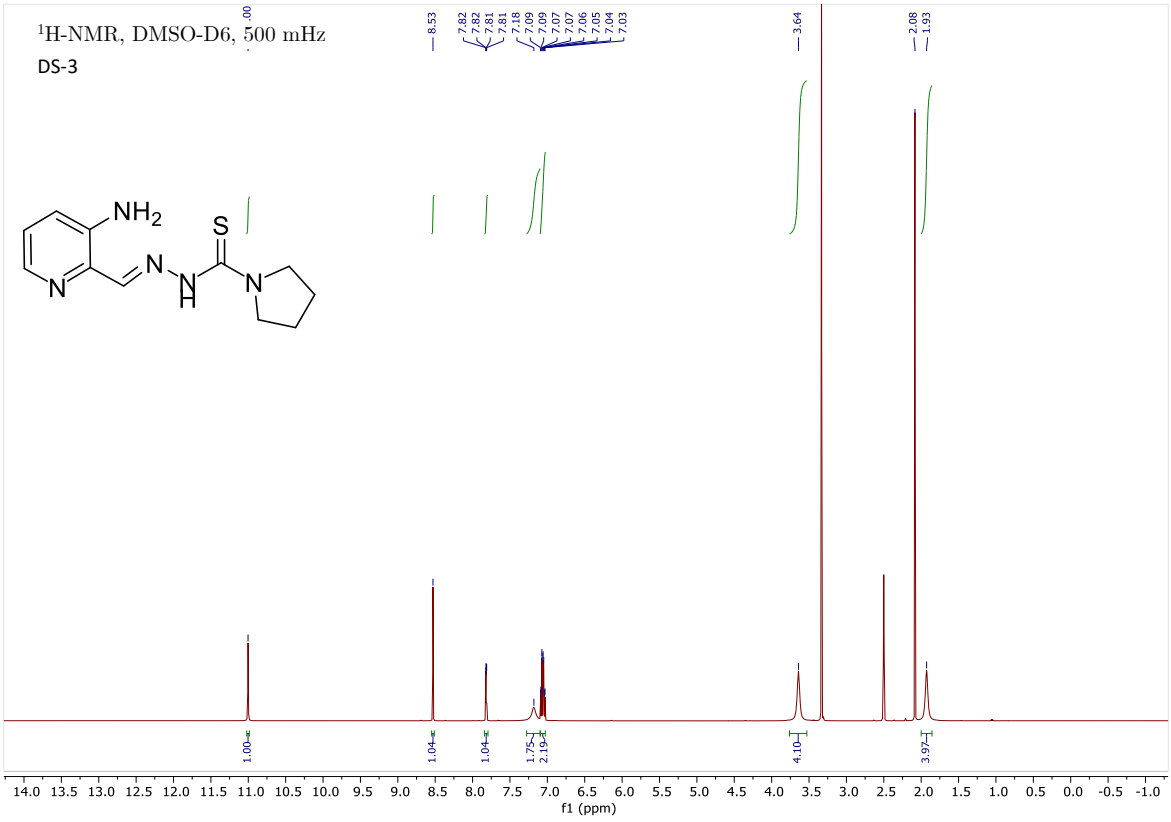
[1]H-NMR, DMSO-D6, 500 mHz
DS-3
NH2
S
N
N
H
N
N
11.00
8.53
7.82
7.82
7.81
7.81
7.18
7.09
7.09
7.07
7.07
7.06
7.05
7.04
7.03
3.64
2.08
1.93
1.00
1.04
1.04
1.75
2.19
4.10
3.97
14.0 13.5 13.0 12.5 12.0 11.5 11.0 10.5 10.0 9.5 9.0 8.5 8.0 7.5 7.0 6.5 6.0 5.5 5.0 4.5 4.0 3.5 3.0 2.5 2.0 1.5 1.0 0.5 0.0 -0.5 -1.0
f1 (ppm)

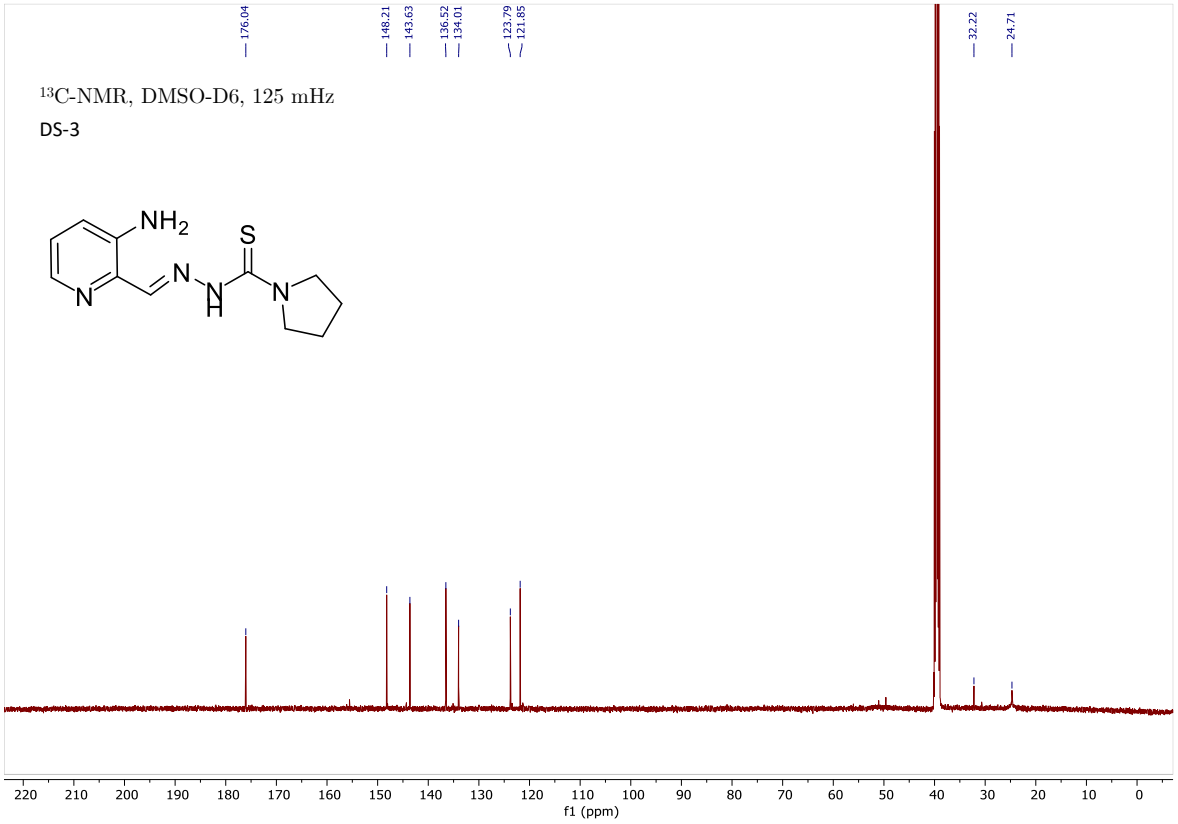
176.04
148.21
143.63
136.52
134.01
123.79
121.85
32.22
24.71
13C-NMR, DMSO-D6, 125 mHz
DS-3
NH2
S
N
N
H
N
N
220 210 200 190 180 170 160 150 140 130 120 110 100 90 80 70 60 50 40 30 20 10 0
f1 (ppm)

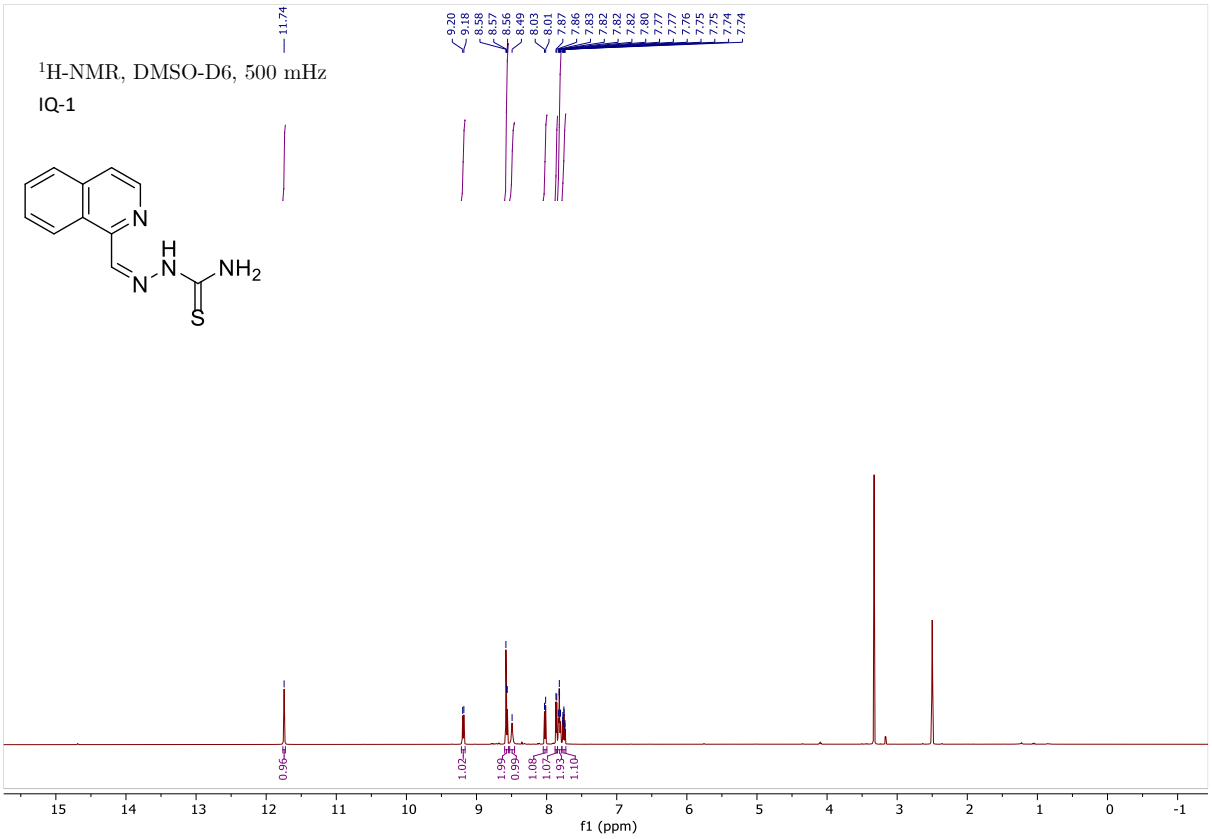
[1]H-NMR, DMSO-D6, 500 mHz
IQ-1
11.74
9.20
9.18
8.58
8.57
8.56
8.49
8.03
8.01
7.87
7.86
7.83
7.82
7.82
7.82
7.80
7.77
7.77
7.76
7.75
7.75
7.74
7.74
0.96
1.02
1.99
0.99
1.08
1.07
1.93
1.10
15
14
13
12
11
10
9
8
7
6
5
4
3
2
1
0
-1
f1 (ppm)

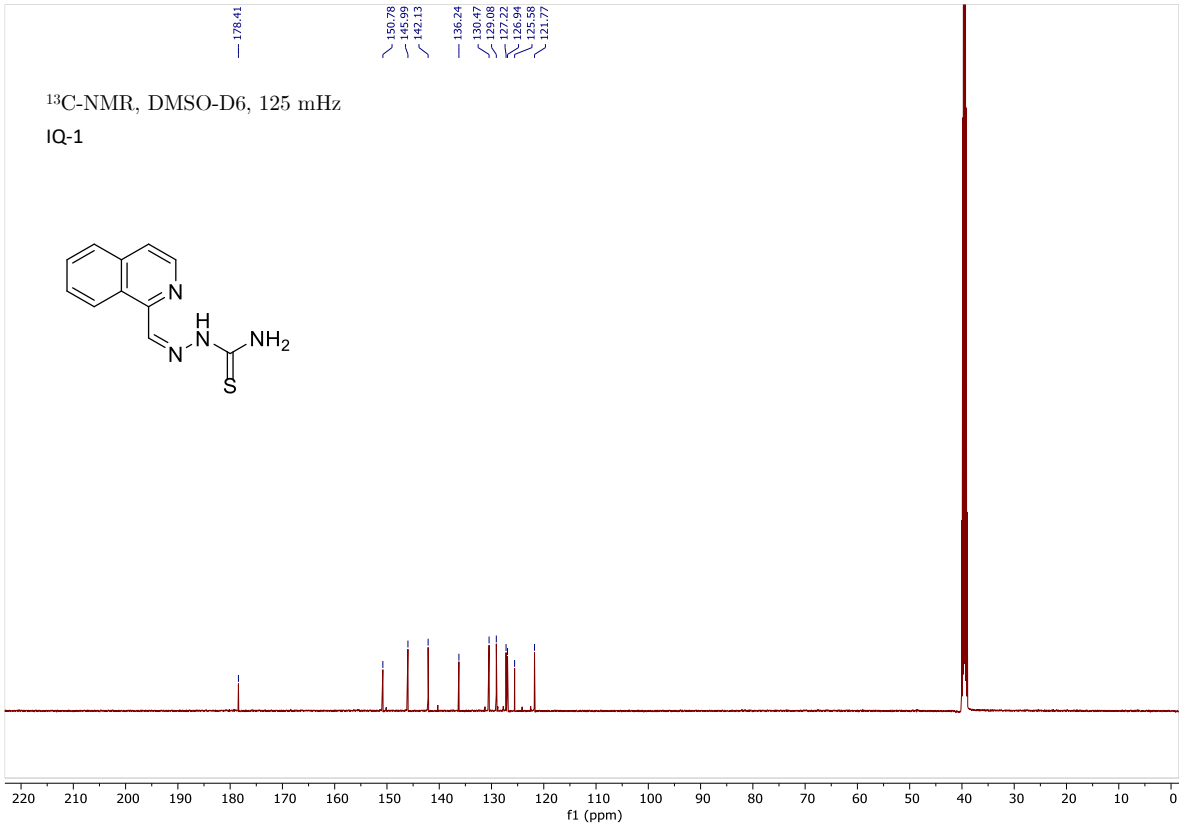
178.41
150.78
145.99
142.13
136.24
130.47
129.08
127.22
126.94
125.58
121.77
13C-NMR, DMSO-D6, 125 mHz
IQ-1
N
H
N
N
NH2
S
220 210 200 190 180 170 160 150 140 130 120 110 100 90 80 70 60 50 40 30 20 10 0
f1 (ppm)

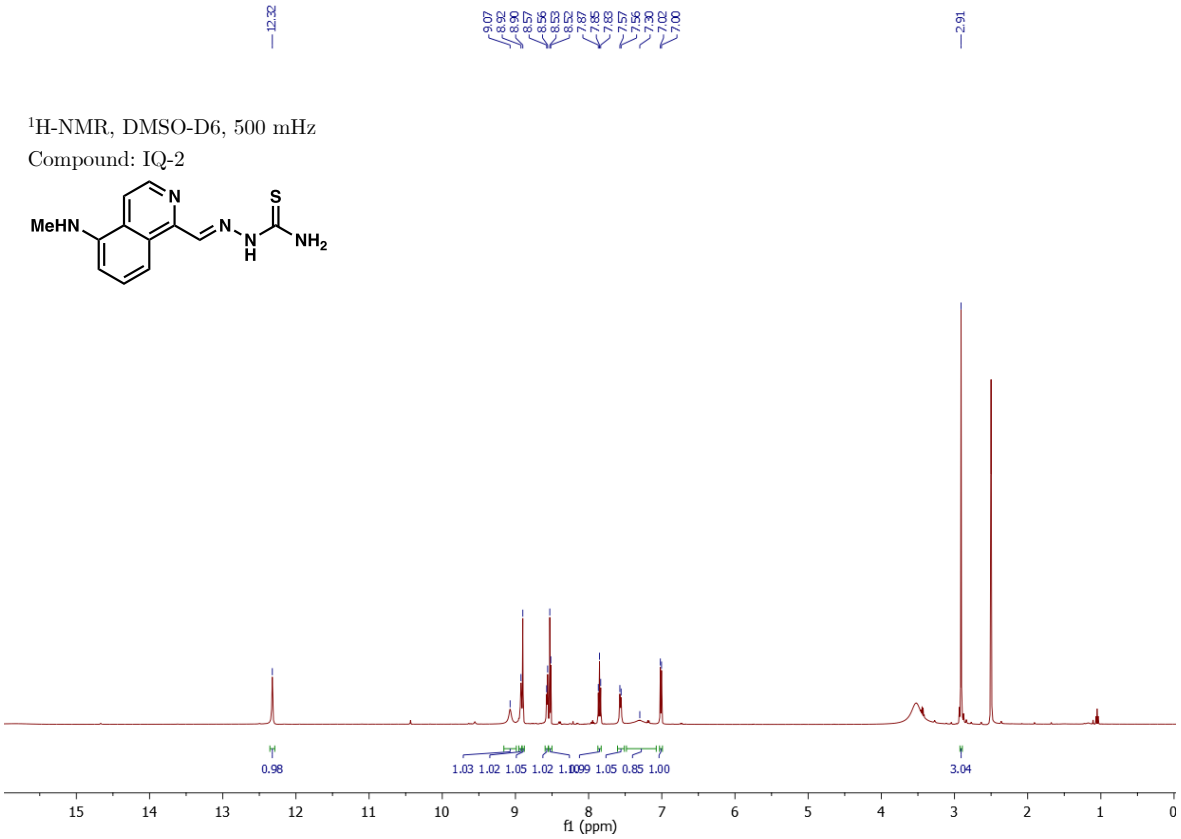

^{1}H-NMR, DMSO-D6, 500 mHz

Compound: IQ-2

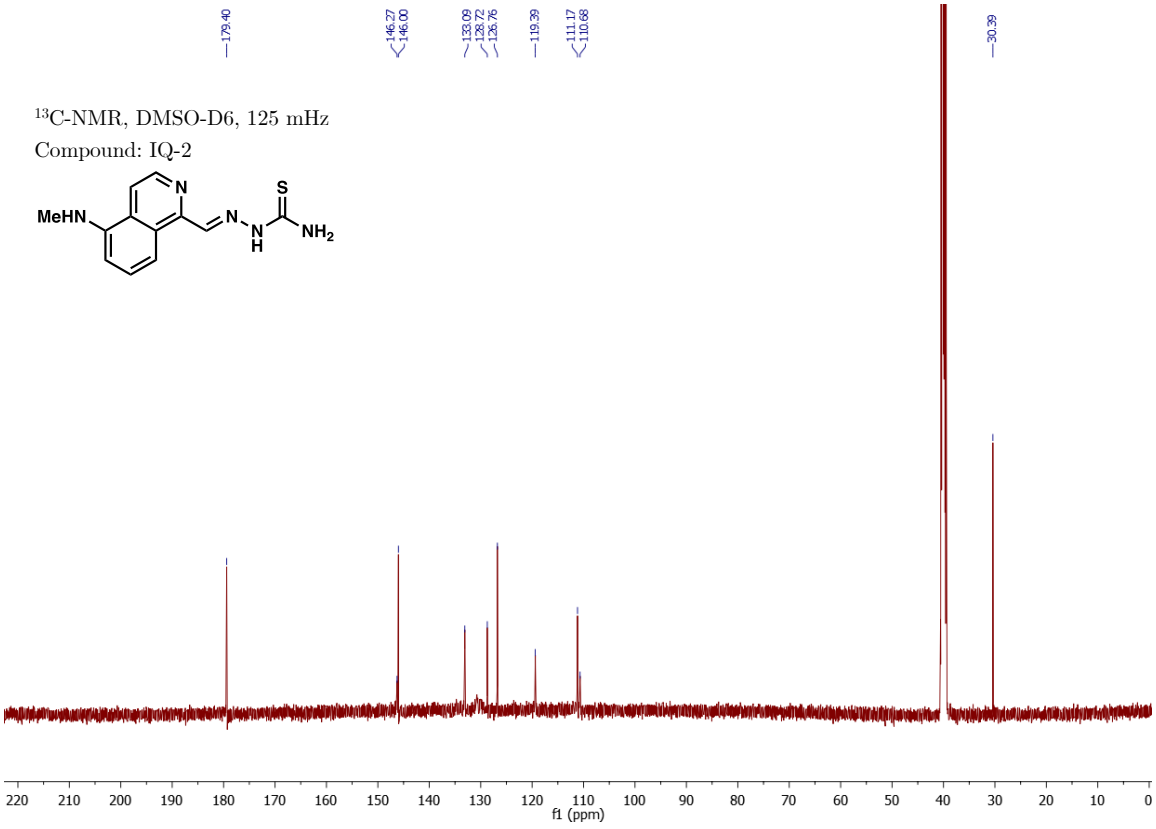
179.40
146.27
146.00
133.09
128.72
126.76
119.39
111.17
110.68
30.39
^{13}C-NMR, DMSO-D6, 125 mHz
Compound: IQ-2
MeHN
N
N
N
H
S
NH$_2$
220 210 200 190 180 170 160 150 140 130 120 110 100 90 80 70 60 50 40 30 20 10 0
f1 (ppm)

[1]H-NMR, DMSO-D6, 500 mHz

Compound: IQ-3

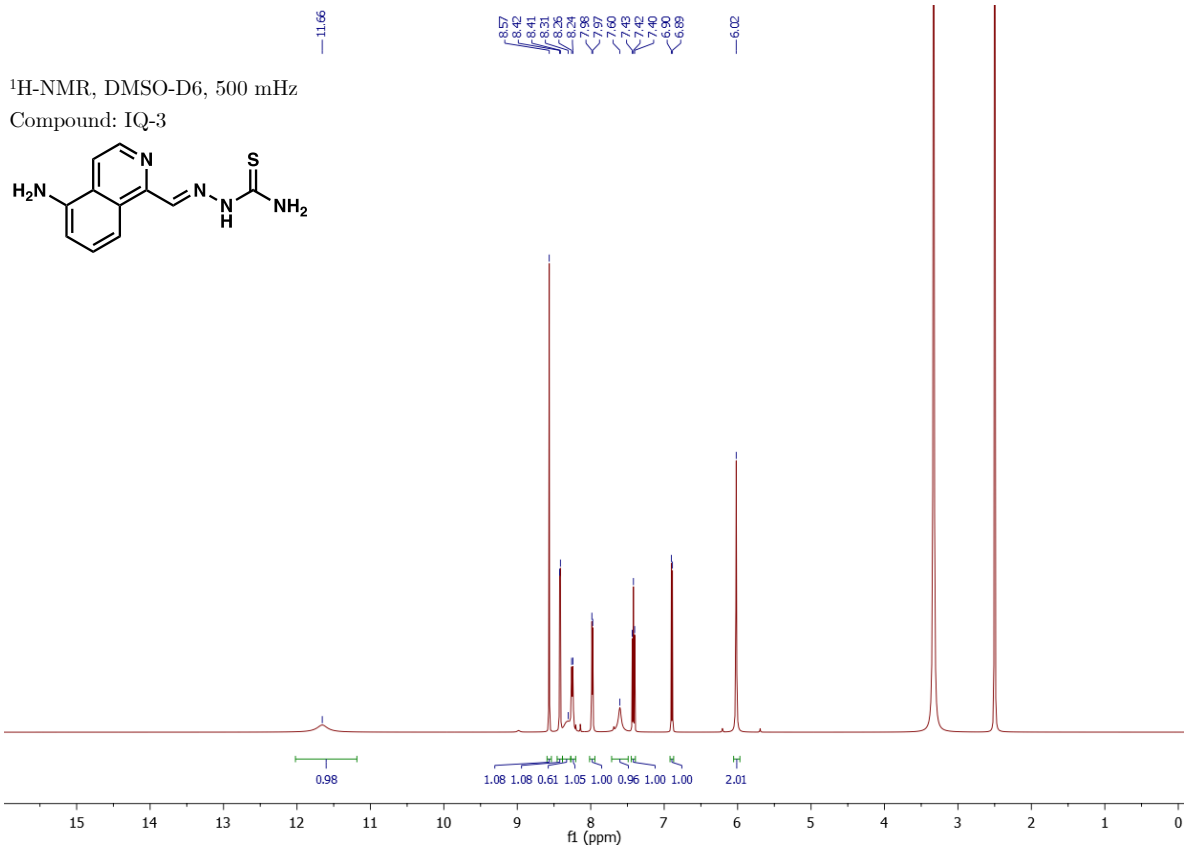

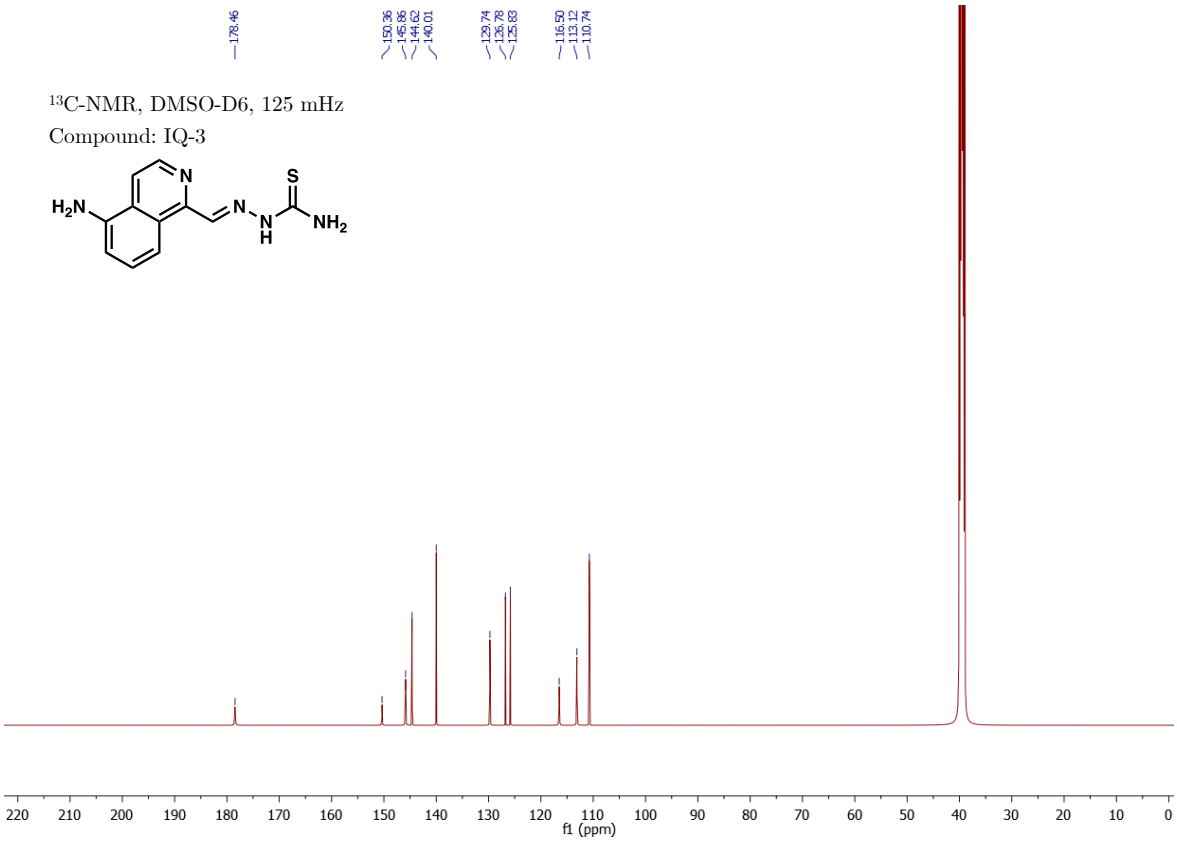
178.46
150.36
145.86
144.62
140.01
129.74
126.78
125.83
116.50
113.12
110.74
13C-NMR, DMSO-D6, 125 mHz
Compound: IQ-3
H2N
N
N
N
H
S
NH2
220 210 200 190 180 170 160 150 140 130 120 110 100 90 80 70 60 50 40 30 20 10 0
f1 (ppm)

HPLC Trace of 3-AP

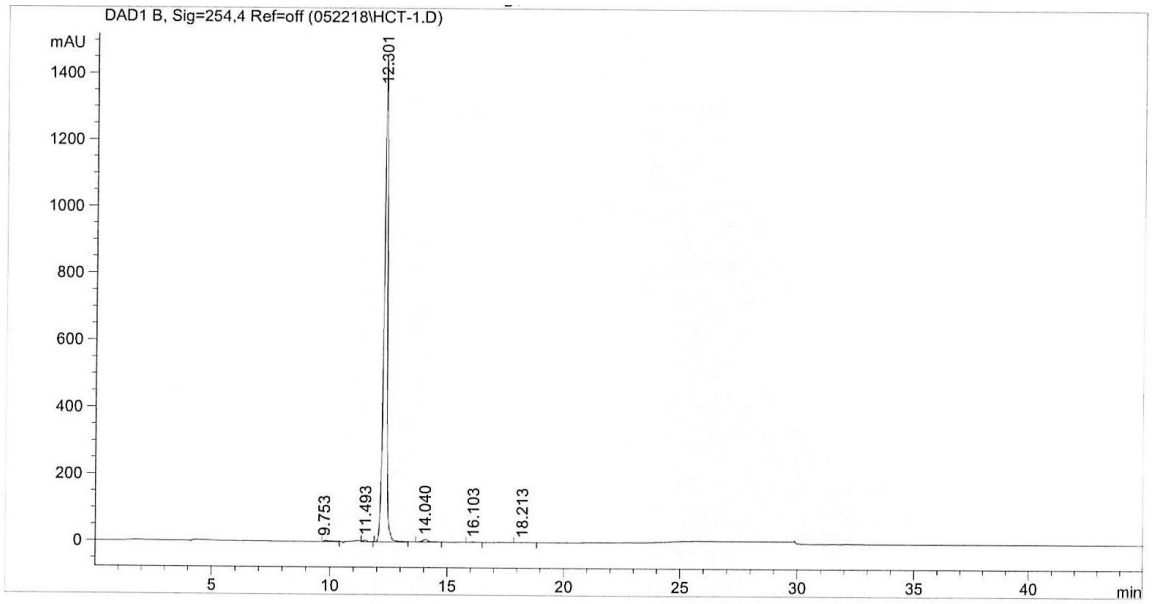


```
=====================================================================
                    Area Percent Report
=====================================================================

Sorted By             :      Signal
Multiplier            :      1.0000
Dilution              :      1.0000
Use Multiplier & Dilution Factor with ISTDs


Signal 1: DAD1 B, Sig=254,4 Ref=off

Peak RetTime Type  Width     Area      Height     Area
  #   [min]        [min]   [mAU*s]     [mAU]       %
----|-------|----|-------|----------|----------|--------|
   1   9.753 BB    0.3760  106.22363    3.41244   0.6923
   2  11.493 VB    0.1884   85.92091    6.40948   0.5600
   3  12.301 BB    0.1586 1.49329e4  1449.52454  97.3237
   4  14.040 BB    0.2868  178.23486    8.16243   1.1616
   5  16.103 BB    0.2359   26.39321    1.58510   0.1720
   6  18.213 BP    0.2372   13.85959 7.52668e-1   0.0903

Totals :                  1.53435e4  1469.84665
```

HPLC Trace of DS-1

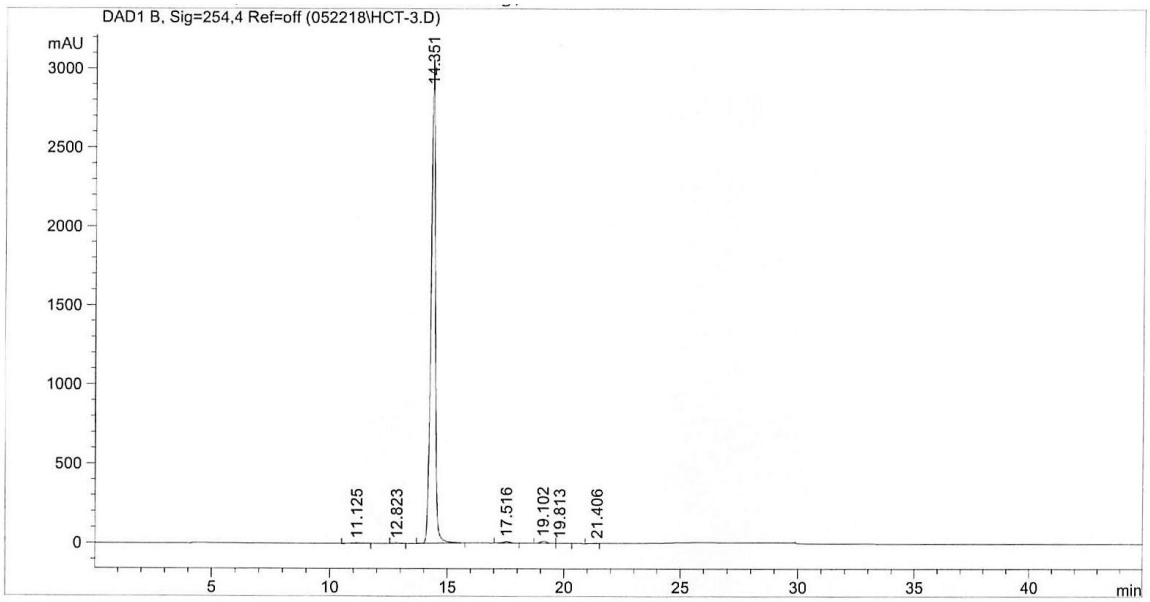


```
=====================================================================
                      Area Percent Report
=====================================================================

Sorted By             :      Signal
Multiplier            :      1.0000
Dilution              :      1.0000
Use Multiplier & Dilution Factor with ISTDs


Signal 1: DAD1 B, Sig=254,4 Ref=off

Peak RetTime Type  Width     Area      Height     Area
  #   [min]        [min]   [mAU*s]     [mAU]       %
----|-------|----|-------|----------|----------|--------|
   1  11.125 PB    0.3597   63.58443    2.50835   0.1581
   2  12.823 PP    0.2097   37.81538    2.72876   0.0941
   3  14.351 PB    0.1988 3.95562e4  3061.06812  98.3828
   4  17.516 BP    0.2872  227.02629   10.51252   0.5647
   5  19.102 PB    0.3133  273.21265   13.66345   0.6795
   6  19.813 BB    0.2409   14.12147 7.65386e-1   0.0351
   7  21.406 PV    0.2393   34.47533    1.94041   0.0857

Totals :                  4.02064e4  3093.18699
```

HPLC Trace of DS-2

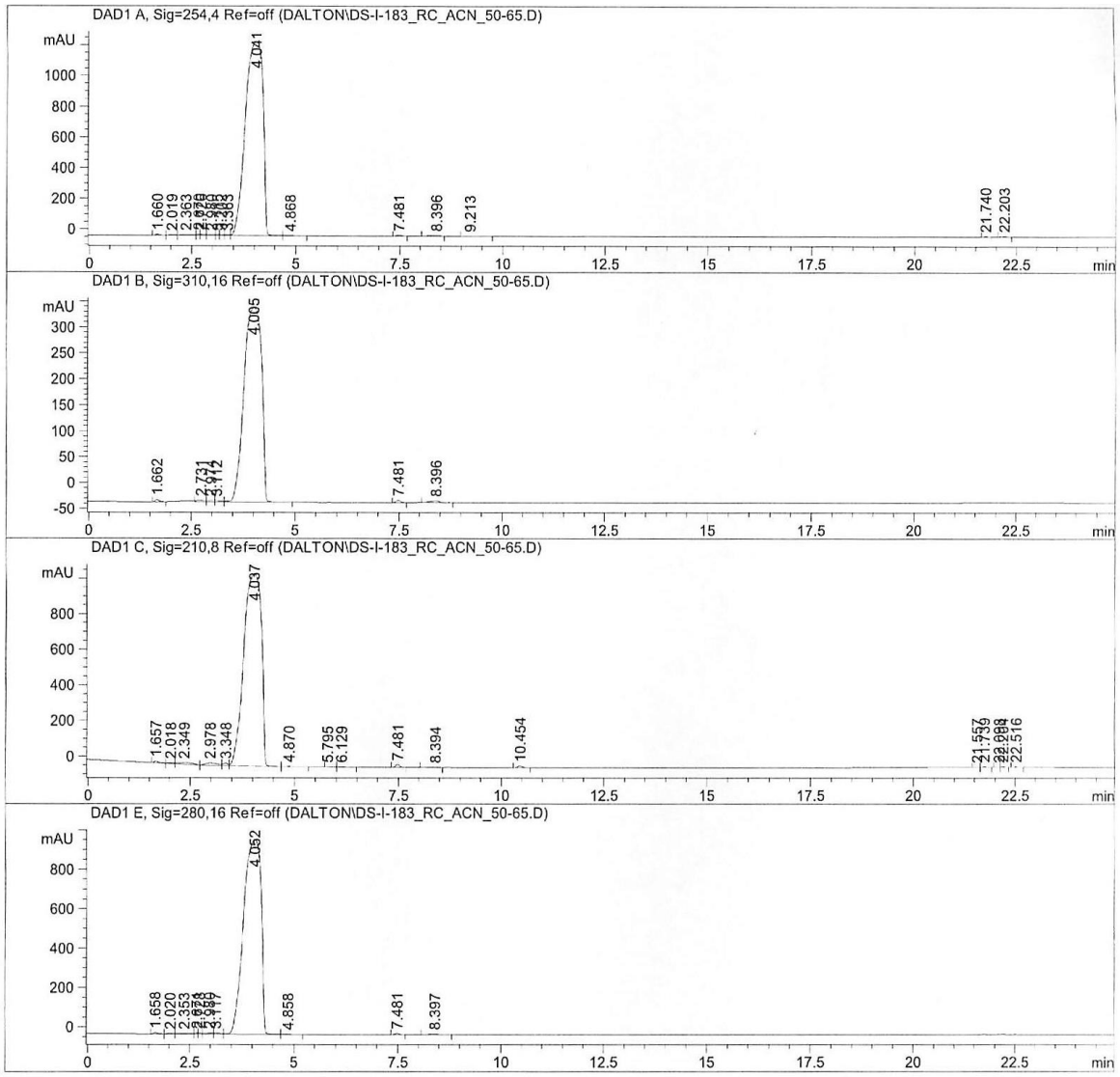

Multiplier: : 1.0000
Dilution: : 1.0000
Use Multiplier & Dilution Factor with ISTDs

Signal 1: DAD1 A, Sig=254,4 Ref=off

Peak #	RetTime [min]	Type	Width [min]	Area [mAU*s]	Height [mAU]	Area %
1	1.660	BV	0.1006	47.50333	6.87336	0.1264
2	2.019	VV	0.1515	34.74604	3.08364	0.0924
3	2.363	VV	0.2927	98.28461	4.36546	0.2615
4	2.670	VV	0.0737	29.17237	5.69744	0.0776
5	2.726	VV	0.1025	42.02406	5.54052	0.1118
6	2.980	VV	0.1544	61.68945	5.12696	0.1641
7	3.115	VV	0.0702	26.07731	5.22307	0.0694
8	3.202	VV	0.0935	32.36994	5.00448	0.0861
9	3.363	VV	0.1070	34.39571	4.72284	0.0915
10	4.041	VV	0.4801	3.70157e4	1269.76550	98.4798
11	4.868	VB	0.1312	18.77062	2.04330	0.0499
12	7.481	BB	0.1141	49.97776	6.77597	0.1330
13	8.396	BV	0.2525	61.62447	3.77487	0.1640
14	9.213	BB	0.1985	14.50054	1.12415	0.0386
15	21.740	VB	0.1043	8.17777	1.13154	0.0218
16	22.203	BB	0.1365	12.06570	1.18824	0.0321
Totals :				3.75870e4	1331.44133	

Signal 2: DAD1 B, Sig=310,16 Ref=off

Peak #	RetTime [min]	Type	Width [min]	Area [mAU*s]	Height [mAU]	Area %
1	1.662	BB	0.0988	36.10815	5.21448	0.3184
2	2.731	BV	0.1688	54.12606	4.07860	0.4772
3	2.974	VV	0.1462	36.19173	3.19301	0.3191
4	3.112	VV	0.1294	30.20480	3.00130	0.2663
5	4.005	VB	0.4847	1.11003e4	375.67584	97.8745
6	7.481	BB	0.1143	33.91515	4.58285	0.2990
7	8.396	BB	0.2513	50.51435	3.04803	0.4454
Totals :				1.13414e4	398.79411	

Peak #	RetTime [min]	Type	Width [min]	Area [mAU*s]	Height [mAU]	Area %
1	1.657	BV	0.1047	76.44569	10.53012	0.2333
2	2.018	VV	0.1534	43.00404	3.81704	0.1313
3	2.349	VV	0.3550	223.42189	8.65932	0.6819
4	2.978	VV	0.2942	256.87891	12.47721	0.7840
5	3.348	VV	0.1083	107.27105	14.50551	0.3274
6	4.037	VV	0.4812	3.17131e4	1084.38831	96.7897
7	4.870	VB	0.0717	7.11174	1.81563	0.0217
8	5.795	BV	0.1520	17.18624	1.56676	0.0525
9	6.129	VB	0.1345	11.33651	1.24233	0.0346
10	7.481	BB	0.1137	125.49698	17.07586	0.3830
11	8.394	BV	0.2323	34.11178	2.15952	0.1041
12	10.454	BB	0.1307	94.20012	11.12925	0.2875
13	21.557	BV	0.0944	6.72836	1.08391	0.0205
14	21.739	VB	0.1142	16.90350	2.09357	0.0516
15	22.098	BV	0.0888	7.20973	1.15599	0.0220
16	22.204	VB	0.0961	13.04452	1.99892	0.0398
17	22.516	BB	0.1233	11.49573	1.29797	0.0351
Totals :				3.27650e4	1176.99723	

Signal 4: DAD1 E, Sig=280,16 Ref=off

Peak #	RetTime [min]	Type	Width [min]	Area [mAU*s]	Height [mAU]	Area %
1	1.658	BV	0.1038	43.34460	6.03526	0.1493
2	2.020	VV	0.1548	24.51723	2.12257	0.0844
3	2.353	VV	0.3037	72.80189	3.12647	0.2507
4	2.671	VV	0.0714	21.27030	4.17916	0.0733
5	2.728	VV	0.0802	23.54875	4.15129	0.0811
6	2.980	VV	0.1741	55.71457	4.05883	0.1919
7	3.117	VV	0.1478	49.17419	4.22443	0.1693
8	4.052	VV	0.4784	2.86564e4	987.94861	98.6862
9	4.858	VB	0.1166	14.16269	1.74627	0.0488
10	7.481	BB	0.1170	46.78601	6.27453	0.1611
11	8.397	BB	0.2427	30.17422	1.88528	0.1039
Totals :				2.90379e4	1025.75270	

HPLC Trace of DS-3

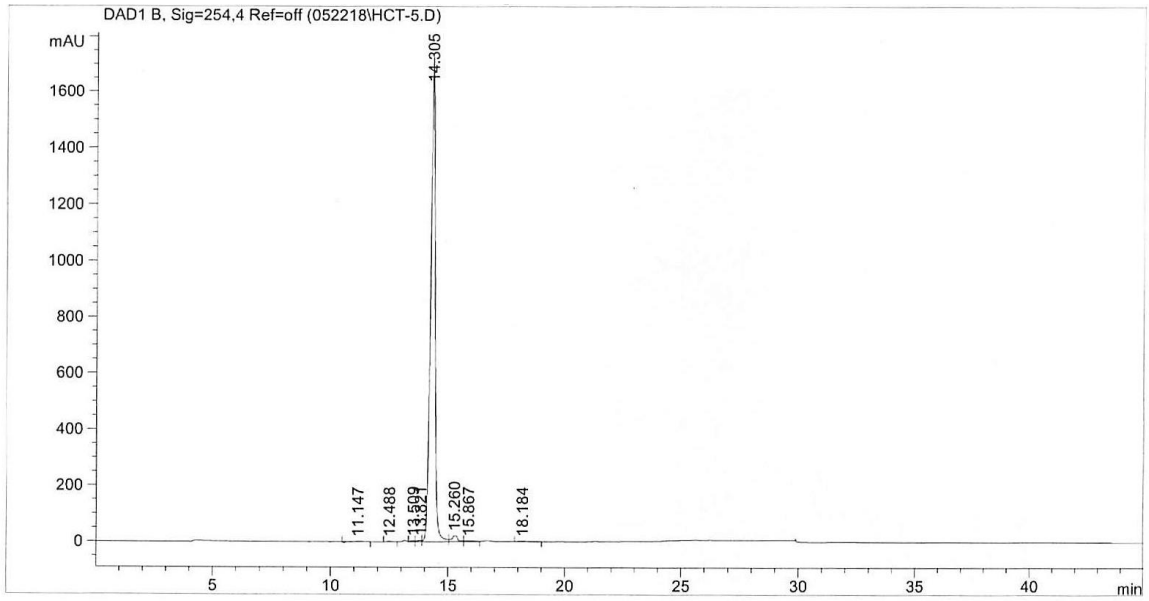


```
=====================================================================
                      Area Percent Report
=====================================================================

Sorted By             :      Signal
Multiplier            :      1.0000
Dilution              :      1.0000
Use Multiplier & Dilution Factor with ISTDs


Signal 1: DAD1 B, Sig=254,4 Ref=off

Peak RetTime Type  Width     Area      Height     Area
  #   [min]        [min]   [mAU*s]     [mAU]       %
----|-------|----|-------|----------|----------|--------|
   1  11.147 PP    0.1957   19.14825    1.58143   0.0805
   2  12.488 PV    0.2157   37.12325    2.58311   0.1561
   3  13.509 VV    0.1844   55.43121    3.91581   0.2331
   4  13.821 VV    0.1781   72.99603    5.36089   0.3070
   5  14.305 VV    0.2067 2.30218e4  1727.18726  96.8245
   6  15.260 VV    0.2382  402.95117   22.11092   1.6947
   7  15.867 VV    0.4348  107.29401    3.15809   0.4513
   8  18.184 BB    0.3365   60.09594    2.32681   0.2527

Totals :                  2.37769e4  1768.22432
```

HPLC Trace of TS-1

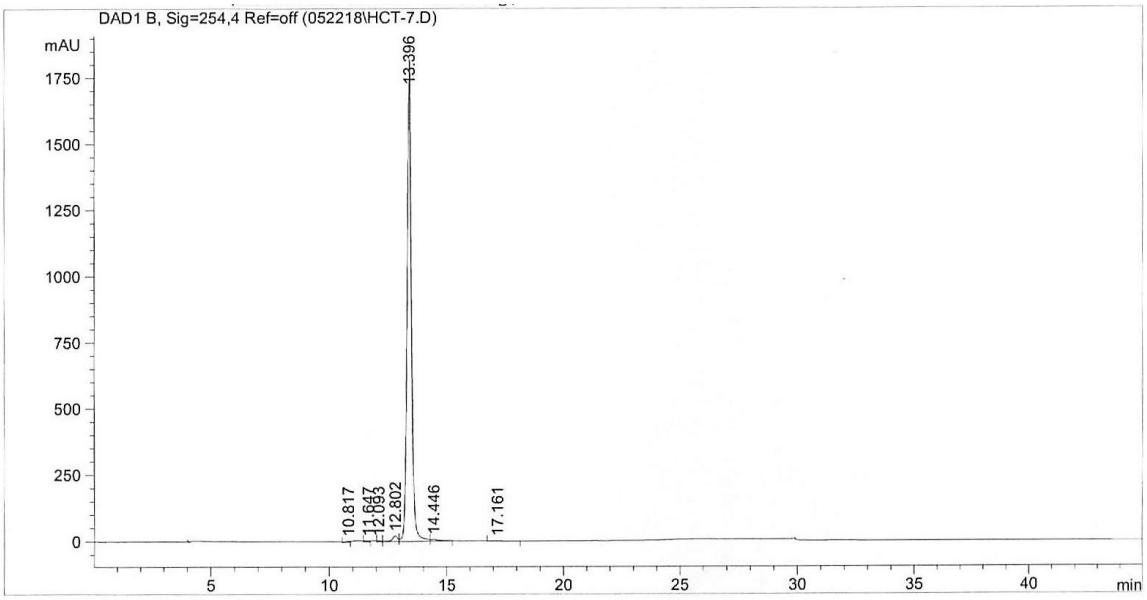


```
=====================================================================
                      Area Percent Report
=====================================================================

Sorted By             :      Signal
Multiplier            :      1.0000
Dilution              :      1.0000
Use Multiplier & Dilution Factor with ISTDs


Signal 1: DAD1 B, Sig=254,4 Ref=off

Peak RetTime Type  Width     Area      Height     Area
  #   [min]        [min]    [mAU*s]     [mAU]       %
----|-------|----|-------|----------|----------|--------|
   1  10.817 PV    0.1576   50.33264    4.34441   0.2130
   2  11.647 VV    0.2279   85.87767    4.72830   0.3634
   3  12.093 VV    0.1851   56.84795    4.52232   0.2406
   4  12.802 VV    0.2609  381.96039   21.25221   1.6165
   5  13.396 VV    0.1880 2.28313e4 1819.92114  96.6236
   6  14.446 VB    0.3778  205.13774    7.11962   0.8682
   7  17.161 PP    0.2167   17.65732    1.04318   0.0747

Totals :                  2.36291e4 1862.93119
```

HPLC Trace of TS-2

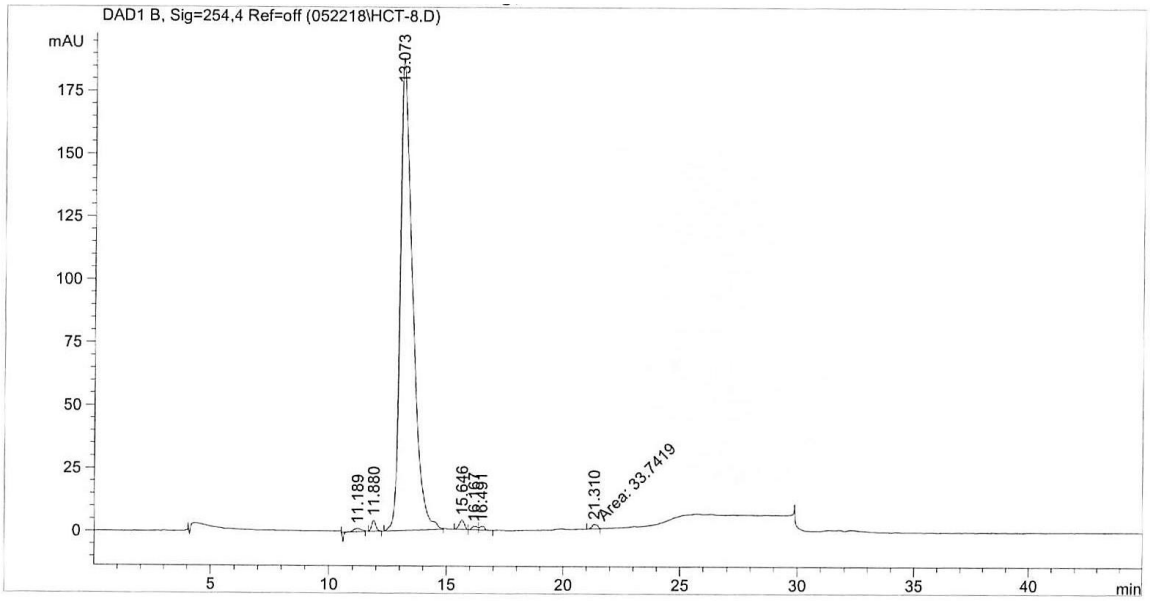


```
=====================================================================
                        Area Percent Report
=====================================================================

Sorted By             :      Signal
Multiplier            :      1.0000
Dilution              :      1.0000
Use Multiplier & Dilution Factor with ISTDs


Signal 1: DAD1 B, Sig=254,4 Ref=off

Peak RetTime Type  Width     Area      Height     Area
  #   [min]        [min]    [mAU*s]    [mAU]       %
----|-------|----|-------|----------|----------|--------|
   1  11.189 PB    0.1983   18.05580    1.31764   0.2531
   2  11.880 BB    0.1899   56.81057    4.37619   0.7965
   3  13.073 BB    0.4963 6921.18945  188.18840  97.0371
   4  15.646 BP    0.1995   56.79727    3.80987   0.7963
   5  16.167 VV    0.2222   23.98722    1.44718   0.3363
   6  16.491 VP    0.2084   21.93814    1.45116   0.3076
   7  21.310 MM    0.2947   33.74192    1.90832   0.4731

Totals :                  7132.52036  202.49875
```

HPLC Trace of TS-3

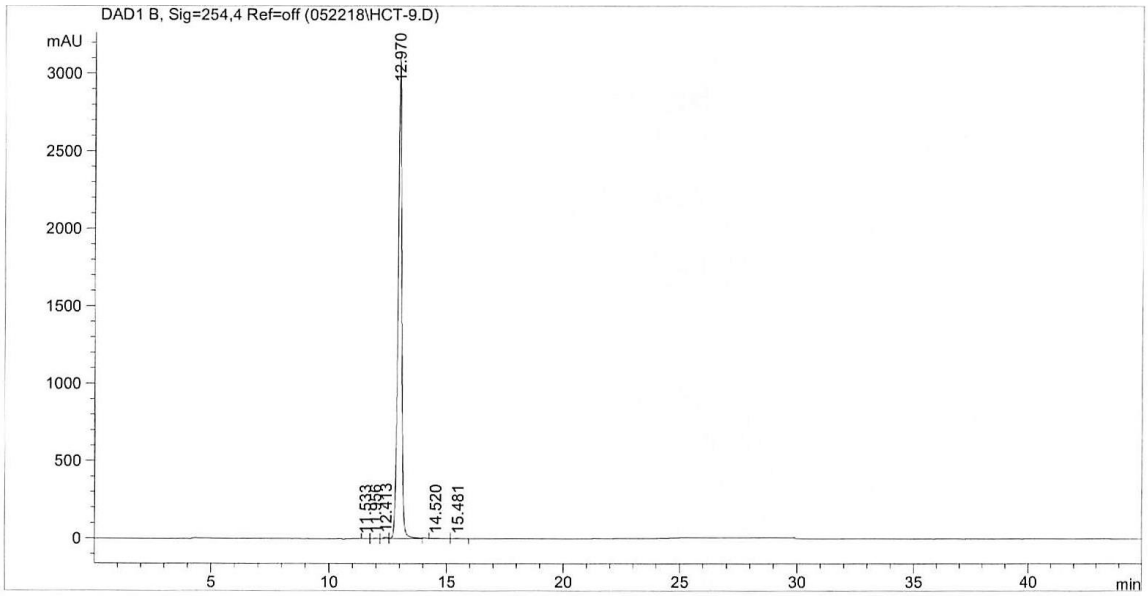


```
=====================================================================
                      Area Percent Report
=====================================================================

Sorted By             :      Signal
Multiplier            :      1.0000
Dilution              :      1.0000
Use Multiplier & Dilution Factor with ISTDs


Signal 1: DAD1 B, Sig=254,4 Ref=off

Peak RetTime Type  Width     Area      Height     Area
  #   [min]        [min]   [mAU*s]     [mAU]       %
----|-------|----|-------|----------|----------|--------|
   1  11.533 VV    0.1807   15.53959    1.27374   0.0438
   2  11.956 VV    0.1919   34.80878    2.76106   0.0982
   3  12.413 VV    0.1867  132.08752   10.86245   0.3727
   4  12.970 VB    0.1733 3.51425e4  3113.60645  99.1462
   5  14.520 BB    0.4033   82.82058    2.74386   0.2337
   6  15.481 BB    0.2772   37.36671    1.73246   0.1054

Totals :                  3.54451e4  3132.98002
```

HPLC Trace of MS-1

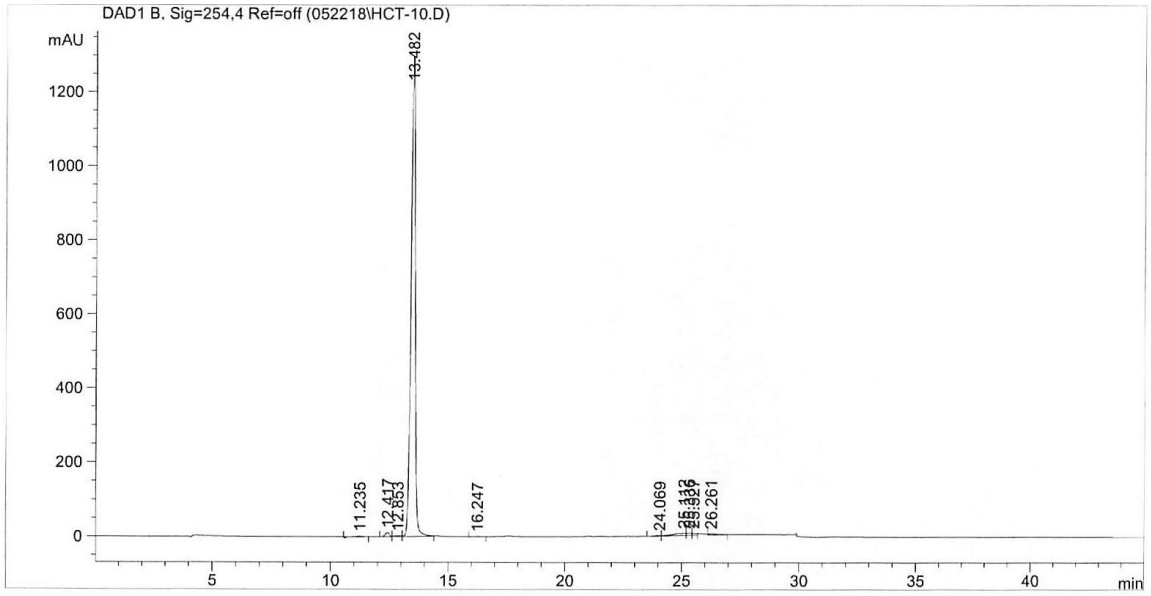


```
=====================================================================
                      Area Percent Report
=====================================================================

Sorted By             :      Signal
Multiplier            :      1.0000
Dilution              :      1.0000
Use Multiplier & Dilution Factor with ISTDs


Signal 1: DAD1 B, Sig=254,4 Ref=off

Peak RetTime Type  Width     Area      Height     Area
  #   [min]        [min]   [mAU*s]     [mAU]       %
----|-------|----|-------|----------|----------|--------|
   1  11.235 PB    0.2838   37.10028    1.86058   0.2255
   2  12.417 VV    0.2021  146.61072   11.33269   0.8910
   3  12.853 VV    0.2626   55.06662    2.63946   0.3347
   4  13.482 VB    0.1886 1.56601e4  1299.73169  95.1713
   5  16.247 PV    0.2798   17.51206 8.35199e-1   0.1064
   6  24.069 PV    0.2458   30.56045    1.55136   0.1857
   7  25.112 VV    0.5028  259.71304    6.26546   1.5784
   8  25.336 VV    0.2056   89.92757    6.39765   0.5465
   9  25.527 VV    0.1703   65.55280    5.28615   0.3984
  10  26.261 BB    0.3770   92.49775    3.27959   0.5621

Totals :                  1.64547e4  1339.17982
```

HPLC Trace of MS-2

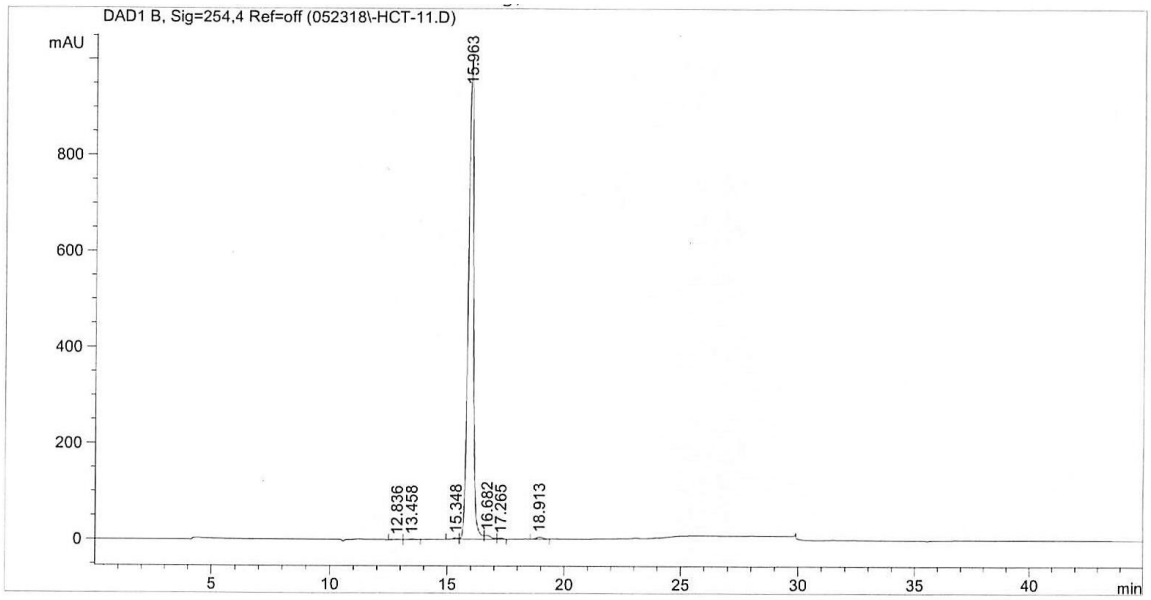


```
=====================================================================
                      Area Percent Report
=====================================================================

Sorted By             :      Signal
Multiplier            :      1.0000
Dilution              :      1.0000
Use Multiplier & Dilution Factor with ISTDs


Signal 1: DAD1 B, Sig=254,4 Ref=off

Peak RetTime Type  Width     Area      Height     Area
  #   [min]        [min]   [mAU*s]     [mAU]       %
----|-------|----|-------|----------|----------|--------|
   1  12.836 PP    0.2047   10.76453 7.14138e-1   0.0657
   2  13.458 VB    0.2405   20.50725    1.14773   0.1252
   3  15.348 BV    0.2546   48.80013    2.98631   0.2980
   4  15.963 VV    0.2442 1.59801e4   999.03613  97.5945
   5  16.682 VV    0.2863  175.69489    8.60316   1.0730
   6  17.265 VP    0.2794   43.55086    2.58927   0.2660
   7  18.913 BV    0.2771   94.55799    4.68381   0.5775

Totals :                  1.63740e4  1019.76055
```

HPLC Trace of MS-3

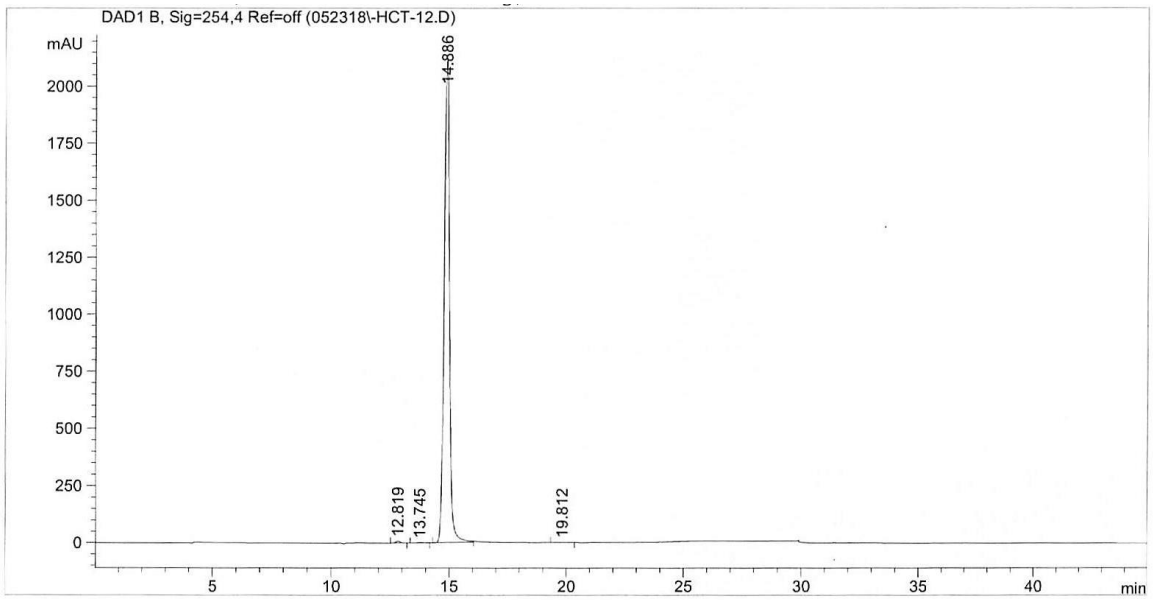


```
=====================================================================
                      Area Percent Report
=====================================================================

Sorted By             :      Signal
Multiplier            :      1.0000
Dilution              :      1.0000
Use Multiplier & Dilution Factor with ISTDs


Signal 1: DAD1 B, Sig=254,4 Ref=off

Peak RetTime Type  Width     Area      Height     Area
  #   [min]        [min]    [mAU*s]     [mAU]       %
----|-------|----|-------|----------|----------|--------|
   1  12.819 BP    0.2197  120.36358    8.66186   0.3655
   2  13.745 BB    0.2781   35.52430    1.77680   0.1079
   3  14.886 PB    0.2346 3.27476e4  2119.93750  99.4388
   4  19.812 BB    0.4063   28.92207 9.01477e-1   0.0878

Totals :                  3.29324e4  2131.27764
```

HPLC Trace of IQ-1

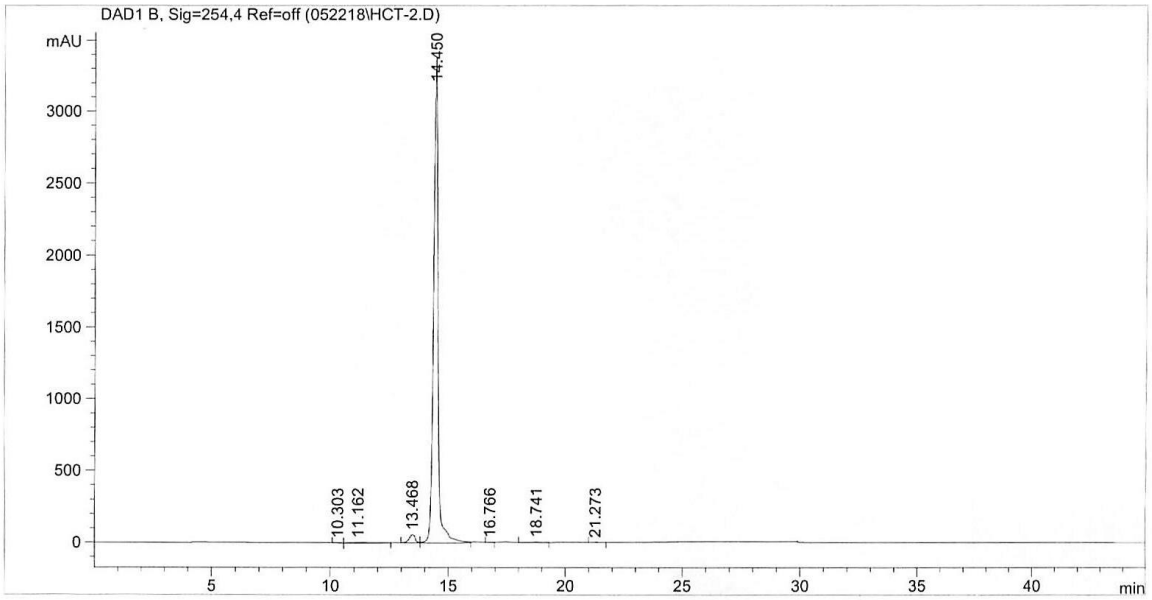


```
======================================================================
                        Area Percent Report
======================================================================

Sorted By             :      Signal
Multiplier            :      1.0000
Dilution              :      1.0000
Use Multiplier & Dilution Factor with ISTDs


Signal 1: DAD1 B, Sig=254,4 Ref=off

Peak RetTime Type  Width     Area      Height     Area
  #   [min]       [min]   [mAU*s]     [mAU]       %
----|-------|----|-------|----------|----------|--------|
   1  10.303 BP    0.2768   69.25489    3.05996   0.1447
   2  11.162 VB    1.0723  469.48703    5.33081   0.9811
   3  13.468 BV    0.2812 1102.03687   58.33940   2.3028
   4  14.450 VV    0.2059 4.59488e4  3395.93848  96.0156
   5  16.766 VV    0.2864   80.94415    3.71239   0.1691
   6  18.741 VV    0.4906  156.56212    4.34655   0.3272
   7  21.273 PB    0.2094   28.48508    1.71805   0.0595

Totals :                  4.78555e4  3472.44563
```

HPLC Trace of IQ-2

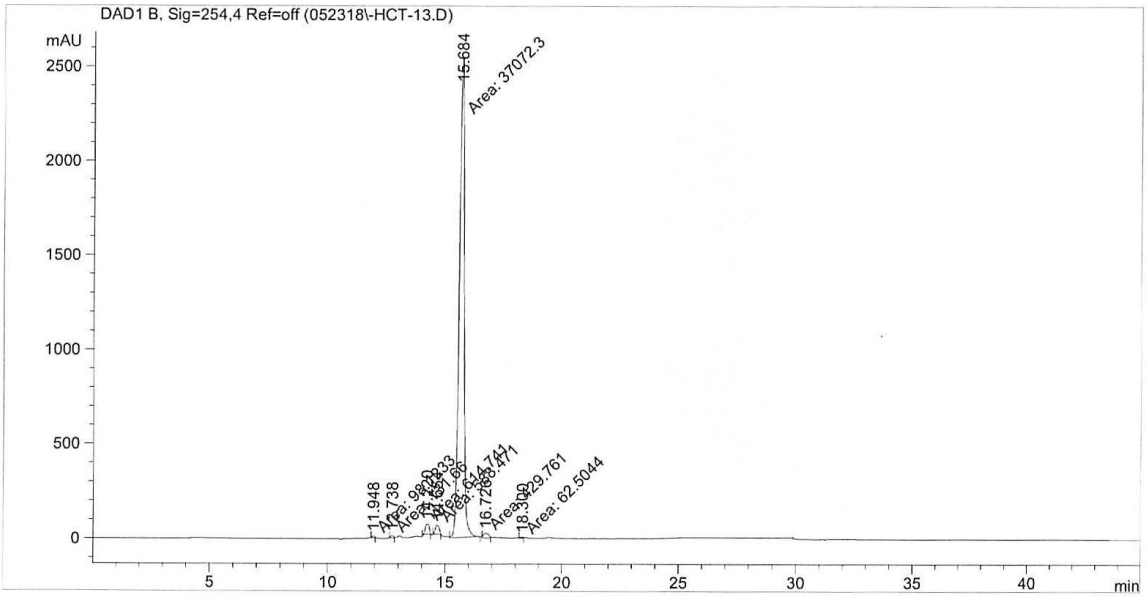


```
=====================================================================
                    Area Percent Report
=====================================================================

Sorted By             :      Signal
Multiplier            :      1.0000
Dilution              :      1.0000
Use Multiplier & Dilution Factor with ISTDs


Signal 1: DAD1 B, Sig=254,4 Ref=off

Peak RetTime Type  Width     Area      Height     Area
  #   [min]        [min]   [mAU*s]     [mAU]       %
----|-------|----|-------|----------|----------|--------|
   1  11.948 MM    0.1486   98.12334   11.00892   0.2516
   2  12.738 MM    0.1684  131.65993   13.03351   0.3376
   3  14.220 MM    0.1882  614.74054   54.44167   1.5764
   4  14.654 MM    0.2011  588.47076   48.76412   1.5090
   5  15.684 MM    0.2423 3.70723e4  2550.12134  95.0631
   6  16.726 MM    0.2764  429.76059   25.91330   1.1020
   7  18.300 MM    0.1926   62.50444    5.40915   0.1603

Totals :                  3.89975e4  2708.69201
```

HPLC Trace of IQ-3

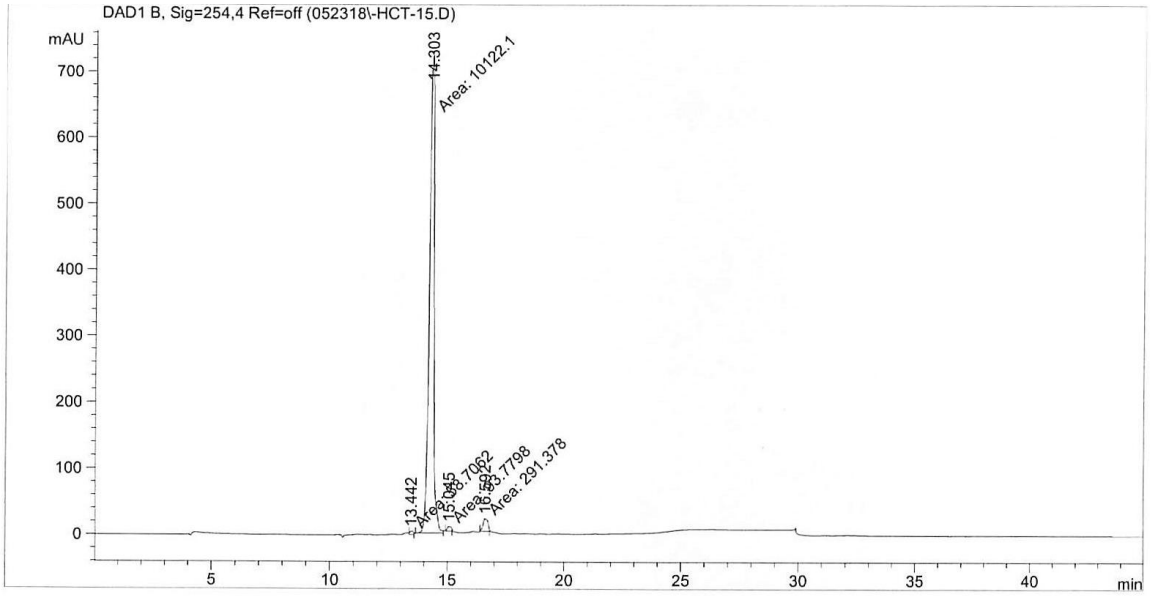


```
=====================================================================
                        Area Percent Report
=====================================================================

Sorted By             :      Signal
Multiplier            :      1.0000
Dilution              :      1.0000
Use Multiplier & Dilution Factor with ISTDs


Signal 1: DAD1 B, Sig=254,4 Ref=off

Peak RetTime Type  Width     Area      Height     Area
  #   [min]        [min]   [mAU*s]     [mAU]       %
----|-------|----|-------|----------|----------|--------|
   1  13.442 MM    0.1763   58.70622    5.54899   0.5556
   2  14.303 MM    0.2331 1.01221e4   723.78229  95.7991
   3  15.045 MM    0.2048   93.77975    7.63180   0.8876
   4  16.592 MM    0.2473  291.37805   19.63848   2.7577

Totals :                  1.05660e4   756.60156
```

10 Publications and presentations

Clemens, D. Lee, B. Plamthottam, S. Tullius, M. Wang, R. Yu, CJ. Li, Z. Dillon, BJ. Zink, JI. and Horwitz, MA. Nanoparticle Formulation of Moxifloxacin and Intramuscular Route of Delivery Improve Antibiotic Pharmacokinetics and Treatment of Pneumonic Tularemia in a Mouse Model (Under review).

Plamthottam, S. Sun, D. Valkenburgh, JV. Valenzuela, J. Ruehle, B. Steele, D. Poddar, S. Hernandez, S. Radu, CG. Zink, JI. Spectrochemical Assays to Understand Structure-Activity Relationships of Anticancer Drug Triapine and its Analogs (Under review).

Yu, CJ. Plamthottam, S. Intracellular iron delivery by an MSN carrier potentiates Fenton reactions *in vitro* (In preparation).

Plamthottam, S. Synthesis of Porous Alumina Nanoparticles—A New Drug Delivery Vehicle (In preparation).

Plamthottam, S. Valenzuela, J. Sun, D. Valkenburgh, JV. Steele, D. Poddar, S. Satyamurthy, N. Radu, CG. Zink, JI. (2018) Spectroscopic Assays to Explore Structure-Activity Relationships of a Phase II Clinical Anti-Cancer Drug. Poster presentation. *255th Annual American Chemical Society Meeting and Exposition, New Orleans, Louisiana.*

Plamthottam, S. (2015) pH Responsive Mesoporous Silica Nanoparticles for Drug Delivery. Oral presentation. *SCIP Southern California Inorganic Photochemistry Conference*.

An, K. Alayoglu, S. Musselwhite, N. Plamthottam, S. Melaet, G. Lindeman, A. & Somorjai, G. A. (2013). Enhanced CO Oxidation Rates at the Interface of Mesoporous Oxides and Pt Nanoparticles. *Journal of the American Chemical Society*.

Garan, S. Plamthottam, S. et al. (2013). An interactive quantitative temporal physiological model of glucose passage and absorption through the gastrointestinal tract and subsequent modulation of insulin and glucagon secretion in humans. *FASEB Journal*. Vol. 27.

Plamthottam, S. (2013) International webinar to HP Internal Learning & Development series, and public access in US, Europe, Asia, Pacific regions. University Hall, Berkeley, CA. (https://bcgc.berkeley.edu/greener-solutions-2012/)

Plamthottam, S. (Spring 2012). Natural inspiration: A biomimetic path to biofuels production, *Berkeley Science Review*, Issue 22.

Plamthottam, S. (July 2011). Biomimetics spotlight: a gecko's special toes, *Berkeley Science Review.*

Plamthottam, S. (November 2011). Green Chemistry: Sustainable Renewal at UC Berkeley, *ACS Green Chemistry Nexus.*

11 Bibliography

1. Gibson, L. T. Mesosilica materials and organic pollutant adsorption: Part A removal from air. *Chemical Society Reviews* (2014). doi:10.1039/c3cs60096c
2. Wan, Y. & Zhao, D. On the controllable soft-templating approach to mesoporous silicates. *Chemical Reviews* (2007). doi:10.1021/cr068020s
3. Li, Z., Barnes, J. C., Bosoy, A., Stoddart, J. F. & Zink, J. I. Mesoporous silica nanoparticles in biomedical applications. *Chemical Society Reviews* 41, 2590–2605 (2012).
4. Beck, J. S. *et al.* A New Family of Mesoporous Molecular Sieves Prepared with Liquid Crystal Templates. *J. Am. Chem. Soc.* (1992). doi:10.1021/ja00053a020
5. Ying, J. Y., Mehnert, C. P. & Wong, M. S. Synthesis and Applications of Supramolecular-Templated Mesoporous Materials. *Angew. Chemie Int. Ed.* (1999).
6. Rühle, B., Saint-Cricq, P. & Zink, J. I. Externally Controlled Nanomachines on Mesoporous Silica Nanoparticles for Biomedical Applications. *ChemPhysChem* (2016). doi:10.1002/cphc.201501167
7. Lu, J., Liong, M., Zink, J. I. & Tamanoi, F. Mesoporous silica nanoparticles as a delivery system for hydrophobic anticancer drugs. *Small* 3, 1341–1346 (2007).
8. Meng, H. *et al.* Use of size and a copolymer design feature to improve the biodistribution and the enhanced permeability and retention effect of doxorubicin-loaded mesoporous silica nanoparticles in a murine xenograft tumor model. *ACS Nano* (2011). doi:10.1021/nn200809t
9. Lee, B. Y. *et al.* Redox-Triggered Release of Moxifloxacin from Mesoporous Silica Nanoparticles Functionalized with Disulfide Snap-Tops Enhances Efficacy Against Pneumonic Tularemia in Mice. *Small* 12, 3690–3702 (2016).
10. Li, Z. *et al.* Mesoporous Silica Nanoparticles with pH-Sensitive Nanovalves for Delivery of Moxifloxacin Provide Improved Treatment of Lethal Pneumonic Tularemia. *ACS Nano* (2015). doi:10.1021/acsnano.5b04306
11. Shahin, S. A. *et al.* Hyaluronic acid conjugated nanoparticle delivery of siRNA against TWIST reduces tumor burden and enhances sensitivity to cisplatin in ovarian cancer. *Nanomedicine Nanotechnology, Biol. Med.* (2018). doi:10.1016/j.nano.2018.04.008
12. Roberts, C. M. *et al.* Nanoparticle delivery of siRNA against TWIST to reduce drug resistance and tumor growth in ovarian cancer models. *Nanomedicine Nanotechnology, Biol. Med.* (2017). doi:10.1016/j.nano.2016.11.010
13. Antholine, W. E., Knight, J. M. & Petering, D. H. Inhibition of Tumor Cell Transplantability by Iron and Copper Complexes of 5-Substituted 2-

Formylpyridine Thiosemicarbazones. *J. Med. Chem.* (1976). doi:10.1021/jm00224a030

14. Aye, Y., Long, M. J. C. & Stubbe, J. Mechanistic studies of semicarbazone triapine targeting human ribonucleotide reductase in vitro and in mammalian cells: Tyrosyl radical quenching not involving reactive oxygen species. *J. Biol. Chem.* 287, 35768–35778 (2012).
15. Le, T. M. *et al.* ATR inhibition facilitates targeting of leukemia dependence on convergent nucleotide biosynthetic pathways. *Nat. Commun.* 8, (2017).
16. Kim, W. *et al.* [^{18} F]CFA as a clinically translatable probe for PET imaging of deoxycytidine kinase activity. *Proc. Natl. Acad. Sci.* (2016). doi:10.1073/pnas.1524212113
17. Vélez, J. *et al.* Mitochondrial Uncoupling and the Reprograming of Intermediary Metabolism in Leukemia Cells. *Front. Oncol.* (2013). doi:10.3389/fonc.2013.00067
18. Manoj C. Desai, N. A. M. *Successful Strategies for the Discovery of Antiviral Drugs*.
19. Wang, Q.-Y. *et al.* Inhibition of Dengue Virus through Suppression of Host Pyrimidine Biosynthesis. *J. Virol.* 85, 6548–6556 (2011).
20. Yeo, K. L. *et al.* Synergistic suppression of dengue virus replication using a combination of nucleoside analogs and nucleoside synthesis inhibitors. *Antimicrob. Agents Chemother.* 59, 2086–2093 (2015).
21. Bonavia, A. *et al.* Identification of broad-spectrum antiviral compounds and assessment of the druggability of their target for efficacy against respiratory syncytial virus (RSV). *Proc. Natl. Acad. Sci. U. S. A.* (2011). doi:10.1073/pnas.1017142108
22. Lockshin, A. *et al.* Antitumor activity and minimal toxicity of concentrated thymidine infused in nude mice. *Cancer Res.* 45, 1797–1802 (1985).
23. Li, Z., Barnes, J. C., Bosoy, A., Stoddart, J. F. & Zink, J. I. Mesoporous silica nanoparticles in biomedical applications. *Chemical Society Reviews* 41, 2590 (2012).
24. Parodi, A. *et al.* Bromelain Surface Modi fi cation Increases the Di ff usion of Silica Nanoparticles in the Tumor Extracellular Matrix. 9874–9883 (2014).
25. Meng, H. *et al.* Autonomous in vitro anticancer drug release from mesoporous silica nanoparticles by pH-sensitive nanovalves. *J. Am. Chem. Soc.* 132, 12690–12697 (2010).
26. Lu, J., Liong, M., Li, Z., Zink, J. I. & Tamanoi, F. Biocompatibility, biodistribution, and drug-delivery efficiency of mesoporous silica nanoparticles for cancer therapy in animals. *Small* 6, 1794–1805 (2010).
27. B, A. K. R., Debnath, S. & Babu, M. N. Nanoemulsion-a Novel Approach for Lipophilic Drugs: A Review. 3, 84–92 (2013).
28. Mehta, S. K., Kaur, G. & Bhasin, K. K. Analysis of Tween based

microemulsion in the presence of TB drug rifampicin. *Colloids Surfaces B Biointerfaces* 60, 95–104 (2007).

29. Garg, J. Emerging trends in nanoemulsion design and therapeutics: A Reveiew. 2, 1–16 (2014).
30. Meng, H. *et al.* Autonomous in vitro anticancer drug release from mesoporous silica nanoparticles by pH-sensitive nanovalves. *J. Am. Chem. Soc.* 132, 12690–12697 (2010).
31. Mackenzie, E. L., Iwasaki, K. & Tsuji, Y. Intracellular Iron Transport and Storage: From Molecular Mechanisms to Health Implications. *Antioxid. Redox Signal.* 10, 997–1030 (2008).
32. Dixon, S. J. & Stockwell, B. R. The role of iron and reactive oxygen species in cell death. *Nature Chemical Biology* 10, 9–17 (2014).
33. Ding, W. Q. & Lind, S. E. Metal ionophores - An emerging class of anticancer drugs. *IUBMB Life* 61, 1013–1018 (2009).
34. Shimada, K. *et al.* Copper-Binding Small Molecule Induces Oxidative Stress and Cell-Cycle Arrest in Glioblastoma-Patient-Derived Cells. *Cell Chem. Biol.* 25, 585–594.e7 (2018).
35. Tarn, D. *et al.* In vitro delivery of calcium ions by nanogated mesoporous silica nanoparticles to induce cancer cellular apoptosis. *Mol. Syst. Des. Eng.* 2, 384–392 (2017).
36. Tan, S., Sagara, Y., Liu, Y., Maher, P. & Schubert, D. The regulation of reactive oxygen species production during programmed cell death. *J. Cell Biol.* 141, 1423–1432 (1998).
37. Blagosklonny, M. V. Cell death beyond apoptosis. *Leukemia* 14, 1502–1508 (2000).
38. Dixon, S. J. *et al.* Ferroptosis: An iron-dependent form of nonapoptotic cell death. *Cell* 149, 1060–1072 (2012).
39. Akladios, F. N., Andrew, S. D. & Parkinson, C. J. Improved cytotoxicity of pyridyl-substituted thiosemicarbazones against MCF-7 when used as metal ionophores. *BioMetals* 29, 157–170 (2016).
40. King, M. A. & Radicchi-Mastroianni, M. A. Effects of caspase inhibition on camptothecin-induced apoptosis of HL-60 cells. *Cytometry* 49, 28–35 (2002).
41. Williams, O. Flow cytometry-based methods for apoptosis detection in lymphoid cells. *Methods Mol. Biol.* 282, 31–42 (2004).
42. Tarn, D., Xue, M. & Zink, J. I. PH-responsive dual cargo delivery from mesoporous silica nanoparticles with a metal-latched nanogate. *Inorg. Chem.* 52, 2044–2049 (2013).
43. Cotí, K. K. *et al.* Mechanised nanoparticles for drug delivery. *Nanoscale* 1, 16–39 (2009).
44. Liu, M., Li, H., Luo, G., Liu, Q. & Wang, Y. Pharmacokinetics and biodistribution of surface modification polymeric nanoparticles. *Arch.*

Pharm. Res. 31, 547–554 (2008).

45. Hwang, A. A. *et al.* Tuberculosis: pH-Responsive Isoniazid-Loaded Nanoparticles Markedly Improve Tuberculosis Treatment in Mice (Small 38/2015). *Small* 11, 5065 (2015).
46. Clemens, D. L. *et al.* Targeted intracellular delivery of antituberculosis drugs to Mycobacterium tuberculosis-infected macrophages via functionalized mesoporous silica nanoparticles. *Antimicrob. Agents Chemother.* 56, 2535–2545 (2012).
47. Fenaroli, F. *et al.* Nanoparticles as drug delivery system against tuberculosis in zebrafish embryos: Direct visualization and treatment. *ACS Nano* 8, 7014–7026 (2014).
48. Chou, T. C. & Talalay, P. Quantitative analysis of dose-effect relationships: the combined effects of multiple drugs or enzyme inhibitors. *Adv. Enzyme Regul.* 22, 27–55 (1984).
49. Chou, T.-C. Theoretical Basis, Experimental Design, and Computerized Simulation of Synergism and Antagonism in Drug Combination Studies. *Pharmacol. Rev.* 58, 621–681 (2006).
50. Schentag, J. J., Nix, D. E. & Adelman, M. H. Mathematical examination of dual individualization principles (I): Relationships between AUC above MIC and area under the inhibitory curve for cefmenoxime, ciprofloxacin, and tobramycin. *DICP, Ann. Pharmacother.* 25, 1050–1057 (1991).
51. Moore, R. D., Lietman, P. S. & Smith, C. R. Clinical Response to Aminoglycoside Therapy: Importance of the Ratio of Peak Concentration to Minimal Inhibitory Concentration. *J. Infect. Dis.* 155, 93–99 (1987).
52. Wright, D. H., Brown, G. H., Peterson, M. L. & Rotschafer, J. C. Application of fluoroquinolone pharmacodynamics. *J. Antimicrob. Chemother.* 46, 669–83 (2000).
53. Kourtis, I. C. *et al.* Peripherally Administered Nanoparticles Target Monocytic Myeloid Cells, Secondary Lymphoid Organs and Tumors in Mice. *PLoS One* 8, (2013).
54. Friedman, A., Claypool, S. & Liu, R. The Smart Targeting of Nanoparticles. *Curr. Pharm. Des.* 19, 6315–6329 (2013).
55. Lu, J., Li, Z., Zink, J. I. & Tamanoi, F. In vivo tumor suppression efficacy of mesoporous silica nanoparticles-based drug-delivery system: Enhanced efficacy by folate modification. *Nanomedicine Nanotechnology, Biol. Med.* 8, 212–220 (2012).
56. Ghosh, S. C. *et al.* Comparison of DOTA and NODAGA as chelators for64Cu-labeled immunoconjugates. *Nucl. Med. Biol.* 42, 177–183 (2015).
57. Li, T. *et al.* Antitumor Activity of cGAMP via Stimulation of cGAS-cGAMP-STING-IRF3 Mediated Innate Immune Response. *Sci. Rep.* 6, 1–14 (2016).

58. Demaria, O. *et al.* STING activation of tumor endothelial cells initiates spontaneous and therapeutic antitumor immunity. *Proc. Natl. Acad. Sci.* 112, 15408–15413 (2015).
59. Baird, J. R. *et al.* Radiotherapy combined with novel STING-targeting oligonucleotides results in regression of established tumors. *Cancer Res.* 76, 50–61 (2016).
60. Fu, J. *et al.* STING agonist formulated cancer vaccines can cure established tumors resistant to PD-1 blockade. *Sci. Transl. Med.* 7, (2015).
61. Deng, L. *et al.* STING-dependent cytosolic DNA sensing promotes radiation-induced type I interferon-dependent antitumor immunity in immunogenic tumors. *Immunity* 41, 543–852 (2014).
62. Deng, L., Liang, H., Fu, S., R.weichselbaum, R. & Fu, Y. X. From DNA damage to nucleic acid sensing: A strategy to enhance radiation therapy. *Clin. Cancer Res.* 22, 20–25 (2016).
63. Finlay, J. *et al.* Mesoporous silica nanoparticle delivery of chemically modified siRNA against TWIST1 leads to reduced tumor burden. *Nanomed - Nanotechnol* 11, 1657–66 (2015).
64. Sun, B. *et al.* Engineering an effective immune adjuvant by designed control of shape and crystallinity of aluminum oxyhydroxide nanoparticles. *ACS Nano* 7, 10834–10849 (2013).
65. Shchukin, D. G. & Caruso, R. A. Template synthesis and photocatalytic properties of porous metal oxide spheres formed by nanoparticle infiltration. *Chem. Mater.* 16, 2287–2292 (2004).
66. Danks, A. E., Hall, S. R. & Schnepp, Z. The evolution of 'sol–gel' chemistry as a technique for materials synthesis. *Mater. Horiz.* 3, 91–112 (2016).
67. Mehrotra, R. C. Synthesis and reactions of metal alkoxides. *J. Non. Cryst. Solids* 100, 1–15 (1988).
68. Park, Y. K., Tadd, E. H., Zubris, M. & Tannenbaum, R. Size-controlled synthesis of alumina nanoparticles from aluminum alkoxides. *Mater. Res. Bull.* 40, 1506–1512 (2005).
69. Jafar Tafreshi, M. & Masoomi Khanghah, Z. Infrared spectroscopy studies on sol-gel prepared alumina powders. *Medziagotyra* 21, 28–31 (2015).
70. Ell, J. D. R. I. J. & Farmer, V. C. Lattice vibrations of boebmite (y-AlOOH): evidence for a Cl ," rather than a 0 :: space group. 34, 1151–1153 (1978).
71. Fripiat, J. J. Proton mobility in solids. I. Hydrogenic vibration modes and proton delocalization in boehmite. *J. Phys. Chem.* 71, 1097–1111 (1967).
72. Tettenhorst, R. & Hofmann, D. A. Crystal Chemistry of Boehmite. *Clays Clay Miner.* 28, 373–380 (1980).
73. Mathews, C. K. The Most Interesting Enzyme in the World. *Structure* 24, 843–844 (2016).
74. Uhlin, U. & Eklund, H. Structure of ribonucleotide reductase protein R1.

Nature 370, 533–539 (1994).
75. Nordlund, P. & Reichard, P. Ribonucleotide Reductases. *Annu. Rev. Biochem.* 75, 681–706 (2006).
76. Aird, K. M. & Zhang, R. Nucleotide metabolism, oncogene-induced senescence and cancer. *Cancer Letters* 356, 204–210 (2015).
77. Le, T. M. *et al.* ATR inhibition facilitates targeting of leukemia dependence on convergent nucleotide biosynthetic pathways. *Nat. Commun.* 8, (2017).
78. Liu, M. C., Lin, T. S., Cory, J. G., Cory, A. H. & Sartorelli, A. C. Synthesis and biological activity of 3- and 5-amino derivatives of pyridine-2-carboxaldehyde thiosemicarbazone. *J. Med. Chem.* 39, 2586–2593 (1996).
79. Cory, J. G. *et al.* Structure-function relationships for a new series of pyridine-2-carboxaldehyde thiosemicarbazones on ribonucleotide reductase activity and tumor cell growth in culture and in vivo. *Adv Enzym. Regul* 35, 55–68 (1995).
80. Finch, R. A., Liu, M. C., Cory, A. H., Cory, J. G. & Sartorelli, A. C. Triapine (3-aminopyridine-2-carboxaldehyde thiosemicarbazone; 3-AP): An inhibitor of ribonucleotide reductase with antineoplastic activity. in *Advances in Enzyme Regulation* 39, 3–12 (1999).
81. Dai, L. *et al.* Ribonucleotide reductase represents a novel therapeutic target in primary effusion lymphoma. *Oncogene* 1–7 (2017). doi:10.1038/onc.2017.122
82. Cory, J. G. *et al.* Inhibitors of ribonucleotide reductase. Comparative effects of amino- and hydroxy-substituted pyridine-2-carboxaldehyde thiosemicarbazones. *Biochem. Pharmacol.* 48, 335–344 (1994).
83. Finch, R. a *et al.* Triapine (3-aminopyridine-2-carboxaldehyde-thiosemicarbazone): A potent inhibitor of ribonucleotide reductase activity with broad spectrum antitumor activity. *Biochem. Pharmacol.* 59, 983–991 (2000).
84. Nutting, C. M. *et al.* Phase II study of 3-AP Triapine in patients with recurrent or metastatic head and neck squamous cell carcinoma. *Ann. Oncol.* 20, 1275–1279 (2009).
85. Traynor, A. M. *et al.* A phase II trial of triapine (NSC# 663249) and gemcitabine as second line treatment of advanced non-small cell lung cancer: Eastern Cooperative Oncology Group Study 1503. *Invest. New Drugs* 28, 91–97 (2010).
86. Chaston, T. B., Lovejoy, D. B., Watts, R. N. & Richardson, D. R. Examination of the antiproliferative activity of iron chelators: Multiple cellular targets and the different mechanism of action of triapine compared with desferrioxamine and the potent pyridoxal isonicotinoyl hydrazone analogue 311. *Clin. Cancer Res.* 9, 402–414 (2003).
87. Lin, Z. P. *et al.* Excess ribonucleotide reductase R2 subunits coordinate the

S phase checkpoint to facilitate DNA damage repair and recovery from replication stress. *Biochem. Pharmacol.* 73, 760–772 (2007).

88. Buss, J. L., Greene, B. T., Turner, J., Torti, F. M. & Torti, S. V. Iron chelators in cancer chemotherapy. *Curr. Top. Med. Chem.* 4, 1623–1635 (2004).
89. Yu, Y., Wong, J., Lovejoy, D. B., Kalinowski, D. S. & Richardson, D. R. Chelators at the cancer coalface: Desferrioxamine to triapine and beyond. *Clinical Cancer Research* 12, 6876–6883 (2006).
90. Kowol, C. R. *et al.* Impact of metal coordination on cytotoxicity of 3-aminopyridine-2- carboxaldehyde thiosemicarbazone (Triapine) and novel insights into terminal dimethylation. *J. Med. Chem.* 52, 5032–5043 (2009).
91. Kappus, H. Overview of enzyme systems involved in bioreduction of drugs and in redox cycling. *Biochem. Pharmacol.* 35, 1–6 (1986).
92. Richardson, D. R. *et al.* 2-Acetylpyridine thiosemicarbazones are potent iron chelators and antiproliferative agents: Redox activity, iron complexation and characterization of their antitumor activity. *J. Med. Chem.* (2009). doi:10.1021/jm801585u